

Topics in Current Chemistry Collections

Journal Editors

Massimo Olivucci, Siena, Italy and Bowling Green, USA

Wai-Yeung Wong, Hong Kong, China

Series Editors

Hagan Bayley, Oxford, UK

Greg Hughes, Codexis Inc, USA

Christopher A. Hunter, Cambridge, UK

Seong-Ju Hwang, Seoul, South Korea

Kazuaki Ishihara, Nagoya, Japan

Barbara Kirchner, Bonn, Germany

Michael J. Krische, Austin, USA

Delmar Larsen, Davis, USA

Jean-Marie Lehn, Strasbourg, France

Rafael Luque, Córdoba, Spain

Jay S. Siegel, Tianjin, China

Joachim Thiem, Hamburg, Germany

Margherita Venturi, Bologna, Italy

Chi-Huey Wong, Taipei, Taiwan

Henry N.C. Wong, Hong Kong, China

Vivian Wing-Wah Yam, Hong Kong, China

Chunhua Yan, Beijing, China

Shu-Li You, Shanghai, China

Aims and Scope

The series *Topics in Current Chemistry Collections* presents critical reviews from the journal *Topics in Current Chemistry* organized in topical volumes. The scope of coverage is all areas of chemical science including the interfaces with related disciplines such as biology, medicine and materials science.

The goal of each thematic volume is to give the non-specialist reader, whether in academia or industry, a comprehensive insight into an area where new research is emerging which is of interest to a larger scientific audience.

Each review within the volume critically surveys one aspect of that topic and places it within the context of the volume as a whole. The most significant developments of the last 5 to 10 years are presented using selected examples to illustrate the principles discussed. The coverage is not intended to be an exhaustive summary of the field or include large quantities of data, but should rather be conceptual, concentrating on the methodological thinking that will allow the non-specialist reader to understand the information presented.

Contributions also offer an outlook on potential future developments in the field.

More information about this series at <http://www.springer.com/series/14181>

Yan Li • Shigeo Maruyama
Editors

Single-Walled Carbon Nanotubes

Preparation, Properties and Applications

With contributions from

Hakim Amara • Moh. R. Amer • Christophe Bichara • Xuan Cao
Yu Cao • Sen Cong • Guodong Dong • E. H. Hasdeo • Jun Hirotani
N. T. Hung • W. Izumida • Il Jeon • Xilai Jia • Esko I. Kauppinen
Patrik Laiho • Meihui Li • Pan Li • Yan Li • Xuelel Liang
Qingzhou Liu • Xiyan Liu • Shigeo Maruyama • Yutaka Matsuo
A. R. T. Nugraha • Yutaka Ohno • Iianmao Peng • R. Saito
Boyuan Tian • Xiao Wang • Fei Wei • Nan Wei • Fanqi Wu • Jiye Xia
Feng Yang • Jin Zhang • Qiang Zhang • Xiulan Zhao • Ming Zheng
Chongwu Zhou

 Springer

Editors

Yan Li
Peking University
Beijing, China

Shigeo Maruyama
The University of Tokyo
Tokyo, Japan

Partly previously published in Top Curr Chem (Z) Volume 374 (2016); Top Curr Chem (Z) Volume 375 (2017); Top Curr Chem (Z) Volume 376 (2018); Topics in Current Chemistry Volume 377 (2019).

ISSN 2367-4067

Topics in Current Chemistry Collections

ISBN 978-3-030-12699-5

© Springer Nature Switzerland AG 2019

This work is subject to copyright. All rights are reserved by the Publisher, whether the whole or part of the material is concerned, specifically the rights of translation, reprinting, reuse of illustrations, recitation, broadcasting, reproduction on microfilms or in any other physical way, and transmission or information storage and retrieval, electronic adaptation, computer software, or by similar or dissimilar methodology now known or hereafter developed.

The use of general descriptive names, registered names, trademarks, service marks, etc. in this publication does not imply, even in the absence of a specific statement, that such names are exempt from the relevant protective laws and regulations and therefore free for general use.

The publisher, the authors and the editors are safe to assume that the advice and information in this book are believed to be true and accurate at the date of publication. Neither the publisher nor the authors or the editors give a warranty, expressed or implied, with respect to the material contained herein or for any errors or omissions that may have been made. The publisher remains neutral with regard to jurisdictional claims in published maps and institutional affiliations.

This Springer imprint is published by the registered company Springer Nature Switzerland AG
The registered company address is: Gewerbestrasse 11, 6330 Cham, Switzerland

Contents

Preface.....	vii
Modeling the Growth of Single-Wall Carbon Nanotubes.....	1
Hakim Amara and Christophe Bichara: Top Curr Chem (Z) 2017, 2019:55 (8, May 2017) DOI 10.1007/s41061-017-0141-8	
Metallic Catalysts for Structure-Controlled Growth of Single-Walled Carbon Nanotubes.....	25
Meihui Li, Xiyan Liu, Xiulan Zhao, Feng Yang, Xiao Wang and Yan Li: Top Curr Chem (Z) 2017, 2019:29 (1, March 2017) DOI 10.1007/s41061-017-0116-9	
Preparation of Horizontal Single-Walled Carbon Nanotubes Arrays.....	69
Pan Li and Jin Zhang: Top Curr Chem (Z) 2016, 2019:85 (30, November 2016) DOI 10.1007/s41061-016-0085-4	
Recent Developments in Single-Walled Carbon Nanotube Thin Films Fabricated by Dry Floating Catalyst Chemical Vapor Deposition	99
Qiang Zhang, Nan Wei, Patrik Laiho and Esko I. Kauppinen: Top Curr Chem (Z) 2017, 2019:90 (27, November 2017) https://doi.org/10.1007/s41061-017-0178-8	
Sorting Carbon Nanotubes.	129
Ming Zheng: Top Curr Chem (Z) 2017, 2019:13 (12, January 2017) DOI 10.1007/s41061-016-0098-z	
Electronic and Optical Properties of Single Wall Carbon Nanotubes	165
R. Saito, A. R. T. Nugraha, E. H. Hasdeo, N. T. Hung and W. Izumida: Top Curr Chem (Z) 2017, 2019:7 (28, December 2016) DOI 10.1007/s41061-016-0095-2	

Review of Electronics Based on Single-Walled Carbon Nanotubes.....	189
---	------------

F , , .



() ()



Modeling the Growth of Single-Wall Carbon Nanotubes

Hakim Amara¹ · Christophe Bichara²

Received: 7 November 2016 / Accepted: 16 April 2017 / Published online: 8 May 2017
© Springer International Publishing Switzerland 2017

Abstract More than 20 years after their discovery, our understanding of the growth mechanisms of single-wall carbon nanotubes is still incomplete, in spite of a large number of investigations motivated by potential rewards in many possible applications. Among the many techniques used to solve this challenging puzzle, computer simulations can directly address an atomic scale that is hardly accessible by other experiments, and thereby support or invalidate different ideas, assumptions, or models. In this paper, we review some aspects of the computer simulation and theoretical approaches dedicated to the study of single-wall carbon nanotube growth, and suggest some ways towards a better control of the synthesis processes by chemical vapor deposition.

Keywords SWNT · Growth mechanisms · Modeling · CVD

1 Introduction

Almost 25 years after their first identification, carbon nanotubes [1] (CNTs), among which the single-wall ones (SWNTs) [2] are most promising for applications related to their electronic properties, still face very difficult challenges regarding their controlled and selective synthesis. Selectivity may concern the tube's electronic

Chapter 1 was originally published as Amara, A. & Bichara C. Top Curr Chem (Z) (2017) 375: 55. DOI 10.1007/s41061-017-0141-8.

✉ Christophe Bichara
bichara@cinam.univ-mrs.fr

¹ Laboratoire d'Etude des Microstructures, ONERA-CNRS, BP 72, 92322 Châtillon Cedex, France

² Aix Marseille University, CNRS, CINAM, Campus de Luminy, Marseille, France

properties (semiconducting or metallic), or, even more challenging, its structure, characterized by its chiral indexes (n , m). Quite amazingly after hundreds of papers devoted to the subject, a very recent review [3] still stresses the lack of complete understanding of the SWNT growth mechanisms and ways towards controlled selectivity. Because its ability to be upscaled to industry requirements, catalytic chemical vapor deposition (CCVD, or CVD here, in short) is the method of choice that is most widely used and investigated. Very briefly, it consists of the decomposition of carbon-bearing molecules on a nanosized catalyst particle, typically a metallic one, which eventually gives rise to a tube that keeps growing until some event causes the growth to stop. All this takes place at high temperature (600–1100 °C), in a complex ambient, with catalyst nanoparticles either bound to a substrate, or floating at the tip of the growing tube. This complex synthesis has been studied by a very large number of techniques. Among these, theoretical modeling and computer simulation stand in a particular position, since they directly address the atomic scale that is relevant to the problem, with a number of approximations, though. An extended review by leading experts has been published recently [4] and we refer the interested reader to it. Our goal here is to give a more personal viewpoint, focusing on some recent results, some of which still in the process of being published, that have been obtained in close collaboration with experimental groups. In fact, we do believe that this is the most fruitful, though not the fastest, way to progress in this difficult field.

While some models [5] discuss kinetic aspects of SWNT growth, neglecting the role of the catalyst nanoparticle, we focus here on catalyst nanoparticles, their interaction with carbon under CVD growth conditions, and their interface with the tube, that are critical to understand nucleation and growth mechanisms. In doing so, we pay attention to thermodynamic aspects of the growth, and, to start with, we can remember that carbon science has a long history. Growing a tube indeed displays some similarities with the growth of carbon fibers, except that the very small nanoparticle and tube diameters induce some peculiarities that are discussed later. As explained in [6], the growth of filamentous carbon on a Ni catalyst results from a gradient of carbon chemical potential between the carbon atoms delivered at the surface of the catalyst by the precursor decomposition, and the carbon sp^2 walls that act as a sink for carbon since they are at a lower Gibbs energy. In this process, the chemical potential of carbon at the nanoparticle surface is fixed by the thermochemical conditions of the precursor decomposition reaction. It can hence be tuned by playing with CVD parameters: temperature, pressure, and composition of the gas feed.

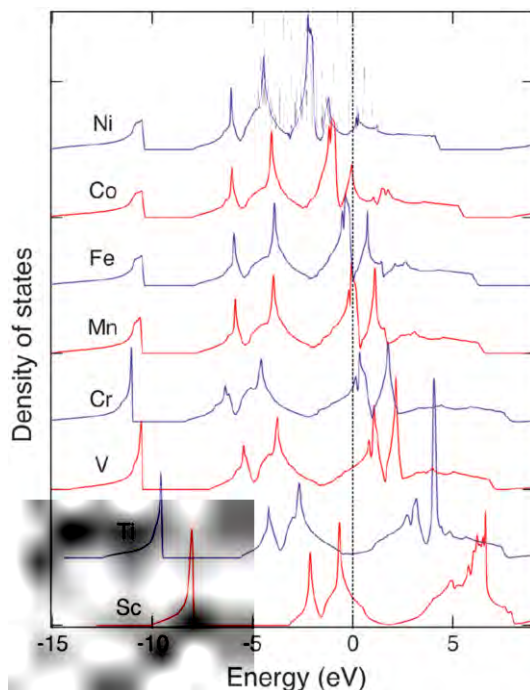
The approach we develop explicitly takes this carbon chemical potential into account, while it is somewhat by-passed in other contributions that are also presented in this paper. Starting from some general considerations on the carbon–metal catalyst interaction, we discuss the atomistic models and computer simulation techniques. Their possibilities and limitations are discussed and we then briefly summarize some peculiarities of the interface between nickel, cobalt, and iron catalysts, and the sp^2 carbon layer forming graphene or nanotube wall. A critical analysis of the different ways to address the nucleation and growth of SWNTs is then proposed, followed by a discussion of our viewpoint on the ways to control the SWNTs' diameter by tuning their “growth mode”. Carbon dissolution in subsurface

or bulk of the nanoparticles and the physical, solid, or molten, state of the nanoparticles are shown to be important since they contribute to modify their surface and interface properties.

2 Metal–Carbon Interactions

Until now, most CCVD experiments offering a reasonable yield and a possible upscaling to industrial dimensions use nanoparticles of late transition metals, or alloys, as catalysts. Fe, Co, and Ni, the lightest elements of these columns 8, 9, 10 of the periodic table have been extensively used. These elements are sometimes used alloyed [7, 8], or in conjunction with other metals such as Mo [9], Cu [10], or, more recently W [11]. The reason why Fe, Co, and Ni have been so popular catalysts is that they display a large enough affinity for carbon, to adsorb carbon precursor molecules and possibly dissolve some carbon, while keeping it in the surface layers. This is sometimes illustrated in the form of a “volcano” plot [12, 13]. Looking at the electronic densities of states of carbides of transition metals of the first row in a (sometimes fictitious) NaCl structures, displayed in Fig. 1, one immediately realizes that a rigid-band model is valid to describe the density of states of carbides. Indeed, at low energy, a narrow band derived from the 2s states of carbon can be identified. At higher energy, a fairly broad band of strongly hybridized states between the p states of carbon and the metallic d states appears, with a pseudogap, exactly separating bonding states from antibonding states in the case of Ti, that is known to

Fig. 1 Density of states of carbides with transition element of the 3d series, in a rocksalt structure, calculated with DFT-GGA. The Fermi level is set to zero. Ref. [14]



form a very stable carbide. For Fe, Co, and Ni, this hybridization effect is weaker, and the Fermi level shifted to higher energies, explaining why carbides of these elements are less stable. The outstanding ability of transition metals to combine strongly with carbon stems from the major role played by covalent bonds formed between the p states of carbon atoms and the valence d states of the metal ones, leading to an hybridized pd band [14, 15].

For Fe, Co, and Ni, this carbon–metal interaction also directly translates into specific features of their phase diagrams that display limited carbon solubility. Solubility limits of carbon in bulk Ni and Co are quite similar, around 4% atomic carbon fraction at their respective eutectic temperatures, with no stable bulk carbide structure reported. Carbon solubility is larger in Fe with (meta-)stable carbide phases observed. Deck and Vecchio [16], who led a systematic study of metals with various carbon solubilities, point out that efficient catalysts have a limited, though non-zero carbon solubility, while metals with vanishing C-solubility or forming stable carbide compounds do not promote SWNT growth. If one considers the possibility to open the parameter space by including alloyed nanoparticles, this conclusion leaves space for discovering other, more efficient and selective catalysts.

Considering bulk thermodynamic properties and phase diagrams is a first step, but does not tell much about the details of carbon–metal interactions. CCVD synthesis of SWNTs is a surface process involving catalyst particles in the 1–5 nm diameter range, where strong nanometric size effects should be expected. Although in situ XPS experiments have been performed during SWNT growth [17–19] or Pd-based catalysis [20], emphasizing the role of subsurface carbon, a real insight in carbon metal interaction is typically provided by ab initio calculations. Such calculations, generally performed within the framework of the density functional theory (DFT), provide accurate estimates of the interaction energy between carbon in various forms, and different metals, considering different configurations: adsorbed on surfaces, at step edges, or in interstitial sites [21, 22]. As shown in Fig. 2, Ni and Pd display [21] rather similar energetics with respect to carbon, with subsurface sites more prone to accept carbon incorporation.

DFT calculations appear as the reference tool to study the relative stability of nanotubes in contact with the nanoparticle from which they grow [23, 24], thus emphasizing the need for adequate tube/catalyst interaction strength, or searching for efficient catalysts, beyond the well-established Fe, Co, and Ni. Such calculations have been used to study the interaction energy of carbon flakes [25, 26] and nanotube caps with catalyst nanoparticles or flat surfaces, searching for preferential lattice matching of the cap [27], and hence tube chiralities. Quite recently, calculations searching for an optimal matching of some tube's chirality with an appropriate lattice plane of crystalline W_6Co_7 [11] or WC [28] have been proposed to support the interpretation of chiral selective CVD experiments, assuming a vapor–solid–solid model [29] of SWNT growth. Whether such perfect crystalline facets actually exist during CVD synthesis of SWNTs is still to be proven, illustrating a classical dilemma of computer simulations in materials science: use highly accurate methods on ideal, though possibly non-relevant

Fig. 2 a Schematic representation of carbon positions at metal surfaces. b Binding energies of monoatomic and diatomic carbon on different late-transition (Ni, Pd, Pt) and coinage (Cu, Ag, Au) metals. Ref. [21]

structures, or approximate ones, able to directly deal with the complexity of the problem (here: high temperature, presence of active carbon, and ambient,...) at the expense of accuracy. Beyond these calculations, interesting new approaches tackle the decomposition of molecular carbon precursors, such as methane [30] or ethanol [31] on the catalyst surface. These results show that CCVD process is indeed more complex than the interaction of atomic carbon with a bare catalyst surface, as often described in computer simulations of SWNT growth. Before returning to our main topic, let us mention that non-metallic catalysts [32–34] have been successfully used to grow nanotubes, though not always with a high enough yield.

dynamics-force biased Monte Carlo computer simulation algorithm, leading to less defective carbon structures. Choosing an alternative at the opposite end of the complexity scale for the description of the interatomic interactions, but still manageable for decent molecular dynamics simulations, Irle et al. [38] used density functional tight binding (DFTB) to simulate the early stages of the nucleation of tubes on various catalysts, such as Fe or Ni [39, 40], or more exotic catalysts, such as alumina [41]. Although lighter than plain DFT calculations, such models still suffer from a non-linear scaling with system sizes, and hence are limited in size- and time-scales. Retaining the physically grounded assumptions of the tight binding approximation, but in a lighter, order N way, the present authors developed a tight binding model for Ni–C alloys, approximated at the fourth moment of the local electronic density of states, and incorporated in a Monte Carlo code working in either canonical or grand canonical ensemble [14].

Beyond these carbon–metal interaction models, additional degrees of complexity should be considered. Among the important factors that are generally overlooked in computer simulations, the ambient and the presence of molecular fragments, in particular hydrogen, oxygen, hydroxyls etc., adsorbed on the nanoparticle surface certainly represent major issues. Except for the recent work of Shibuta et al. [30], and Khalikov et al. [42], the decomposition of the carbon precursor at the catalyst surface is generally not taken into account. Also, in real supported CVD processes, the substrate, quite often an oxide (SiO_2 , Al_2O_3 ...) plays an important role to stabilize the catalyst nanoparticle along the growth. A strong interaction between the nanoparticle and its support will change its shape and thermodynamic properties. This has been studied [43, 44], in relation with in situ TEM observation of SWNT growth [45].

Once an interatomic energy model has been selected, one has to choose a computer simulation technique to simulate some aspects of the CVD synthesis, since, quite obviously, a full atomistic description of the process is not possible, and approximations have to be made. The most straightforward idea is to use molecular dynamics simulations to “throw” carbon atoms onto the cluster surface, and to regularly feed new carbon atoms in the gas phase to keep its density almost constant. This approach suffers from many drawbacks. The first is the short computed time scale, leading to observed growth rates that are often orders of magnitude faster than the experimental one. The most recent and longest simulations [46], though, growing nanometer long tubes over a few 100-ns MD trajectories, are closer to, but still higher than experimental growth rates. The second is that the key quantity to address the reactivity of carbon at the surface of a catalyst is its chemical potential, which is fixed by the thermochemistry of the precursor decomposition reaction, and not simply by a gas phase pressure. An interesting discussion of this thermodynamic aspect in the case of the growth of filamentous carbon is given by Snoeck et al. [6]. The statistical mechanical framework to deal with this carbon chemical potential is the grand canonical ensemble that can be conveniently sampled by Monte Carlo simulations. However, these computer simulation techniques are designed to deal with thermodynamic equilibrium situations, and not with growth. In the present instance, its use can be justified assuming a local thermodynamic equilibrium at the tube nanoparticle interface, because growth is slow as compared to the high atomic mobility at typical

CVD temperatures [47]. Clearly, choices have to be made, which will emphasize different aspects of the growth process.

These challenging requirements explain why only a few groups actively worked on the understanding of the SWNT growth mechanisms, using various computer simulation approaches, and focusing on different aspects of the problem.

4 Properties of the sp^2 Carbon Wall–Metal Catalyst Interface

At the heart of the SWNT synthesis mechanism lies the close contact between the growing tube and the metal nanoparticle that enables the molecular feedstock to decompose, yielding atomic carbon that is then incorporated in the tube wall. Apart from the nanometric scale of the process in the case of SWNTs, similar behaviors have been observed and discussed in the context of carbon nanowires and graphene growth, and valuable insight has been gained in these somewhat easier cases.

The burst of experimental and theoretical work devoted to the mechanisms of graphene growth on different substrates, reviewed by Batzill [48], brings useful and sometimes surprising information. Different experimental and theoretical studies [21, 49] have shown that, in the case of graphene growth on face-centered cubic (111) nickel surfaces, the most favorable place to incorporate individual carbon atoms or dimers is in octahedral subsurface interstitial sites. On a free Ni surface, upon increasing carbon feed and at high temperature, carbon atoms would diffuse towards the bulk, and a carbon concentration gradient, with a carbon enrichment close to the surface would be observed. Quite surprisingly though, once a graphene layer is formed on the surface of Ni, a depletion of carbon close to the interface is observed. This has been evidenced experimentally [50], using in situ, depth-resolved X-ray photoemission spectroscopy (XPS) during graphene growth, a technique that is quite efficient to address this surface science problem. As illustrated in Fig. 4, this has also been independently observed [51], using both tight binding and DFT calculations, and similar experimental in situ XPS technique.

This latter reference also shows that the adhesion energy of a graphene layer on a Ni surface becomes weaker when carbon atoms are present in Ni subsurface. Empirically tuning the work of adhesion between the tube and the metal nanoparticle, Ribas et al. [52] have shown the importance of this parameter to enable the nucleation and growth of a tube, and avoid catalyst encapsulation. In this respect, the role of dissolved carbon in the nanoparticle is fundamental, since it will affect the interfacial and wetting properties of Ni (and also Co and Fe), as shown in the early 1970s for bulk metal drops on graphite [53]: for these elements, the contact angle of a bulk metal drop on a graphite surface increases from 50° to 120°, when the fraction of carbon dissolved in the metal increases from 0 to about 2.7 wt%. Remembering Young–Dupré’s equation:

$$1 + \cos \theta = \frac{W_{\text{adh}}(x_{\text{C}})}{\gamma_{\text{M}(x_{\text{C}})}},$$

where θ is the contact angle, W_{adh} is the work of adhesion, and $\gamma_{\text{M}(x_{\text{C}})}$ is the surface energy of the metal nanoparticle, at a carbon concentration x_{C} , one can see that a vanishing work of adhesion and a lower but finite surface energy, both resulting from the increase of x_{C} , lead to an increase of the contact angle θ . According to our calculations [54], displayed in Fig. 5, this effect is particularly marked for small nanoparticles that can incorporate larger carbon fractions (up to about $x_{\text{C}} = 0.20\text{--}0.25$) than macroscopic ones. Both carbon depletion close to Ni surface, and change of wetting and interfacial properties induced by carbon dissolution in the nanoparticles, will have a significantly stronger effect in the case of SWNT growth than for larger, macroscopic systems. These calculations, performed for Ni, are probably qualitatively valid for Co and Fe. Indeed, DFT-based calculation of surface energies of Fe [55] show a dependence on the surface coverage by carbon atoms, which remains limited because only crystalline structures are considered.

Fig. 5 Wetting properties of Ni on sp^2 carbon. **a** Contact angles of a Ni nanoparticle on graphene after performing Monte Carlo simulations at 1000 K (*red triangles*) and 1400 K (*green squares*) for different carbon concentration. Ref [54]. **b** Experimental contact angle of an Ni droplet containing carbon deposited on graphite at 1550 °C. Ref. [53]

5 Nucleation of Carbon Caps

From a fundamental point of view, nucleation is a stochastic and rare event, the frequency of which is related to the magnitude of its driving force. In the present instance, this driving force is the excess of carbon chemical potential, relative to that of C atoms dissolved in the NP, at the saturation limit. Quite generally, most direct computer simulations of nucleation rely on exceedingly large driving forces to observe nucleation [56] in the short time of the simulation. Sophisticated biased methods [57] have been proposed to address this problem. In spite of this, most computer simulation studies devoted to SWNT synthesis are in fact dealing with nucleation mechanisms, because they involve smaller numbers of atoms, while the total number of atoms in the computer simulation box remains an issue for reasonably accurate carbon–metal interaction models. There is also a widespread belief that the SWNT structure can be controlled at the nucleation step. This might seem reasonable since C–C bonds are quite strong, and difficult to break and reform in order to heal or form a defect (non-hexagonal ring) that could modify the tube chirality. However, a number of in situ TEM investigations [17, 58] of SWNT growth tend to indicate that very short nanotube nuclei, say below 3 nm, as typically considered in computer simulations, are not stable. Along the same line, post-mortem statistical investigations of SWNT length distribution suggested [59] that a critical length threshold (around 5 nm) exists, beyond which stable and sustainable growth would take place. In addition, this study exhibits some nanoparticles giving birth to two tube nuclei. Since no such configuration is observed for longer, stable tubes, one has to conclude that one of the nuclei disappeared or both merged, a possibility that has been nicely illustrated numerically (see Fig. 6) in the computer simulations of Neyts et al. [60], and post-mortem TEM observations.

In spite of this possible limitation, studying the SWNT nucleation mechanisms is still quite relevant since it can provide guidance in the quest for better, more selective catalysts. As early as 2004, using an empirical atomic interaction model, Ding et al. [35] demonstrated that small Fe catalyst nanoparticles should be carbon-saturated in order to nucleate a (very defective) tube cap. This is illustrated in Fig. 7. Almost simultaneously, an impressive attempt to directly simulate the nucleation of

Fig. 6 Formation of two small caps during the first steps of the nucleation process from: a atomic scale modelization. Ref. [60]; b post-mortem TEM observations. Ref. [59]

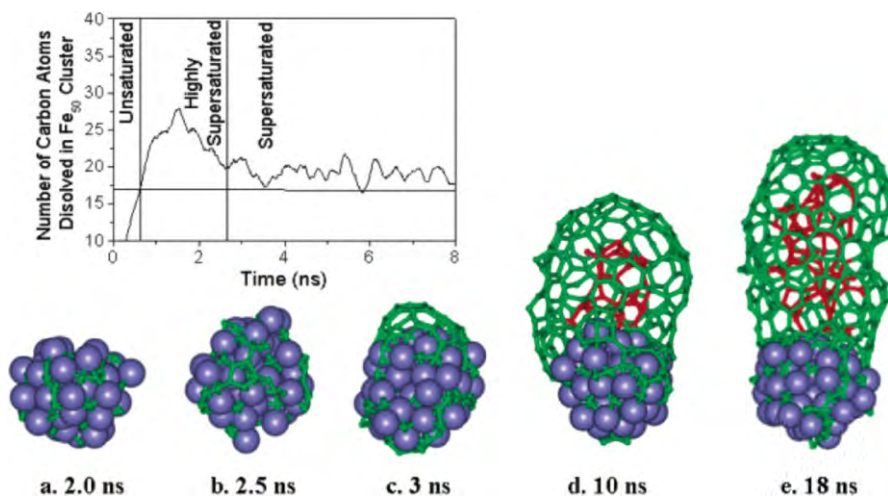


Fig. 7 *Top* evolution of the carbon concentration inside the nanoparticle during the formation of the tube. *Bottom* simulation growth evolution of a carbon nanotube from a cluster containing 50 Fe atoms at 900 K. Carbon atoms inside the tubular structure are represented in *red*. Ref. [35]

a tube cap on a small Fe nanoparticle using DFT-based molecular dynamics has been proposed by Raty et al. [61]. However, it was soon realized that such a calculation was too far from real experimental conditions, because of a too high C incorporation rate and a too short total simulated time. An intermediate route was then proposed by the Irlé/Morokuma group [62], using their DFTB Molecular Dynamics modeling, which is a somewhat more efficient trade-off between chemical accuracy and computing efficiency. Page et al. [63] compared SWNT nucleation on Ni and Fe small nanoparticles of less than 100 atoms, pointing out differences between these two metal catalysts that could be attributed to differences in the strength of metal–carbon interactions. In the case of Ni, a study [64] taking into account carbon chemical potential as the control variable to calculate carbon sorption isotherms using grand canonical Monte Carlo simulations, enabled to investigate the energetics and the role of carbon atoms, either dissolved inside the nanoparticle, in sub-surface, or segregated outside. Cap nucleation was shown to take place in a well-defined chemical potential range, when a critical concentration of surface carbon atom is reached. In both studies, this cap formation follows the same process, described in Fig. 8: saturation of sub-surface with carbon atom, formation of polyynes weakly bound to the surface that ultimately connect each other to form Y-shaped junctions and then 5- and 6-membered rings.

The caps structures observed in these simulations are far from being perfect, with an excess of 5- and 7-membered rings as compared to ideal ones formed with six pentagons, the rest being hexagons. Whether this is due to the too short time scales spanned by the computer simulation or a genuine effect, characteristic of the early stages of tube nucleation is indeed an interesting question that would influence the way one can envision strategies towards a controlled and selective SWNT synthesis. If the cap formation takes place at random, selectivity should be searched

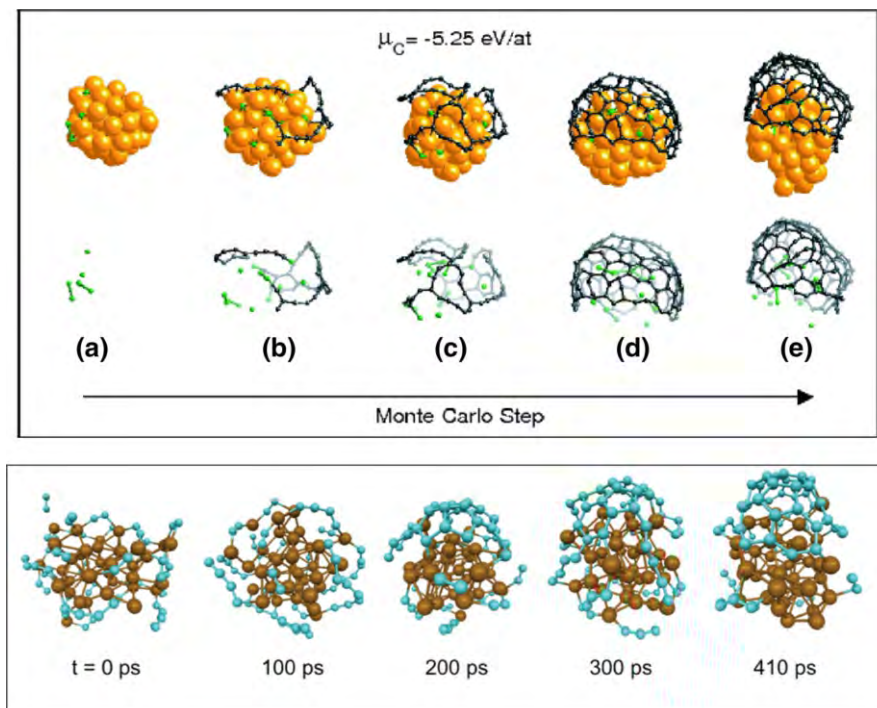


Fig. 8 *Upper panel* grand Canonical Monte Carlo simulations on a Ni cluster at 1000 K and $\mu_C = -5.25 \text{ eV/at}$. Different stages of the nucleation of a C cap are presented, where linear chains act as precursors to grow a graphene network on the Ni surface. Ni atoms are orange, outer C atoms are black, surface or bulk C atoms are green. Ref. [64]. *Lower panel* nucleation of a tube cap on an Fe_{38} nanoparticle simulated by DFTB-based molecular dynamics. Polyne chains are formed first, then cross forming Y-junctions and ring are formed, starting with pentagons. Obvious similarities exist between MC and MD approaches. Ref. [38]

elsewhere, either during growth itself, or by removing (etching) undesirable tubes during the synthesis or after it. If the cap structure is fixed at the very early stages of the nucleation, a smart engineering of the catalyst and growth conditions could lead to selectivity. This issue is quite complex, not yet solved up to now, and different groups have followed different approaches [3].

Focusing here on theoretical contributions, we first note that, according to Penev et al. [65], no significant energy differences were observed among the large number (4548!) of cap structures studied, thus precluding a selectivity based on the energetics of the cap alone. One might then consider possible energy differences between cap structures, originating from the interaction of the cap with the catalyst, in the spirit of the early work of Reich et al. [27], followed by Gomez-Gualdron and Balbuena [66], and Wang et al. [67]. These calculations shed useful light on the electronic structure of the metal/carbon cap junction, which plays a major role for incorporating carbon atoms at the rim of the tube, but do not provide strong evidence for preferential chiralities. In addition, they are performed on idealized pure metal structures, —flat Ni layer, Co or Ni clusters, while there is little doubt

that carbon is dissolved close to the surface for such metals under growth conditions [68]. Quantum chemistry or DFT-based calculations investigated in detail the electronic structure of the cap/catalyst interface [67].

Summarizing theoretical studies of tube nucleation and cap formation mechanisms, it seems that they provide no strong support of the idea that the tube structure can be controlled at the nucleation step. What has been proposed, however, is that a matching could exist between a given tube structure and the solid-state particle from which it grew [11]. In this paper, DFT-based calculations were performed at 0 K, to study the matching of tubes with different chiralities on a (0, 0, 12) plane of a W_6Co_7 nanoparticle, in order to explain CVD experiments performed at 1030 °C, implicitly assuming a crystal structure and neglecting the temperature-induced disorder.

This raises the question of the catalyst nanoparticle's state under reaction conditions at high temperature, in the presence of a complex gaseous ambient, and usually interacting with a substrate. This very complex problem cannot be treated in full, and a number of approximations have to be made. Apart from the work of Jiang et al. [69], who calculated Fe–C phase diagrams of nanoparticles in the 1.1–1.6 nm range, with and without alumina substrate, the latter is generally neglected. Ding et al. [70] and Engelmann et al. [71] studied the melting behavior of Fe–C and Ni–C clusters, respectively. A full phase diagram calculation for Ni–C clusters, including F.C.C. and icosahedral Ni structures between 55 and 807 Ni atoms, has recently been proposed by Magnin et al. [72]. This phase diagram is simply a translation in the concentration-temperature space of the carbon sorption isotherms, calculated in a chemical potential-temperature space [73], but it enables one to understand directly the differences brought about by the nanometric size of the nanoparticles, as compared to a bulk system. Both are displayed in Figs. 9 and 10. The most striking ones, as far as nucleation and growth of SWNTs are concerned, are the important downshift of the eutectic temperature, and the existence of a crystalline core–molten shell domain, instead of the solid–liquid two-phase domain of the bulk phase diagram. These calculations also indicate that, on Ni nanoparticles below 3 nm, nucleation will take place on a non-crystalline surface for temperatures above ~800 K, meaning that for Ni or similar metals, no epitaxial control of the tube structure during the nucleation and growth can be expected.

6 Modeling the Growth of Carbon Nanotubes

Apart from the work of Gavillet et al. [74], investigating how C atoms can diffuse and attach to the tube rim, thus supporting a root growth mechanism, papers reporting simulations where tubes are grown up to a decent length usually rely on simplified carbon–metal interaction models. For many of these, a model validation is not always available, leaving the reader with unanswered questions about their range of applicability. However, similar SWNT growth mechanisms on Ni nanoparticles, involving the formation and coalescence of polyynes chains that forms the carbon rings, have been evidenced using approximate TB-based GCMC calculations and more accurate DFTB-based molecular dynamics [75], thus

Fig. 9 Carbon sorption isotherms on face-centered cubic, Wulff-shaped, nanoparticles, with 201, 405, and 807 Ni atoms. Carbon fraction (x_C) inside the nanoparticle is plotted as a function of temperature and C chemical potential (μ_C). Four different temperatures are considered. Ref. [73]

mutually supporting the robustness of these findings. In both cases, though, and in other similar calculations [52, 63] as well, the poor quality of the structures generated is a major problem: most direct computer simulations of nanotube growth are impaired by an excess of defects created probably because of the too short time range spanned. Very recently, MD simulations of a few 100 ns have been performed [46] and seem to overcome this hurdle. Beyond a certain fraction of defects, we are more dealing with amorphous sp^2 bonded carbon, than real tubes. On the opposite, some perfect tubes have been grown [76], but make use of a questionable modified Monte Carlo algorithm. Simply growing a tube on the computer is not very interesting, if grown tubes are too defective to enable defining their chirality. Trying to understand how defects can be healed [77], is more relevant. The role of the metal catalyst in the healing process has been underlined [78–80], suggesting that once a defect survives the early stages of the growth, close to the catalyst nanoparticle, it has a lower probability to get healed.

Beyond these important though somewhat neglected issues, two highly debated questions concerning growth mechanisms and a possible control of the tubes' chirality during their synthesis have been addressed from a theory and modeling point of view. The first one concerns the respective role of thermodynamic and kinetic contributions to the chiral selectivity. The screw dislocation model of nanotube growth, proposed by Yakobson et al. [5], predicts that the growth rate should be proportional to the tube's chiral angle. It has been validated by some experiments, among which in situ Raman spectroscopy on individual growing tubes

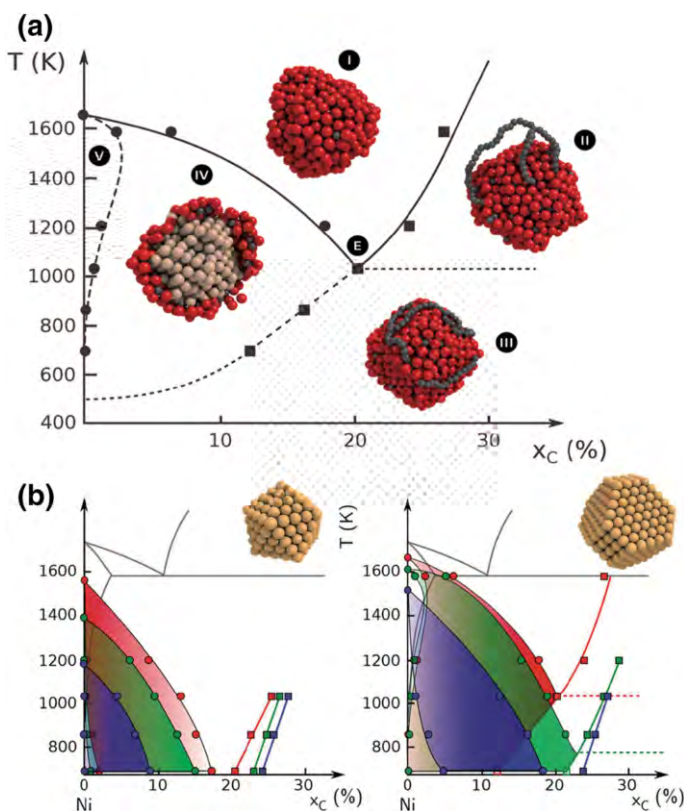


Fig. 10 **a** Ni–C phase diagram for a Ni nanoparticle with 807 Ni atoms, as calculated from grand Canonical Monte Carlo simulations. Different phases can be identified: *I* homogeneous liquid solution; *II* C segregation at the surface of liquid NP; *III* C segregation at the surface of mostly solid NP; *IV* solid core (beige)/liquid shell (red) nanoparticle, with upper liquid cap removed to visualize the crystalline core; *V* solid solution. **b** Size-dependent Ni–C phase diagrams for icosahedral (left 55, 147, and 309 Ni atoms) and face-centered cubic (right 201, 405, and 807 Ni atoms) nanoparticles compared to the bulk one (full black line). Ref. [72]

[81]. In this kinetic approach, the main point of controversy is the neglect of the catalyst nanoparticle and CVD conditions, while many reports [82–84] underline the role of the catalyst, substrate, pressure, and temperature on the resulting (n, m) distribution of nanotubes formed. The second one concerns the structure of the catalyst nanoparticle under growth conditions. Assuming a crystalline structure of the catalyst, Artyukhov et al. [85] developed a model showing that chiral distribution results from antagonistic trends. Thermodynamic stability criterion favors a flat contact between the tube and the nanoparticle crystalline surface, hence the zig-zag or armchair edges, while the above-mentioned kinetic factor would favor chiral tubes. As a result, shown in Fig. 11, a strong preference towards (n, n–1) chiralities is predicted. Interestingly, somewhat similar lattice-matching arguments have been used to explain recent findings of favored (12, 6) [11] and (8, 4) [28] chiralities. Quite obviously, some clarification is needed, and we now focus

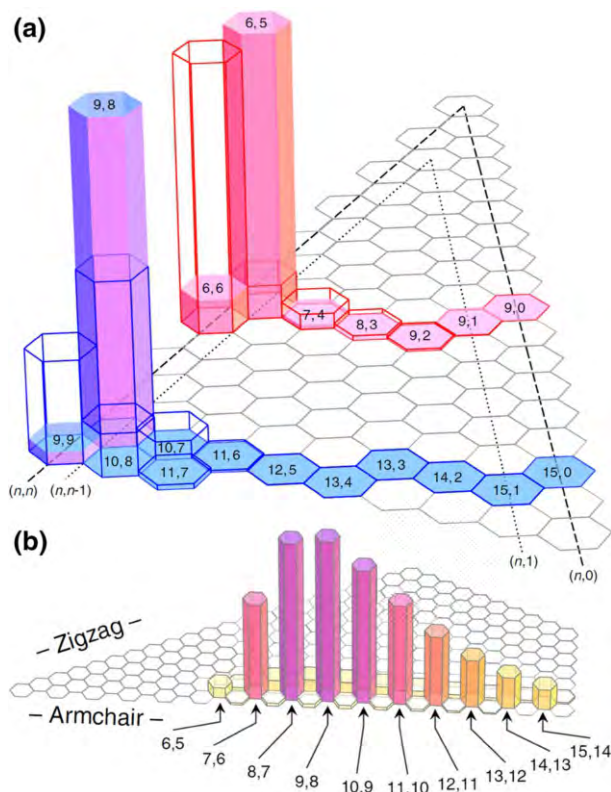


Fig. 11 a Chiral distributions resulting from the models proposed by Ding et al. [5] (empty bars), further refined by Artyukhov et al. [85] (full bars) in the case of a solid-state catalyst. b In the latter model, interfacial energies calculated by molecular dynamics lead to very sharp $(n, n-1)$ probability distributions, even though the temperature considered is significantly higher than experimental ones

on less controversial situations where the nanoparticle is soft enough—fully liquid or with a solid core—disordered shell structure—to adapt itself to the tube structure.

7 Controlling Growth Modes

If a full control of the tube's chirality is a highly desirable, yet very difficult goal, establishing a relationship between the diameter of the tube and that of the nanoparticle from which it grows is already quite useful. A systematic TEM analysis of this relation has been performed by Fiawoo et al. [59], who proposed to discriminate between so-called “perpendicular” and “tangential” growth modes (see Figs. 12, 13). The former corresponds to situations where the tube diameter is significantly smaller than that of the particle from which it grew, the latter, sometimes called “octopus” in reference to the carbon chains crawling around the nanoparticles, to the case where both diameters are almost equal. Quite recently, significant progress has been achieved in this direction, based on the understanding

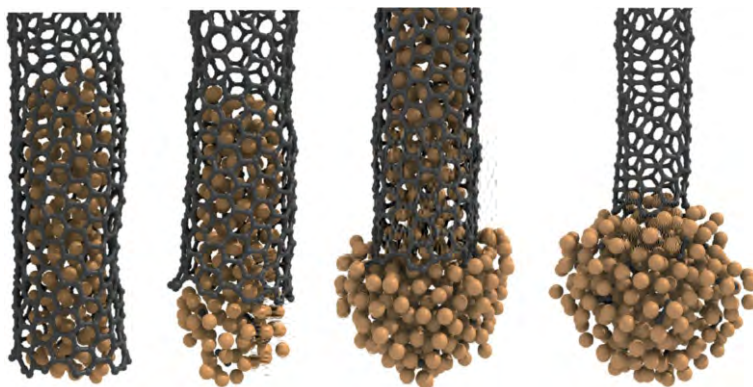


Fig. 12 Sketch of nanotube/nanoparticle geometries resulting from our Monte Carlo relaxations at 1200 K, ranging from tangential (*left*) to perpendicular (*right*), when C content inside the NP increases. Courtesy Y. Magnin

[54] of the interplay between carbon solubility in typical catalysts such as Fe, Co, and Ni, and their wetting properties with respect to the sp^2 carbon wall of the tube. Since the following results are still in the process of being published, we give some more details on the consequences of the carbon concentration dependence of these interfacial properties on the control of the growth mode. It is characterized by the tube/nanoparticle diameter ratio, and finding a way to tune them is indeed essential, because many important properties depend on the tube diameter. Small-diameter tubes display a smaller number of (n, m) types, making a (n, m) selective growth in principle easier. Selective etching of metallic tubes has been shown [86] to be more efficient for smaller diameter tubes, probably because larger curvature makes small diameter tubes more reactive.

To control tube diameter, a first step is to start with a narrow size distribution of catalyst nanoparticles, which is now well under control experimentally. The second step is then to play with the growth mode, and here the input from joint experimental, essentially TEM [59], and computer simulations studies, proves essential. Turning back to the carbon solubility issue, the following computer simulation results provide direct visual evidence: we start by putting nanoparticles with 219 Ni atoms and variable fractions of carbon inside, in contact with SWNTs with different chiralities, and diameters around 0.9–1.2 nm. After relaxation at 1400 K with our TBMC code, we notice that the pure Ni nanoparticle is almost completely “sucked” in the SWNT and that the fully saturated one (with about 25% carbon dissolved in) remains outside. Between these two extreme cases, a partial wetting of the inner part of the tube is observed to increase with decreasing carbon fraction dissolved in the nanoparticle. This is displayed in Fig. 12. Visual inspection reveals that the metal inside the tube has a very small or vanishing fraction of carbon dissolved in, while the outer part of the nanoparticle retains most of the carbon atoms that were initially put in the Ni nanoparticle. This reminds us of the carbon depletion effect in Ni layers close to a Ni/graphene interface observed in [50, 51]. This splitting of the Ni nanoparticle into two parts, an almost pure one

Fig. 13 **a** *Left* typical carbon sorption isotherm showing the relation between the carbon chemical potential (μ_C) and the mole fraction x_C of carbon dissolved in the catalyst nanoparticle. *Right* diameter ratios $R_d = D_{\text{SWNT}}/D_{\text{NP}}$ (x -axis), plotted for different carbon concentrations (y -axis), and different tube chiralities, displayed with *different colors*. As indicated by the *dashed lines*, the growth mode depends on the driving force for carbon incorporation: small μ_C favors large R_d , while larger μ_C leads to smaller R_d . Courtesy Y. Magnin. **b** TEM images of SWCNTs grown by tangential mode (*left*) and perpendicular mode (*right*) from Fe NP. Courtesy M. He

inside the tube, and another one containing the remaining or totality of dissolved carbon outside the tube, is observed only for tubes with a diameter larger than ~ 0.8 nm. No metal can penetrate inside tubes with a smaller diameter. Alternatively, when tubes and nanoparticles are very large, in particular in the case of thicker multi wall carbon nanotubes, we can reasonably expect that the carbon depletion effect close to the sp^2 wall has a more limited influence. However, this tendency to form inhomogeneous nanoparticles with respect to their carbon content is relevant for the growth of high-quality SWNTs to be used in electronic applications, grown at high temperatures and in a 1–3 nm diameter range.

From these simulations, we can define an aspect ratio $R_d = \frac{d_{\text{SWNT}}}{d_{\text{NP}}}$, and calculate it by assuming a spherical shape of the outer part of the nanoparticle. This aspect ratio, plotted in Fig. 13, depends strongly on the carbon fraction dissolved in the nanoparticle (x_C), and seems to depend slightly on the tube chirality. This figure also

presents two TEM images of tubes grown on Fe nanoparticles displaying two different growth modes. The “perpendicular” one, with $R_d < 1$, has been obtained with CO as a feedstock, while CH₄ has been used for the “tangential” one, with $R_d \approx 1$. In the former, the tube/nanoparticle contact is reduced to a line, and in the latter, a much larger contact area between the tube and the nanoparticle is formed by the tube rim and the inner part of the tube that is wetted by the metal catalyst. This suggests (at least) two ways to control the growth mode, and hence the tube diameter distribution.

The first one is to play with the carbon chemical potential resulting from the catalytic decomposition of the feedstock on the nanoparticle surface. The carbon fraction inside the nanoparticle is indeed related to it via carbon sorption isotherms, such as those calculated in [73]. This is illustrated in Fig. 9. This provides a possible explanation to the experiments by Yao et al. [87] who used a temperature modulation to modify the tube diameter during its growth. At higher temperature, carbon solubility in the catalyst (Co or Fe) nanoparticle increases, hence the growth tends to be more “perpendicular”. Lowering temperature reversibly gives larger diameter tubes. Another straightforward way to achieve this experimentally is to change the feedstock. This has been done by He [88] who demonstrated that tube diameter could be reversibly modified by alternating CO and CH₄ feedstocks to create tube junctions with large diameter differences. In both cases, the observed reversibility indicates that the nanoparticle size is unaffected, leaving a change in carbon fraction dissolved in the nanoparticle as the only option to explain the observed modulation. Beyond these two proven techniques, one can imagine that shifting the equilibrium of the feedstock decomposition reaction by modulating the ambient, or the pressure of one of the reactants or products, might be an alternative.

The second one is to modify carbon solubility of the catalyst nanoparticle. We have tested numerically [89] the effect of changing it in our tight-binding model for nickel. Thanks to its physically grounded roots, it is quite easy to change the heat of solution of carbon inside Ni by simply shifting the relative positions of the nickel d- and carbon p-bands, keeping all other parameters constant. In doing so, we see in Fig. 14 that chemical potential thresholds to start incorporating carbon in the nanoparticles are shifted, as well as the solubility limits. Quite interestingly, we also note that lower carbon solubility enhances the differences between face-centered cubic and icosahedral nanoparticles. This might provide an explanation to the experimental observation [90] that, under the same CVD conditions, tubes would grow from fcc gold nanoparticles and not from icosahedral ones. How these growth modes can influence the SWNT structure is the next important question that is not yet fully understood.

8 Conclusions

In this paper, we show that computer simulation provides useful insight into the mechanisms of SWNT growth by CCVD. Highly accurate DFT-based calculations are used to investigate fundamentals of metal–carbon interactions, and give quantitative estimates of binding energies between tubes and metal surfaces or

Fig. 14 *Left* carbon sorption isotherms calculated at 1000 K, using grand Canonical Monte Carlo simulations for nanoparticles with 201, 309, and 405 Ni atoms. Different Ni–C models have been used, corresponding to different carbon solubilities. *Right* schematic representation of icosahedral and face-centered cubic nanoparticles, with different facets are presented. Ref.: Aguiar-Hualde et al. [89]

nanoparticles in different situations. Interatomic interaction potentials with various levels of complexity and accuracy are used to drive molecular dynamics or Monte Carlo simulations, which enables simulating different aspects of the SWNT synthesis, such as nucleation, growth, or defect healing. Apart from the paper by Ding et al. [23], growth termination mechanisms that are of great practical importance, have not been extensively investigated yet by atomistic models, and are not discussed.

A central point in this review is to stress the importance of considering the mutual interaction between the growing tube and the catalyst nanoparticle from which it grows. In most computer simulations, under growth conditions, the surface of the nanoparticle in contact with the tube appears to be disordered, even if its core sometimes remains crystalline [72]. Wetting properties of the metallic nanoparticle, with respect to the sp^2 carbon wall of the tube are shown to play an important role by controlling the growth modes. For Ni, taken as a typical and simple example, these interfacial properties, and hence the growth modes, depend on the carbon fraction dissolved in the nanoparticle. So do the growth modes, and hence the tube diameter.

From a more general point of view, if modeling and computer simulations significantly contributed to a better atomic scale understanding of SWNT growth

mechanisms over the last 10 years, a lot remains to be done to uncover the mechanisms underlying the experiments that have recently reported a (n, m) selective growth [11]. Apart from some stability calculations performed under conditions that might be far from the real experimental ones, and a kinetic model [5], based on a spiral growth hypothesis, that is not strongly supported by experimental evidence, no general and predictive model concerning the tube (n, m) structure is currently available. This leaves open challenges for future work.

Acknowledgements The research leading to these results has received funding from the European Union Seventh Framework Programme (FP7/2007-2013) under Grant Agreement No. 604472 (IRENA project) and French Research Funding Agency under Grant No. ANR-13-BS10-0015-01 (SYNAPSE project). Drs. M. He, Y. Magnin and J.-M. Aguiar-Hualde are gratefully acknowledged for making some of their results available prior to publication.

References

- Iijima S (1991) *Nature* 354:56–58
- Iijima S, Ichihashi T (1993) *Nature* 363:603–605
- Liu C, Cheng HM (2016) *J Am Chem Soc* 138:6690–6698
- Page AJ, Ding F, Irlé S, Morokuma K (2015) *Rep Prog Phys* 78:36501
- Ding F, Harutyunyan AR, Yakobson BI (2009) *Proc Natl Acad Sci* 106:2506–2509
- Snœck J, Froment GF, Fowles M (1997) *J Catal* 169:240–249
- Chiang W, Sankaran RM (2009) *Nat Mater* 8:882–886
- Chiang W-H, Sankaran RM (2012) *Carbon NY*. 50:1044–1050
- Bachilo SM, Balzano L, Herrera JE, Pompeo F, Resasco DE, Weisman RB (2003) *J Am Chem Soc* 125:11186–11187
- He M, Chernov AI, Fedotov PV, Obratsova ED, Sainio J, Rikkinen E, Jiang H, Zhu Z, Tian Y, Kauppinen EI, Niemelä M, Krause AOI (2010) *J Am Chem Soc* 132:13994–13996
- Yang F, Wang X, Zhang D, Yang J, Luo D, Xu Z, Wei J, Wang J-Q, Xu Z, Peng F, Li X, Li R, Li Y, Li M, Bai X, Ding F, Li Y (2014) *Nature* 510:522–524
- Nørskov JK, Bligaard T, Logadottir A, Bahn S, Hansen LB, Bollinger M, Bengaard H, Hammer B, Slijivancanin Z, Mavrikakis M, Xu Y, Dahl S, Jacobsen CJH (2002) *J Catal* 209:275–278
- Robertson J (2012) *J Mater Chem* 22:19858
- Amara H, Roussel J-M, Bichara C, Gaspard J-P, Ducastelle F (2009) *Phys Rev B* 79:14109
- Schwarz KJ (1977) *Phys C Solid State Phys* 10:195–210
- Deck C, Vecchio K (2006) *Carbon NY* 44:267–275
- Hofmann S, Sharma R, Ducati C, Du G, Mattevi C, Cepek C, Cantoro M, Pisana S, Parvez A, Cervantes-Sodi F, Ferrari AC, Dunin-Borkowski R, Lizzit S, Petaccia L, Goldoni A, Robertson J (2007) *Nano Lett* 7:602–608
- Hofmann S, Blume R, Wirth CT, Cantoro M, Sharma R, Ducati C, Hävecker M, Zafeiratos S, Schnoerch P, Oestereich A, Teschner D, Albrecht M, Knop-Gericke A, Schlögl R, Robertson J (2009) *J Phys Chem C* 113:1648–1656
- Rinaldi A, Tessonnier J-P, Schuster ME, Blume R, Girgsdies F, Zhang Q, Jacob T, Abd Hamid SB, Su DS, Schlögl R (2011) *Angew Chem Int Ed Engl* 50:3313–3317
- Teschner D, Borsodi J, Wootsch A, Révay Z, Hävecker M, Knop-Gericke A, Jackson SD, Schlögl R (2008) *Science* 320:86–89
- Yazyev OV, Pasquarello A (2008) *Phys Rev Lett* 100:1–4
- Hu X, Björkman T, Lipsanen H, Sun L, Krashenninnikov AV (2015) *J Phys Chem Lett* 6:3263–3268
- Ding F, Larsson P, Larsson JA, Ahuja R, Duan H, Rosén A, Bolton K (2008) *Nano Lett* 8:463–468
- Silvearv F, Larsson P, Jones SLT, Ahuja R, Larsson JAJ (2015) *Mater Chem C* 3:3422–3427
- Fan X, Buczko R, Puzetzy A, Geohegan DB, Howe J, Pantelides S, Pennycook S (2003) *Phys Rev Lett* 90
- Yuan Q, Gao J, Shu H, Zhao J, Chen X, Ding F (2012) *J Am Chem Soc* 134:2970–2975
- Reich S, Li L, Robertson J (2006) *Chem Phys Lett* 421:469–472

28. Zhang S, Kang L, Wang X, Tong L, Yang L, Wang Z, Qi K, Deng S, Li Q, Bai X, Ding F, Zhang J (2017) *Nature* 543:234–238
29. Li M, Liu X, Zhao X, Yang F, Wang X, Li Y (2017) *Top Curr Chem* 375:29
30. Shibuta Y, Arifin R, Shimamura K, Oguri T, Shimojo F, Yamaguchi S (2013) *Chem Phys Lett* 565:92–97
31. Oguri T, Shimamura K, Shibuta Y, Shimojo F, Yamaguchi S (2014) *Chem Phys Lett* 595–596:185–191
32. Takagi D, Hibino H, Suzuki S, Kobayashi Y, Homma Y (2007) *Nano Lett* 7:2272–2275
33. Liu B, Ren W, Gao L, Li S, Pei S, Liu C, Jiang C, Cheng H-M (2009) *J Am Chem Soc* 131:2082–2083
34. Takagi D, Kobayashi Y, Homma Y (2009) *J Am Chem Soc* 131:6922–6923
35. Ding F, Bolton K, Rosén A (2004) *J Phys Chem B* 108:17369–17377
36. Martinez-Limia A, Zhao J, Balbuena PB (2007) *J Mol Model* 13:595–600
37. Neyts EC, Shibuta Y, van Duin ACT, Bogaerts A (2010) *ACS Nano* 4:6665–6672
38. Page AJ, Ohta Y, Irle S, Morokuma K (2010) *Acc Chem Res* 43:1375–1385
39. Ohta Y, Okamoto Y, Irle S, Morokuma K (2008) *ACS Nano* 2:1437–1444
40. Page AJ, Minami S, Ohta Y, Irle S, Morokuma K (2010) *Carbon NY* 48:3014–3026
41. Page AJ, Saha S, Li H-B, Irle S, Morokuma K (2015) *J Am Chem Soc* 137:9281–9288
42. Khalilov U, Bogaerts A, Neyts EC (2015) *Nat Commun* 6:10306
43. Burgos JC, Jones E, Balbuena PB (2011) *J Phys Chem C* 115:7668–7675
44. Growth SCN, Diego AG, Gómez-Gualdrón DA, McKenzie G, Alvarado JF, Balbuena PB (2012) *ACS Nano* 6:720–735
45. Gomez-Ballesteros JL, Burgos JC, Lin PA, Sharma R, Balbuena PB (2015) *RSC Adv* 5:106377–106386
46. Yoshikawa R, Maruyama S (private communication)
47. Lin M, Ying Tan JP, Boothroyd C, Loh KP, Tok ES, Foo Y-L (2006) *Nano Lett* 6:449–452
48. Batzill M (2012) *Surf Sci Rep* 67:83–115
49. Moors M, Amara H, Visart De Bocarmé T, Bichara C, Ducastelle F, Kruse N, Charlier J-C (2009) *ACS Nano* 3:511–516
50. Benayad A, Li X (2013) *J Phys Chem C* 117:4727–4733
51. Weatherup RS, Amara H, Blume R, Dlubak B, Bayer BC, Diarra M, Bahri M, Cabrero-Vilatela A, Caneva S, Kidambi PR, Martin M, Deranlot C, Seneor P, Schlögl R, Ducastelle F, Bichara C, Hofmann S (2014) *J Am Chem Soc* 136:13698–13708
52. Ribas MA, Ding F, Balbuena PB, Yakobson BI (2009) *J Chem Phys* 131:224501
53. Naidich YV, Perevertailo VM, Nevodnik GM (1971) *Powder Met Met Ceram* 10:45–47
54. Diarra M, Zappelli A, Amara H, Ducastelle F, Bichara C (2012) *Phys Rev Lett* 109:185501
55. Riikonen S, Krashennnikov AV, Nieminen R (2010) *Phys Rev B* 82:1–13
56. Honeycutt JD, Andersen HC (1984) *Chem Phys Lett* 108:535–538
57. van Duijneveldt JS, Frenkel D (1992) *J Chem Phys* 96:4655
58. Picher M, Lin PA, Gomez-Ballesteros JL, Balbuena PB, Sharma R (2014) *Nano Lett* 14:6104–6108
59. Fiawoo M-FC, Bonnot A-M, Amara H, Bichara C, Thibault-Pénissou J, Loiseau A (2012) *Phys Rev Lett* 108:195503
60. Neyts EC, van Duin ACT, Bogaerts A (2011) *J Am Chem Soc* 133:17225–17231
61. Raty J-Y, Gygi F, Galli G (2005) *Phys Rev Lett* 95:96103
62. Ohta Y, Okamoto Y, Irle S, Morokuma K, Page AJ, Wang Y (2009) *Nano Res* 2:755–767
63. Page AJ, Yamane H, Ohta Y, Irle S, Morokuma K (2010) *J Am Chem Soc* 132:15699–15707
64. Amara H, Bichara C, Ducastelle F (2008) *Phys Rev Lett* 100:56105
65. Penev ES, Artyukhov VI, Yakobson BI (2014) *ACS Nano* 8:1899–1906
66. Gomez-gualdrón DA, Balbuena PB (2009) *J Phys Chem C* 113:698–709
67. Wang Q, Yang S-W, Yang Y, Chan-Park MB, Chen Y (2011) *J Phys Chem Lett* 2:1009–1014
68. Wirth CT, Hofmann S, Robertson J (2009) *Diam Relat Mater* 18:940–945
69. Jiang A, Awasthi N, Kolmogorov A, Setyawan W, Börjesson A, Bolton K, Harutyunyan AR, Curtarolo S (2007) *Phys Rev B* 75:1–12
70. Ding F, Bolton K, Rosén A (2004) *J Vac Sci Technol A Vac Surf Film* 22:1471
71. Engelmann Y, Bogaerts A, Neyts EC (2014) *Nanoscale* 6:11981–11987
72. Magnin Y, Zappelli A, Amara H, Ducastelle F, Bichara C (2015) *Phys Rev Lett* 205502:1–5
73. Diarra M, Amara H, Ducastelle F, Bichara C (2012) *Phys Status Solidi* 249:2629–2634

74. Gavillet J, Loiseau A, Journet C, Willaime F, Ducastelle F, Charlier J-C (2001) *Phys Rev Lett* 87:275504
75. Page AJ, Irle S, Morokuma K (2010) *J Phys Chem C* 114:8206–8211
76. Xu Z, Yan T, Ding F (2015) *Chem Sci* 6:4704–4711
77. Page AJ, Ohta Y, Okamoto Y, Irle S, Morokuma K (2009) *J Phys Chem C* 113:20198–20207
78. Karoui S, Amara H, Bichara C, Ducastelle F (2010) *ACS Nano* 4:6114–6120
79. Diarra M, Amara H, Bichara C, Ducastelle F (2012) *Phys Rev B* 85:245446
80. Yuan Q, Xu Z, Yakobson BI, Ding F (2012) *Phys Rev Lett* 108:245505
81. Rao R, Liptak D, Cherukuri T, Yakobson BI, Maruyama B (2012) *Nat Mater* 11:1–4
82. Lolli G, Zhang L, Balzano L, Sakulchaicharoen N, Tan Y, Resasco DE (2006) *J Phys Chem B* 110:2108–2115
83. Wang B, Poa CHP, Wei L, Yang Y, Chen Y (2007) *J Am Chem Soc* 129:9014–9019
84. He M, Jiang H, Kauppinen EI, Lehtonen J (2012) *Nanoscale* 4:7394
85. Artyukhov VI, Penev ES, Yakobson BI (2014) *Nat Commun* 5:4892
86. Li J, Ke CT, Liu K, Li P, Liang S, Finkelstein G, Wang F, Liu J (2014) *ACS Nano* 8:8564–8572
87. Yao Y, Li Q, Zhang J, Liu R, Jiao L, Zhu YT, Liu Z (2007) *Nat Mater* 6:293–296
88. He M, Magnin Y, Amara H, Jiang H, Cui H, Fossard F, Castan A, Kauppinen E, Loiseau A, Bichara C (2017) *Carbon* 113:231–236
89. Aguiar-Hualde J-M, Magnin Y, Amara H, Bichara C, submitted to *Carbon*. <http://arxiv.org/abs/1702.06742>
90. He M, Amara H, Jiang H, Hassinen J, Bichara C, Ras RHA, Lehtonen J, Kauppinen EI, Loiseau A (2015) *Nanoscale* 7:20284–20289



Metallic Catalysts for Structure-Controlled Growth of Single-Walled Carbon Nanotubes

Meihui Li^{1,2} · Xiyan Liu¹ · Xiulan Zhao¹ ·
Feng Yang¹ · Xiao Wang¹ · Yan Li^{1,2} 

Received: 30 November 2016 / Accepted: 28 January 2017 / Published online: 1 March 2017
© Springer International Publishing Switzerland 2017

Abstract Single-walled carbon nanotubes (SWNTs) have shown great potential in various applications attributed to their unique structures and outstanding structure-dependent properties. The structure-controlled growth of SWNTs is a crucial issue for their advanced applications and has been a great challenge in this field for two decades. Metal catalyst-mediated SWNT growth is believed to be very efficient. In this review, progresses in diameter and chirality controlled growth of SWNTs with metal catalysts is summarized from several aspects, including growth mechanism and theory, effects of catalysts, and the chemical vapor deposition conditions. The design, preparation, handling and dispersion, and the size evolution of metal catalysts are all discussed. The influences of growth environment including the type, composition, and pressure/concentration of the carbon source as well as the temperature on the selectivity toward the nanotube structure are analyzed. We also discuss some of the challenges and trends in this field.

Keywords Single-walled carbon nanotubes · Metallic catalyst · Chemical vapor deposition · Controlled growth · Diameter · Chirality

M. Li, X. Liu and X. Zhao contributed equally to this work.

Chapter 2 was originally published as Li, M., Liu, X., Zhao, X., Yang, F., Wang, X. & Li, Y. Top Curr Chem (Z) 375: 29. DOI 10.1007/s41061-017-0116-9.

✉ Feng Yang
fengyang@pku.edu.cn

✉ Yan Li
yanli@pku.edu.cn

¹ Beijing National Laboratory of Molecular Sciences, Key Laboratory for the Physics and Chemistry of Nanodevices, State Key Laboratory of Rare Earth Materials Chemistry and Applications, College of Chemistry and Molecular Engineering, Beijing 100871, China

² Academy for Advanced Interdisciplinary Studies, Peking University, Beijing 100871, China

Abbreviations

AFI	Zeolite AlPO ₄ -5
AFM	Atomic force microscope
APTES	3-Aminopropyltriethoxysilane
CVD	Chemical vapor deposition
DFT	Density functional theory
Dps	DNA-binding proteins
E ₁₁	First van Hove optical transition energy
E-TEM	Environmental transmission electron microscopy
EDS	Energy-dispersive X-ray spectroscopy
FCCVD	Floating catalyst CVD
FFT	Fast Fourier transform
FTIR	Fourier transform infrared spectroscopy
G6OH	Sixgeneration polyamidoamine dendrimers with 100% hydroxyl termination
HAADF	High angle annular dark field
HMDS	1,1,1,3,3,3-Hexamethyldisilazane
PAMAM	Polyamidoamine
POM	Polyoxometalate
PS- <i>b</i> -PFEMS	Polystyrene- <i>block</i> -polyferrocenylethylmethylsilane
PS- <i>b</i> -PVP	Polystyrene- <i>block</i> -polyvinylpyridine
ptz	Pyrazine
RBM	Radial breathing mode
SDBS	Sodium dodecyl benzene sulfonate
SOG	Spin-on-glass
STEM	Scanning transmission electron microscope
SWNTs	Single-walled carbon nanotubes
TEM	Transmission electron microscope
UHV	Ultrahigh vacuum
UV–Vis–NIR	Ultraviolet/visible/near-infrared
VLS	Vapor–liquid–solid
VSS	Vapor–solid–solid

1 Introduction

Single-walled carbon nanotubes (SWNTs) are one of the most widely studied materials in the past two decades. Their outstanding properties endowed by their unique structure have shown great potential in various applications such as nanoelectronics [1–4], sensors [5, 6], energy conversation and storage [7–10], biomedicine [11, 12], and functional composites [13–15]. A SWNT can be seen as a cylinder formed by rolling up a piece of graphene sheet along the chiral vector $C_h = na_1 + ma_2$ (where a_1 and a_2 are lattice unit vectors of the graphene sheet) from the origin point (0, 0) toward the point (n , m) on the graphene sheet, as shown

in Fig. 1. Not only the structure of each SWNT but also its band structure is uniquely defined by its chiral index (n, m) [16, 17]. Therefore, the structure-controlled synthesis of SWNTs has been one of the most important topics in the field.

Chemical vapor deposition (CVD) synthesis method has become the most promising method for structure-controlled growth of SWNTs because it offers more parameters to achieve better control of the catalysts, substrates, and growth conditions [18]. It is also easier to be scaled up. In a CVD process, carbon precursors convert into SWNTs through interacting with the catalyst, which means SWNTs nucleate and grow from active catalyst nanoparticles. Therefore, the structure of catalyst nanoparticles, including size, composition, morphology, and their evolution during the CVD process plays a critical role in the selective synthesis of SWNTs.

In this review, we start from the introduction on the growth mechanism of SWNTs, then describe the structure-controlled growth of SWNTs through catalytic nanoparticles engineering and the evolution of catalyst nanoparticles during SWNTs process. The effect of the CVD conditions is also included. We also discuss the challenges and opportunities toward the structure controlled growth of SWNTs.

2 Growth Mechanism of SWNTs

In order to control the structure of SWNTs, such as diameter and chirality, it is very important to understand the growth mechanism. Catalytic nanoparticles are usually used to initiate the growth of SWNTs, though there are a few reports about non-metallic catalysts such as SiC, Ge, Si [19], and BN [20], oxide nanoparticles such as

Fig. 1 Schematic illustration of a (6, 5) SWNT rolled up from a graphene sheet. The chiral indices (n, m) uniquely define the structure of a SWNT

SiO_2 [21–24], Al_2O_3 [24], and TiO_2 [25], and crystalline diamond particles [26]. Metallic nanoparticles, including Fe, Cu, Co, Ni, Pt, Pd, Mn, Mo, Cr, Sn, Au, Mg, Al, and Rh, have been intensively used for SWNT growth [27–30] because they are believed to be generally more efficient than non-metal catalysts. Various metallic catalysts have different activities in catalyzing the decomposition of the carbon precursors, which always affect the properties of the as-grown SWNTs [27, 31]. For instance, cleaner SWNTs with smaller diameters and narrower size distributions were obtained from Cu catalyst when compared with Fe [32]. It is believed that the metal catalyst-driven growth of SWNTs is generally via a vapor–liquid–solid (VLS) mechanism (Fig. 2a), which was originally used to explain the growth of silicon whiskers from liquid Au droplets on silicon substrate [33]. In this process, carbon species diffuses on the surface of metal nanoparticles and then decompose into carbon species, which are dissolved to form a liquid alloy between metal and carbon. When the liquid catalyst particles are saturated with carbon, the carbon atoms begin to precipitate from the surface of a particle to form the cap of a SWNT [34–37]. Jourdain and Bichara summarized the four roles of the catalysts in SWNT growth [38]. Similar to the case of normal heterogeneous catalytic reactions, the catalysts catalyze the decomposition of carbon source and manage the reaction and diffusion of carbon intermediates on the surface and within the catalyst particles. These are the first two roles of metallic catalysts. The other two roles are serving as the nucleation sites for carbon caps and keeping the sites active to grow nanotubes.

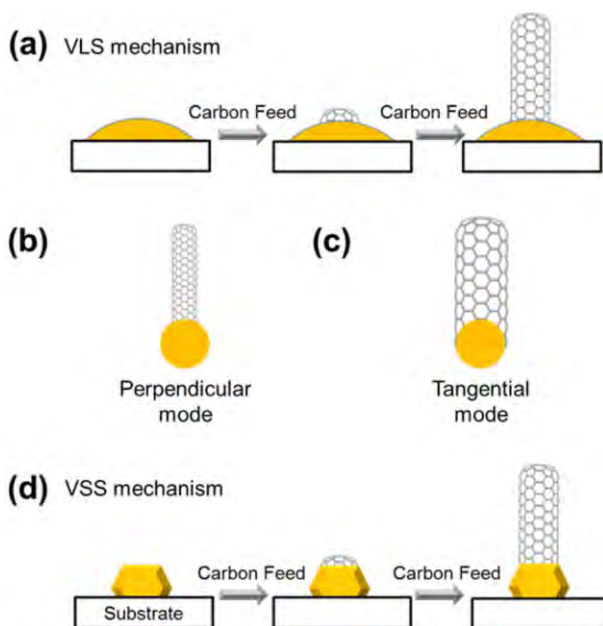


Fig. 2 Schemes of different SWNT growth mechanisms. **a** VLS mechanism. **b** Perpendicular mode. **c** Tangential mode. **d** VSS mechanism. VLS mechanism and tangential nucleation mode give the possibility of controlling the diameter of SWNTs via control the properties of catalytic nanoparticles (Corresponding figure is reproduced with permission [44], Copyright 2016, American Chemical Society)

Therefore, it is reasonable to conclude that catalysts are extremely important for the structure-controlled growth of SWNTs [27].

Loiseau et al. found that there are two nucleation modes describing the contact between the graphitic wall of the tubes and the particle, i.e. tangential mode and perpendicular mode [39]. In the case of tangential mode, the graphitic wall of the tube grows tangentially with respect to the nanoparticle surface (Fig. 2c), while in the perpendicular mode, the graphitic wall stands perpendicularly on the surface of the nanoparticle (Fig. 2b). The diameter of the resulting SWNT is similar to the size of the catalytic nanoparticle when growing via the tangential mode, while in perpendicular mode, the diameter of a SWNT will be smaller and independent from the size of the catalytic nanoparticle. There is a competition between the two nucleation modes. According to the simulation study, the perpendicular growth mode often happens when the growth condition is far from the local thermodynamic equilibrium [39]. It is proposed that the presence of nitrogen [40–42] or sulfur [43] in carbon feeding stock also leads to the growth in perpendicular mode because the heteroatoms can interact with the surface of catalytic nanoparticles.

Statics on the structure distribution of SWNTs grown by different processes shows that components with larger chiral angle (θ) normally have higher contents in the samples [45]. According to theoretical studies including molecular dynamics (MD) simulations and static density functional theory (DFT) calculations [45–47], there is a strong dependence of SWNT growth rate on chiral angle θ , and the growth of SWNTs with larger chiral angle is favorable. This rule was further proved experimentally [48, 49]. Yakobson et al. combined the thermodynamics of tube-catalyst interface and the kinetic growth theory to discuss the chirality selectivity in SWNT growth [50]. Catalyst particles in liquid state have irregular and highly mobile structures; therefore, the kinetic route of selection becomes dominant, resulting in the selective growth of $(2m, m)$ tubes with the fastest growth. The energetic preference towards achiral tubes and the faster growth kinetics of chiral nanotubes work together leading to the enriched growth of near-armchair SWNTs such as $(6, 5)$, $(7, 5)$, and $(9, 8)$ tubes. By using metal catalysts with uniform size, SWNTs enriched with a specified chirality in $(n, n - 1)$ or $(2m, m)$ regime may be synthesized. However, it is very difficult to reach a high selectivity in any chirality other than $(n, n - 1)$ or $(2m, m)$ types with ordinary metal catalysts.

Beyond the normal VLS growth of SWNTs with metal catalysts, there is another possibility of growing SWNTs via the vapor–solid–solid (VSS) mechanism (Fig. 2d), in which the catalyst nanoparticles do not melt and remain solid state during the CVD process. Robertson et al. proposed an epitaxial nucleation model of SWNTs [51, 52]. Through ab initio calculations, they showed that the formation of some specific types of caps is favored by their epitaxial relationship to the surface structure of solid-state catalyst and subsequently the tubes with corresponding chiralities grow preferentially. Based on the VSS mechanism, they proposed an idea for the chirality-selective growth of nanotubes by controlling the type of caps that form on the catalyst at the nucleation stage [51]. However, Yakobson et al. showed later that the energy variability associated with the carbon nanotube caps is tiny compared to that of the interfaces between nanotubes and catalyst nanoparticles [53]. As a result, the differentiation between the formation energy of caps cannot be

a dominant factor determining the chiral distribution. The chirality selective growth may be realized by tuning the interaction between nanotube edges and catalysts through the selection of different metals and manipulating the structures. Balbuena et al. [54] suggested that a sufficiently strong metal-substrate interaction keep the crystallinity of the metal catalyst at high temperature and subsequently limits the diffusion of carbon atoms into the body of the nanoparticle. This leads to the favorable growth of carbon structures templated by the metal surface. The nucleation normally occurs on metal atoms at the steps with lowest coordination.

It seems VSS mechanism offers better opportunities for realizing chirality selective growth. If the “contact” epitaxial matching between the metal atoms of the catalyst nanocrystal and the edge structure of a SWNT is specific enough, a cap with determined structure will be formed epitaxially and subsequently a SWNT with specified chirality will be produced [44].

3 Catalysts for Diameter-Controlled Growth of SWNTs

Diameter control is a basic part of SWNTs structure control. Many of SWNT properties are related to their diameter. For instance, the bandgap of a semiconducting SWNT is approximately inversely proportional to its diameter [17]. Therefore, it is of great interest to produce SWNTs with desired diameter and narrow diameter distribution. According to the growth mechanism, there is a positive correlation between the size of catalytic nanoparticles and the diameters of SWNTs. The size control of catalyst nanoparticles at the very first step of the growth is the most significant part in diameter control of SWNTs. In this part, we will discuss the methodology in the size control of catalyst nanoparticles, the dispersion and evolution of nanocatalysts in CVD process, and the diameter-controlled growth of SWNTs.

3.1 Size-Controlled Preparation of Metallic Nanocatalysts

3.1.1 Capping Agent-Assisted Preparation of Nanoparticles with Narrow Size Distribution

Capping agents have been widely used to control the size of nanoparticles in solution-based preparations. Capping agents can adsorb on the surface of nanoparticles by coordination or static charge interactions to prevent the un-desired growth of particles and obtain nanoparticles with smaller size and narrower size distribution. Liu et al. used a mixture of long-chain carboxylic acid and long-chain amine as protective and dispersive agent and prepared uniform iron-molybdenum nanoparticles with the diameters varied from 3 to 14 nm and standard deviation as small as $\sim 7\text{--}8\%$ (Fig. 3) [55]. The ratio of metal precursor to capping agents and the ratio of acid to amine both affect the size of synthesized nanoparticles. Lieber's group obtained nearly monodispersed iron nanoparticles with average diameters of 3, 9, and 13 nm by changing the carbon chain length of the carboxylic acid surfactant, and the carbon nanotubes produced were with the average diameters of 3, 7, and 12 nm, respectively [56].

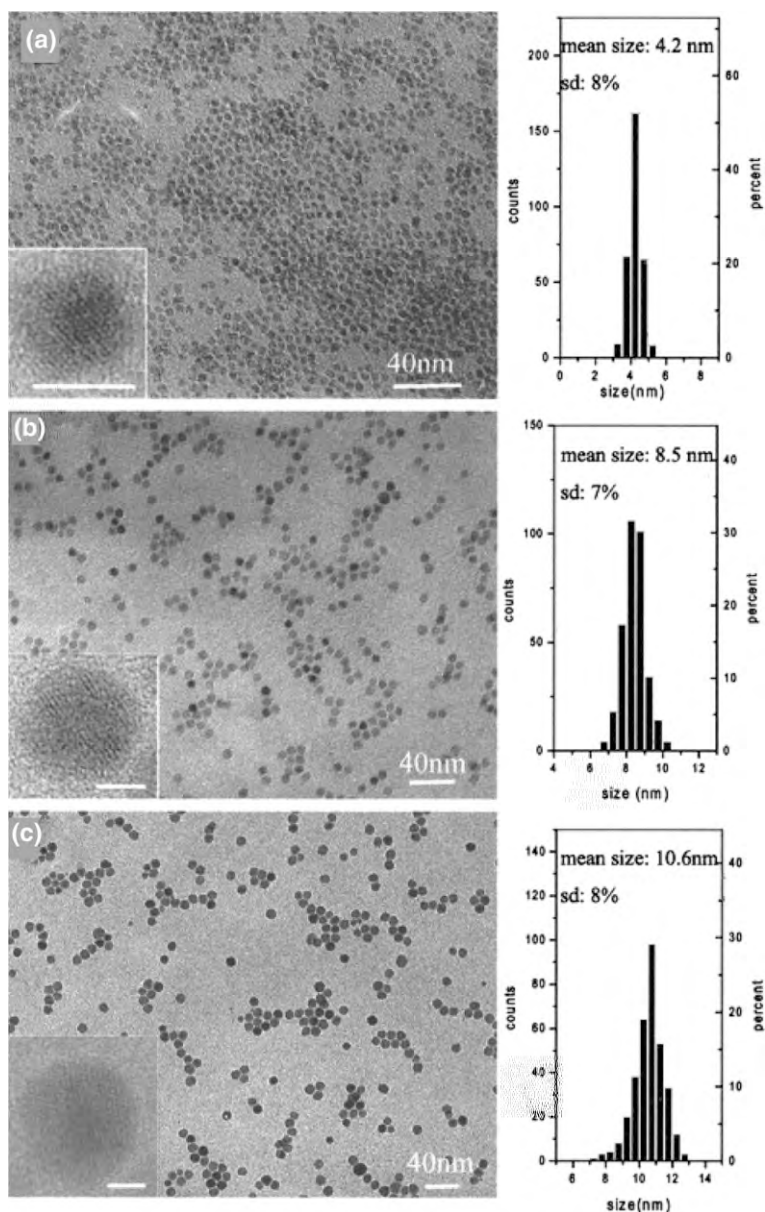


Fig. 3 Transmission electron microscope (TEM) images of Fe-Mo nanoparticles synthesized under typical conditions (with a 1:1 mixture of bis-2-ethylhexylamine and octanoic acid at a concentration of 0.100 mmol) (a) and 2.50 mmol (b) or 5.00 mmol (c) of protective agent was used. The scale bars in the inserts are all 4 nm (Corresponding figure is reproduced with permission [55], Copyright 2001, American Chemical Society)

3.1.2 Using Precursors with Uniform Size to Prepare Mono-Dispersed Nanoparticles

Metal-Loaded Protein Precursors Dai's group used ferritin, an iron-storage protein, to synthesize discrete iron oxide nanoparticles with controllable diameters and grew SWNTs from these nanoparticles on substrate by CVD (Fig. 4) [57]. The apo-ferritin protein is made of 24 polypeptide subunits, with a central core ~ 8 nm in diameter and can store up to 4500 iron atoms. They synthesized two types of catalytic nanoparticles with different diameters by changing the Fe loading in apo-ferritin precursor. The diameters of catalytic Fe_2O_3 nanoparticles produced by loading ~ 200 and ~ 1100 Fe atoms were 1.5 ± 0.4 and 3.0 ± 0.9 nm, respectively, while the diameters of as-grown SWNTs were 1.9 ± 0.3 and 3.7 ± 1.1 nm,

Fig. 4 a Schematic image of process for SWNT synthesis from discrete nanoparticles by CVD. Diameter distribution for Fe_2O_3

respectively. Researchers also filled cobalt [58] and gold [59] atoms into apo-ferritin shells and obtained uniform catalytic nanoparticles to grow SWNTs. Ferritin with narrower size distribution, which is favorable for producing catalyst nanoparticles with uniform size, can be obtained by sedimentation velocity centrifugation [60].

In addition to ferritin [61, 62], Jeong et al. also used DNA-binding proteins (Dps) [63] to load Fe. There is an iron compound with the size of ~ 4 nm in the hollow space of Dps [64]. The SWNTs (diameter 1.1 ± 0.3 nm) were grown by using iron nanoparticles (size 2.4 ± 0.5 nm) derived from Dps on silicon wafer or suspended on pillars. In addition, polymerized hemoglobin containing 11 Hb molecules was also used as the catalyst precursor of SWNTs synthesis. SWNTs with very narrow diameter distribution of 1.08 ± 0.26 nm were obtained from the iron oxide nanoparticles with an average diameter of 1.30 ± 0.36 nm [65].

Dendrimers and Copolymer Mediated Preparation Polymers such as dendrimers [66–69] and block copolymers [70–76] can be used to control the size of catalytic nanoparticles. Dai's group first used six generation polyamidoamine dendrimers with 100% hydroxyl termination (G6OH), which is a kind of dendrimer of polyamidoamine (PAMAM), to transfer Fe(III) ions onto the SiO₂ substrate with good dispersion [69]. The G6OH molecules have ion complexation capability from the tertiary amines of the outmost shells and each molecule can seize a maximum of 64 Fe(III) ions. The Fe(III) loaded G6OH molecules were dispersed on the substrate and transformed into iron oxide nanoparticles by annealing. These iron oxide nanoparticles were reduced to form uniform Fe nanoparticles with the size of 1–2 nm, which further catalyzed the growth of SWNTs with a narrow diameter distribution of 1–2 nm. The size of the eventually formed Fe nanoparticles can be adjusted by the size of the dendrimers, the density of the functional groups on the shells of the dendrimers, and the loading of Fe(III), hence the diameter of the resultant nanotubes can also be manipulated [66–68].

Block copolymer molecules are composed of fragments with different properties. The phase separation of block copolymers occurs at a certain temperature and forms periodic nanostructures [75, 76]. This property makes it possible for them to serve as a template for the preparation and deposition of metal catalyst nanoparticles on substrates (Fig. 5).

Polystyrene-*block*-polyvinylpyridine (PS-*b*-PVP) block copolymers have pyridine sites to coordinate with transition metal ions and the complexes can form spherical micelles in toluene, in which metal-PVP complex present at the core and PS chain at the outer shell, shown in Fig. 5. By further annealing and reduction, well-dispersed uniform metal nanoparticles were obtained to grow SWNTs [70–73]. Liu et al. applied PS-PVP micelles loaded with different amount of FeCl₃ as catalyst precursors for SWNT growth [70]. They tried the Fe/PVP ratios of 0.6, 0.2, and 0.06. The as-formed nanoparticles after O₂ plasma treatment were well-dispersed with uniform size according to the atomic force microscope (AFM) measurements (Fig. 6). The average sizes of the nanoparticles are 6.6, 3.0, and 1.9 nm, respectively, while the diameters of the SWNTs produced are 2.7 ± 0.3 , 1.2 ± 0.1 , and 0.9 ± 0.1 nm, respectively. Lu et al. and Belcher et al. used PS-PVP block copolymer micelles to produce a series of transition metal nanoparticles such as iron, cobalt, nickel [72], molybdenum [71], and bimetallic Fe–Mo [71] with

controlled size and then to produce high quality SWNTs with narrow size distribution. Similar to the Fe/PVP system, by changing the ratio of metal/PVP, both the sizes of nanoparticles and SWNTs were tuned [71].

Different from the pristine PS-*b*-PVP block copolymers, PS-*b*-PFEMS already holds iron atoms in the structure and, therefore, can be directly used to prepare Fe nanoparticles for SWNT growth [74]. Using Fe nanoparticles produced by this method, SWNTs with diameters of 1 nm or less were prepared.

Nanocluster Precursors Polyoxometalate (POM) clusters are a family of polyatomic oxyanions of several transition metals (such as Mo, W, V, Nb, and Ta). There are enormous numbers of polyoxometalate clusters. Most of them have discrete cluster structures of definite sizes and shapes formed by metallic oxide

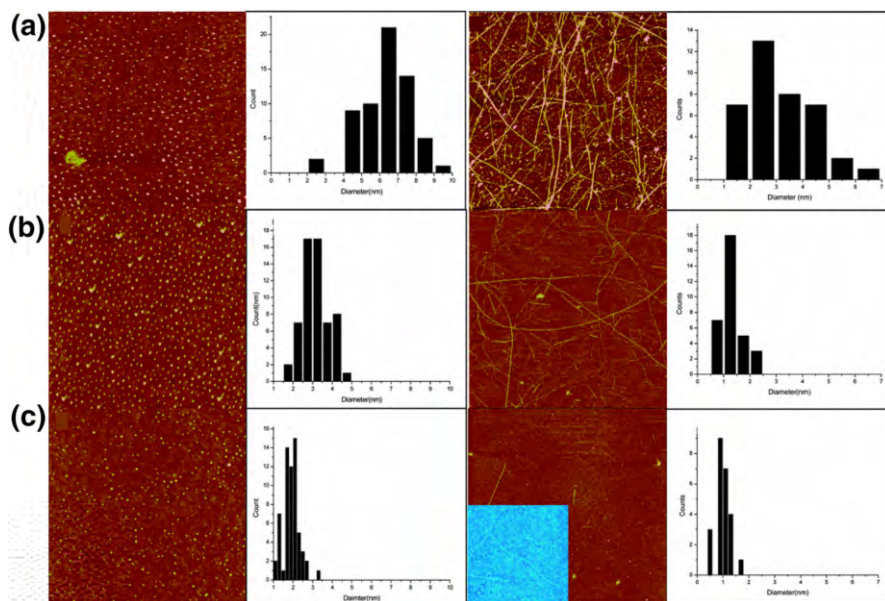


Fig. 6 AFM image and diameter distributions of nanoclusters formed and nanotubes grown on the surface with different ratios between FeCl_3 and the PVP block: **a** FeCl_3 : PVP = 0.6; **b** FeCl_3 : PVP = 0.2; **c** FeCl_3 : PVP = 0.06. All images are $3 \times 3 \mu\text{m}^2$ (Corresponding figure is reproduced with permission [70], Copyright 2004, American Chemical Society)

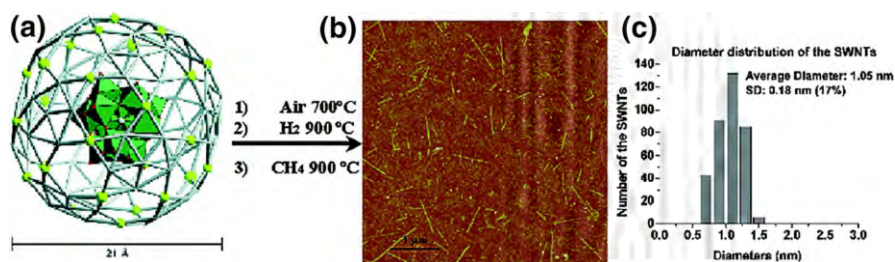


Fig. 7 **a** The single-crystal “cluster-within-a-cage” structure of FeMoC cluster; **b** AFM images of the SWNTs grown from FeMoC nanoclusters; **c** diameter distribution of the SWNTs grown from FeMoC nanoclusters (Corresponding figure is reproduced with permission [80], Copyright 2002, American Chemical Society)

Barron et al. systematically studied the FeMoC system [81]. They found that pure FeMoC is inactive as a pre-catalyst for the growth of SWNTs because an individual FeMoC molecule may not contain sufficient metal atoms to make an active catalyst. SWNTs can only grow when FeMoC clusters form small aggregations with the size of around ~ 4 nm or excess iron is added. The diameters of the SWNTs grown from the cluster precursors with well-controlled aggregation are very uniform and can also be adjusted as shown in Table 1.

Table 1 Comparison of lengths and diameters for SWNTs grown from FeMoC catalyst system

Growth method	Substrate	Average length ^a (μm)	Average diameter (nm)	References
FeMoC	Si	>1	1.3 (± 0.50)	[80]
FeMoC-ethanol ^b	Si	>1	1.1 (± 0.1)	[81]
FeMoC-ethanol ^b	SOG	0.3	2.1 (± 0.1)	[81]
FeMoC-ptz (1:25) ^b	SOG	>1	1.25 (± 0.25)	[81]
FeMoC-ptz-Fe(NO ₃) ₃ (1:25:25) ^b	SOG	>1	1.6 (± 0.2)	[81]

Corresponding table is reproduced with permission [81], Copyright 2006, Royal Society of Chemistry
SOG spin-on-glass, *ptz* pyrazine

^a The length of the as grown SWNT will depend on the reaction time

^b Reaction time 15 min

Li et al. also used FeMoC clusters as the catalyst precursors. But instead of silicon wafers, they grew horizontally aligned SWNTs on ST-cut quartz substrates [83]. Because MoO₃ is easy to be vaporized at the temperature above 600 °C, the annealing process in air is unfavorable for obtaining uniform catalyst nanoparticles. It was also found that the size of the catalyst nanoparticles as well as the diameter of the produced SWNTs is remarkably dependent on the growth temperatures. The diameter of the SWNTs was adjusted from 0.76 to 1.53 nm when the growth temperature was changed from 900 to 970 °C.

3.1.3 Catalyst Nanoparticles Confined in Porous Materials

Mesoporous materials such as MCM-41 [87] present nanometer-scaled channels which can serve as templates to confine the size of the catalytic nanoparticles. Various types of metals including Co [88–95], Fe [96, 97], Ni [95], Mo [98], Nb [98], and Fe–Zn [97] have been incorporated into MCM-41.

Haller et al. used Co and Ni incorporated MCM-41 to grow SWNTs [95]. All the procedures including annealing, reduction, and growth were performed at 700 °C. The MCM-41 template maintained its structure after successive reaction cycles. This result shows that mesoporous materials have enough thermal stability to act as the templates confining the size of catalyst nanoparticles for tube growth.

The pore sizes of MCM-41 also can be tuned. Haller et al. used alkyl templates with different carbon chain lengths of 10–18 carbon atoms to prepare Co incorporated MCM-41. The pore sizes changes from 1.8 to 3.5 nm according to the nitrogen physisorption measurements [88]. In another work, they prepared Co–MCM-41 with C12 and C16 alkyl chains and resulted in pore diameters of 2.6 and 3.3 nm, respectively [90]. The diameter of the SWNTs grown by such confined catalysts was normally smaller than the pore size of the mesoporous materials. The average diameters of the SWNTs produced from the Co–MCM-41 with pore sizes of 2.6 and 3.3 nm were determined to be ~ 0.67 and ~ 0.85 nm, respectively.

The loading of metals can be adjusted. Pfefferle et al. [91] found that Co–MCM-41 samples with different cobalt loadings have different stability against reduction.

It could lead to producing tubes with a narrow distribution of diameters until the co-loading of ~ 4 wt%. In the case of an Fe–MCM-41 system, the diameter of SWNTs produced from a 2 wt% Fe-loaded sample is well controlled to 0.67–1.28 nm, but the multi-walled carbon nanotubes became predominant when the Fe-loading was increased to 3 wt% [96].

The type and composition of the metal also affect the diameters of produced SWNTs. The diameters of SWNTs produced from Mo–MCM-41 and Nb–MCM-41 are 1.06–2.9 and 1.08–2.3 nm, respectively [98]. The Fe–Zn–MCM-41 can produce SWNTs with a narrow diameter distribution in the range of 1.5–2.5 nm when the Fe:Zn ratio is 3:1.

Other than the silica-based mesoporous materials, Ago et al. also used porous MgO as the catalyst support to perform the diameter-controlled growth of SWNTs [99]. The produced tubes show a narrow diameter distribution with a mean diameter of 0.93 nm, while the crystalline MgO-supported catalysts resulted in a very broad distribution in the nanotube diameters under the same conditions.

In addition to the metal-loaded mesoporous materials, SWNTs can also be synthesized within the channels of microporous zeolite. In the latter case, no metallic catalysts are needed. For example, ultrathin SWNTs with a diameter of 0.42 ± 0.02 nm were prepared by the pyrolysis of tripropylamine molecules in the channels of zeolite $\text{AlPO}_4\text{-5}$ (AFI) single crystals [100–104].

3.2 Dispersion of Catalytic Nanoparticles

In addition to the size of the catalytic nanoparticles, the dispersion and deposition of catalysts on substrates are also important in the controlled growth of SWNTs. This procedure should be well designed to avoid the aggregation of catalysts or catalyst precursors.

There are different approaches to disperse catalysts onto substrate to control the diameter of SWNTs. Sputtering a thin film of catalytic metal thin film on the surface with a defined thickness is a simple method to prepare catalysts and to grow carbon nanotubes with narrow diameter distribution [105, 106]. Arc plasma deposition can also deposit catalyst thin film with controlled thickness and composition. All these approaches have different control range on the nanotube diameters [107].

Solution-mediated process is another route. Modifying the catalyst surface with capping agents, increase of surface charge, and the presence of surfactants can all improve the solubility of catalyst nanoparticles or catalyst precursors [108–110]. The good dispersibility of nanoparticles is one of the important issues for preparing the uniform catalysts on substrates. The other important issues are the surface property of substrates and the interaction between the nanoparticles and substrates.

The nanoparticles can be deposited onto the substrates relying on electrostatic interactions [80], hydrophobic interactions [111], and coordination interactions [112]. For example, if simply dropping the aqueous solution of nanoclusters onto a substrate, the nanoclusters will aggregate along with the evaporation. Liu et al. [80] used 3-aminopropyltriethoxysilane (APTES) to modify the silicon dioxide surface. Upon the self-assembly of APTES on silicon dioxide surface, an amine group terminated surface was obtained and the surface becomes positively charged. Through the

Coulombic attraction, the negatively charged nanoclusters were bonded strongly with the positively charged -NH_2 groups on the substrate to obtain well-dispersed nanoclusters, which benefits the formation of uniform catalyst nanoparticles. Surface modification have also be done taking advantage of hydrophobic interaction [111]. The self-assembly of 1,1,1,3,3,3-hexamethyldisilazane (HMDS) can make the surface of Si/SiO₂ substrate hydrophobic, as shown in Fig. 8. Then the Fe/Mo nanoparticles capped with alkyl amine and alkyl carboxylic acid, which show a hydrophobic surface property, can be uniformly distributed on the substrates [55] (Fig. 8).

3.3 Evolution of Catalytic Nanoparticles

It is generally accepted that metal nanoparticles tend to aggregate during the calcination and reduction processes. The nanoparticles may also undergo Ostwald ripening [113] during the reduction and CVD processes. The smaller particles evaporate and the larger particles continue to grow. All the above processes lead to larger nanoparticles with broader size distribution, which is definitely unfavorable for controlling the diameter distribution of as-grown SWNTs and should be avoided as much as possible.

3.3.1 Evolution of Fe Nanoparticles During Calcination and Reduction

Before introducing the carbon source into the CVD system, the precursors normally need to undergo calcination and reduction processes to from catalytic metal nanoparticles. During these processes, the size and morphology of the catalysts change and affect the SWNT growth. We will use the iron nanoparticle as a model to understand how the nanoparticles change in these processes and how to control them.

The evolution of nanoparticles was generally studied by systematic nanoparticle-size analysis at each step before and during CVD process under typical growth conditions without any carbon feeding using AFM and transmission electron microscope (TEM). The different processes involved during reduction are sketched in Fig. 9.

At the first stage, the average size decreases after calcination because of the removal of the organic components in the precursor [61], the evaporation also lead to the size decrease of the nanoparticles [114, 115]. Then two competing processes, Ostwald ripening and subsurface diffusion, govern the morphological change of the catalyst particles at annealing process [114, 116]. After a few minutes of annealing, Ostwald ripening begins, larger particles appear, and the density of particles decreases, which leads to broadening particle diameter distributions [117, 118]. When elongating the annealing time, the catalytic nanoparticles embed into the substrate [62], especially in the system of Fe nanoparticles/Al₂O₃ substrates [118]. The cross-sectional TEM observation confirmed that Fe nanoparticles indeed diffused into the alumina layer (Fig. 10). Spectroscopic investigations developed by Colaïanni et al. revealed that the surface diffusion of Fe into Al₂O₃ can be initiated at temperatures as low as 600 °C [119]. If Fe was deposited between two layers of Al₂O₃, Fe nanoparticles with a narrow distribution can be obtained to grow SWNTs

Fig. 8 **a** Schematic representation of the chemical modification on substrate surface. Photo of a water droplet on different substrates: **b** bare substrate; **c** modified with HMDS at room temperature for 1 min, **d** 150 °C for 30 min; AFM images, height measurement, and diameter distribution of the Fe/Mo NPs on different substrate surfaces: **e** bare substrate; **f** modified by HMDS for 1 min at room temperature; **g** annealed 150 °C for 30 min (Corresponding figure is reproduced with permission [111], Copyright 2015, Huang S)

with uniform diameter via moderating the annealing time to control the state of the diffusion [120].

While continuing to prolong the annealing time, there is another process: the Fe atoms precipitate from the sapphire subsurface and the particles start Ostwald ripening at the high temperature again [121].

In the reduction process, hydrogen is crucial to form the nanoparticles with proper size especially when the catalyst precursor is a metal thin film [116]. Hydrogen helps to break down the metal thin film to form small particles. A

Fig. 9 Illustration of catalyst particle evolution model during reduction

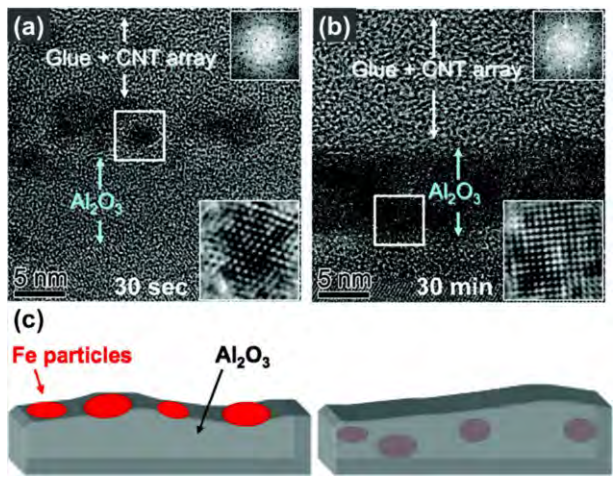
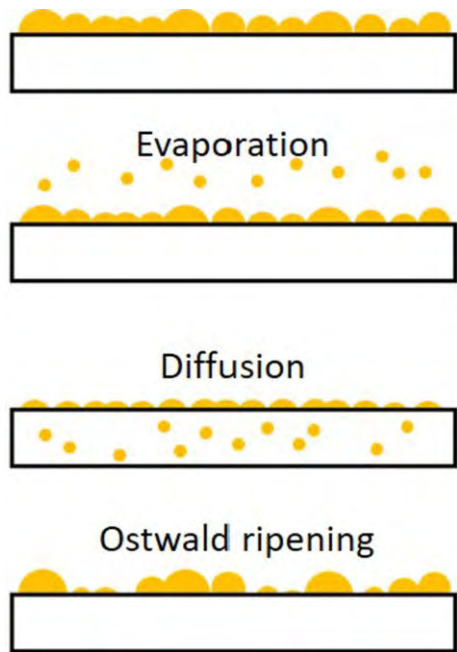


Fig. 10 Cross-sectional TEM images of the Fe catalyst and Al_2O_3

sufficient amount of hydrogen can fully guarantee the reduction of metal oxide nanoparticles and produce small metal nanoparticles. Hata et al. found that under the same conditions, when the concentration of hydrogen was 90%, the average size

of as-formed catalyst particles was 2–3 nm, but when using 10% hydrogen, the particle size was larger than 5 nm.

3.3.2 Prevent Aggregation and Ripening of Catalytic Nanoparticles

It is always helpful to prevent the aggregation of catalyst nanoparticles by lowering the particle density. Jeong et al. found that when the density of catalytic nanoparticles decreased, diameter distribution of the nanotubes became narrower [75]. At the lowest catalyst density, only a single peak of radial breathing mode (RBM) corresponded to the tube diameter of 1.08 nm was observed from Raman spectra, suggesting the growth of homogeneous SWNTs.

The conditions for preparing catalytic nanoparticles, such as the time and temperature of annealing and reduction and the amount of reduction gas exposed, are also important. By manipulating the catalyst formation temperature and H₂ exposure condition, Hata et al. adjusted the size distribution of Fe nanoparticles originated from Fe thin film, and eventually produced SWNT forest with the controlled diameters ranging from 1.9 to 3.2 nm at a suitable growth condition [116]. They investigated the relationship between the particle sizes of the catalyst and their surface energies and found that the increase in decreasing the size of particle. They used high concentration of H₂ to increase the surface energy of Fe nanoparticles, thus reducing the SWNT diameters. While the tube diameter showed a direct proportionality with catalyst formation temperature, the lower temperature reduced the aggregation and Ostwald ripening efficiently, shown in Fig. 11. Park et al. [122] also reported lower temperature can suppress catalyst agglomeration and Ostwald ripening. Moderating the reduction time is also helpful to maintain the size of catalytic nanoparticles and consequently the diameter of as-produced SWNTs [114] (Fig. 11).

By using the competition relationship between Ostwald ripening, substrate diffusion and atom evaporation, the aggregation and ripening can also be suppressed. Ago et al. controlled the size of Fe nanoparticles by annealing in ultrahigh vacuum (UHV) [121]. They found that the thermal annealing in UHV for 1 h combined with H₂ reduction reduced the size of Fe nanoparticles and narrowed its distribution, which resulted in the growth of horizontally aligned SWNTs with uniform-diameter. 76% of the nanotubes have diameters between 1.3 and 1.4 nm. The UHV in the high temperature improved the evaporation of Fe atoms, which is the main reason for the decreasing of the Fe nanoparticle size. Substrate diffusion still exists in the UHV-assisted CVD process, which results in size increase of Fe nanoparticles when prolonging the annealing time.

Last, bimetallic or trimetallic catalysts have frequently been used to prevent the aggregation of the catalytic nanoparticles, in which one of the components can serve as active part while the others serve as dispersant or protector [97, 107, 123, 124]. These kinds of multi-component metallic catalysts can achieve a good selectivity of both diameter and chirality of SWNTs, which will be discussed in details in next part of the review.

In summary, the diameter of the carbon nanotubes is closely related to the size of the catalysts. To achieve diameter-controlled growth of SWNTs, the size of the

Fig. 11 **a** Fourier transform infrared spectroscopy (FTIR) spectra of SWNT forests synthesized from various catalyst formation conditions. The *red trapezia* indicates the region of first van Hove optical transition energy (E_{11}) of SWNT. SWNT diameters converted from E_{11} positions are shown at the *right side* of each spectrum. Plots of diameters obtained from FTIR (**b**), forest mass densities (**c**), forest heights (**d**), and G/D-band ratios measured from Raman spectroscopy (**e**) as a function of the catalyst formation conditions (temperature and total flow rate) for SWNT forests synthesized with fixed hydrogen concentration of 90% (Corresponding figure is reproduced with permission [116], Copyright 2013, WILEY-VCH Verlag GmbH & Co. KGaA, Weinheim)

catalyst nanoparticles should be well-controlled and maintained via the following procedures: first, synthesize the catalytic particles with designed size and narrow size distribution by using catalyst precursors with uniform size such as nanoclusters, iron-loaded ferritin or confined by mesoporous materials and block copolymers; second, make the catalyst particles well-dispersed on substrates with the help of surfactants and/or surface-modification of substrates; third, maintain the size of catalyst nanoparticles by preventing aggregation and Ostwald ripening.

4 Chirality-Selective Growth of SWNTs

As stated above, the property of SWNTs is fully determined by their structures, which are described by their chiral index. A SWNT sample composed of nanotubes with a single chirality and identical band structure presents homogenous property, which is desired in many high-end applications such as nanoelectronics [125, 126], photovoltaic process [127, 128], and bioimaging [129, 130]. Therefore, to control the chirality distribution of SWNTs in catalytic CVD synthesis and produce SWNTs with uniform properties is essential to explore and achieve their potential applications [40, 131]. Catalyst design plays a key role in the efforts toward chirality-controlled synthesis of SWNTs.

4.1 Bimetallic Catalysts

Resasco et al. used CoMo bimetallic catalyst with an initial Co:Mo molar ratio of 1:3 to grow SWNTs. After a CO CVD synthesis at 750 °C, the (6, 5) and (7, 5) tubes represented 38% of all species as shown in Fig. 12a [132]. Then they optimized the CVD process by varying the temperature, the carbon feed composition, and the supporting materials for catalysts. A (*n*, *m*) population distribution of 54% (6, 5) SWNTs characterized by optical absorption was obtained using CoMo catalyst under the reaction condition of growth temperature at 700 °C, CO as the carbon feed composition, and SiO₂ as the catalyst support [133]. They suggested that the bimetallic CoMo catalyst precursor contains highly dispersed molybdenum oxide covered by a CoMoO₄ layer. Upon exposure to CO, the molybdenum oxide is partially converted into molybdenum carbide. Co is reduced by CO from the CoMoO₄ layer and the metallic Co migrates to the surface of catalyst, nucleating into small catalytic nanoparticles. The molybdenum oxide/carbide stabilizes the Co nanoparticles against aggregation in high-temperature sintering. Such Co nanoparticles with uniform size can therefore grow SWNTs with narrow (*n*, *m*) distribution.

Kauppinen et al. developed a FeCu bimetallic catalyst that provides a predominant growth of (6, 5) SWNTs with a CO CVD process at 600 °C [134, 135]. The formation of Fe particles in the FeCu bimetallic catalyst can be realized at 600 °C, which is lower than the reduction temperature of monometallic Fe catalyst (>700 °C). The XPS characterizations show a higher binding energy of Fe 2p_{3/2} in FeCu catalyst, suggesting that Cu plays an important role in the Fe reduction process. They further observed the formation of catalyst nanocrystals and the growth of SWNTs using in situ environmental transmission electron microscopy (E-TEM) (Fig. 12b) [136]. They found that Fe only exists and is anchored on the surface of the reduced Cu in the form of small particles. The Cu-stabilized Fe nanoparticles then grow SWNTs with narrow chirality distribution.

Maruyama et al. studied bimetallic the CoCu catalysts supported on SiO₂ film on a scanning transmission electron microscope (STEM) by using energy-dispersive X-ray spectroscopy (EDS) and high-angle annular dark field (HAADF) imaging [137] (Fig. 12c). It was observed that Co catalysts were anchored on Cu nanoparticles. Furthermore, the presence of SiO₂ is also necessary because it can stabilize Cu which has a low melting point. They conclude that in the CoCu bimetallic catalyst system, Cu anchors the Co catalysts to inhibit the formation of larger nanoparticles, protecting small Co particles from being overloaded by carbon precursors and assisting the thorough reduction of Co nanoparticles. The threefold effect of Cu makes the structure selective growth of high-quality SWNT forests with a possible sub-nanometer-diameter.

The enrichment of (6, 5) SWNTs were also obtained with CoMn [92] and CoCr [93] catalysts. In some other bimetallic catalysts, such as FeCo [138, 139], FeCr [140], and FeMn [79], the preferential growth of (6, 5) and (7, 5) SWNTs were observed. It seems there is a positive correlation between the temperature and the tube diameter of enriched chirality. It was found that lower temperature benefits the formation of (6, 5) tubes and higher temperature enhances the growth of (7, 5) tubes [79, 141–143]. Similarly, it was observed in CoPt catalysts that the population of (6,

Fig. 12 Characterization of bimetallic catalysts and SWNTs grown. **a** Photoluminescence emission intensities under various excitation energies for the SWNTs grown from CoMo catalyst (Corresponding figure is reproduced with permission [132], Copyright 2003, American Chemical Society). **b** Bright field E-TEM image of a SWNT grown from Cu-supported metallic Fe nanoparticles (Corresponding figure is reproduced with permission [136], Copyright 2012, American Chemical Society). **c** Elemental mapping image by EDS showing Co nanoparticles are anchored by Cu in the bimetallic CoCu catalyst. EDS-STEM mapping of Co and Cu overlapped on high-resolution HAADF-STEM (Corresponding figure is reproduced with permission [137], Copyright 2015, Royal Society of Chemistry)

5) SWNTs is the highest among all species in the product grown at 800 °C, but (7, 6) becomes dominant at 850 °C [142].

4.2 Supported Catalysts

He and Kauppinen et al. achieved the selective growth of (6, 5) SWNTs on partially reduced Co–SiO₂ catalyst at a low growth temperature of 600 °C (Fig. 13a) [144]. Co₂SiO₄ possibly forms on the surface of SiO₂. They suggested that because of the modest reduction temperature, the catalyst precursor Co²⁺ is partially reduced to metallic Co by CO and anchors on the surface by unreduced Co²⁺ and Co⁺ as the

anchoring sites, which constrain the mobility of the reduced metallic Co and thus facilitate the formation of sub-nanometer nanoparticles. As-formed sub-nanometer Co nanoparticles can then catalyze the growth of a small diameter of SWNTs with a narrow chirality distribution.

They further realized the preferential growth of semiconducting SWNTs ($\sim 90\%$) with an exceptionally large population of 53% (6, 5) tubes with Co–MgO catalyst [145]. They carefully observed the structure of catalyst and the growth of SWNTs in situ using a high-resolution E-TEM. The Co cations in the $\text{Co}_x\text{Mg}_{1-x}\text{O}$ solid solution catalyst precursor were reduced in the solid phase by CO and then quickly migrated to the surface and finally crystallized into metal nanoparticles. The nanoparticles showed a narrow size distribution with a mean value of 1.8 nm. Well defined (0 1 1) patterns for both fcc MgO ($a = 0.422$ nm) and fcc Co ($a = 0.354$ nm) demonstrates unambiguously an epitaxial relationship between Co nanoparticles and the MgO matrix as shown in Fig. 13b. Because the mismatch in the lattice constants between the two materials is as large as $\sim 16\%$, the Co nanocrystal is severely strained to match the lattice of the MgO matrix. The misfit strain causes the deformation of the Co lattice and leads to the formation of smaller Co nanoparticles to decrease the interface area between MgO and Co. Therefore, SWNTs with small diameter and narrow chirality distribution were produced.

Ago et al. used CoMo-based catalyst to grow aligned SWNTs on the A-plane, R-plane, and C-plane sapphire substrates, respectively. The preferential growth of near-zigzag (16, 2) tubes at 900 °C and (15, 1) tubes at 800 °C was observed on the A-plane, while the preferential growth of near-armchair (9, 8) tubes at 750 °C on the R-plane was observed. They suggested that the dissimilar atomic structures of the A- and R-plane sapphire surfaces may induce differences in the particle morphology, thereby affects the chirality distribution of the produced SWNTs [146].

4.3 Preparing Catalysts via Intermediates with Uniform Size

With CoSO_4 as the precursor of Co, Chen et al. developed a series of supported monometallic Co catalyst, namely Co–TUD-1 [147] and Co– SiO_2 [148–150], and grew SWNTs with the enrichment of (9, 8) species. They proposed that the formation of Co_9S_8 nanoparticles with a narrow size distribution is crucial in this process [151]. Co_9S_8 nanoparticles, as an intermediary compound, is reduced to metallic Co nanoparticles with uniform size and further grow (9, 8)-enriched SWNTs (Fig. 14b). Photoluminescence results showed the chirality selectivity toward (9, 8) nanotubes is 37.9% among semiconducting nanotubes.

4.4 Solid-State Catalysts

In the VSS process, the solid state catalyst nanoparticles keep their morphology while the tubes are growing. This offers the opportunity to control the structure of SWNTs by epitaxial growth from the solid state catalyst [152] with well-defined structures [44].

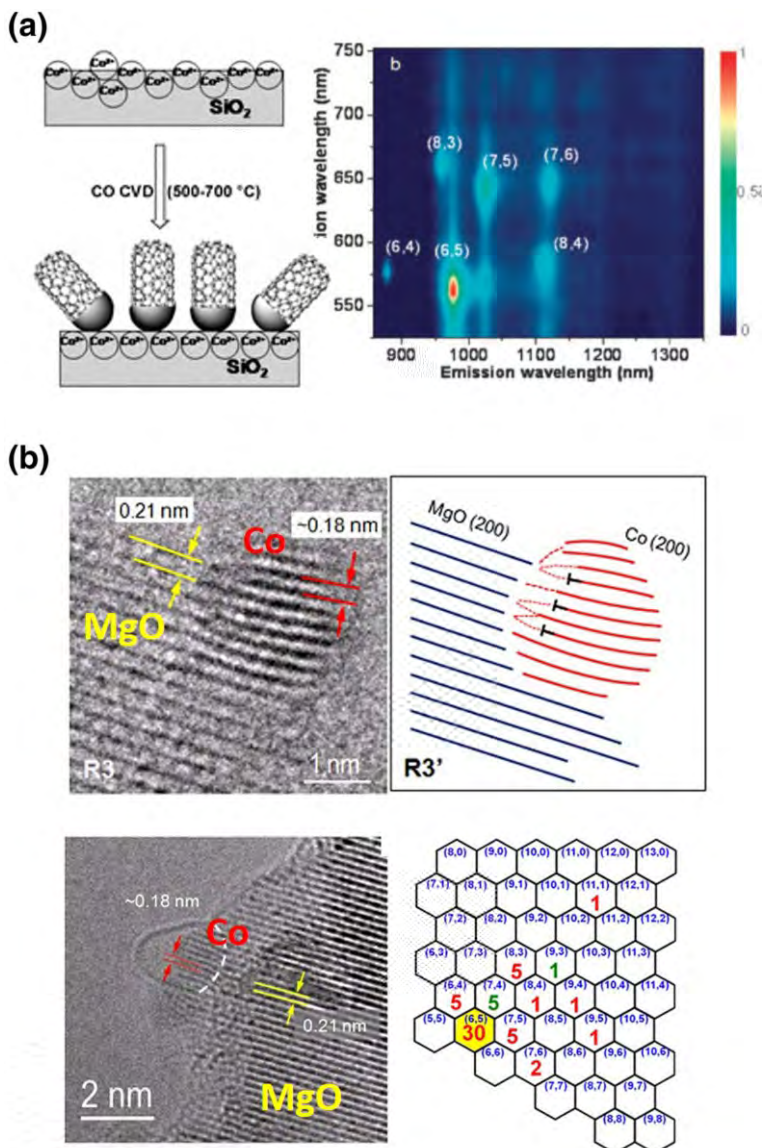


Fig. 13 Characterization of supported catalysts and grown SWNTs. **a** Schematic illustration of SWNT growth on a partially reduced Co-SiO₂ supported catalyst and contour plot of normalized photoluminescence emission intensities under the various excitation energies for SWNTs with Co-SiO₂ catalyst (Corresponding figure is reproduced with permission [144], Copyright 2010, Royal Society of Chemistry). **b** In situ E-TEM studies of the epitaxially formed Co nanoparticles in Co-MgO catalyst, and a schematic representation of the Co-MgO lattice configurations. In situ HRTEM lattice images showing carbon cap formation on epitaxial Co nanoparticles formed from the Co_{0.5}Mg_{1-x}O solid solution and chirality map measured from electron diffraction analysis (Corresponding figure is reproduced with permission [145], Copyright 2013, Nature Publishing Group)

Sankaran et al. observed shifts of chirality distributions of as-grown SWNTs by tuning the composition of $\text{Ni}_x\text{Fe}_{1-x}$ nanoparticles. An enrichment of (8, 4) SWNTs was observed when the composition of the catalyst was $\text{Ni}_{0.27}\text{Fe}_{0.73}$ (Fig. 15a) [153]. Since Fe was incorporated into the Ni lattice, an expansion of the Ni fcc

(Fig. 15b) [155]. Only small Mo nanoparticles are carbonized into stable Mo_2C and act as the catalyst. This might be one of the reasons that (8, 4) SWNTs with a small diameter were produced.

The presence of catalyst support is often helpful for maintaining the solid state of catalysts and may influence the morphology and structure of the particles. FePt nanoparticles were fabricated on a single-crystal MgO substrate by sputtering deposition. These FePt nanoparticles were partially (1 1 1)-facetted and the as-grown tubes show higher content of metallic SWNTs [156]. Similar results were obtained with FePtAu–MgO catalyst [157]. A pre-treatment of Co on SiO_2/Si substrate with NH_3 brought about an obvious enrichment of (6, 5) SWNTs, which may be caused by the change of facet distribution of the Fe catalyst nanoparticles [42].

4.5 Intermetallic Compound Catalysts

Inspired by the high selectivity of enzyme-catalyzed reactions, Li et al. consider that catalysts with lower crystalline symmetry and unique atomic arrangements are more suitable for chirality-selective growth of SWNTs because such catalysts can offer more specific structural recognition of SWNTs with different (n, m) . Tungsten-based intermetallic compounds were used as catalysts. The high melting point originating from the presence of W, endows them the ability to maintain the crystal structure during the CVD process, while satisfying catalytic activity for SWNT growth is enabled by another component (Fe, Co, Ni, etc.). More importantly, such intermetallic compounds have unique structures, which is crucial for ensuring high selectivity of produced SWNTs. A heteropoly acid containing W and Co is used to prepare intermetallic catalyst nanoparticles under moderate conditions. They achieved highly preferential growth of (12, 6) SWNTs with an exceptionally large population well above 92% (94.4% from micro-Raman spectra, 92.5% from ultraviolet/visible/near-infrared [UV–Vis–NIR] absorption spectra, and 94.9% from AFM-Raman combined method) with W_6Co_7 catalyst based on the epitaxial nucleation [158] (Fig. 16b). Through in situ HRTEM measurements at 1100 °C, W_6Co_7 nanoparticles clearly exhibited lattice fringes during the whole heating process. HRTEM images of the SWNT-catalyst interfaces show that the (12, 6) tubes are always perpendicular to the (0 0 12) plane of the W_6Co_7 catalyst. DFT simulations revealed a perfect geometric match between the (12, 6) tube and (0 0 12) plane and a poor match for all of the other tubes examined. The above results suggest that the lower structural symmetry and the inhomogeneity of different planes in W_6Co_7 critically favor the specific structural matching between the catalyst nanoparticles and SWNTs, thus resulting in chirality-selective SWNT growth.

Similarly, as the DFT simulations showed that the (16, 0) SWNT exhibits a good structural match to the (1 1 6) plane of the W_6Co_7 catalyst (Fig. 16a). Then the dominant growth of zigzag (16, 0) tubes at a content of $79.2 \pm 2.2\%$ under the optimized growth conditions was realized by using catalysts with higher abundance of (1 1 6) planes [159] (Fig. 16c). They also achieved highly preferential growth of

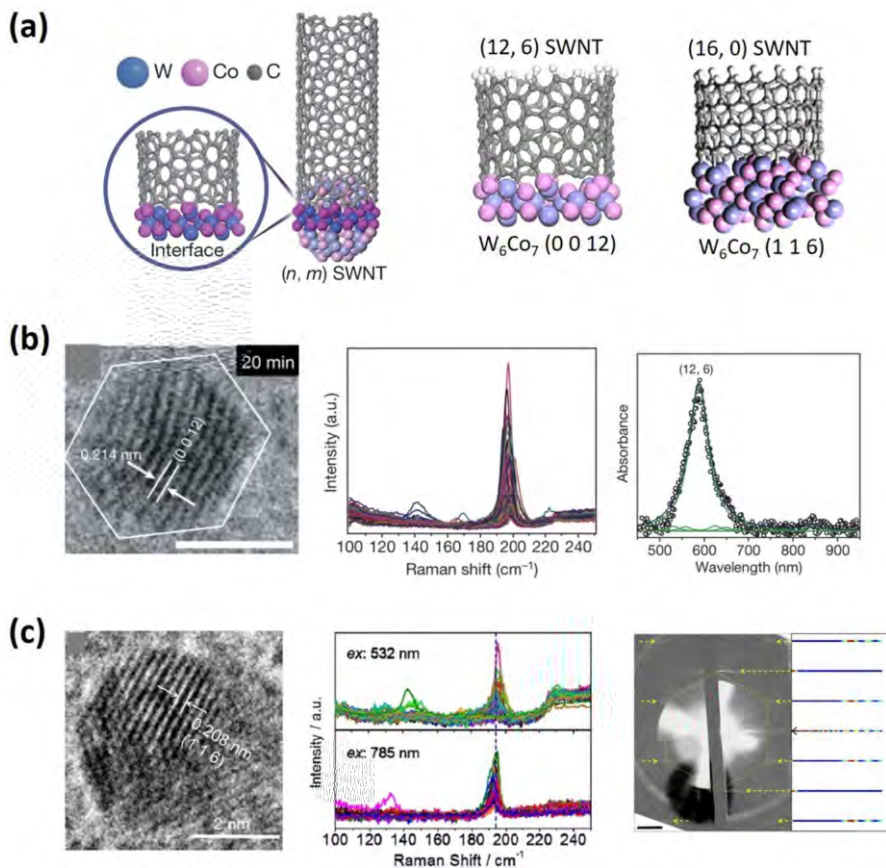


Fig. 16 **a** Templated growth of a SWNT with specified (*n*, *m*) from W_6Co_7 intermetallic compound catalyst (Corresponding figure is reproduced with permission [158, 159], Copyright 2015, Nature Publishing Group and Copyright 2015, American Chemical Society). DFT simulations of (12, 6) tubes on the W_6Co_7 (0 0 12) plane, and (16, 0) tubes on the W_6Co_7 (1 1 6) plane. **b** Characterizations of catalyst structure with in situ HRTEM images of W_6Co_7 catalyst particles in vacuum, showing a clear (0 0 12) plane. Raman spectra and UV-Vis-NIR absorption characterizations of SWNTs using W

above 97% (14, 4) SWNTs, which exhibits a good structural match to the enriched (1 0 10) plane of the W_6Co_7 catalyst prepared by H_2/H_2O [160].

Maruyama et al. used in-plane TEM to reveal morphology differences after reducing CoW catalyst at different temperature. An intermediate structure of Co_6W_6C is unambiguously identified and associated with the selective growth of (12, 6) SWNTs at 50-70% [161].

4.6 Summary of Chirality-Specific Growth

Two factors, thermodynamic preference to tubes with lower formation energy, or kinetic preference of tubes with higher growth speed, play competitive roles in defining the distribution of SWNT chirality [50]. SWNTs with structural selectivity produced with various metal catalysts were concluded in Fig. 17. Epitaxial growth of SWNTs using intermetallic compound catalysts with well-defined structure may be a key solution to the challenge of chirality-specific growth.

It is worthy to point out that the detection methods are also shown in Fig. 17. This information is necessary for us reasonably to analyze and compare the results. Indeed, many techniques, including electron diffraction, optical absorption, Raman spectroscopy, Rayleigh scattering, and photoluminescence, have been used for quantitative analysis of the SWNT abundance [162]. However, the applicability of these methods to the tube samples should be taken into account. For instance, photoluminescence can only be used for semiconducting SWNTs [163]. Raman spectroscopy works for all types of SWNTs, although it suffers from the limitation of resonance windows [164]. Nevertheless, this limitation can be largely overcome by using multiple wavelengths and tunable lasers [165, 166]. Electron diffraction is normally applied for suspended SWNTs [167]. Thus, it is possible to lose information of the short tubes because it is difficult to put them across a gap for detection. Optical absorption is applicable for SWNTs well-dispersed in solutions, but hindered by the low resolution or weak differentiation between certain chiralities [133]. A new optical absorption method was developed by Wang et al. to realize the detection of individual tubes on substrates [168]. A new Rayleigh scattering based method was also developed by Jiang et al., which can easily show the structural uniformity of the tubes by the color of the tube images [169]. These two methods are both applicable to SWNTs on substrates; however, the substrates must be very clean and the SWNTs should be well aligned and sufficiently long. From the above, the selection of suitable techniques is important for obtaining

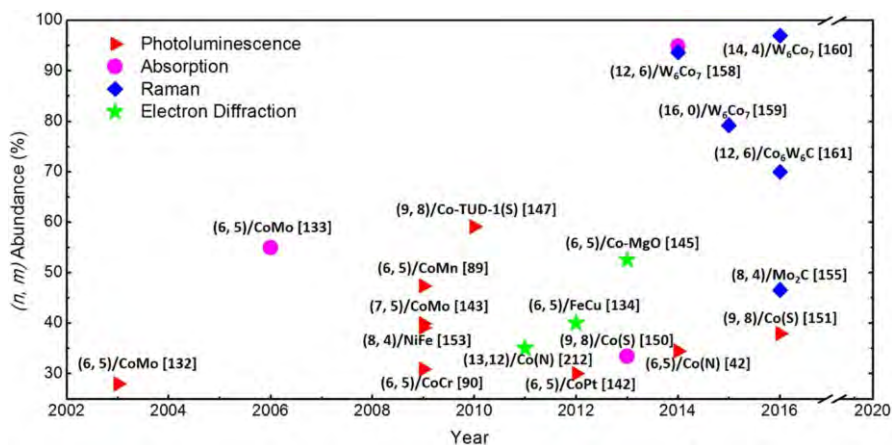


Fig. 17 Reports on selective SWNT growth using metal catalysts

reliable quantification of SWNTs. Normally, a combination of several techniques [158, 170] is needed to acquire a reasonable result.

5 Effect of the CVD Conditions on the Selective Growth of SWNTs

Catalysts play a very important role in the controlled preparation of SWNTs. However, the influence of growth conditions cannot be ignored. The change of growth conditions will directly affect the carbon supply and the catalyst activity, thus affect the growth of SWNTs. At present, there is no universal criteria guiding researchers to get the best growth conditions, but people have accumulated a lot of experience after years of research.

Many carbon-containing molecules can be used as carbon source to grow SWNTs in CVD, such as alcohols [138], hydrocarbons [171, 172], and carbonic oxide [132]. At present, the most commonly used carbon sources in CVD processes are ethanol, carbon monoxide, methane, ethylene, and acetylene. The thermodynamic stability of the carbon source is very different. The decomposition of methane requires higher temperatures, while the pyrolysis of acetylene, ethylene, and ethanol is easier since they decompose exothermally at atmospheric pressure [173]. The main reaction path is disproportionation of CO into carbon and CO₂, when there are no other reactants (e.g. H₂ [174]) in the system. As the reaction is highly exothermic, the reaction equilibrium shifts toward the reverse reaction direction when increasing the temperature. Obviously, this difference in decomposition of the carbon source will directly affect the SWNT growth. On the other hand, the carbon precursors not only present carbon, but also other elements such as hydrogen or oxygen. When the carbon source is decomposed, many hydrogen- and oxygen-containing by-products such as hydrogen and hydroxyl radicals will be produced. These by-products may significantly affect the growth of carbon nanotubes according to many studies on SWNT synthesis [175–180]. Therefore, the carbon source is an important factor in the controlled growth of SWNTs [181, 182].

5.1 Effect of Carbon Precursor Species

Resasco et al. used CO and CH₄ as the carbon sources to grow SWNTs and found only CO resulted a narrow (*n*, *m*) distribution with a single dominating (6, 5) chirality of 54% (Fig. 18a) [133]. As stated above, the disproportionation of CO is exothermic, while the dehydrogenative decomposition of CH₄ is endothermic. Furthermore, the by-products of CH₄ pyrolysis are reductive hydrogen-containing species, while those from CO disproportionation are the oxidative oxygen-containing species. The larger diameter and broader chirality distribution of CH₄-generated tubes may be attributed to the hydrogen produced by the CH₄ decomposition. Hydrogen can accelerate the reduction and sintering of the catalysts, meanwhile, it also decreases the surface fugacity of carbon atoms then hinders the nucleation of carbon on the catalyst surface [183, 184]. Therefore, carbon nanotubes with large-diameter and broader distribution are obtained.

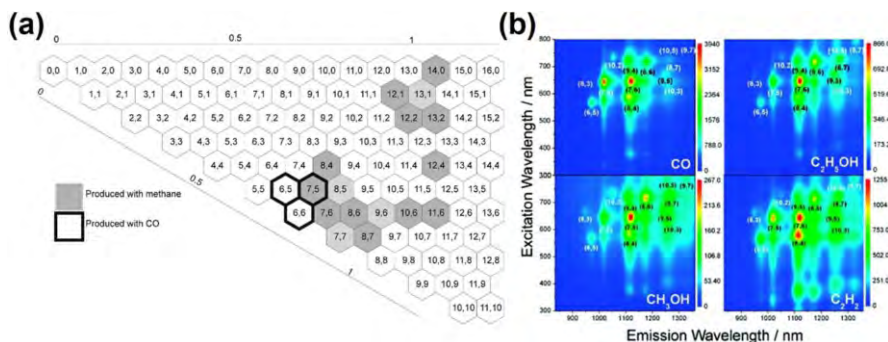


Fig. 18 Effect of carbon species on chirality of SWNTs: **a** chirality maps of SWNT samples produced from two different carbon precursors: CH₄ and CO (Corresponding figure is reproduced with permission [133], Copyright 2006, American Chemical Society). **b** Photoluminescence excitation intensity maps of sodium dodecyl benzene sulfonate (SDBS)-dispersed SWNTs produced from four different carbon precursors on CoMo catalysts (Corresponding figure is reproduced with permission [185], Copyright 2007, American Chemical Society)

Chen et al. [185] used four types of carbon precursors including CO, C₂H₅OH, CH₃OH, and C₂H₂ to grow SWNTs with CoMo catalysts. The chirality distribution of the SWNTs produced by CO was the narrowest and dominated by (7, 6), (7, 5), and (8, 4) tubes, while C₂H₅OH and CH₃OH produced more tubes with larger diameters, namely (8, 6), (9, 5), and (8, 7), and the chirality distribution was also much wider (Fig. 18b). C₂H₂ decomposes much faster than CO. The carbon feeding rate to cobalt surface is also different, leading to different (*n*, *m*) selectivity. He et al. found that SWNTs with narrow diameter distribution of 0.7–1.6 nm were produced by using CO as the carbon source, while large diameter SWNTs ranging from 1.0 to 4.7 nm were produced by using CH₄ as the carbon source [186].

In addition to the decomposition rate of carbon stocks, the decomposition products also affect the selectivity in the growth of SWNTs [176, 179]. Liu et al. selectively grew aligned semiconducting nanotubes by introducing methanol in the growth process [175]. The selectivity was caused by the ·OH radical produced from methanol, which can selectively etch metallic SWNTs because of their smaller ionization potential compared to semiconducting ones.

5.2 Effect of Carbon Feeding

In addition to the carbon source species, the carbon feeding rate (concentration of carbon source) also directly affects the growth of the carbon nanotubes [187–190]. Liu's group synthesized uniform small-diameter SWNTs at a low flow rate of ethane [188]. The average diameter and the diameter distribution of SWNTs increased with the increase of ethane concentration. The diameter of the SWNTs increased with the increasing ethane feeding rates (Fig. 19b). Based on these results, a hypothesis on conditioned activation was proposed. At a given carbon feeding condition, catalysts have an optimal size to nucleate SWNTs. The greater degree of the catalyst's diameter deviation from the optimum size, the less likely it can catalyze the growth of the carbon nanotubes. Smaller nanoparticles are poisoned due to “overfeeding” and larger

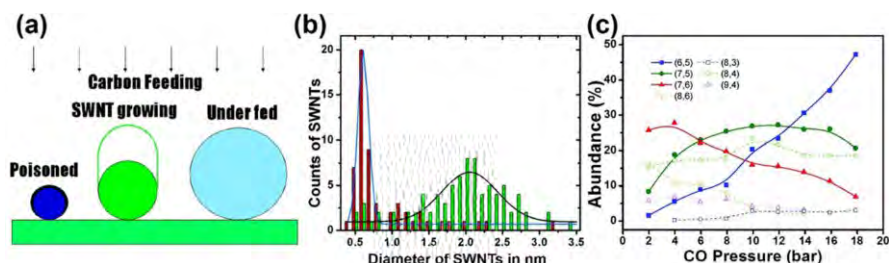


Fig. 19 Effect of source feeding on diameter and chirality of SWNTs: **a** under a given carbon feeding rate, only particles with a moderate and suitable size can nucleate growth (Corresponding figure is reproduced with permission [188], Copyright 2006, American Chemical Society). **b** Diameter distributions of SWNTs grown at different ethane concentrations at 800 °C by AFM measurement: red, 4200 ppm; green, 14,400 ppm (Corresponding figure is reproduced with permission [188], Copyright 2006, American Chemical Society). **c** Abundances of dominant (*n*, *m*) chiral tubes identified by photoluminescence analysis systematically altered with changing CO pressure (Corresponding figure is reproduced with permission [193], Copyright 2007, American Chemical Society)

nanoparticles are inactive due to “underfeeding”. Thus, it is necessary to adjust the carbon source supply rate for the catalyst of given size.

The pressure of the carbon source also directly influences the supply of carbon, which in turn affects the growth of the carbon nanotubes [191–194]. Chen et al. selectively produced bulk SWNT samples with different dominant chiralities enriched by adjusting the pressure of CO on CoMo catalysts from 2 to 18 bar (Fig. 19c) [193]. The higher CO pressure may increase the concentration of the active carbon interacting with Co clusters. Maruyama [195] and Resasco et al. [196] had proposed that carbon caps are formed when carbon in the catalyst particles is saturated. Under higher CO pressure, SWNT growth may be initiated faster and produce thinner tubes, for example (6, 5) and (8, 3). Under lower CO pressure, it should take a longer period for the catalyst nanoparticles to be saturated and form a stable carbon cap. At this period, Co clusters may continuously aggregate due to high-temperature sintering and grow larger to produce larger diameter SWNTs such as (7, 6) and (9, 4). Maruyama group also systematically studied the optimum ethanol pressure for vertically aligned single-walled carbon nanotubes at different CVD temperatures and found that the optimized pressure increases with CVD temperature [191]. SWNT arrays with diameters of 1.47 ± 0.39 and 1.76 ± 0.53 nm were obtained at 60 and 1300 Pa of ethanol pressure, respectively. In addition, higher density of horizontally aligned SWNTs were achieved at lower carbon pressure [194].

5.3 Effect of Growth Temperature

Obviously, growth temperature can influence the growth of SWNTs by changing decomposition of the carbon source or the size of the catalysts [89, 133, 134, 139, 141, 188, 197]. Pfefferle’s group synthesized SWNTs with different diameter distributions through changing reaction temperatures [197]. The diameter of SWNTs shifted systematically from 0.6–0.8 to 1.8–2.0 nm by increasing the reaction temperature from 550 to 950 °C. They speculated that the

Fig. 20 Effect of growth temperature on diameter and chirality of SWNTs: **a** Diameter distribution of SWNTs synthesized at 600, 700, and 800 °C using CoMn–MCM-41 bimetallic catalyst (Corresponding figure is reproduced with permission [198], Copyright 2010, American Chemical Society). **b** Normalized photoluminescence emission intensities of SWNTs grown at temperatures of 600, 750, and 800 °

increase in the diameter of SWNTs was related to the change of the Co catalyst diameters. At low temperature, the average particle diameter of the catalysts was small because the catalyst migrated slowly and the degree of agglomeration was low. Small size catalysts nucleated smaller diameter carbon nanotubes, while large size catalysts sintered at high temperature and grew large diameter carbon nanotubes. A similar phenomenon was found when they used bimetallic CoMn supported on MCM-41 silica templates as catalysts (Fig. 20a) [198].

Fouquet [141] and Chen [89] also found a similar tendency with Co catalyst on Si/SiO₂ substrate. The dominating chirality of the SWNTs grown with CoMo–SiO₂ catalysts changes with temperature and higher chiral enrichment was obtained at lower temperature [133]. The SWNT distribution shifted from a dominant (6, 5) at 700–800 °C to (7, 6) and (8, 7) at 850 °C. Using FeCo [139] and FeCu [134] as the catalysts, the chirality distribution was also changed at different growth temperature (Fig. 20b). Zhang et al. found that when increasing the temperature in the carbon nanotube growth process, the diameter of the carbon nanotubes becomes smaller, and vice versa [199]. Temperature may affect the morphology and the interfacial energy between the catalyst and the SWNT. By periodically changing the growth temperatures, they realized the production of SWNTs with narrow distribution of small chiral angles [200].

5.4 Effect of Additive Species

In addition to carbon source, other additive species may also be used to modulate the growth of SWNTs by regulating the decomposition of carbon stocks [201–204], adjusting the activity and surface property of catalysts [41, 204–207], and selectively etching the more reactive tubes [189, 208–210].

Sulfur has been widely used as an additive species in the growth of SWNTs. It is believed that sulfur can act as the initiator of carbon nanotubes to increase the yield [201]. Generally, sulfur as the growth promoter yielded SWNTs with larger diameters by facilitating the localized nucleation of SWNTs. Cheng [203] and Liu [202] respectively produced large diameter semiconducting SWNTs and metallic SWNTs using sulfur as the growth promoter combined with the appropriate CVD conditions. Chen et al. selectively grew large-diameter (9, 8) nanotubes with 51.7% abundance among semiconducting tubes and 33.5% over all tube species [150]. Sulfur could limit the aggregation of Co atoms [148] to make the catalyst size suitable for the chiral selectivity toward (9, 8) tubes. They proved the formation of Co_9S_8 nanoparticles with narrow size distribution acting as the intermediates made the final Co catalyst uniform [151].

In addition to sulfur, nitrogen is also used as an additive in the growth of SWNTs. Maruyama et al. modulated the mean diameter of the vertically aligned SWNTs from approximately 2–1 nm through adding 5 vol% acetonitrile to ethanol as the carbon feedstock during the growth [41]. When the growth condition was near the thermodynamic equilibrium, SWNT was nucleated through the tangential mode [39]. When acetonitrile was introduced to the system, the decomposed nitrogen atoms absorbed on the surface of the catalyst particles. Compared with carbon, nitrogen interacts more strongly with the Co nanoparticles, thus the nitrogen on the Co nanoparticle surface hinders the formation of the carbon sp^2 network, and hence the tangential growth mode can hardly be maintained. Therefore, the SWNTs grow via the perpendicular growth mode and the diameter of SWNTs is much smaller than the size of the catalysts. Through this method, the diameter of SWNTs can be controlled independent of catalyst preparation [207].

However, the types of nitrogen-containing compounds will directly affect the growth of carbon nanotubes [211, 212]. Kauppinen et al. produced (*n*, *m*)-selective SWNTs with over 90% SWNTs having large chiral angles in the range of 20° – 30° and about 50% in the range of 27° – 29° by introducing NH_3 into the floating catalyst CVD (FCCVD) process. The average diameter increased from 1.60 to 1.67 nm rather than decreasing when NH_3 increased from 0 to 500 ppm [212]. The abundances of the three main chiralities (13, 12), (12, 11), and (13, 11) is 13, 8, and 8%, respectively. NH_3 , as a strong etchant, selectively etched off more reactive SWNTs with smaller chiral angles [213] and smaller diameters [214], resulting in selective growth.

There are still many other additives used as etchants to control the growth of carbon nanotubes, for example, H_2O [84, 189, 215], O_2 [203, 216], CO_2 [210], and H_2 [208, 209]. Many reports have shown that the selective elimination of SWNTs is diameter-dependent (Fig. 21) [84, 175]. The smaller SWNTs are more active because the larger strain associated with greater curvature [217]. At the same time, metallic-SWNTs are preferentially etched and removed by oxidation of the etchant due to their smaller ionization potential [218]. Liu [84] and Cheng [203] et al. synthesized semiconducting SWNTs by controlling the diameter of the SWNTs and introducing the etchant at the same time. Liu controlled the diameter of the SWNTs by using uniform stable FeW nanoclusters as the catalyst precursors and improved semiconducting selectivity by adding H_2O etchant (Fig. 21). The introduction of the

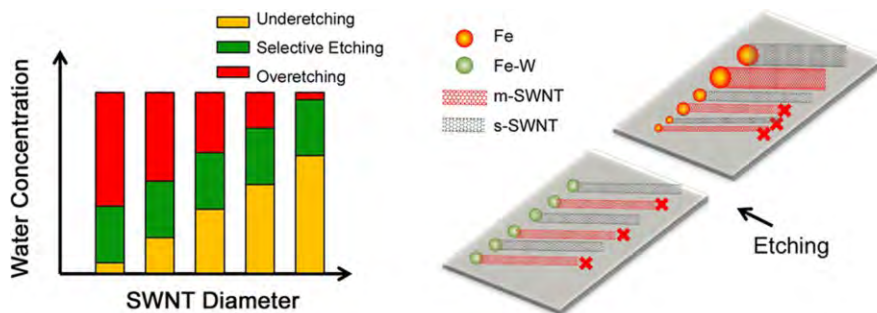


Fig. 21 Schematic illustration of the tube diameter-dependent and electronic-type-dependent etching mechanisms (Corresponding figure is reproduced with permission [84], Copyright 2014, American Chemical Society)

etchant will usually produce larger diameter semiconducting SWNTs. Kauppinen et al. [210] found that the mean diameters of the SWNTs was efficiently altered from 1.2 to 1.9 nm by the addition of appropriate amounts of CO_2 to the carbon source (CO) in FCCVD.

5.5 Effect of the Growth Environment

From above discussion, we know the specific structure of catalyst plays an important role in the synthesis of single-chirality carbon nanotubes. Furthermore, the growth environment also directly affects the chirality of the SWNTs. We found that the selective growth of SWNTs with W_6Co_7 catalysts changed following the CVD conditions [44, 159]. All of the W_6Co_7 catalysts were prepared at 1030 °C and then different ratios of Ar-carried ethanol and hydrogen were used to grow SWNTs at 1030 °C. Higher ethanol/ H_2 ratios resulted in better selectivity toward (12, 6) tubes, and smaller ethanol/ H_2 ratios resulted in SWNTs of larger diameter (Fig. 22) [44]. We also found that the selective growth of (16, 0) tubes can only be achieved at the high H_2 concentration (Table 2) [159]. As discussed previously, hydrogen may lower the carbon fugacity on the catalyst surface and consequently delay the nucleation of caps. We propose that the higher H_2 ratio in the feed gas suppresses

Fig. 22 Effect of the ethanol/ H_2 ratios on the chirality distribution of SWNTs. (a-c) Raman spectra (excitation at 633 nm) of SWNT samples grown at 1030 °C under Ar fluxes of **a** 20, **b** 120, and **c** 200 $\text{cm}^3 \text{min}^{-1}$ through the ethanol bubbler (ice-water bath). The H_2 feed rate was fixed at 50 $\text{cm}^3 \text{min}^{-1}$ (Corresponding figure is reproduced with permission [44], Copyright 2016, American Chemical Society)

Table 2 Statistics on the RBM peaks and the corresponding (*n*, *m*) for the sample grown at 1050 °C by introducing different flow rates of H₂ and constant Ar flow

	H ₂ flow (cm ³ ·min ⁻¹)					
	120		70		30	
	(<i>n</i> , <i>m</i>)	%	(<i>n</i> , <i>m</i>)	%	(<i>n</i> , <i>m</i>)	%
Corresponding table is reproduced with permission [159], Copyright 2015, American Chemical Society Each analysis was based on more than 200 RBM peaks collected with Raman 532, 633, and 785 nm excitations	(16, 0)	39.5	(16, 0)	14.6	(16, 0)	0.9
	(12, 6)	15.5	(12, 6)	27.1	(12, 6)	61.4
	(11, 10)	9.7	(14, 4)	12.5	(12, 8)	5.2
	(10, 6)	9.0	(12, 8)	7.8	(13, 6)	4.7
	(13, 6)	7.2	(17, 6)	7.2	(14, 4)	3.9
	(10, 5)	5.8	(13, 6)	6.2	(11, 8)	3.4
	(14, 4)	3.2	(11, 10)	5.6		
	(12, 8)	3.0	(16, 8)	5.6		

the growth kinetics of all types of tubes and the kinetically unfavorable growth of zigzag tubes are effectively improved.

It can be seen the regulation of growth conditions is very important in the controlled preparation of carbon nanotubes. Only under the suitable growth conditions, the catalyst with controlled structure will be able to catalyze the selective growth of SWNTs with designed chirality. However, the regulation of growth conditions is very complex. There is no very effective way to guide us to find the optimal conditions quickly yet. Therefore, more studies are needed for us to eventually generalize some common rules.

6 Summary

It is obvious that the catalysts play a critical role in the selective growth of SWNTs. We can control the diameter of SWNTs by controlling the catalyst size and the SWNT chirality through further controlling the structure of the catalyst. However, since the growth temperature is high, to constrain the size and structure of catalyst particles is not easy. The catalysts need to have high melting points to maintain a fixed structure and the structure of the catalyst should be unique to improve the selectivity. Tungsten-based intermetallic compounds with unique atomic arrangements and high melting points are the suitable candidates of catalysts for structure-specified growth of SWNTs. Besides the catalysts, the CVD conditions are also very important. The CVD conditions not only affect the nucleation and growth of the SWNTs, but also affect the property of catalysts. Therefore, the highly chirality-selective growth of SWNTs can be realized only by the cooperation of the structural template effect of the catalyst and the optimized CVD conditions.

Acknowledgements This research is financially supported by Ministry of Science and Technology of the People's Republic China (2016YFA0201904), National Natural Science Foundation of China (21631002, U1632119, and 91333105).

References

1. Kharlamova MV (2016) Advances in tailoring the electronic properties of single-walled carbon nanotubes. *Prog Mater Sci* 77:125–211
2. Chen K, Gao W, Emaminejad S, Kiriya D, Ota H, Nyein HYY, Takei K, Javey A (2016) Printed carbon nanotube electronics and sensor systems. *Adv Mater* 28(22):4397–4414
3. Islam AE, Rogers JA, Alam MA (2015) Recent progress in obtaining semiconducting single-walled carbon nanotubes for transistor applications. *Adv Mater* 27(48):7908–7937
4. Nanot S, Haroz EH, Kim JH, Hauge RH, Kono J (2012) Optoelectronic properties of single-wall carbon nanotubes. *Adv Mater* 24(36):4977–4994
5. Meyyappan M (2016) Carbon nanotube-based chemical sensors. *Small* 12(16):2118–2129
6. Cao Q, Rogers JA (2009) Ultrathin films of single-walled carbon nanotubes for electronics and sensors: a review of fundamental and applied aspects. *Adv Mater* 21(1):29–53
7. Wen L, Li F, Cheng HM (2016) Carbon nanotubes and graphene for flexible electrochemical energy storage: from materials to devices. *Adv Mater* 28(22):4306–4337
8. Ni JF, Li Y (2016) Carbon nanomaterials in different dimensions for electrochemical energy storage. *Adv Energy Mater* 6(17):1600278
9. Liu Y, Wang S, Peng LM (2016) Toward high-performance carbon nanotube photovoltaic devices. *Adv Energy Mater* 6(17):1600522
10. Zhang Z, Wei L, Qin X, Li Y (2015) Carbon nanomaterials for photovoltaic process. *Nano Energy* 15:490–522
11. Mehra NK, Jain NK (2016) Multifunctional hybrid-carbon nanotubes: new horizon in drug delivery and targeting. *J Drug Target* 24(4):294–308
12. Liang F, Chen B (2010) A review on biomedical applications of single-walled carbon nanotubes. *Curr Med Chem* 17(1):10–24
13. Banerjee S, Hemraj-Benny T, Wong SS (2005) Covalent surface chemistry of single-walled carbon nanotubes. *Adv Mater* 17(1):17–29
14. Niyogi S, Hamon MA, Hu H, Zhao B, Bhowmik P, Sen R, Itkis ME, Haddon RC (2002) Chemistry of single-walled carbon nanotubes. *Acc Chem Res* 35(12):1105–1113
15. Hirsch A (2002) Functionalization of single-walled carbon nanotubes. *Angew Chem Int Ed* 41(11):1853–1859
16. Saito R, Dresselhaus G, Dresselhaus MS (1998) Physical properties of carbon nanotubes. Imperial College Press, London
17. Saito R, Fujita M, Dresselhaus G, Dresselhaus MS (1992) Electronic structure of chiral graphene tubules. *Appl Phys Lett* 60(18):2204–2206
18. Zhang Q, Huang JQ, Zhao MQ, Qian WZ, Wei F (2011) Carbon nanotube mass production: principles and processes. *ChemSusChem* 4(7):864–889
19. Takagi D, Hibino H, Suzuki S, Kobayashi Y, Homma Y (2007) Carbon nanotube growth from semiconductor nanoparticles. *Nano Lett* 7(8):2272–2275
20. Tang DM, Zhang LL, Liu C, Yin LC, Hou PX, Jiang H, Zhu Z, Li F, Liu B, Kauppinen EI, Cheng H (2012) Heteroepitaxial growth of single-walled carbon nanotubes from boron nitride. *Sci Rep* 2:971
21. Chen Y, Zhang J (2011) Diameter controlled growth of single-walled carbon nanotubes from SiO₂ nanoparticles. *Carbon* 49(10):3316–3324
22. Yu D, Zhang Q, Dai L (2010) Highly efficient metal-free growth of nitrogen-doped single-walled carbon nanotubes on plasma-etched substrates for oxygen reduction. *J Am Chem Soc* 132(43):15127–15129
23. Liu B, Ren W, Gao L, Li S, Pei S, Liu C, Jiang C, Cheng H-M (2009) Metal-catalyst-free growth of single-walled carbon nanotubes. *J Am Chem Soc* 131(6):2082–2083
24. Huang S, Cai Q, Chen J, Qian Y, Zhang L (2009) Metal-catalyst-free growth of single-walled carbon nanotubes on substrates. *J Am Chem Soc* 131(6):2094–2095
25. Kang L, Hu Y, Liu L, Wu J, Zhang S, Zhao Q, Ding F, Li Q, Zhang J (2015) Growth of close packed semiconducting single-walled carbon nanotube arrays using oxygen-deficient TiO₂ nanoparticles as catalysts. *Nano Lett* 15(1):403–409
26. Takagi D, Kobayashi Y, Homma Y (2009) Carbon nanotube growth from diamond. *J Am Chem Soc* 131(20):6922–6923
27. Li Y, Cui R, Ding L, Liu Y, Zhou W, Zhang Y, Jin Z, Peng F, Liu J (2010) How catalysts affect the growth of single-walled carbon nanotubes on substrates. *Adv Mater* 22(13):1508–1515

28. Li P, Zhang X, Liu J (2016) Aligned single-walled carbon nanotube arrays from rhodium catalysts with unexpected diameter uniformity independent of the catalyst size and growth temperature. *Chem Mater* 28(3):870–875
29. Takagi D, Homma Y, Hibino H, Suzuki S, Kobayashi Y (2006) Single-walled carbon nanotube growth from highly activated metal nanoparticles. *Nano Lett* 6(12):2642–2645
30. Yuan D, Ding L, Chu H, Feng Y, McNicholas TP, Liu J (2008) Horizontally aligned single-walled carbon nanotube on quartz from a large variety of metal catalysts. *Nano Lett* 8(8):2576–2579
31. Peng F, Liu Y, Cui RL, Gao DL, Yang F, Li Y (2012) Direct growth of single-walled carbon nanotubes on substrates. *Chin Sci Bull* 57(2–3):225–233
32. Cui R, Zhang Y, Wang J, Zhou W, Li Y (2010) Comparison between copper and iron as catalyst for chemical vapor deposition of horizontally aligned ultralong single-walled carbon nanotubes on silicon substrates. *J Phys Chem C* 114(37):15547–15552
33. Wagner RS, Ellis WC (1964) Vapor–liquid–solid mechanism of single crystal growth. *Appl Phys Lett* 4(5):89–90
34. Saito Y (1995) Nanoparticles and filled nanocapsules. *Carbon* 33(7):979–988
35. Gavillet J, Loiseau A, Journet C, Willaime F, Ducastelle F, Charlier JC (2001) Root-growth mechanism for single-wall carbon nanotubes. *Phys Rev Lett* 87(27):275504
36. Gavillet J, Thibault J, Stephan O, Amara H, Loiseau A, Bichara C, Gaspard J-P, Ducastelle F (2004) Nucleation and growth of single-walled nanotubes: the role of metallic catalysts. *J Nanosci Nanotechnol* 4(4):346–359
37. Harris PJF (2007) Solid state growth mechanisms for carbon nanotubes. *Carbon* 45(2):229–239
38. Jourdain V, Bichara C (2013) Current understanding of the growth of carbon nanotubes in catalytic chemical vapour deposition. *Carbon* 58:2–39
39. Fiawoo MF, Bonnot AM, Amara H, Bichara C, Thibault-Pénisson J, Loiseau A (2012) Evidence of correlation between catalyst particles and the single-wall carbon nanotube diameter: a first step towards chirality control. *Phys Rev Lett* 108(19):195503
40. Shulaker MM, Hills G, Patil N, Wei H, Chen H-Y, Wong H-SP, Mitra S (2013) Carbon nanotube computer. *Nature* 501(7468):526–530
41. Thurakitseree T, Kramberger C, Kumamoto A, Chiashi S, Einarsson E, Maruyama S (2013) Reversible diameter modulation of single-walled carbon nanotubes by acetonitrile-containing feedstock. *ACS Nano* 7(3):2205–2211
42. Fouquet M, Bayer BC, Esconjauregui S, Thomsen C, Hofmann S, Robertson J (2014) Effect of catalyst pretreatment on chirality-selective growth of single-walled carbon nanotubes. *J Phys Chem C* 118(11):5773–5781
43. Yu F, Yang M, Li F, Su C, Ma B, Yuan Z, Chen J, Ma J (2012) The growth mechanism of single-walled carbon nanotubes with a controlled diameter. *Physica E* 44(10):2032–2040
44. Yang F, Wang X, Li M, Liu X, Zhao X, Zhang D, Zhang Y, Yang J, Li Y (2016) Templated synthesis of single-walled carbon nanotubes with specific structure. *Acc Chem Res* 49(4):606–615
45. Ding F, Harutyunyan AR, Yakobson BI (2009) Dislocation theory of chirality-controlled nanotube growth. *Proc Natl Acad Sci* 106(8):2506–2509
46. Gomez-Gualdrón DA, Balbuena PB (2008) The role of cap chirality in the mechanism of growth of single-wall carbon nanotubes. *Nanotechnology* 19:485604
47. Li H-B, Page AJ, Irle S, Morokuma K (2012) Single-walled carbon nanotube growth from chiral carbon nanorings: prediction of chirality and diameter influence on growth rates. *J Am Chem Soc* 134(38):15887–15896
48. Rao R, Liptak D, Cherukuri T, Yakobson BI, Maruyama B (2012) *In situ* evidence for chirality-dependent growth rates of individual carbon nanotubes. *Nat Mater* 11(3):213–216
49. Liu B, Liu J, Tu X, Zhang J, Zheng M, Zhou C (2013) Chirality-dependent vapour-phase epitaxial growth and termination of single-wall carbon nanotubes. *Nano Lett* 13(9):4416–4421
50. Artyukhov VI, Penev ES, Yakobson BI (2014) Why nanotubes grow chiral. *Nat Commun* 5:4892
51. Reich S, Li L, Robertson J (2006) Control the chirality of carbon nanotubes by epitaxial growth. *Chem Phys Lett* 421(4–6):469–472
52. Reich S, Li L, Robertson J (2006) Epitaxial growth of carbon caps on Ni for chiral selectivity. *Phys Status Solidi (b)* 243(13):3494–3499
53. Penev ES, Artyukhov VI, Yakobson BI (2014) Extensive energy landscape sampling of nanotube end-caps reveals no chiral-angle bias for their nucleation. *ACS Nano* 8(2):1899–1906
54. Gómez-Gualdrón DA, Zhao J, Balbuena PB (2011) Nanocatalyst structure as a template to define chirality of nascent single-walled carbon nanotubes. *J Chem Phys* 134(1):014705

55. Li Y, Liu J, Wang Y, Wang ZL (2001) Preparation of monodispersed Fe–Mo nanoparticles as the catalyst for CVD synthesis of carbon nanotubes. *Chem Mater* 13(3):1008–1014
56. Cheung CL, Kurtz A, Park H, Lieber CM (2002) Diameter-controlled synthesis of carbon nanotubes. *J Phys Chem B* 106(10):2429–2433
57. Li YM, Kim W, Zhang YG, Rolandi M, Wang DW, Dai HJ (2001) Growth of single-walled carbon nanotubes from discrete catalytic nanoparticles of various sizes. *J Phys Chem B* 105(46):11424–11431
58. Jeong GH, Yamazaki A, Suzuki S, Yoshimura H, Kobayashi Y, Homma Y (2005) Cobalt-filled apoferritin for suspended single-walled carbon nanotube growth with narrow diameter distribution. *J Am Chem Soc* 127(23):8238–8239
59. Takagi D, Yamazaki A, Otsuka Y, Yoshimura H, Kobayashi Y, Homma Y (2007) Gold-filled apoferritin for investigation of single-walled carbon nanotube growth on substrate. *Chem Phys Lett* 445(4–6):213–216
60. Lukas D, Jason G, Thomas H, Matthias M, Roland R, Christofer H (2009) Narrowing SWNT diameter distribution using size-separated ferritin-based Fe catalysts. *Nanotechnology* 20(35):355601
61. Jeong G-H, Suzuki S, Kobayashi Y, Yamazaki A, Yoshimura H, Homma Y (2005) Effect of nanoparticle density on narrow diameter distribution of carbon nanotubes and particle evolution during chemical vapor deposition growth. *J Appl Phys* 98(12):124311
62. Jeong G-H, Yamazaki A, Suzuki S, Kobayashi Y, Homma Y (2006) Behavior of catalytic nanoparticles during chemical vapor deposition for carbon nanotube growth. *Chem Phys Lett* 422(1–3):83–88
63. Grant R, Filman D, Finkel S, Kolter R, Hogle J (1998) The crystal structure of DPS, a ferritin homolog that binds and protects DNA. *Nat Struct Mol Biol* 5(4):294–303
64. Jeong G-H, Yamazaki A, Suzuki S, Yoshimura H, Kobayashi Y, Homma Y (2007) Production of single-walled carbon nanotubes with narrow diameter distribution using iron nanoparticles derived from DNA-binding proteins from starved cells. *Carbon* 45(5):978–983
65. Kim H-J, Seo SW, Lee J, Jung G, Lee K-H (2014) The synthesis of single-walled carbon nanotubes with narrow diameter distribution using polymerized hemoglobin. *Carbon* 69:588–594
66. Alvarez NT, Orbaek A, Barron AR, Tour JM, Hauge RH (2010) Dendrimer-assisted self-assembled monolayer of iron nanoparticles for vertical array carbon nanotube growth. *ACS Appl Mater Inter* 2(1):15–18
67. Placidus BA, Baratunde AC, Timothy DS, Xianfan X, Timothy SF (2007) Dendrimer-assisted controlled growth of carbon nanotubes for enhanced thermal interface conductance. *Nanotechnology* 18(38):385303
68. Hirano I, Imaoka T, Yamamoto K (2013) Preparation of carbon nanotubes using iron oxide(III) nanoparticles size-controlled by phenylazomethine dendrimers. *J Inorg Organomet Poly Mater* 23(1):223–226
69. Choi HC, Kim W, Wang D, Dai H (2002) Delivery of catalytic metal species onto surfaces with dendrimer carriers for the synthesis of carbon nanotubes with narrow diameter distribution. *J Phys Chem B* 106(48):12361–12365
70. Fu Q, Huang S, Liu J (2004) Chemical vapor depositions of single-walled carbon nanotubes catalyzed by uniform Fe_2O_3 nanoclusters synthesized using diblock copolymer micelles. *J Phys Chem B* 108(20):6124–6129
71. Sreekar B, Alfonso R, Jifa Q, Jing K, Angela MB (2006) Block-copolymer assisted synthesis of arrays of metal nanoparticles and their catalytic activities for the growth of SWNTs. *Nanotechnology* 17(20):5080
72. Lu J, Yi SS, Kopley T, Qian C, Liu J, Gulari E (2006) Fabrication of ordered catalytically active nanoparticles derived from block copolymer micelle templates for controllable synthesis of single-walled carbon nanotubes. *J Phys Chem B* 110(13):6655–6660
73. Lu J, Kopley T, Dutton D, Liu J, Qian C, Son H, Dresselhaus M, Kong J (2006) Generating suspended single-walled carbon nanotubes across a large surface area via patterning self-assembled catalyst-containing block copolymer thin films. *J Phys Chem B* 110(22):10585–10589
74. Lu JQ, Kopley TE, Moll N, Roitman D, Chamberlin D, Fu Q, Liu J, Russell TP, Rider DA, Manners I (2005) High-quality single-walled carbon nanotubes with small diameter, controlled density, and ordered locations using a polyferrocenylsilane block copolymer catalyst precursor. *Chem Mater* 17(9):2227–2231

75. Hashimoto T, Kimishima K, Hasegawa H (1991) Self-assembly and patterns in binary mixtures of Si block copolymer and PPO. *Macromolecules* 24(20):5704–5712
76. Winey KI, Thomas EL, Fetters LJ (1991) Ordered morphologies in binary blends of diblock copolymer and homopolymer and characterization of their intermaterial dividing surfaces. *J Chem Phys* 95(12):9367–9375
77. Coronado E, Gómez-garcía CJ (1995) Polycxometalates: from magnetic clusters to molecular materials. *Comments Inorg Chem* 17(5):255–281
78. Edgar K, Spencer JL (2006) The synthesis of carbon nanotubes from müller clusters. *Curr Appl Phys* 6(3):419–421
79. He M, Fedotov PV, Chernov A, Obratsova ED, Jiang H, Wei N, Cui H, Sainio J, Zhang W, Jin H, Karppinen M, Kauppinen EI, Loiseau A (2016) Chiral-selective growth of single-walled carbon nanotubes on Fe-based catalysts using CO as carbon source. *Carbon* 108:521–528
80. An L, Owens JM, McNeil LE, Liu J (2002) Synthesis of nearly uniform single-walled carbon nanotubes using identical metal-containing molecular nanoclusters as catalysts. *J Am Chem Soc* 124(46):13688–13689
81. Anderson RE, Colorado JR, Crouse C, Ogrin D, Maruyama B, Pender MJ, Edwards CL, Whitsitt E, Moore VC, Koveal D, Lupu C, Stewart MP, Smalley RE, Tour JM, Barron AR (2006) A study of the formation, purification and application as a SWNT growth catalyst of the nanocluster $[H_x-PMo_{12}O_{40} C_4 H_4 Mo_7 Fe_{30} (O_2 CMe)_{15} O_{254} (H_2 O)_{98}]$. *Dalton Trans* 25(25):3097–3107
82. Goss K, Kamra A, Spudat C, Meyer C, Kögerler P, Schneider CM (2009) CVD growth of carbon nanotubes using molecular nanoclusters as catalyst. *Phys Status Solidi (b)* 246(11–12):2494–2497
83. Peng F, Luo D, Sun H, Wang J, Yang F, Li R, Yang J, Li Y (2013) Diameter-controlled growth of aligned single-walled carbon nanotubes on quartz using molecular nanoclusters as catalyst precursors. *Chin Sci Bull* 58(4–5):433–439
84. Li J, Ke C-T, Liu K, Li P, Liang S, Finkelstein G, Wang F, Liu J (2014) Importance of diameter control on selective synthesis of semiconducting single-walled carbon nanotubes. *ACS Nano* 8(8):8564–8572
85. Müller A, Das SK, Kögerler P, Bögge H, Schmidtmann M, Trautwein AX, Schünemann V, Krickemeyer E, Preetz W (2000) A new type of supramolecular compound: molybdenum-oxide-based composites consisting of magnetic nanocapsules with encapsulated Keggin-ion electron reservoirs cross-linked to a two-dimensional network. *Angew Chem* 112(19):3555–3559
86. Muller A, Das SK, Bögge H, Schmidtmann M, Botar A, Patrut A (2001) Generation of cluster capsules (I_h) from decomposition products of a smaller cluster (Keggin- T_d) while surviving ones get encapsulated: species with core-shell topology formed by a fundamental symmetry-driven reaction. *Chem Commun* 7(7):657–658
87. Beck JS, Vartuli JC, Roth WJ, Leonowicz ME, Kresge CT, Schmitt KD, Chu CTW, Olson DH, Sheppard EW, McCullen SB, Higgins JB, Schlenker JL (1992) A new family of mesoporous molecular sieves prepared with liquid crystal templates. *J Am Chem Soc* 114(27):10834–10843
88. Lim S, Ciuparu D, Pak C, Dobek F, Chen Y, Harding D, Pfefferle L, Haller G (2003) Synthesis and characterization of highly ordered Co-MCM-41 for production of aligned single walled carbon nanotubes (swnt). *J Phys Chem B* 107(40):11048–11056
89. Chen Y, Ciuparu D, Lim S, Yang Y, Haller GL, Pfefferle L (2004) Synthesis of uniform diameter single-wall carbon nanotubes in Co-MCM-41: effects of the catalyst prereduction and nanotube growth temperatures. *J Catal* 225(2):453–465
90. Ciuparu D, Chen Y, Lim S, Haller GL, Pfefferle L (2004) Uniform-diameter single-walled carbon nanotubes catalytically grown in cobalt-incorporated MCM-41. *J Phys Chem B* 108(2):503–507
91. Chen Y, Ciuparu D, Lim S, Haller GL, Pfefferle LD (2006) The effect of the cobalt loading on the growth of single wall carbon nanotubes by Co disproportionation on Co-MCM-41 catalysts. *Carbon* 44(1):67–78
92. Loebick CZ, Derrouiche S, Marinkovic N, Wang C, Hennrich F, Kappes MM, Haller GL, Pfefferle LD (2009) Effect of manganese addition to the Co-MCM-41 catalyst in the selective synthesis of single wall carbon nanotubes. *J Phys Chem C* 113(52):21611–21620
93. Zoican Loebick C, Derrouiche S, Fang F, Li N, Haller GL, Pfefferle LD (2009) Effect of chromium addition to the Co-MCM-41 catalyst in the synthesis of single wall carbon nanotubes. *Appl Catal A* 368(1–2):40–49
94. Wei L, Bai S, Peng W, Yuan Y, Si R, Goh K, Jiang R, Chen Y (2014) Narrow-chirality distributed single-walled carbon nanotube synthesis by remote plasma enhanced ethanol deposition on cobalt incorporated MCM-41 catalyst. *Carbon* 66:134–143

95. Lim S, Wang C, Yang Y, Ciuparu D, Pfefferle L, Haller GL (2007) Evidence for anchoring and partial occlusion of metallic clusters on the pore walls of MCM-41 and effect on the stability of the metallic clusters. *Catal Today* 123(1–4):122–132
96. Amama PB, Lim S, Ciuparu D, Yang Y, Pfefferle L, Haller GL (2005) Synthesis, characterization, and stability of Fe–MCM-41 for production of carbon nanotubes by acetylene pyrolysis. *J Phys Chem B* 109(7):2645–2656
97. Atchudan R, Pandurangan A, Somanathan T (2009) Bimetallic mesoporous materials for high yield synthesis of carbon nanotubes by chemical vapour deposition techniques. *J Mol Catal A: Chem* 309(1–2):146–152
98. Subashini D, Pandurangan A (2007) Synthesis of mesoporous molecular sieves as catalytic template for the growth of single walled carbon nanotubes. *Catal Commun* 8(11):1665–1670
99. Ago H, Imamura S, Okazaki T, Saitoj T, Yumura M, Tsuji M (2005) CVD growth of single-walled carbon nanotubes with narrow diameter distribution over Fe/MgO catalyst and their fluorescence spectroscopy. *J Phys Chem B* 109(20):10035–10041
100. Tang ZK, Sun HD, Wang J, Chen J, Li G (1998) Mono-sized single-wall carbon nanotubes formed in channels of ALPO

118. Kim SM, Pint CL, Amama PB, Zakharov DN, Hauge RH, Maruyama B, Stach EA (2010) Evolution in catalyst morphology leads to carbon nanotube growth termination. *J Phys Chem Lett* 1(6):918–922
119. Colaizzi ML, Chen PJ, Yates JT (1990) Spectroscopic studies of the thermal modification of the Fe/Al₂O₃ interface. *Surf Sci* 238(1):13–24
120. Song W, Jeon C, Kim YS, Kwon YT, Jung DS, Jang SW, Choi WC, Park JS, Saito R, Park C-Y (2010) Synthesis of bandgap-controlled semiconducting single-walled carbon nanotubes. *ACS Nano* 4(2):1012–1018
121. Ago H, Ayagaki T, Ogawa Y, Tsuji M (2011) Ultrahigh-vacuum-assisted control of metal nanoparticles for horizontally aligned single-walled carbon nanotubes with extraordinary uniform diameters. *J Phys Chem C* 115(27):13247–13253
122. Youn SK, Yazdani N, Patscheider J, Park HG (2013) Facile diameter control of vertically aligned, narrow single-walled carbon nanotubes. *RSC Adv* 3(5):1434–1441
123. Wang X, Yue WB, He MS, Liu MH, Zhang J, Liu ZF (2004) Bimetallic catalysts for the efficient growth of SWNTs on surfaces. *Chem Mater* 16(5):799–805
124. Xiang R, Einarsson E, Murakami Y, Shiomi J, Chiashi S, Tang Z, Maruyama S (2012) Diameter modulation of vertically aligned single-walled carbon nanotubes. *ACS Nano* 6(8):7472–7479
125. Wei L, Liu BL, Wang XT, Gui H, Yuan Y, Zhai SL, Ng AK, Zhou CW, Chen Y (2015) (9, 8) single-walled carbon nanotube enrichment via aqueous two-phase separation and their thin-film transistor applications. *Adv Elec Mater* 1(11):1500151
126. He XW, Gao WL, Xie LJ, Li B, Zhang Q, Lei SD, Robinson JM, Haroz EH, Doorn SK, Wang WP, Vajtai R, Ajayan PM, Adams WW, Hauge RH, Kono J (2016) Wafer-scale monodomain films of spontaneously aligned single-walled carbon nanotubes. *Nat Nanotechnol* 11(7):633–639
127. Jain RM, Howden R, Tvrđy K, Shimizu S, Hilmer AJ, McNicholas TP, Gleason KK, Strano MS (2012) Polymer-free near-infrared photovoltaics with single chirality (6, 5) semiconducting carbon nanotube active layers. *Adv Mater* 24(32):4436–4439
128. Isborn CM, Tang C, Martini A, Johnson ER, Otero-de-la-Roza A, Tung VC (2013) Carbon nanotube chirality determines efficiency of electron transfer to fullerene in all-carbon photovoltaics. *J Phys Chem Lett* 4(17):2914–2918
129. Diao S, Hong GS, Robinson JT, Jiao LY, Antaris AL, Wu JZ, Choi CL, Dai HJ (2012) Chirality enriched (12, 1) and (11, 3) single-walled carbon nanotubes for biological imaging. *J Am Chem Soc* 134(41):16971–16974
130. Yomogida Y, Tanaka T, Zhang M, Yudasaka M, Wei X, Kataura H (2016) Industrial-scale separation of high-purity single-chirality single-wall carbon nanotubes for biological imaging. *Nat Commun* 7:12056
131. De Volder MF, Tawfick SH, Baughman RH, Hart AJ (2013) Carbon nanotubes: present and future commercial applications. *Science* 339(6119):535–539
132. Bachilo SM, Balzano L, Herrera JE, Pompeo F, Resasco DE, Weisman RB (2003) Narrow (*n, m*)-distribution of single-walled carbon nanotubes grown using a solid supported catalyst. *J Am Chem Soc* 125(37):11186–11187
133. Lolli G, Zhang L, Balzano L, Sakulchaicharoen N, Tan Y, Resasco DE (2006) Tailoring (*n, m*) structure of single-walled carbon nanotubes by modifying reaction conditions and the nature of the support of CoMo catalysts. *J Phys Chem B* 110(5):2108–2115
134. He M, Chernov AI, Fedotov PV, Obratsova ED, Sainio J, Rikkinen E, Jiang H, Zhu Z, Tian Y, Kauppinen EI (2010) Predominant (6, 5) single-walled carbon nanotube growth on a copper-promoted iron catalyst. *J Am Chem Soc* 132(40):13994–13996
135. He M, Chernov AI, Obratsova ED, Jiang H, Kauppinen EI, Lehtonen J (2012) Synergistic effects in FeCu bimetallic catalyst for low temperature growth of single-walled carbon nanotubes. *Carbon* 52:590–594
136. He M, Liu B, Chernov AI, Obratsova ED, Kauppi I, Jiang H, Anoshkin I, Cavalca F, Hansen TW, Wagner JB, Nasibulin AG, Kauppinen EI, Linnekoski J, Niemelä M, Lehtonen J (2012) Growth mechanism of single-walled carbon nanotubes on iron–copper catalyst and chirality studies by electron diffraction. *Chem Mater* 24(10):1796–1801
137. Cui K, Kumamoto A, Xiang R, An H, Wang B, Inoue T, Chiashi S, Ikuhara Y, Maruyama S (2016) Synthesis of subnanometer-diameter vertically aligned single-walled carbon nanotubes with copper-anchored cobalt catalysts. *Nanoscale* 8(3):1608–1617
138. Maruyama S, Kojima R, Miyauchi Y, Chiashi S, Kohno M (2002) Low-temperature synthesis of high-purity single-walled carbon nanotubes from alcohol. *Chem Phys Lett* 360(3):229–234

139. Miyauchi Y, Chiashi S, Murakami Y, Hayashida Y, Maruyama S (2004) Fluorescence spectroscopy of single-walled carbon nanotubes synthesized from alcohol. *Chem Phys Lett* 387(1–3):198–203
140. He M, Fedotov PV, Obraztsova ED, Viitanen V, Sainio J, Jiang H, Kauppinen EI, Niemelä M, Lehtonen J (2012) Chiral-selective growth of single-walled carbon nanotubes on stainless steel wires. *Carbon* 50(11):4294–4297
141. Fouquet M, Bayer B, Esconjauregui S, Blume R, Warner J, Hofmann S, Schlögl R, Thomsen C, Robertson J (2012) Highly chiral-selective growth of single-walled carbon nanotubes with a simple monometallic Co catalyst. *Phys Rev B* 85(23):235411
142. Liu B, Ren W, Li S, Liu C, Cheng H-M (2012) High temperature selective growth of single-walled carbon nanotubes with a narrow chirality distribution from a CoPt bimetallic catalyst. *Chem Commun* 48(18):2409–2411
143. Wang B, Yang Y, Li L-J, Chen Y (2009) Effect of different catalyst supports on the (*n*, *m*) selective growth of single-walled carbon nanotube from Co–Mo catalyst. *J Mater Sci* 44(12):3285–3295
144. He M, Chernov AI, Fedotov PV, Obraztsova ED, Rikkinen E, Zhu Z, Sainio J, Jiang H, Nasibulin AG, Kauppinen EI, Niemelä M, Krause AOI (2011) Selective growth of SWNTs on partially reduced monometallic cobalt catalyst. *Chem Commun* 47(4):1219–1221
145. He M, Jiang H, Liu B, Fedotov PV, Chernov AI, Obraztsova ED, Cavalca F, Wagner JB, Hansen TW, Anoshkin IV, Obraztsova EA, Belkin AV, Sairanen E, Nasibulin AG, Lehtonen J, Kauppinen EI (2013) Chiral-selective growth of single-walled carbon nanotubes on lattice-mismatched epitaxial cobalt nanoparticles. *Sci Rep* 3:1460
146. Ishigami N, Ago H, Imamoto K, Tsuji M, Iakoubovskii K, Minami N (2008) Crystal plane dependent growth of aligned single-walled carbon nanotubes on sapphire. *J Am Chem Soc* 130(30):9918–9924
147. Wang H, Wang B, Quek XY, Wei L, Zhao J, Li LJ, Chan-Park MB, Yang Y, Chen Y (2010) Selective synthesis of (9, 8) single walled carbon nanotubes on cobalt incorporated TUD-1 catalysts. *J Am Chem Soc* 132(47):16747–16749
148. Wang H, Goh K, Xue R, Yu D, Jiang W, Lau R, Chen Y (2013) Sulfur doped Co/SiO₂ catalysts for chirally selective synthesis of single walled carbon nanotubes. *Chem Commun* 49(20):2031–2033
149. Wang H, Ren F, Liu C, Si R, Yu D, Pfefferle LD, Haller GL, Chen Y (2013) CoSO₄/SiO₂ catalyst for selective synthesis of (9, 8) single-walled carbon nanotubes: effect of catalyst calcination. *J Catal* 300:91–101
150. Wang H, Wei L, Ren F, Wang Q, Pfefferle LD, Haller GL, Chen Y (2013) Chiral-selective CoSO₄/SiO₂ catalyst for (9, 8) single-walled carbon nanotube growth. *ACS Nano* 7(1):614–626
151. Yuan Y, Karahan HE, Yildrm C, Wei L, Birer O, Zhai S, Lau R, Chen Y (2016) “Smart poisoning” of Co/SiO₂ catalysts by sulfidation for chirality selective synthesis of (9, 8) single-walled carbon nanotubes. *Nanoscale* 8(40):17705–17713
152. Zhu H, Suenaga K, Wei J, Wang K, Wu D (2008) A strategy to control the chirality of single-walled carbon nanotubes. *J Cryst Growth* 310(24):5473–5476
153. Chiang WH, Sankaran RM (2009) Linking catalyst composition to chirality distributions of as-grown single-walled carbon nanotubes by tuning Ni_xFe_{1–x} nanoparticles. *Nat Mater* 8(11):882–886
154. Dutta D, Chiang W-H, Sankaran RM, Bhethanabotla VR (2012) Epitaxial nucleation model for chiral-selective growth of single-walled carbon nanotubes on bimetallic catalyst surfaces. *Carbon* 50(10):3766–3773
155. Kang L, Deng S, Zhang S, Li Q, Zhang J (2016) Selective growth of subnanometer diameter single-walled carbon nanotube arrays in hydrogen-free CVD. *J Am Chem Soc* 138(39):12723–12726
156. Ohashi T, Shima T (2015) Synthesis of vertically aligned single-walled carbon nanotubes with metallic chirality through facet control of catalysts. *Carbon* 87:453–461
157. Ohashi T, Iwama H, Shima T (2016) Growth of vertically aligned single-walled carbon nanotubes with metallic chirality through faceted FePt–Au catalysts. *J Appl Phys* 119(8):084303
158. Yang F, Wang X, Zhang D, Yang J, Luo D, Xu Z, Wei J, Wang J-Q, Xu Z, Peng F, Li X, Li R, Li Y, Li M, Bai X, Ding F, Li Y (2014) Chirality-specific growth of single-walled carbon nanotubes on solid alloy catalysts. *Nature* 510(7506):522–524
159. Yang F, Wang X, Zhang D, Qi K, Yang J, Xu Z, Li M, Zhao X, Bai X, Li Y (2015) Growing zigzag (16, 0) carbon nanotubes with structure-defined catalysts. *J Am Chem Soc* 137(27):8688–8691
160. Yang F, Wang X, Si J, Zhao X, Qi K, Jin C, Zhang Z, Li M, Zhang D, Yang J, Zhang Z, Xu Z, Peng L-M, Bai X, Li Y (2016) Water-assisted preparation of high-purity semiconducting (14, 4) carbon nanotubes. *ACS Nano* 11(1):186–193

161. An H, Kumamoto A, Takezaki H, Ohyama S, Qian Y, Inoue T, Ikuhara Y, Chiashi S, Xiang R, Maruyama S (2016) Chirality specific and spatially uniform synthesis of single-walled carbon nanotubes from sputtered Co–W bimetallic catalyst. *Nanoscale* 8(30):14523–14529
162. Zhang D, Yang J, Li Y (2013) Spectroscopic characterization of the chiral structure of individual single-walled carbon nanotubes and the edge structure of isolated graphene nanoribbons. *Small* 9(8):1284–1304
163. Bachilo SM (2002) Structure-assigned optical spectra of single-walled carbon nanotubes. *Science* 298(5602):2361–2366
164. Dresselhaus MS, Dresselhaus G, Saito R, Jorio A (2005) Raman spectroscopy of carbon nanotubes. *Phys Rep* 409(2):47–99
165. Maultzsch J, Telg H, Reich S, Thomsen C (2005) Radial breathing mode of single-walled carbon nanotubes: optical transition energies and chiral-index assignment. *Phys Rev B* 72(20):205438
166. Araujo PT, Pesce PBC, Dresselhaus MS, Sato K, Saito R, Jorio A (2010) Resonance Raman spectroscopy of the radial breathing modes in carbon nanotubes. *Physica E* 42(5):1251–1261
167. Qin L-C (2006) Electron diffraction from carbon nanotubes. *Rep Prog Phys* 69(10):2761–2821
168. Liu K, Hong X, Zhou Q, Jin C, Li J, Zhou W, Liu J, Wang E, Zettl A, Wang F (2013) High-throughput optical imaging and spectroscopy of individual carbon nanotubes in devices. *Nat Nanotechnol* 8(12):917–922
169. Wu W, Yue J, Lin X, Li D, Zhu F, Yin X, Zhu J, Wang J, Zhang J, Chen Y (2015) True-color real-time imaging and spectroscopy of carbon nanotubes on substrates by enhanced Rayleigh scattering. *Nano Res* 8(8):2721–2732
170. Naumov AV, Kuznetsov OA, Harutyunyan AR, Green AA, Hersam MC, Resasco DE, Nikolaev PN, Weisman RB (2009) Quantifying the semiconducting fraction in single-walled carbon nanotube samples through comparative atomic force and photoluminescence microscopies. *Nano Lett* 9(9):3203–3208
171. Kong J, Soh HT, Cassell AM, Quate CF, Dai H (1998) Synthesis of individual single-walled carbon nanotubes on patterned silicon wafers. *Nature* 395(6705):878–881
172. Pattinson SW, Ranganathan V, Murakami HK, Koziol KKK, Windle AH (2012) Nitrogen-induced catalyst restructuring for epitaxial growth of multiwalled carbon nanotubes. *ACS Nano* 6(9):7723–7730
173. Haynes WM (2015–2016) CRC handbook of chemistry and physics. CRC Press, Hammond
174. Geurts FWAH, Sacco A (1992) The relative rates of the boudouard reaction and hydrogenation of CO over Fe and Co foils. *Carbon* 30(3):415–418
175. Ding L, Tselev A, Wang J, Yuan D, Chu H, McNicholas TP, Li Y, Liu J (2009) Selective growth of well-aligned semiconducting single-walled carbon nanotubes. *Nano Lett* 9(2):800–805
176. Che Y, Wang C, Liu J, Liu B, Lin X, Parker J, Beasley C, Wong HSP, Zhou C (2012) Selective synthesis and device applications of semiconducting single-walled carbon nanotubes using isopropanol as feedstock. *ACS Nano* 6(8):7454–7462
177. Li W-S, Hou P-X, Liu C, Sun D-M, Yuan J, Zhao S-Y, Yin L-C, Cong H, Cheng H-M (2013) High quality, highly concentrated semiconducting single-wall carbon nanotubes for use in field effect transistors and biosensors. *ACS Nano* 7(8):6831–6839
178. Hou P-X, Li W-S, Zhao S-Y, Li G-X, Shi C, Liu C, Cheng H-M (2014) Preparation of metallic single-wall carbon nanotubes by selective etching. *ACS Nano* 8(7):7156–7162
179. Ibrahim I, Kalbacova J, Engemaier V, Pang J, Rodriguez RD, Grimm D, Gemming T, Zahn DRT, Schmidt OG, Eckert J, Rummeli MH (2015) Confirming the dual role of etchants during the enrichment of semiconducting single wall carbon nanotubes by chemical vapor deposition. *Chem Mater* 27(17):5964–5973
180. Futaba DN, Goto J, Yasuda S, Yamada T, Yumura M, Hata K (2009) General rules governing the highly efficient growth of carbon nanotubes. *Adv Mater* 21(47):4811–4815
181. Resasco DE, Herrera JE, Balzano L (2004) Decomposition of carbon-containing compounds on solid catalysts for single-walled nanotube production. *J Nanosci Nanotechnol* 4(4):398–407
182. Barnard JS, Paukner C, Koziol KK (2016) The role of carbon precursor on carbon nanotube chirality in floating catalytic chemical vapour deposition. *Nanoscale* 8(39):17262–17270
183. Boudart M (1989) Virtual pressure and virtual fugacity in catalysis and electrocatalysis. *Catal Lett* 3(2):111–115
184. Iglesia E, Baumgartner JE, Price GL (1992) Kinetic coupling and hydrogen surface fugacities in heterogeneous catalysis: I. Alkane reactions on Te/NaX, H-ZSM5, and Ga/H-ZSM5. *J Catal* 134(2):549–571

185. Wang B, Poa CHP, Wei L, Li LJ, Yang Y, Chen Y (2007) (*n, m*) selectivity of single-walled carbon nanotubes by different carbon precursors on Co–Mo catalysts. *J Am Chem Soc* 129(29):9014–9019
186. He M, Jiang H, Kauppinen EI, Lehtonen J (2012) Diameter and chiral angle distribution dependencies on the carbon precursors in surface-grown single-walled carbon nanotubes. *Nanoscale* 4(23):7394–7398
187. Qi H, Yuan DN, Liu J (2007) Two-stage growth of single-walled carbon nanotubes. *J Phys Chem C* 111(17):6158–6160
188. Lu C, Liu J (2006) Controlling the diameter of carbon nanotubes in chemical vapor deposition method by carbon feeding. *J Phys Chem B* 110(41):20254–20257
189. Zhou W, Zhan S, Ding L, Liu J (2012) General rules for selective growth of enriched semiconducting single walled carbon nanotubes with water vapor as *in situ* etchant. *J Am Chem Soc* 134(34):14019–14026
190. Wang Y, Liu Y, Li X, Cao L, Wei D, Zhang H, Shi D, Yu G, Kajiura H, Li Y (2007) Direct enrichment of metallic single-walled carbon nanotubes induced by the different molecular composition of monohydroxy alcohol homologues. *Small* 3(9):1486–1490
191. Einarsson E, Murakami Y, Kadowaki M, Maruyama S (2008) Growth dynamics of vertically aligned single-walled carbon nanotubes from *in situ* measurements. *Carbon* 46(6):923–930
192. Navas H, Maruyama B, Weaver K, Paillet M, Zahab A-A, Fossard F, Loiseau A, Quesnel E, Anglaret E, Jourdain V (2014) Interplay of interfacial compounds, catalyst thickness and carbon precursor supply in the selectivity of single-walled carbon nanotube growth. *Carbon* 80:599–609
193. Wang B, Wei L, Yao L, Li LJ, Yang Y, Chen Y (2007) Pressure-induced single-walled carbon nanotube (*n, m*) selectivity on Co–Mo catalysts. *J Phys Chem C* 111(40):14612–14616
194. Inoue T, Hasegawa D, Badar S, Aikawa S, Chiashi S, Maruyama S (2013) Effect of gas pressure on the density of horizontally aligned single-walled carbon nanotubes grown on quartz substrates. *J Phys Chem C* 117(22):11804–11810
195. Shibuta Y, Maruyama S (2003) Molecular dynamics simulation of formation process of single-walled carbon nanotubes by CCVD method. *Chem Phys Lett* 382(3–4):381–386
196. Balbuena PB, Zhao J, Huang S, Wang Y, Sakulchaicharoen N, Resasco DE (2006) Role of the catalyst in the growth of single-wall carbon nanotubes. *J Nanosci Nanotechnol* 6(5):1247–1258
197. Li N, Wang X, Ren F, Haller GL, Pfefferle LD (2009) Diameter tuning of single-walled carbon nanotubes with reaction temperature using a Co monometallic catalyst. *J Phys Chem C* 113(23):10070–10078
198. Zoican Loebick C, Podila R, Reppert J, Chudow J, Ren F, Haller GL, Rao AM, Pfefferle LD (2010) Selective synthesis of subnanometer diameter semiconducting single-walled carbon nanotubes. *J Am Chem Soc* 132(32):11125–11131
199. Yao Y, Li Q, Zhang J, Liu R, Jiao L, Zhu YT, Liu Z (2007) Temperature-mediated growth of single-walled carbon-nanotube intramolecular junctions. *Nat Mater* 6(4):293–296
200. Zhao Q, Xu Z, Hu Y, Ding F, Zhang J (2016) Chemical vapor deposition synthesis of near-zigzag single-walled carbon nanotubes with stable tube-catalyst interface. *Sci Adv* 2(5):1501729
201. Cheng HM, Li F, Su G, Pan HY, He LL, Sun X, Dresselhaus MS (1998) Large-scale and low-cost synthesis of single-walled carbon nanotubes by the catalytic pyrolysis of hydrocarbons. *Appl Phys Lett* 72(25):3282–3284
202. Li J, Otsuka K, Zhang X, Maruyama S, Liu J (2016) Selective synthesis of large diameter, highly conductive and high density single-walled carbon nanotubes by thiophene-assisted chemical vapor deposition method on transparent substrates. *Nanoscale* 8(29):14156–14162
203. Yu B, Liu C, Hou P-X, Tian Y, Li S, Liu B, Li F, Kauppinen EI, Cheng H-M (2011) Bulk synthesis of large diameter semiconducting single-walled carbon nanotubes by oxygen-assisted floating catalyst chemical vapor deposition. *J Am Chem Soc* 133(14):5232–5235
204. Zhang L, Hou P-X, Li S, Shi C, Cong H-T, Liu C, Cheng H-M (2014) *In situ* TEM observations on the sulfur-assisted catalytic growth of single-wall carbon nanotubes. *J Phys Chem Lett* 5(8):1427–1432
205. Koziol KKK, Ducati C, Windle AH (2010) Carbon nanotubes with catalyst controlled chiral angle. *Chem Mater* 22(17):4904–4911
206. Yuan Y, Wei L, Jiang W, Goh K, Jiang R, Lau R, Chen Y (2015) Sulfur-induced chirality changes in single-walled carbon nanotube synthesis by ethanol chemical vapor deposition on a Co/SiO₂ catalyst. *J Mater Chem A* 3(7):3310–3319

207. Thurakitseree T, Kramberger C, Zhao P, Aikawa S, Harish S, Chiashi S, Einarsson E, Maruyama S (2012) Diameter-controlled and nitrogen-doped vertically aligned single-walled carbon nanotubes. *Carbon* 50(7):2635–2640
208. Zhang G, Qi P, Wang X, Lu Y, Mann D, Li X, Dai H (2006) Hydrogenation and hydrocarbonation

Preparation of Horizontal Single-Walled Carbon Nanotubes Arrays

Pan Li^{1,2} · Jin Zhang¹

© 2016 The Author(s)
 Licensed under the Creative Commons Attribution 4.0 International License.

Abstract

Horizontal single-walled carbon nanotubes (SWCNTs) arrays were prepared by a chemical vapor deposition (CVD) method using a nickel catalyst. The arrays were grown on a silicon substrate with a nickel catalyst layer. The growth temperature was 1000 °C, and the growth time was 10 min. The arrays were characterized by scanning electron microscopy (SEM), transmission electron microscopy (TEM), and Raman spectroscopy. The SEM images showed that the arrays were composed of many small nanotubes. The TEM images showed that the nanotubes were single-walled. The Raman spectra showed that the nanotubes were of high quality.

Chapter 3 was originally published as Li, P. & Zhang, J. Top Curr Chem (Z) (2016) 374: 85. DOI 10.1007/s41061-016-0085-4.



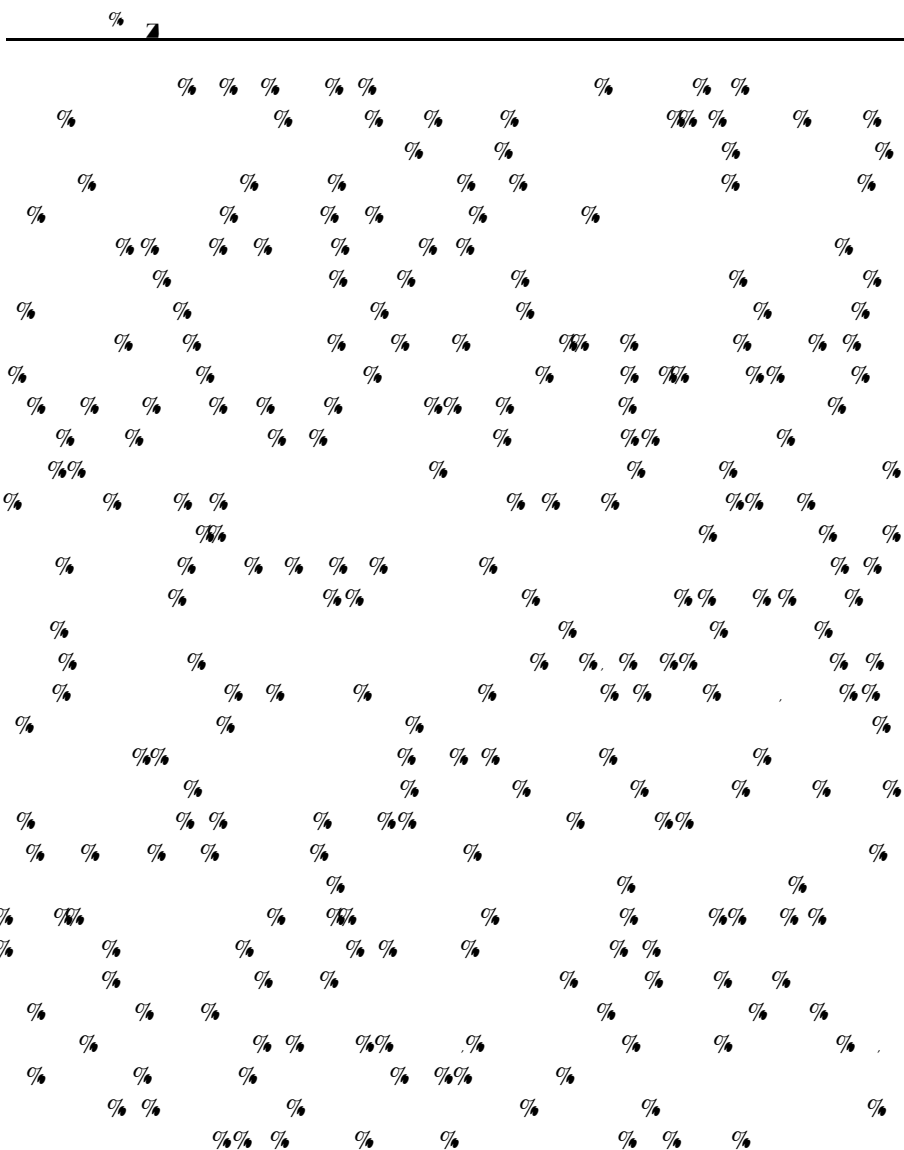
✉

Horizontal single-walled carbon nanotubes (SWCNTs) arrays were prepared by a chemical vapor deposition (CVD) method using a nickel catalyst. The arrays were grown on a silicon substrate with a nickel catalyst layer. The growth temperature was 1000 °C, and the growth time was 10 min. The arrays were characterized by scanning electron microscopy (SEM), transmission electron microscopy (TEM), and Raman spectroscopy. The SEM images showed that the arrays were composed of many small nanotubes. The TEM images showed that the nanotubes were single-walled. The Raman spectra showed that the nanotubes were of high quality.

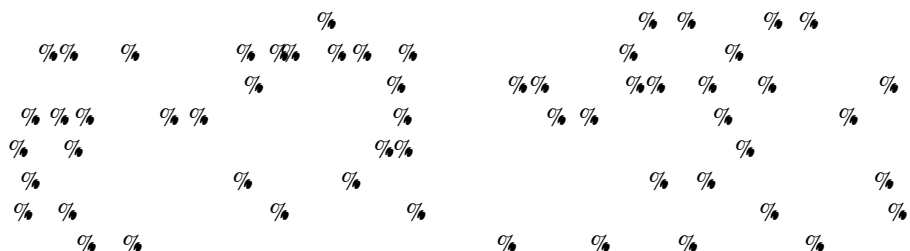
Keywords

1 Introduction

Keywords



2 Orientational Growth of SWNTs



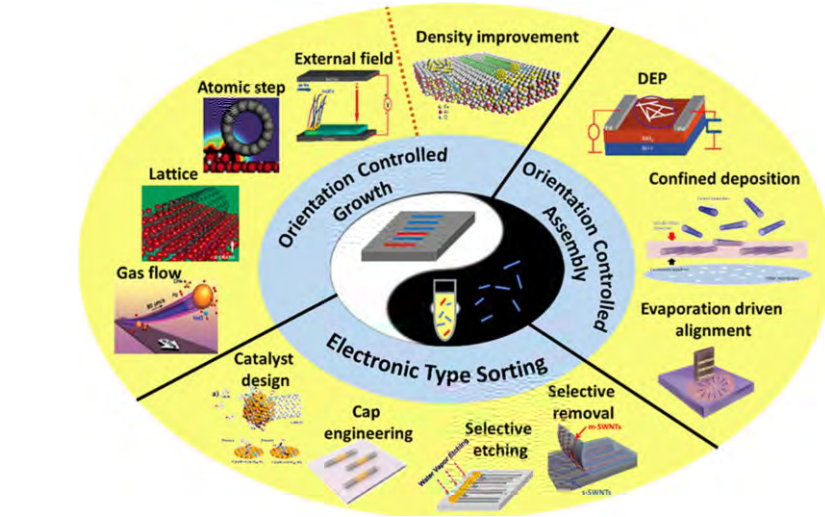
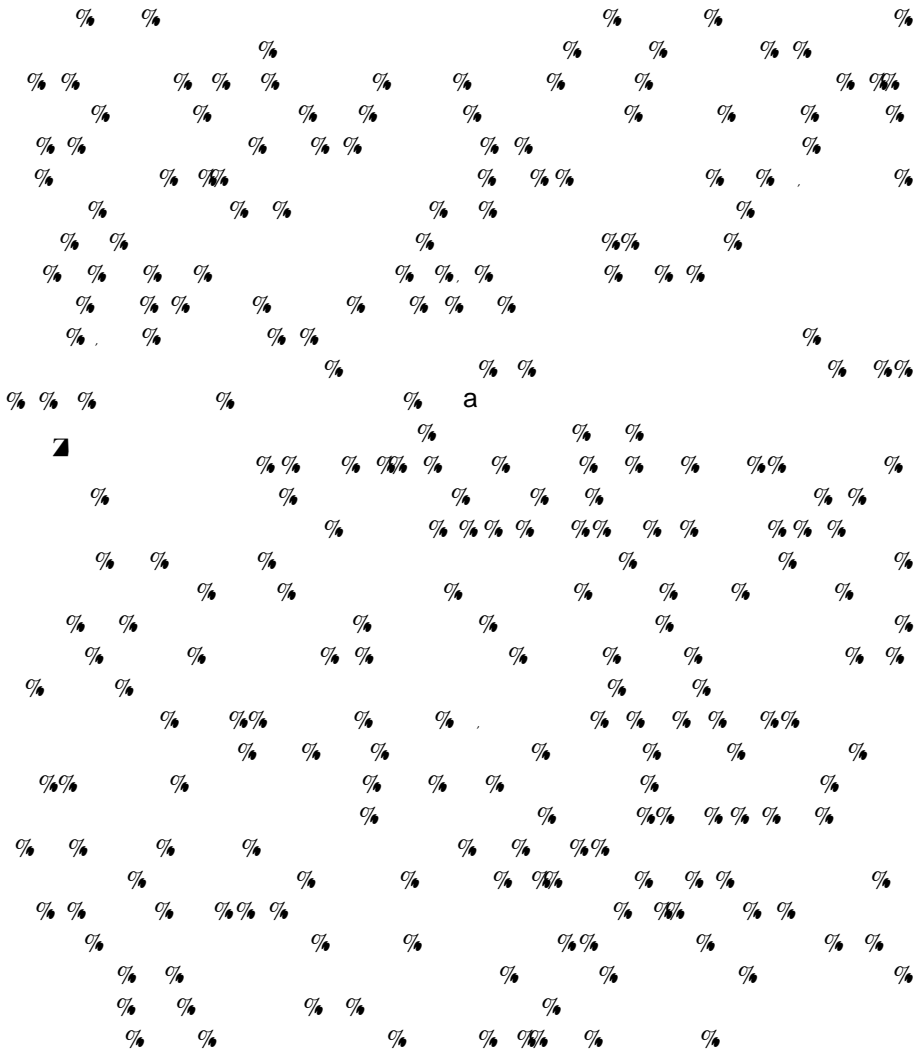


Fig. 1

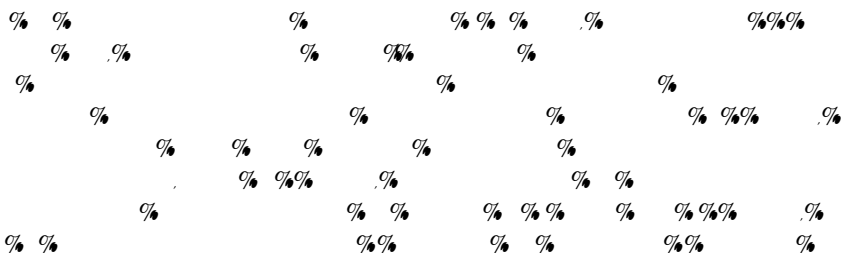
2.1 Gas Flow-Directed Growth

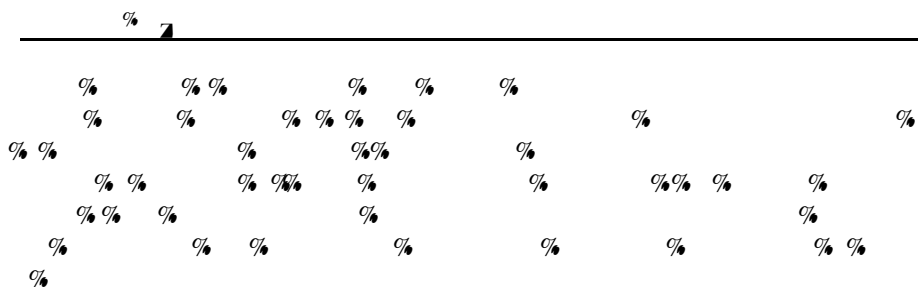
[illegible]

2.2 Surface Structure-Guided Growth

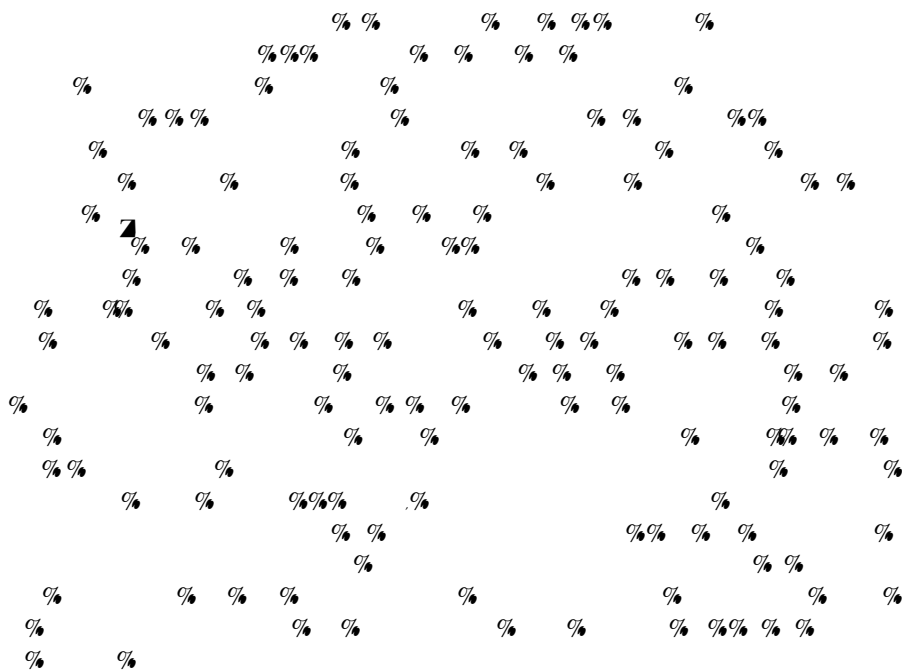


2.3 External Field-Directed Growth



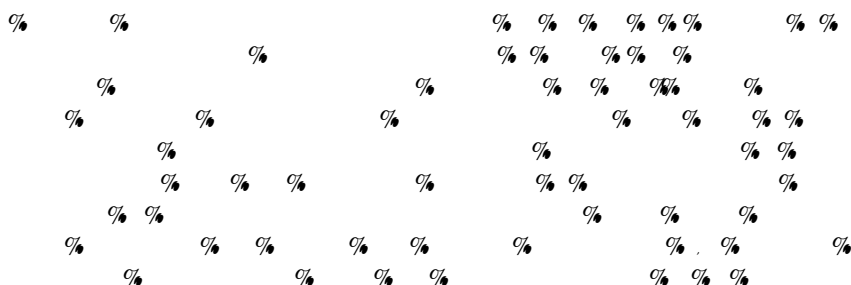


2.5 Growth of Arrays of Complex SWNT Structures



3 Selective Preparation of s-/m-SWNT Arrays

3.1 Catalyst Design



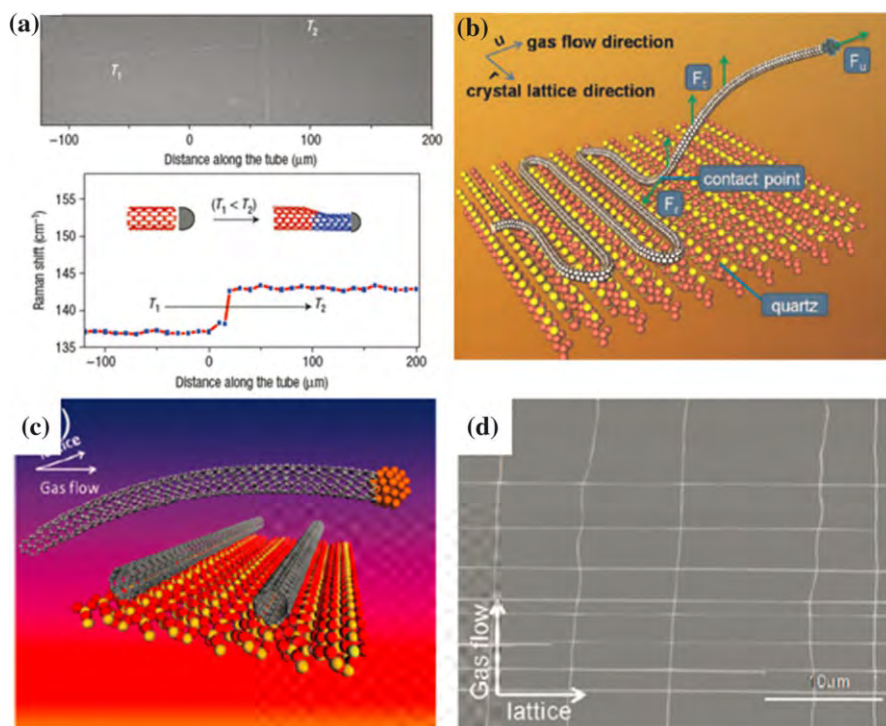


Fig. 4

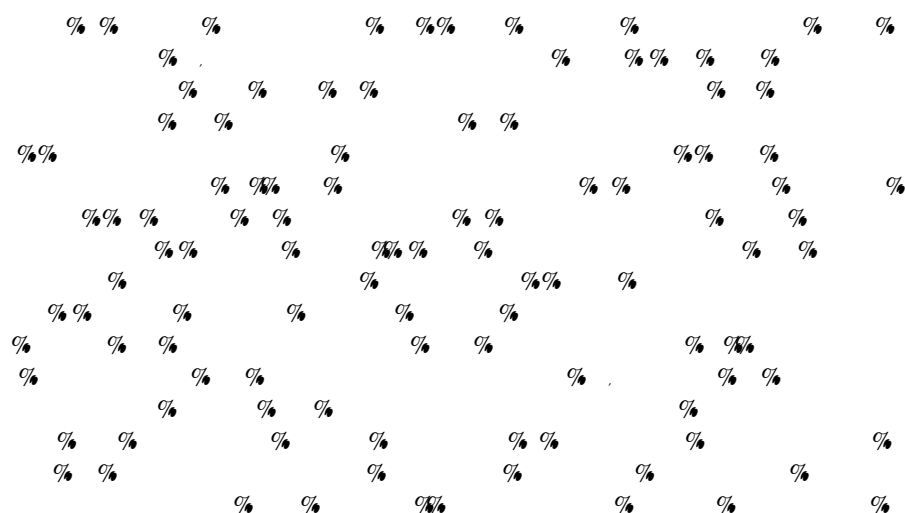
b

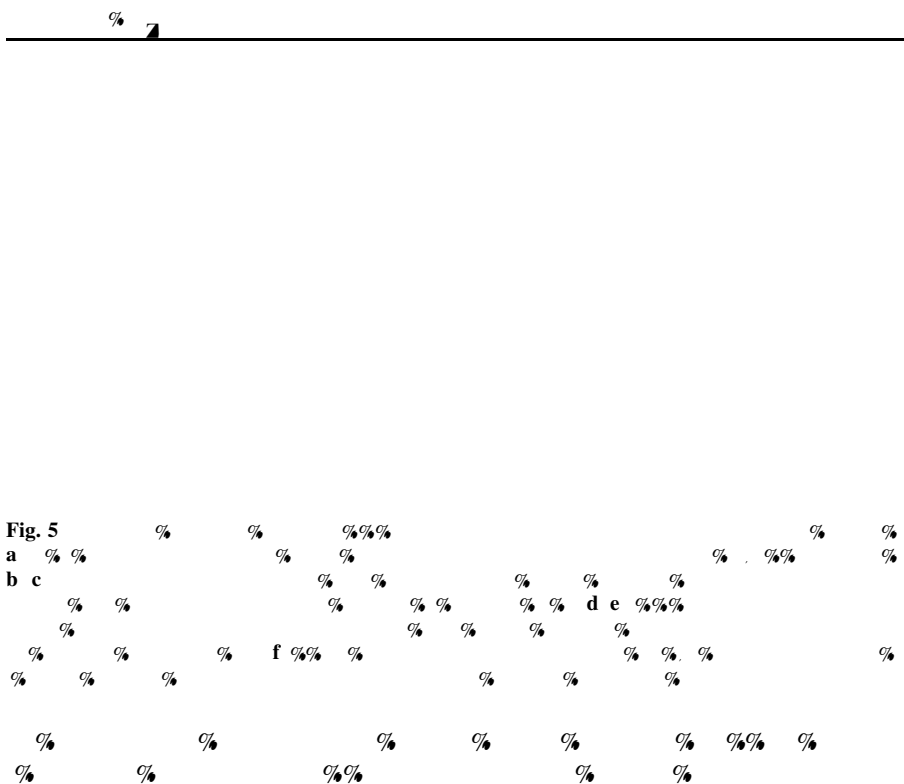
c

d

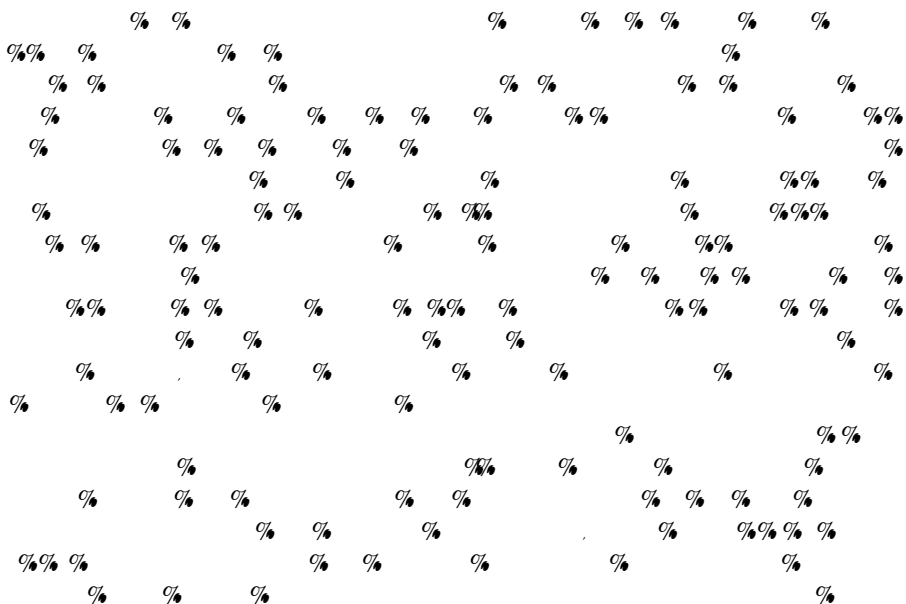
a

cross-bar





3.1.1 Monometal Catalyst



%

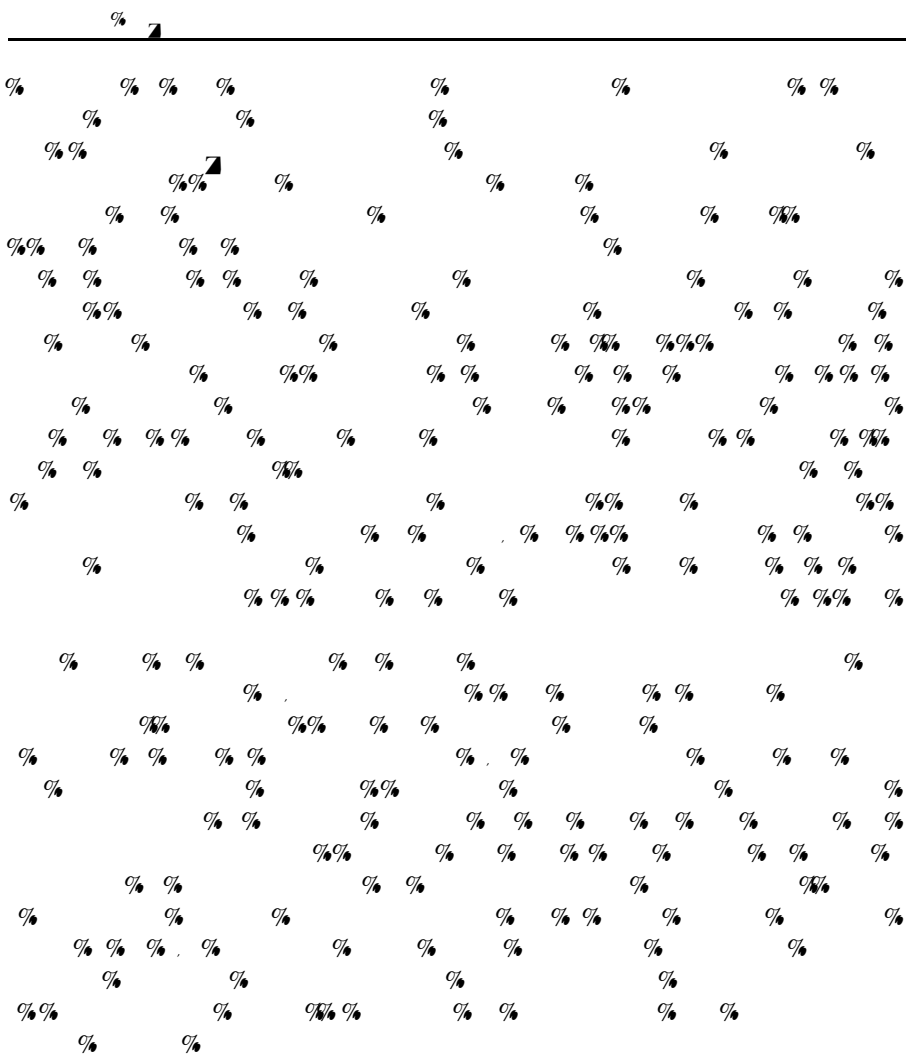
3.1.2 Bimetal Catalyst

%

3.1.3 Nonmetal Catalyst

C

X



3.3 In Situ Etching Method



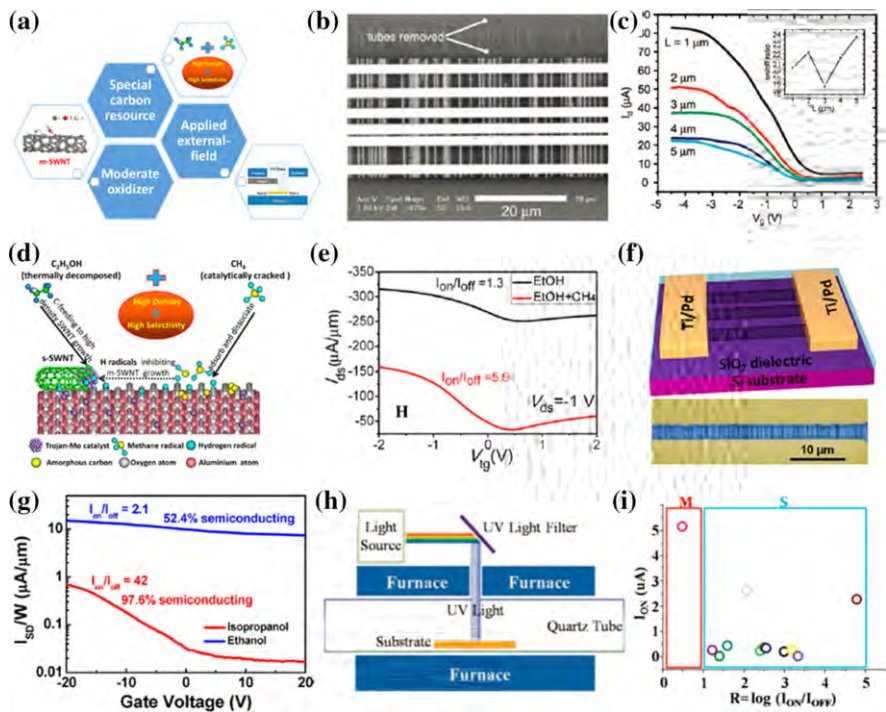
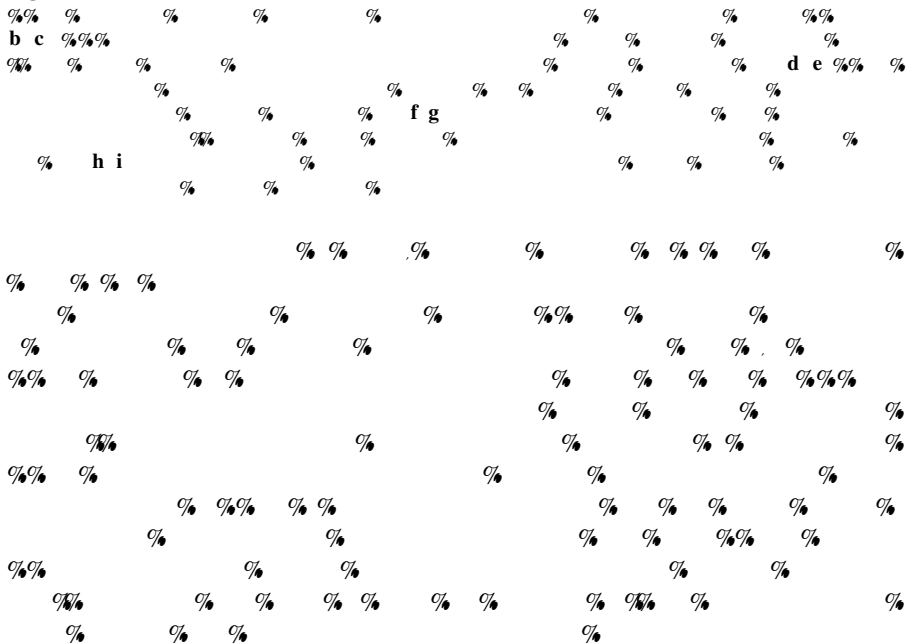
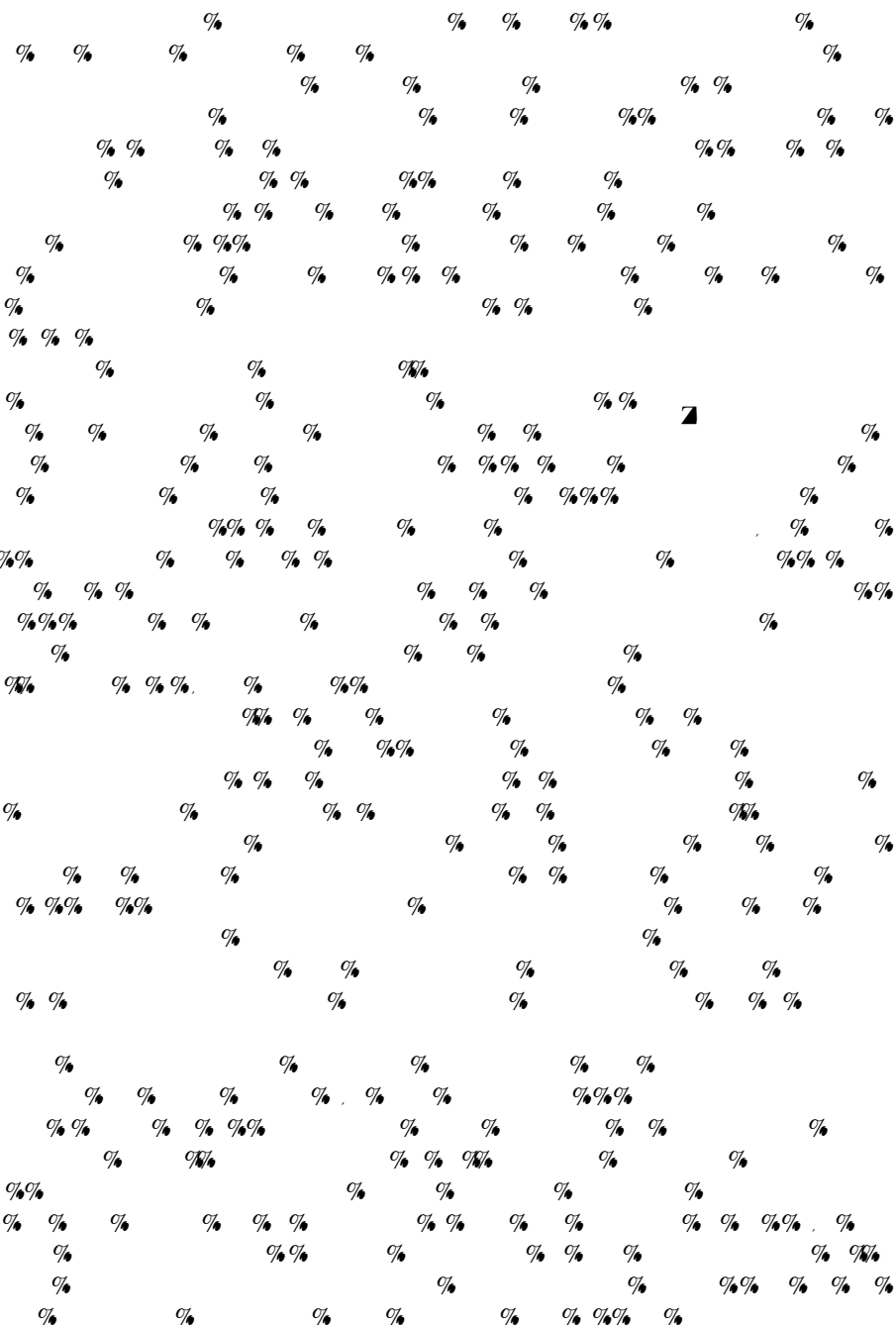


Fig. 7





[illegible]

4 Self-Assembly from SWNT Solution

4.1 Dielectrophoresis (DEP)

[illegible]

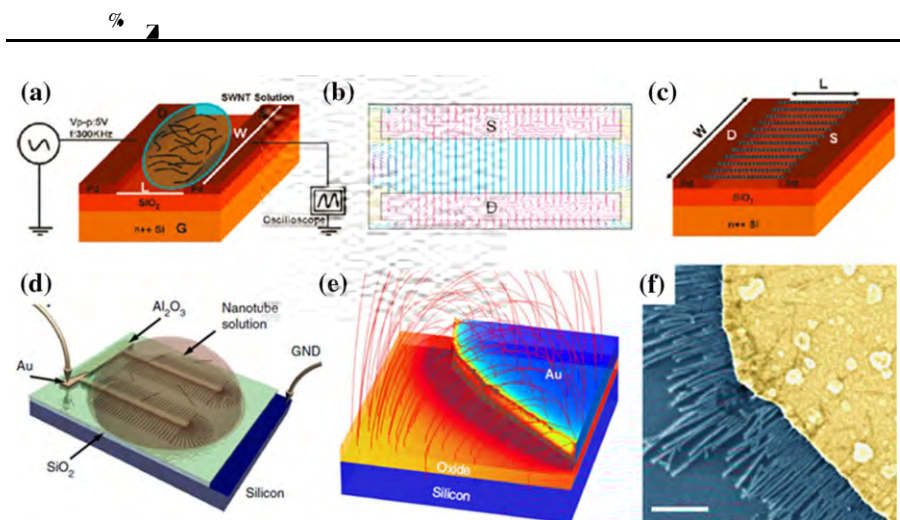


Fig. 9 (a) Schematic diagram of a SWCNT device on a Si/SiO₂ substrate. (b) Schematic diagram of a SWCNT device on a Si/SiO₂ substrate. (c) Schematic diagram of a SWCNT device on a Si/SiO₂ substrate. (d) Schematic diagram of a SWCNT device on a Si/SiO₂ substrate. (e) 3D schematic diagram of a SWCNT device on a Si/SiO₂ substrate. (f) SEM image of a SWCNT device on a Si/SiO₂ substrate.

4.2 Surface Modification-Assisted Adsorption

Surface modification-assisted adsorption is a technique used to enhance the adsorption capacity of a material. This is achieved by modifying the surface of the material with functional groups or other chemical species that can interact with the adsorbate. The modified surface can then act as a binding site for the adsorbate, increasing the overall adsorption capacity. This technique is widely used in various applications, including environmental remediation, catalysis, and sensing.

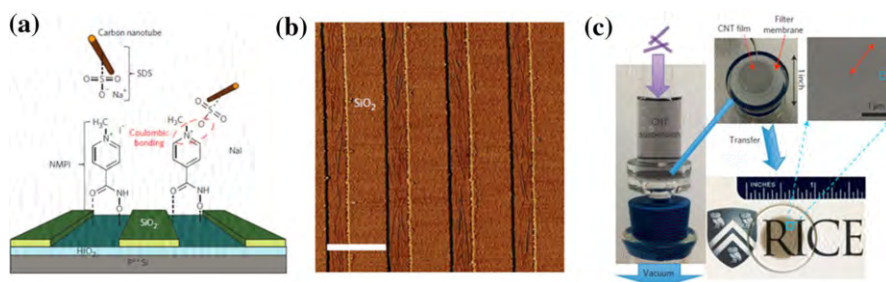
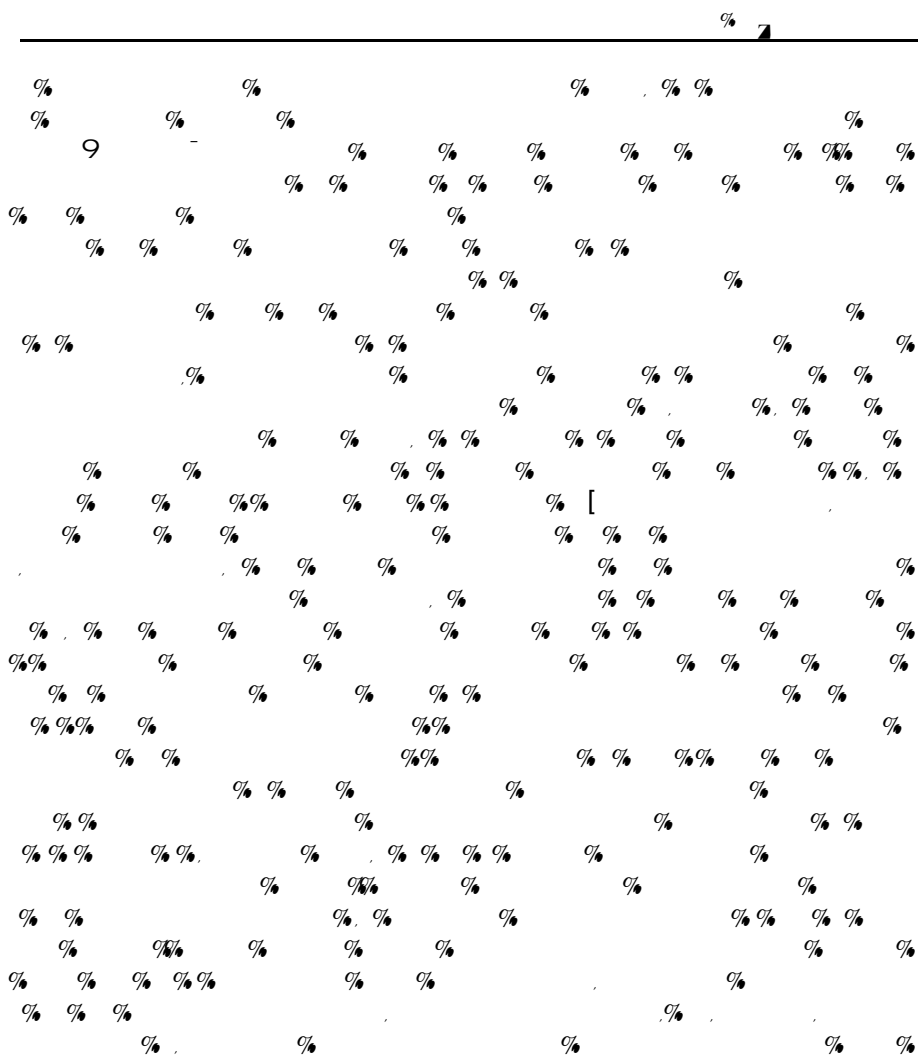


Fig. 10

(a) Schematic of the synthesis of a CNT film. It shows a carbon nanotube being added to a solution of SDS and NaOH. The solution is then mixed with a solution of a pyridine derivative (H₂C-NH-CO-NH) and a pyridine derivative (H₂C-NH-CO-NH) to form a covalent bonding. The resulting mixture is then deposited onto a SiO₂/Si substrate. (b) SEM image of the CNT film showing a dense network of nanotubes. (c) Schematic of the transfer of the CNT film from the substrate to a filter membrane. The process involves a vacuum and a transfer step, resulting in a CNT film on a filter membrane.

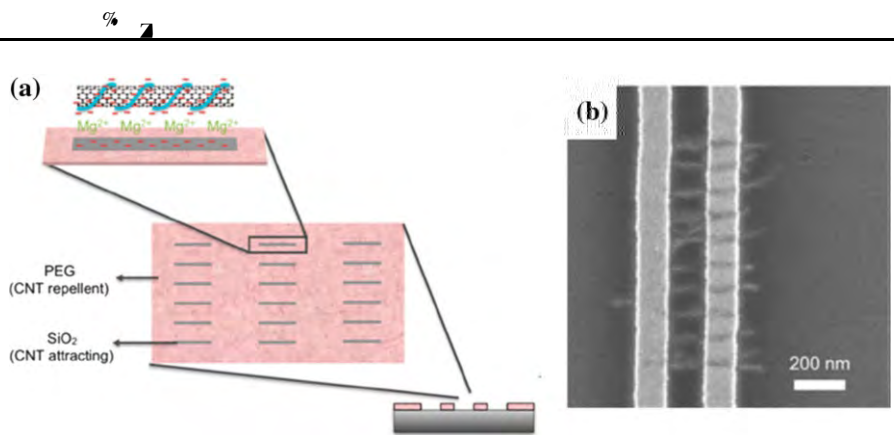


Fig. 11

4.3 Langmuir–Blodgett and Langmuir–Schaefer Techniques

4.4 Evaporation-Driven Self-Assembly

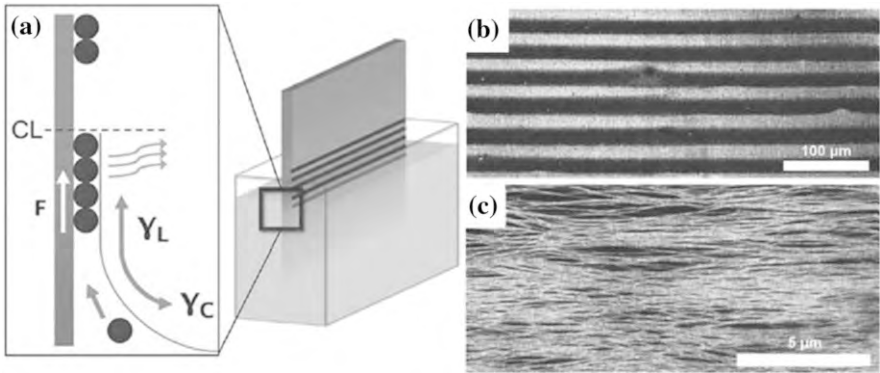
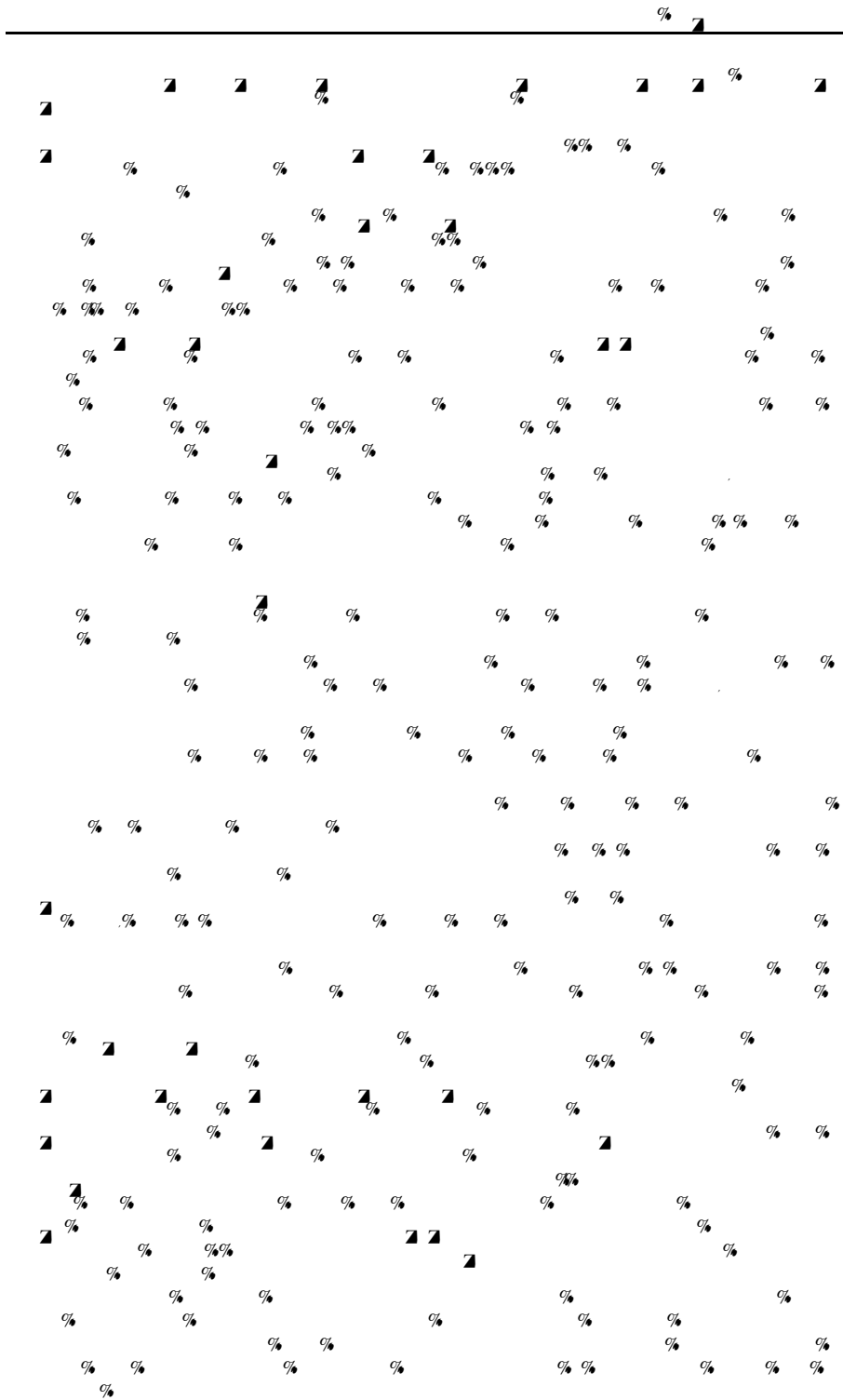


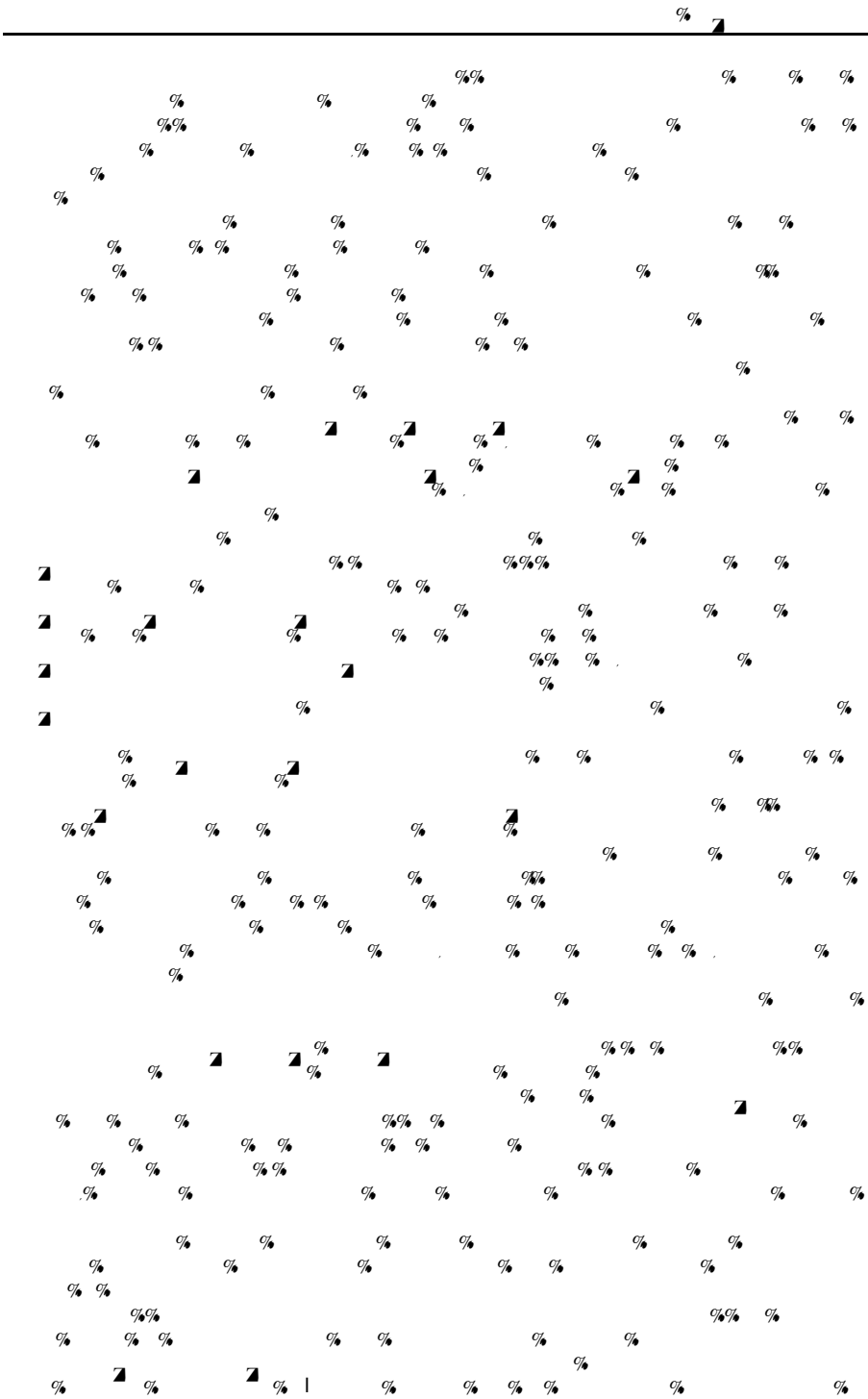
Fig. 12

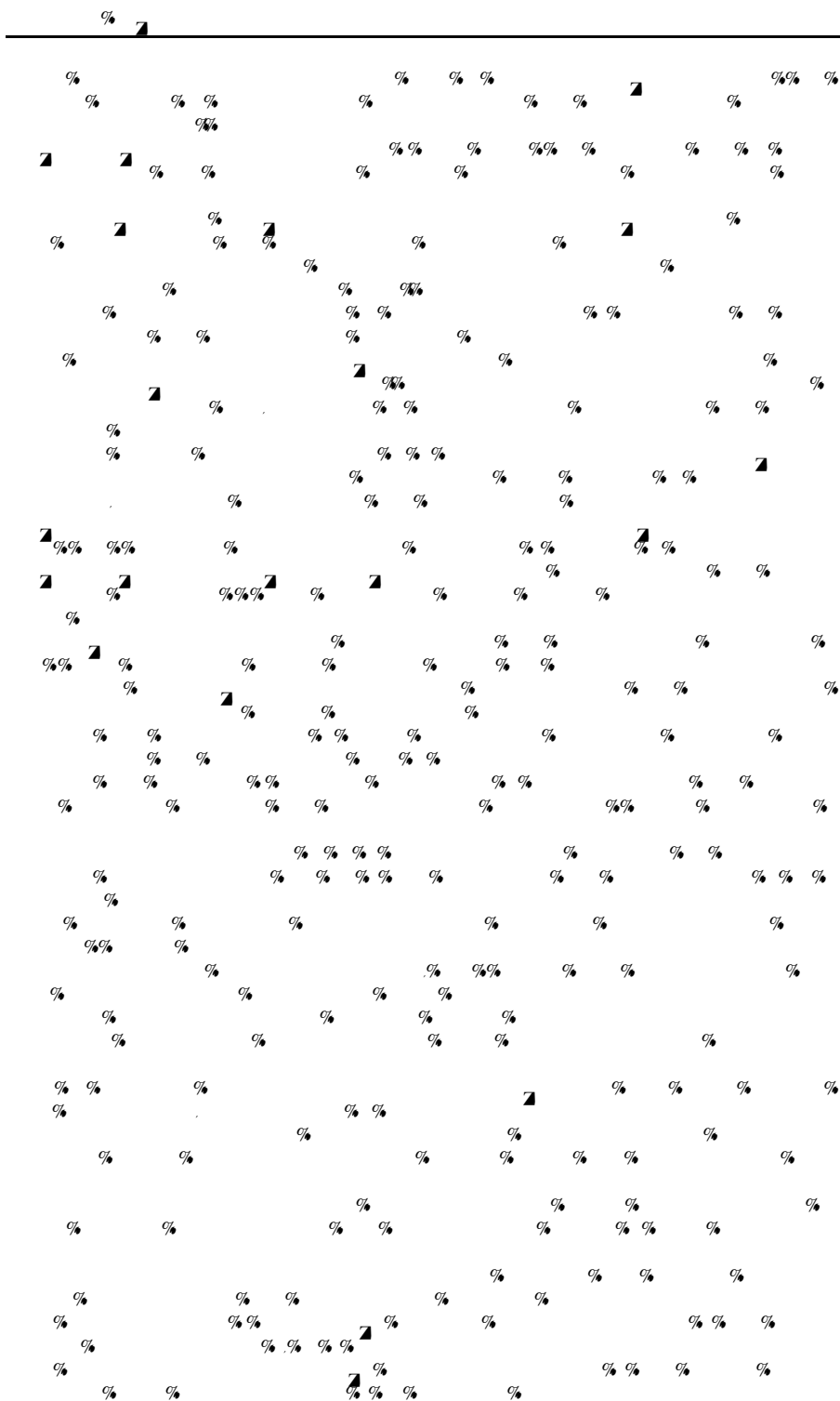
5 Conclusions

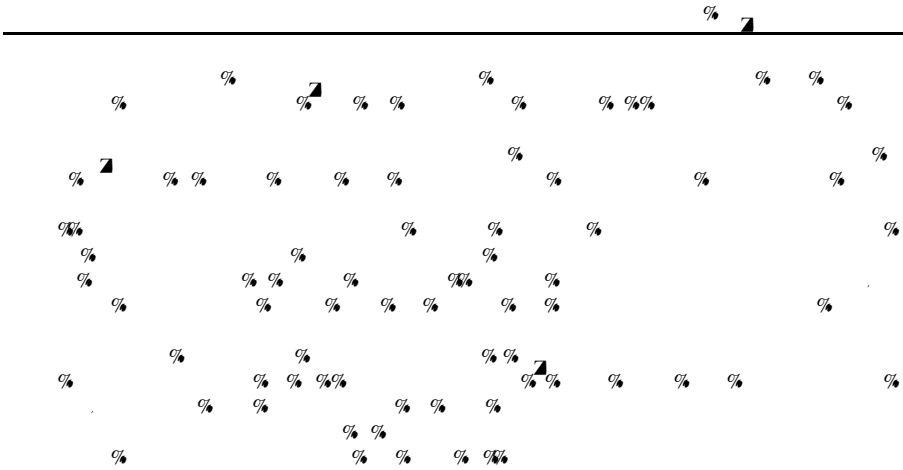
% %

A large, abstract, black and white graphic resembling a dense, chaotic pattern of small, irregular shapes and lines, possibly representing a complex data visualization or a stylized map. The pattern is composed of numerous small, dark, irregular shapes and lines scattered across a light background, creating a complex, textured appearance. The shapes vary in size and orientation, some appearing as small dots, others as elongated lines or clusters. The overall effect is one of a highly detailed, intricate, and somewhat random arrangement of elements.









Recent Developments in Single-Walled Carbon Nanotube Thin Films Fabricated by Dry Floating Catalyst Chemical Vapor Deposition

Qiang Zhang¹  Nan Wei¹ € Patrik Laiho¹ € Esko I. Kauppinen¹

Received: 14 September 2017 / Accepted: 13 November 2017 / Published online: 27 November 2017
Springer International Publishing AG, part of Springer Nature 2017

Abstract Transparent conducting films (TCFs) are critical components of many optoelectronic devices that pervade modern technology. Due to their excellent optoelectronic properties and flexibility, single-walled carbon nanotube (SWNT) films are regarded as an important alternative to doped metal oxides or brittle and expensive ceramic materials. Compared with liquid-phase processing, the dry floating catalyst chemical vapor deposition (FCCVD) methodps(rega)-8.1(ion)-240.(dry)]TJc5.7

Keywords Single-walled carbon nanotubes Dry floating catalyst chemical vapor deposition Transparent conducting film Touch displays

1 Introduction

Since their discovery, carbon nanotubes (CNTs) have been the subject of intensive research [1–3]. CNTs can be thought of as graphene sheets rolled up in certain directions, designated by pairs of integers, existing as both single-walled nanotubes (SWNTs) and multiwalled nanotubes (MWNTs) [4, 5]. Compared with MWNTs, SWNTs have been shown to exhibit very distinct properties, providing greater potential for use of this outstanding structural material in nano- and macroscale applications [1, 6]. Depending on their chirality and diameter, SWNTs can be either semiconducting, metallic, or semimetallic in nature [7]. Both experiments and theory have confirmed that CNTs possess excellent and unique characters, which originate from their molecular structure [7]; For example, SWNTs possess high conductivity (up to $4 \times 10^5 \text{ S cm}^{-1}$) [8], excellent current-carrying capacity (up to 10^9 A cm^{-2}) [9], excellent charge-carrier mobility (up to $10^5 \text{ cm}^2 \text{ V}^{-1} \text{ s}^{-1}$ at room temperature) [10], excellent thermal conductivity (up to $3500 \text{ W m}^{-1} \text{ K}^{-1}$) [11], and excellent mechanical performance (Young's modulus in the range of 1–2 TPa) [12, 13].

Over recent decades, numerous academic and industrial groups have explored use of SWNTs in diverse potential applications [1, 14]. In particular, SWNTs with various types of architecture and different dimensions have been synthesized and investigated worldwide to fully utilize the excellent properties of individual SWNTs [15–18]. Thin films is an emerging research area, offering the advantage of statistical averaging for better reproducibility [14, 19–21]. The collective behavior of two-dimensional (2D) SWNT films can provide unique physical properties and enhanced device performance [22]. Their superior properties, including mechanical flexibility, optical transparency, unique electric properties, high surface area, etc., result in great potential for use of CNT films the applications in energy fields, electronic devices, displays, sensors, etc [19, 20]. However, some important challenges remain to be resolved: (1) controlled fabrication of SWNT films with good reproducibility, (2) utilization of the excellent properties of individual SWNTs at macroscopic level, and (3) prediction or exploration of new properties offered by macroscopic SWNT assemblies.

To date, several methods have been developed to fabricate CNT films. Specifically, two main types of process, i.e., liquid-phase and dry processing, have been used to assemble CNT films [19]. Liquid-phase processing involves deposition of tubes from surfactant solution or superacids to form CNT thin films, which is readily scalable. However, a practical challenge with such liquid-phase methods is that the low solubility and strong intertube interactions of SWNTs make it difficult to obtain submonolayer SWNT thin films with uniform, moderate to high coverage and without significant presence of bundles [23, 24]. Complete removal of residual surfactants and acids is also a difficult problem. Dry methods for fabrication of CNT

films mainly include three approaches: growth directly by on-substrate CVD, drawing from a vertically aligned CNT forest grown on a solid substrate, or deposition directly from a floating catalyst chemical vapor deposition (FCCVD) system. CNT networks can be grown directly on a substrate by CVD. The orientation, density, and even chiral distribution of the CNTs can be controlled by using selected and regulated catalysts on the substrate [25–27]. However, such on-substrate CVD normally requires multistep processing and has low yield. The aligned CNT films drawn from a CNT forest are anisotropic [28]. However, devices based on aligned CNT film components offer poor statistical reproducibility. SWNT films cannot be obtained from the CNT forest method. In addition, intricate treatment is needed to obtain MWNT films from a CNT forest for special applications; For example, laser trimming and metal deposition increase the transmittance and conductivity, respectively, when using MWNT films as transparent conductive films [29]. On the other hand, film fabrication by the FCCVD method is based on direct deposition of an SWNT aerosol synthesized by the FCCVD method [22, 30–32]. FCCVD is low-cost and readily scalable and offers good control over the morphology of the CNTs or bundles in the thin film, including their length, diameter, density, etc., which are critical parameters for film performance. In particular, films fabricated by the FCCVD method can contain individual SWNTs of theoretically unlimited length [33]. These characteristics will lead to many novel results and great improvements in CNT applications.

This review focuses on fabrication of films using the dry FCCVD method, as well as corresponding SWNT synthesis, thin-film fabrication and performance regulation, transparency and conductivity characteristics, random bundle films, patterned films, and individual CNT networks; in addition, various applications, especially as transparent conductive electrodes (TCEs), are highlighted. The final section concludes with some long-standing problems and identifies topics warranting further investigation in the near future.

2 CNT Synthesis Process and Mechanism

The research fields of CNT synthesis and CNT films are interdependent. Many key advances in CNT catalysts and synthesis lead immediately to new results in film fabrication, performance, and applications. There are three major methods of CNTs production: arc discharge, laser ablation, and chemical vapor deposition (CVD) [34]. Owing to its high yield and relatively mild synthesis conditions, CVD is the most common method used for CNT growth. However, most products synthesized by CVD are mainly powder like or supported on different substrates. FCCVD, as a special CVD method, has attracted tremendous attention. Since the catalyst particles and CNTs are suspended in gas phase as an aerosol throughout the entire CNT formation process, the FCCVD method is more flexible and controllable [29], not only being an effective approach to mass-produce CNTs of good quality [36] but also enabling direct synthesis of different SWNT architectures, such as continuous fibers [18, 37], transparent films [22, 31], and CNT sponges [38].

Many features of FCCVD can affect the morphology and properties of the resulting CNTs, with catalyst composition, catalyst size, carbon source, temperature, and gas-phase chemistry being the five principal parameters [39, 40]. The most effective catalysts for FCCVD are formed from pyrolysis of easily sublimed organometallic compounds, such as ferrocene, carbonyl iron, dimethoate, or metal nanoparticles generated using a hot-wire or spark system [35, 41, 42]. In 1998, Cheng et al. first applied the FCCVD method to synthesize SWNTs using ferrocene as catalyst [6, 43]. This result suggested that FCCVD is a potential method for high-yield production of CNTs. The catalyst size is slightly larger than the diameter of the resulting nucleated CNTs, a phenomenon also observed in on-substrate CVD and in situ growth in environmental transmission electron microscope [41]. Many excellent carbon sources for production of CNTs are known, including hydrocarbons and carbon monoxide (CO) [40]. Hydrocarbons thermally self-decompose into carbon clusters (C_xH_y), which are then absorbed by the catalyst. This process contributes to rapid and high-yield growth of CNTs [44]. However, high partial pressure of the hydrocarbon or temperature may result in production of surplus amorphous carbon [45]. CO as carbon source is significantly different from hydrocarbons; It decomposes only at the surface of the catalyst nanoparticles, liberating carbon atoms for CNT formation, since the disproportionation reaction $2CO(g) \rightarrow C(s) + CO_2(g)$ requires the presence of a catalyst surface [35, 36]. This reaction can greatly reduce byproduct generation. SWNT production based on CO disproportionation has been carried out at either high or atmospheric pressure (Fig. 1), and both methods are widely applied for commercial production of SWNTs and films. In 2001, Smalley's group [36] developed the high-pressure CO (HiPCO)

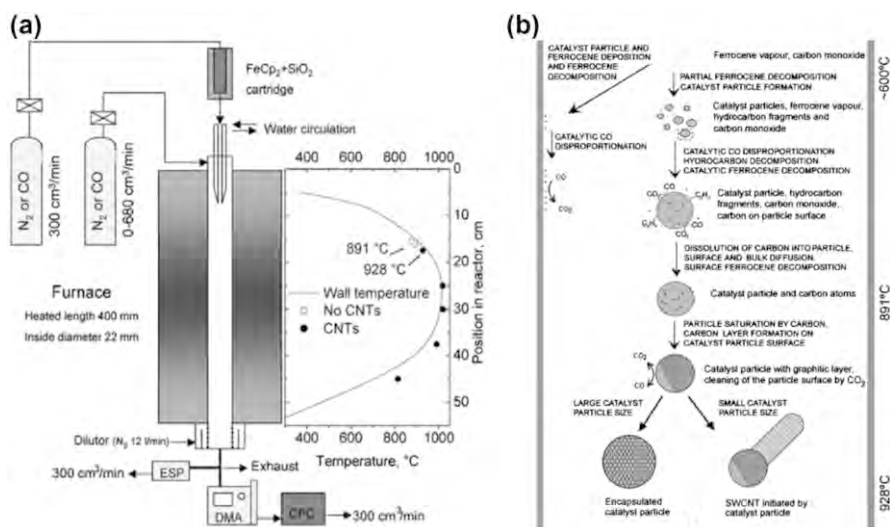


Fig. 1 High-quality SWCNTs synthesized with CO as carbon source at atmospheric pressure based on FCCVD [54]. Copyright 2006 Elsevier. **a** Schematic of experimental setup and wall temperature profile for FCCVD synthesis of SWCNTs with ferrocene as catalyst. Open circles indicate sampling locations where CNTs were not observed; solid circles indicate conditions for CNT sampling. **b** Schematic of SWCNT formation mechanism in FeCp₂-CO system at temperature of 1000 °C

approach to produce large quantities of SWNTs in presence of iron nanoparticles formed from decomposition of iron pentacarbonyl. More recently, He et al. [46] and tubes grown using CO, methane, ethanol, and toluene by electron diffraction methods. The optimal etching between the

carbon and CNTs. In 2014, Liu et al.

etchant to selectively etch semiconducting SWNTs (s-SWNTs) (Fig.2) [49].

of the

indicating laminar flow conditions for catalyst particle formation and SWNT growth. Use of this type of equipment can effectively reduce catalyst deposition on the reactor wall. The aerosol of catalyst or precursor, carbon source, and carrier gas are introduced through the injector probe into the high-temperature zone of the vertical CVD reactor. Floating CNTs and bundles can be directly and continuously obtained at the reactor end. The mechanism for SWNT formation in the $\text{FeCp}_2\text{-CO}$ system is shown in Fig. 1b. Decomposition of FeCp_2 vapor results in catalyst particle formation and likely release of hydrocarbon fragments. Catalyst particles are formed by nucleation and continue to grow through collision processes. In addition, catalyst particle growth can continue as a result of ferrocene vapor decomposition on the particle surfaces. Depending on their size, the catalyst particles either nucleate growth of a SWNT or become inactive by growing too large (usually above 3 nm in diameter). In addition, through a series of CNT growth experiments, the growth window for temperature for the CO system was determined to be 891 to 928 °C [54]. In addition to high-quality SWNTs, a novel hybrid material, viz. nanobuds, in which fullerenes and SWNTs are combined into a single structure in which the fullerenes are covalently bonded onto the outer surface of the SWNTs, was invented at Aalto University. In 2007, based on the $\text{FeCp}_2\text{-CO}$ system, carbon nanobuds (CNBs) were synthesized with increasing H_2O and CO_2 concentrations during the FCCVD process for synthesis of CNT [33, 55]. Due to their unique structure, CNBs possess advantageous properties compared with SWCNTs or fullerenes alone, including field-emission characteristics when in nonbonded configuration.

3 CNT Film Fabrication

Recently, the demand for TCFs has surged due to the expansion of the commercial market for optoelectronic devices such as liquid-crystal displays (LCDs), touch panels, photovoltaics, and organic light-emitting diodes (OLEDs) [56, 57]. In 2014, sales of TCFs in the LCD industry, which has led consumption for years, were approximately USD 1.5 billion [58]. In addition, the commercial market for TCFs in the solar industry is expected to exceed USD 16.3 billion by 2017 [59], and the market for TCFs in touch panels is anticipated to reach about USD 5 billion by 2019 [60].

Indium tin oxide (ITO) is the most widely used and current industry-standard transparent conductor material, offering excellent optoelectronic properties with low sheet resistance (R_s , from 10 to 100 Ω/sq) at high transmittance ($> 85\%$) [57]. However, as a brittle ceramic, the limitations of its physical property have presented many challenges for development of flexible electronics [57, 61]. In addition, the high refractive index of ITO may result in images displayed on touch screens becoming washed out [61, 62]. Recently, various novel materials, including silver nanowires, metal mesh, graphene, and CNT films, have emerged as ITO replacement materials [56]. Owing to their low surface resistance due to the high conductivity of metal compared with ITO, silver nanowire films and metal mesh offer benefits for use in large-area touch displays [63]. However, there are also some severe problems with application of silver nanowires and metal meshes as TCFs,

such as performance stability and high ambient light reflectance [64]. The high cost and complex process of graphene synthesis seriously limit development of graphene for use as TCF [65]. Among these promising candidates, CNT TCFs exhibit great potential because of their high stretchability, mechanical flexibility, chemical stability, color neutrality, less haze, wider spectral range, etc. [56, 59, 66, 67].

4 2D Network Film

As mentioned above, FCCVD is a promising technique for SWNT film fabrication. It enables direct, single-step fabrication of clean, ready-to-use SWNT networks for use as high-performance TCFs. Currently, there are three main approaches for CNT film fabrication based on FCCVD, as shown in Fig. 3. The individual tubes or bundles produced by the FCCVD method are suspended in a carrier gas. Films can then be obtained by deposition of the CNTs or bundles onto a membrane filter [30, 31] or FCCVD chamber wall [22], or by direct transformation of the CNT aerosol into an aerogel [68]. The specific processes of film fabrication are discussed and compared below.

Fig. 3 Schematics of CNT film fabrication processes based on FCCVD, where CNTs and bundles are directly deposited onto a membrane filter (**a**) or FCCVD chamber wall (**b**), or **c** the CNT aerosol is transformed into an aerogel in the FCCVD reactor

CNT films can be prepared by dry deposition, combining the FCCVD method with an aerosol filtration system, as shown in Fig. 3a. The aerosol containing individual SWNTs and their small bundles is collected by a membrane filter at the outlet of the reactor to form a SWNT network. The sheet resistance and transmittance can be controlled by adjusting the network deposition time or reactor dimensions and conditions. In 2010, Kaskela et al. [31] integrated SWNTs collected on a nitrocellulose filter based on the laminar flow reactor with CO as carbon source and CO₂ as additive to enhance the catalyst particle activity (Fig. 4a). The micro-morphology of the SWNT film was a continuous 2D network, as shown in Fig. 4b. The sheet resistance of the SWNT films with bundle length of 9.4 μm ranged from 80 to 100 Ω/sq at a transmission of $T = 90\%$ after HNO₃ doping. Since such SWNT

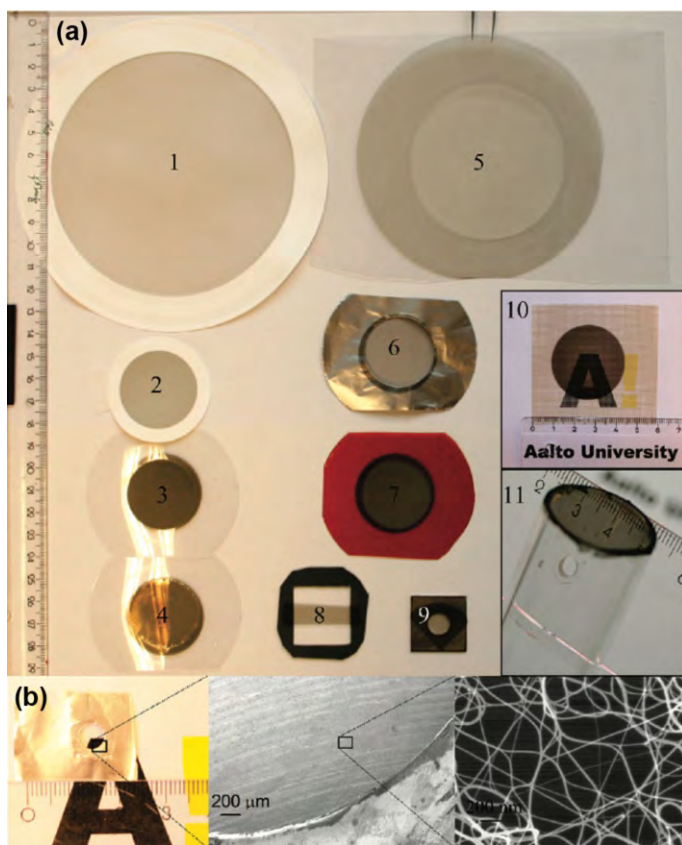


Fig. 4 Various SWNT films prepared by FCCVD [30] (Copyright 2011 American Chemical Society): **a** SWCNT films collected on nitrocellulose filters (1, 2), pristine (3) and ethanol-densified (4) films suspended over polyethylene terephthalate (PET), freestanding films (FSFs) on PET (5), aluminum foil (6), and Kapton (7), a strip film suspended over a rectangular hole (8), and on cold-rolled steel (9). Insets show semi-freestanding film on polyetheretherketone substrate (10) and a film suspended over the open end of a glass tube (11). **b** Set of images showing submonolayer FSF suspended over 5-mm openings in aluminum foil

films are collected on low-adhesion filters, they can be easily transferred to practically any substrate, including flexible polymers, glass, quartz, and various metals, using a simple press. SWNT films with various thicknesses and sizes on different substrates are shown in Fig. 4. This simple film fabrication method is also called direct dry transfer [31]. In addition, the CNT aerosol can also be deposited onto the substrate surface downstream of the FCCVD system by using an electric field thermophoretic technique for thin-film manufacture [69].

The press transfer method is compatible with roll-to-roll fabrication methods, thus opening up further upscaling potential for industrialized production. In particular, Carbon NanoBud (CNB) film, a special SWNT film from Canatu, is already in commercial production [62]. Homogeneous and patterned CNB films can be manufactured on large size sheets by combining the CNB aerosol synthesis method with room-temperature deposition. The film conductivity of CNB film at given transparency has doubled approximately every 12 months since 2007. In 2013, CNB films with properties of 100 Ω/sq at 94% and 270 Ω/sq at 98% were commercially available. The facility allowed capacity of up to 500,000 m^2/month by Canatu. In addition, film performance of 100 Ω/sq at >95% has been demonstrated [62].

Ma et al. [22] directly prepared SWNT films with methane as carbon source, argon as carrier gas, FeCp_2 as catalyst, and sulfur as promoter in 2007. During their preparation process, the CNTs are deposited on the FCCVD chamber wall in the high-temperature zone, then grow continuously to form CNT films (Fig. 3b) that can be easily peeled off after growth. The thickness of such freestanding and homogeneous SWNT films, with area up to several tens of square centimeters, can be regulated from 100 nm to 1 μm (Fig. 5a, b, c). These SWNT films are composed of highly entangled bundles about 30 nm in diameter and from tens to hundreds of micrometers in length (Fig. 5d, e). The diameter of the nanotubes in the bundles is about 1–2 nm. The bundles in the films are firmly connected with each other, as they grow to forming a continuous, preferentially 2D network at high temperature (Fig. 5e). Due to these good and long interbundle connections, such directly synthesized films offer good electrical and mechanical properties, with electrical conductivity of 2000 S/cm and strength of 360 MPa. Figure 5 f, g shows transmittance spectra from the ultraviolet to mid-infrared and the sheet resistance of freestanding SWNT films of different thicknesses. For 100-nm-thick film with sheet resistance of 50 Ω/sq , which was the thinnest intact film that could be peeled off the wall of the quartz tube, the transmittance in the visible region of the spectrum was above 70%.

In addition, freestanding CNT films can also be fabricated by transformation of the CNT aerosol into an aerogel using a well-designed FCCVD system. In 2013, Zhou et al. [68] introduced a blown aerosol technique into the process of CNT synthesis by FCCVD for continuous CNT film production (Fig. 3c). With injection of the feedstock for CNT synthesis and the carrier gas, transparent tubular films with diameter of ~ 100 mm were continuously blown out from the outlet of the FCCVD system at speed of ~ 120 m/h. The surface resistance of the as-synthesized SWNT films was ~ 200 Ω/sq at transmission of $T = 90\%$, for the optimized conditions. In

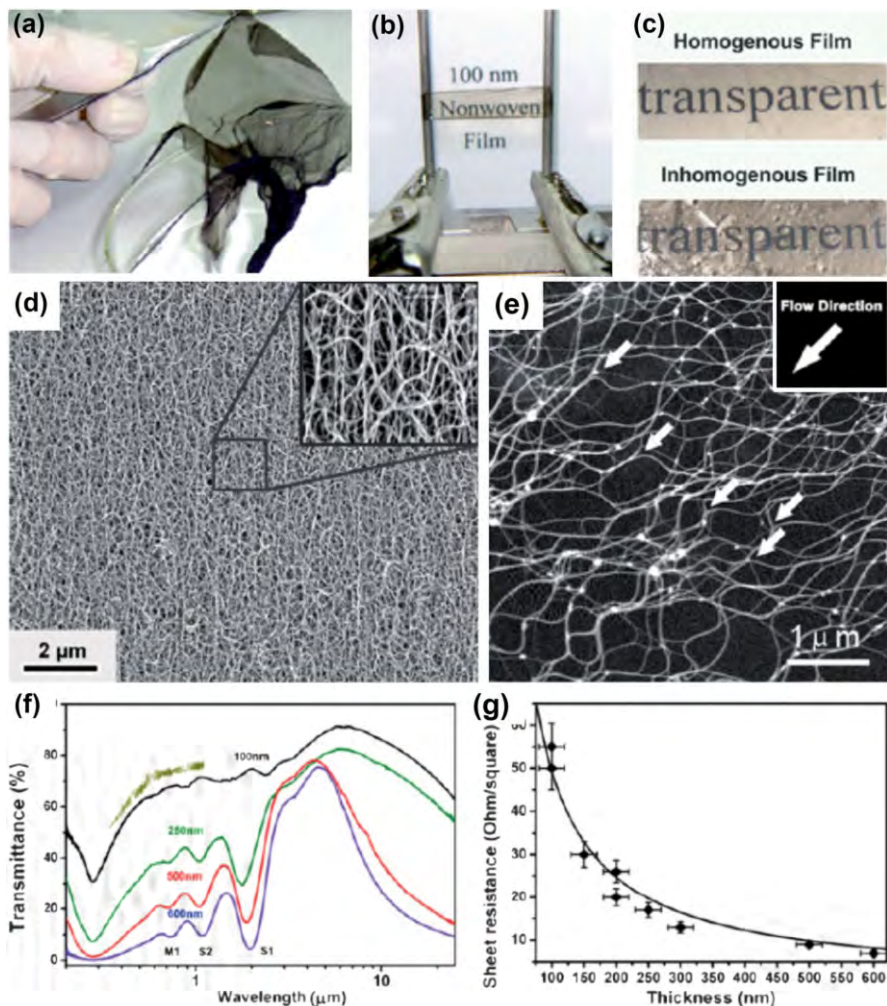


Fig. 5 **a** As-grown 250-nm-thick SWCNT nonwoven film. **b** Transparent 100-nm-thick film standing freely between metallic pillars. **c** 150-nm-thick homogeneous (upper) and inhomogeneous films. The importance of homogeneity is clear. **d** Large-scale scanning electron microscopy (SEM) image of 250-nm-thick film; inset shows higher magnification. **e** SEM image of SWCNT network in a single layer; white arrows indicate Y-type junctions and flow direction. **f** Transmittance spectra for as-grown films of different thicknesses. Numbers above curves indicate thickness, and the uppermost short curve corresponds to 100-nm-thick film on glass substrate. S1, S2 represent the electronic transitions for the semiconducting SWCNTs in the films, and M1 represents that of the metallic nanotubes. **g** Sheet resistance versus thickness of SWCNT films. The solid line is the best fit curve according to the definition of electrical conductivity [22]. Reprinted with permission from [22]. Copyright 2007 American Chemical Society

addition, the conductivity anisotropy could be regulated from 1 to 8 by increasing the film collection speed, resulting in more aligned bundles in the film.

5 Patterned Film Fabrication

Other than usual film manufacture, deposition of patterned films is another critical step for relevant final products such as touch panels and displays. Such patterning of CNT films can also overcome the tradeoff between transmittance and conductivity in TCFs. Patterned films are not uniformly transparent but may still meet many of the application requirements, as long as the features of the pattern are thin enough to not be recognized by the naked eye.

In the case of rectangular patterns, to a first-order approximation, the transmittance roughly equals the CNT coverage, while the conductance is proportional to the grid thickness:

$$R \propto \frac{\rho}{tf};$$

$$T \propto 1 - f \exp(-\alpha t);$$

where R is the sheet resistance, T is the film transmittance, ρ is the resistivity of the CNT grid, t is the grid thickness, α is the absorption coefficient of the CNT grid, and f is the duty cycle of the grid pattern, viz. $f \propto \frac{W}{A}$, where W is the CNT grid width and A is the grid pitch (Fig. 6d). Instead of vanishing, the transmittance approaches $1 - f$ as the pattern becomes thicker. Therefore, conductance and transmittance are

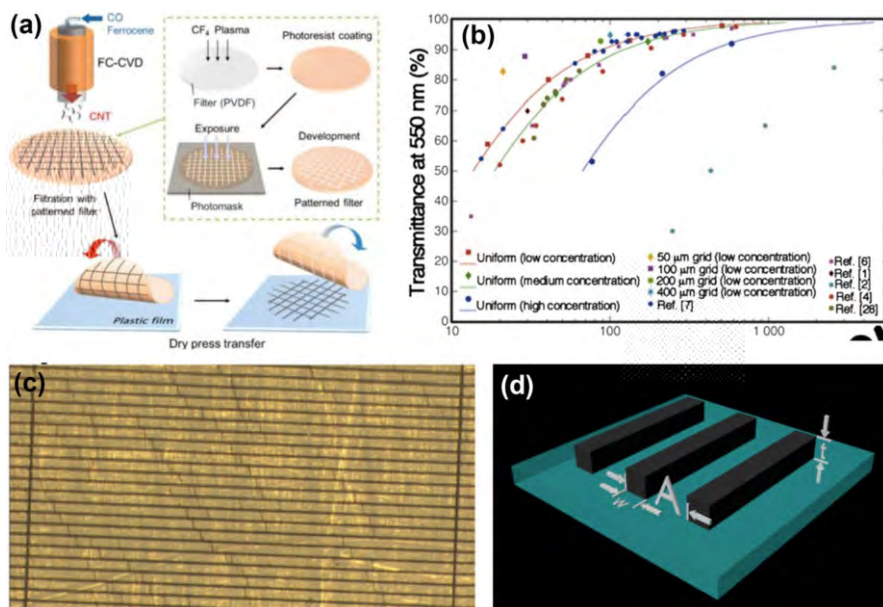


Fig. 6 Patterned carbon nanotube films: **a** Fabrication steps for patterned carbon nanotube film utilizing patterned filters [73]. Copyright 2014 American Chemical Society. **b** Comparison of sheet resistance between patterned and uniform carbon nanotube films and **c** optical image of patterned carbon nanotube films with rectangular geometry [33]. Copyright 2016 Elsevier. **d** Structural parameters of the rectangular pattern geometry

no longer strongly coupled. The factors limiting the conductivity are the quality of the CNTs and how thick the grid can be.

A few pioneering studies have been carried out on how to pattern carbon nanotube films. Inkjet printing is a facile method to make arbitrary patterns with linewidth above 50 microns [70]. On smaller scales, some specific patterns can be formed with the aid of polymer [71] or laser methods [72].

Among these methods, one approach is particularly well suited to the FCCVD method. This method utilizes dry transfer and photolithographically patterned filter membranes to achieve resolution down to microns, overcoming the tradeoff mentioned above. Fukaya et al. reported a 46% increase in conductivity for patterned compared with uniform film [73]. In a follow-up study, Kaskela et al. reported record-breaking performance of 69 Ω/sq at 97% transmittance [33].

Improving the uniform film quality still matters in the patterned case, since it provides better base material, achieving the target conductance with lower thickness and material consumption. The conductivity versus transmittance characteristic can be further improved if the pattern can be made thicker; For example, a 40-nm-thick film can transmit 75% of light at 550 nm [30], corresponding to an absorption coefficient of $\alpha = 72,000/\text{cm}$. Improvement in the carbon nanotube quality results in little change in film density, so the absorption coefficient remains roughly unaltered. However, improvement in tube-tube contact and length will reduce the film resistivity, as shown in a recent report in which films of individual carbon nanotubes reached 89 Ω/sq at 90% transmittance [33] with figure of merit of $\alpha\rho = 9.38$ and thus $\rho \propto 1/3 \times 10^{-6} \Omega \cdot \text{m}$ or 7700 $S \cdot \text{cm}$. To achieve 10 Ω/sq at 90% transmittance, the grid thickness required is 1.3 microns. This thickness could be reduced further by applying better CNTs or through use of doping techniques, which will have lower $\alpha\rho$.

The value of 1.3 microns is not very thick for TCFs. However, few attempts have been made to form patterned random carbon nanotube films of such thickness. In previous attempts, the thickness of the densified film was around 0.15 microns, being limited by the thickness of the photoresist [73]. It is reasonable to expect that increasing the thickness of the photoresist, or development of new patterning techniques for thicker CNT films, will help CNT TCFs to reach better performance and wider application scenarios.

6 Characterization, requirements, and performance of CNT films fabricated by FCCVD for use as TCFs

Low sheet resistance and high light transmission across the UV–Vis–NIR spectrum are pursued for ideal transparent conducting films. Practically, sheet resistance can be measured directly using the four-point probe, two-point conductivity probe, or two-line method, while transmission can be obtained by measuring the UV–Vis absorbance of the TCF. Because the transmittance of a film decreases through absorption as its thickness is increased, there is a tradeoff between these two parameters [74]. Therefore, a figure of merit (FOM) should be defined to compare

various TCFs, combining transmission and sheet resistance and being independent of thickness.

According to existing literature, two main FOMs are used for comparison of TCFs [75], i.e., $\alpha\rho$ and $\sigma_{dc}=\sigma_{OP}$, where α , ρ , σ_{dc} , and σ_{OP} are the absorption coefficient, resistivity, direct-current (dc) electrical conductivity, and optical conductivity of a uniform TCF, respectively. The sheet resistance of a uniform film is defined as $R_s \propto \rho/t$, where t is the film thickness. According to the Beer–Lambert law, the transmission of light (T) through a film of homogeneous material can be modeled as $T \propto \exp(-\alpha t)$. Combining these two equations yields

$$T \propto \exp\left(-\frac{\alpha\rho}{R_s}\right); \quad (2)$$

$\alpha\rho$ is a constant parameter for a uniform and homogeneous material. In addition to Eq. (1), the following is another formula commonly used to describe the relationship between R_s and T for TCFs [76]:

$$T \propto 1 - \frac{Z_0}{2R_s} \frac{\sigma_{OP}}{\sigma_{dc}}; \quad (3)$$

where Z_0 is the characteristic impedance of vacuum ($\sim 376.73 \Omega$). Both σ_{dc} and σ_{OP} are fundamental properties of the material, therefore $\sigma_{dc}=\sigma_{OP}$ is also a useful FOM for TCF evaluation. It is worth noting that Eq. (2) is based on the assumption that the film thickness is much less than the wavelength of interest. In the case of CNT films as TCFs, their thickness is generally <50 nm. Therefore, $\sigma_{dc}=\sigma_{OP}$ is valid as a FOM to evaluate their performance of CNT films as TCFs. Degiorgi et al. measured a σ_{OP} value of 200 S/cm at 550 nm for buckypaper composed of SWNTs [77]. This value applies for SWNT films obtained by FCCVD, because σ_{OP} is independent of doping level but varies with the number of walls in the CNTs.

Good candidates for use in TCFs will have higher FOM, $\alpha\rho$ and $\sigma_{dc}=\sigma_{OP}$, meaning a material with high conductivity and low optical absorption [78]. Based on Eqs. (1) and (2), $\alpha\rho \propto \frac{Z_0}{2} \frac{\sigma_{OP}}{\sigma_{dc}}$ can be obtained by performing a Taylor expansion in $T=R_s$ to first order. Hence, $\alpha\rho$ and $\sigma_{dc}=\sigma_{OP}$ are phenomenologically equivalent. Because $\sigma_{dc}=\sigma_{OP}$ is dimensionless and simple, we use it to compare the properties required for practical applications of CNT TCFs in Table 1.

The requirements on the optoelectronic properties of TCFs vary depending on the application [19]. The minimal requirements for practical application of TCFs are presented in Table 1. CNT films offer various advantages in terms of physical flexibility, excellent optical properties, and chemical stability, compared with ITO or other candidate TCFs. However, the conductivity of even state-of-the-art SWNT films must still be improved to meet industrial requirements for certain applications in order to replace ITO (Table 1); For example, transparent electrodes for photovoltaic devices require high transmittance above 90% and conductivity of R_s below 10 Ω/sq for efficient energy harvesting, which means $\frac{\sigma_{OP}}{\sigma_{dc}} > 348:5$. Based on theoretical and experimental results, the optoelectronic properties of SWNT films depend on many parameters, including the morphology (length, diameter, and

Table 1 Minimal requirements for practical applications of TCFs and performance of SWNT films as TCFs

TCF or application	<i>T</i> (%)	<i>R_s</i> (Ω/sq)	<i>σ_{dc}/σ_{OP}</i>	Comment	Refs.
Photovoltaic electrode	90	10	348.5		[19, 59]
ITO	90	10–100	348.5–34.8	Mature, low sheet resistance, high transparency; costly, brittle, high reflection	[19, 57]
Patterned SWNT film produced by FCCVD	97	69	178	Overcomes the tradeoff between <i>T</i> and <i>R_s</i> ; costly, time-consuming	[33, 66]
	87	29	90		
MWNT film from CNT forest	83	24	80.4	Efficient process, less impurities, anisotropic conductivity; aligned CNT forest required, laser ablation and metal deposition	[29]
	90	208	16.8		
CNB film obtained by FCCVD	95	100	72.6	Mature, efficient process, good control over thickness; residual catalyst, chemical doping	[62]
OLED display electrode	90	50	69.7		[19, 59]
SWNT film obtained by liquid-phase processing	78–90	30–300	65–5	Fast and simple process, uniform films; chemical doping, high pollution	[19, 59, 106]
SWNT film deposited on filter by FCCVD	90	80–100	43.6–34.8	Mature, efficient process, laser ablation and metal deposition; residual catalyst, chemical doping	[31, 92, 126]
Individual SWNT film obtained by FCCVD	90	89	39.2	Better performance for thin-film transistors; low yield, time-consuming, short CNTs	[33, 98]
LCD screen electrode	85	100	22.3		[19, 59]
Enriched metallic SWCNT film obtained by FCCVD	90	160	21.8	88% M-SWNT, simple process; chemical doping, unclear mechanism	[49]
SWNT film deposited on reactor wall by FCCVD	70	50	19.3	Without further chemical doping, without hydrogen; poor uniformity, large-scale production limited, little control over thickness,	[22]
Continuous tubular SWNT film obtained by FCCVD	90	200	17.4	High yield, without hydrogen, without further chemical doping; high synthesis temperature, poor uniformity	[68]
Touch panel electrode	85	500	4.5		[19, 62]

The requirements of various applications for TCFs are in bold

orientation) of the SWNTs and bundles, the quality, purity, and chirality of the SWNTs, doping, etc. [79–82].

Since the contact resistance between individual SWNTs or bundles is orders of

pristine and nitric-acid-treated SWNT networks obtained by FCCVD, as shown in Fig. 7. At room temperature, the conductivity of a SWNT or bundle was found to be ohmic, with values close to 3–16 k Ω / μ m. The resistance of their junctions was much higher, ranging from 29 to 532 k Ω and decreasing with increasing SWCNT or bundle diameter. The contact resistance also depended on the contact morphology [86]. Compared with X junctions, the contact resistance of Y junctions is orders of magnitude lower [15], because they benefit from carrier transport via longer interbundle connections. The contact resistance of both types of junction is inversely proportional to the diameters of CNT branches. They also found that moderate nitric acid treatment reduced the sheet resistance by a factor of 4 by reducing the average junction resistance by a factor of 3, while the resistance of the nanotubes remained largely unaltered. These results suggest that the mechanism for resistance reduction on doping is related to contact modulation with no major impact on the conductance of the SWNTs themselves [87]. However, in the case of defective or substitutionally doped SWNTs, the resistance of the SWNTs or their bundles may be much larger due to scattering on lattice defects, dominating the total resistance of the thin film [88, 89].

As mentioned above, interbundle and intertube contacts dominate the overall resistance of typical SWNT networks. Therefore, increasing bundle length correlates with decreasing sheet resistance at constant optical transparency, as longer bundles reduce the amount of high-resistance interbundle contacts in the network [90]. An exponential relationship between conductance and average CNT bundle length has been found experimentally [91]. Although longer CNTs do benefit fabrication of more conducting films, they are more difficult to disperse, particularly at high concentration. This intrinsic contradiction complicates and compromises many liquid-phase methods for CNT film fabrication. For the dry FCCVD method, however, no such problem exists. The length of the SWNTs produced depends on the residence time and growth rate, since SWNT growth occurs in a certain region (growth zone) in the FCCVD method. Kaskela et al. [31] deposited TCFs containing SWNT bundles of various lengths, synthesized in different reactors of various sizes based on the FCCVD method. With bundle length improvement from 1.3 μ m to

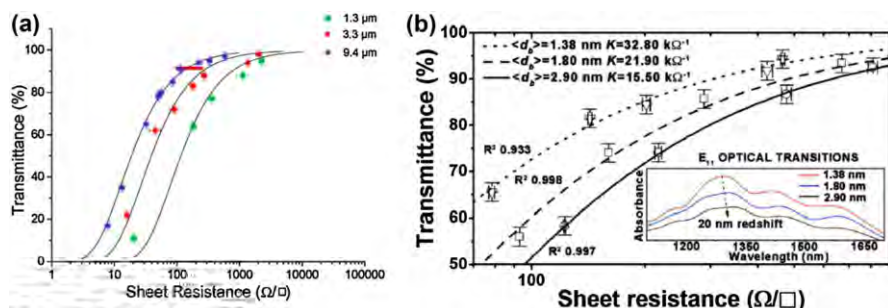


Fig. 8 Effect of bundle length and diameter on optoelectronic performance of SWNT films. With **a** increasing bundle length [31] or **b** decreasing bundle diameter [98], the performance of the SWNT films as TCFs was improved. Copyright 2010 American Chemical Society and Copyright 2009 AIP Publishing LLC

9.4 μm , the optoelectronic performance of the SWNT films was greatly improved, as shown in Fig. 8a. Moreover, a hybrid carbon source was applied to tune the bundle length based on different decomposition temperatures. Anoshkin et al. [92] fabricated SWNT films using a hybrid carbon source of CO and ethylene. SWNT film doped with gold chloride (AuCl_3) exhibited sheet resistance as low as $73\ \Omega/\text{sq}$ at transmittance of 90%. In addition, Reynaud et al. [93] obtained similar results when using toluene and ethylene as carbon sources. In general, use of a hydrocarbon carbon source leads to higher growth rate of CNTs compared with CO. For certain catalyst–carbon systems, use of appropriate additives including water, CO_2 , sulfur, etc. can improve the CNT growth rate [37, 53, 94].

In addition to the nanotube or bundle length, the mean bundle size is expected to have a large, but relatively little understood effect on the performance of the resulting thin film. Due to van der Waals interactions between them, SWNTs have a strong tendency to aggregate into bundles during synthesis and processing. At the individual SWNT level, dielectric screening caused by adjacent SWNTs modulates the electronic properties of an SWNT. Optically, this can be observed as a redshift caused by decreased exciton lifetime.

Some work has been carried out on the dependence of the performance of thin films based on liquid processing on the bundle diameter. However, the conclusions are inconsistent, owing to the complex processes and numerous influencing factors. Hecht et al. [91] and Shin et al. [95]. studied the performance of films fabricated using vacuum filtration of SWNT dispersions, where the bundle length and diameter were controlled by using different sonication times. Hecht et al. could not reach

conductivity, although the contacts between them can be expected to be quite conductive due to the large contact areas between SWNTs arranged in this manner.

In contrast to liquid-phase processing, the bundle diameter can be controlled by regulating the catalyst and CNT concentration without affecting the length or chirality distribution when using FCCVD. Based on this fact, the aerosol CVD system can be used to reveal the essential relationship between film performance and bundle diameter. Mustonen et al. [98] studied the effect of bundle diameter (1.38, 1.80, and 2.90 nm) on TCE performance by deliberately aggregating aerosol-synthesized SWNTs in gas phase after synthesis [98], as shown in Fig. 8b. They concluded that films collected from a more bundled population of the same SWNTs performed worse and that the performance decrease could be described using a semiempirical model, assuming that the conductivity within the bundles is not higher compared with that in individual SWNTs, in accordance with Han et al. [96], and that the contact resistances between bundles are lower compared with those between individual SWNTs, in accordance with Znidarsic et al. [85]. Compared with earlier studies carried out using liquid dispersions, these experiments had the advantage that the properties of the individual SWNTs remained unchanged and the only variable was the amount of bundling. The conclusion that less bundled SWNTs are beneficial to improve the thin film conductivity is further supported by the studies of Mustonen et al. [42] and Kaskela et al. [33]. In these studies, the films fabricated from shorter (mean SWNT length 4 μm), nearly nonbundled SWNTs, displayed similar performance to earlier published films [31] consisting of longer SWNT bundles (mean bundle length 8–10 μm). The short SWNTs were synthesized at low concentration and thus undergoing almost no bundling during synthesis.

The ratio of metallic to semiconducting SWNTs in the network is also crucial to the film conductivity, based on two facts [99, 100]. Firstly, at room temperature, the resistance of an individual m-SWNT (10^{-4} – 10^{-3} Ω cm) is much lower than that of its semiconducting counterpart (10 Ω cm) [101, 102]. In addition, the contact resistance of metal–semiconducting (M–S) heterojunctions is ~ 1 M Ω at ambient temperature, one order of magnitude higher than for metal–metal (M–M) or semiconducting–semiconducting (S–S) junctions (~ 20 k Ω) [86, 103], although doping is likely to reduce this difference [85]. Because of the nature of CNT networks as a mixture of semiconducting and metallic objects, almost all of the junctions are heterojunctions. Simulation results for the conductance versus proportion of semiconducting tubes of a SWNT thin film are shown in Fig. 9 [4]. Because of the low resistance of M–M and S–S contacts, the conductance of films composed of pure metallic or semiconducting tubes is quite high (point A and E). With increasing proportion of semiconducting SWNTs (from point A to point B), the conductance becomes dominated by Schottky barriers (M–S junctions) rather than metallic tubes. When the proportion of semiconducting tubes approaches 80% (point B to D), the conductance is blocked. For small amounts of metallic tubes in the network (from point D to E), the film conductivity increases as charges pass along paths formed by semiconducting SWNTs, bypassing the Schottky barriers. In 2014, Hou et al. [49] used the FCCVD method to prepare enriched m-SWNT films by introducing hydrogen as etchant gas. With increasing m-SWNT content, the

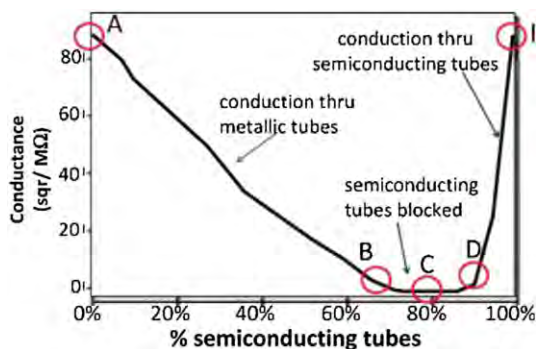


Fig. 9 Expected conductance as function of proportion of semiconducting tubes (assuming for simplicity that an unblocked semiconducting tube conducts as well as a metallic tube) [104]. Reprinted with permission from [101], Copyright 2009 American Chemical Society. Conductance versus percentage of semiconducting CNTs in network, simulated for density three times the percolation threshold; CNT length, positions, and orientations are the same for different M/S ratios

sheet resistance at transmittance of 90% decreased from 500 Ω/sq to 160 Ω/sq , as shown in Fig. 9b.

7 Applications of SWNT Films in Touch Sensors and Display Electrodes

Transparent conducting films based on SWNTs are vital components in a range of electronic devices, such as touch screens [61, 62], LCDs [105, 106], OLEDs [107, 108], and solar cells [109, 110]. Currently, touch displays are the most mature application of SWNT TCFs [62], whereas most other applications of CNTs remain at laboratory stage. Resistive and capacitive touch panels can already be manufactured in factories and purchased on the market, indicating that practical applications of SWNT films have already started.

In 2013, Anisimov et al. [62] discussed recent progress in achieving characteristics and applications of TCFs based on Canatu's CNB technology. The combination of aerosol synthesis and direct dry printing allows homogeneous or patterned deposition on any substrate at room temperature and pressure, resulting in a simple, scalable, one-step, low-cost, and environmentally friendly thin-film manufacturing process that improves the quality and performance of final products. Direct dry printing is applicable to both sheet and roll-to-roll implementations and can be combined with conventional screen, gravure, and flexo printing to enable production of continuous rolls of complex, multilayered components. These advances are significant because they will enable flexible and even three-dimensional (3D)-shaped touch sensors, high-optical-quality touch displays with almost no reflection and high outdoors contrast, and cost-effective manufacturing through dry roll-to-roll processing.

Deposition of homogeneous and patterned CNB films can be achieved by combining the aerosol synthesis method with room-temperature deposition based on a modification of the aforementioned filter transfer technique. The conductivity of

CNB films of given transparency has doubled approximately every 12 months since 2007. Figure [10](#)

initial change of a few percent. In another similar test with 140,000 bending cycles, the change in resistivity was less than 7%. The Canatu facility allows capacity of up to 500,000 m²/month. Together, these results indicate that CNB films can indeed be used as a substitute for ITO electrodes in consumer electronics.

Most touch sensors and displays require fine patterning with minimum feature sizes of 25–50 μm. For ITO, photolithography with eight steps is commonly used for such fine patterning. However, fine patterning of CNB films is achieved via laser

and early design knowhow of display pixel geometry to reduce the moiré effect between the display and sensor. Metal mesh manufacture is also demanding, as the bonding equipment needs to be tightly controlled. CNB sensors are display design agnostic due to the pattern invisibility and random orientation of CNB deposition.

Based on the availability of flexible and cost-effective CNB films with excellent and stable performance, touch sensors (Fig. 11) and high-optical-quality touch displays (Fig. 12) have been manufactured. Specifically, a CNB-based two-layer glass–film–film (GFF) structure demonstrator was created, showing only 2.2% reflection and 40% better contrast in bright ambient light compared with a comparable structure using ITO. For 3D-shaped rigid touch sensing, formability with 1 mm radius edges and 120% stretching was achieved.

The 13.3-inch-diagonal CNB projected-capacitive touch sensors were manufactured (Fig. 12b) based on the process shown in Fig. 12a. The touch stack was of glass–film–film (GFF) type with sense and drain electrodes (Fig. 12a).

The 13.3-inch-diagonal CNB projected-capacitive touch sensors were manufactured (Fig. 12b) based on the process shown in Fig. 12a. The touch stack was of glass–film–film (GFF) type with sense and drain electrodes (Fig. 12a).

Table 3. Compared with ITO and metal mesh touch modules, CNB touch modules have the lowest haze.

A highly transparent 3D-shaped demonstrator with slider, wheel, and button touch was also created (Fig. 12c), based on the FIM process with CNB on thin polycarbonate substrate and clear poly(methyl methacrylate) overmold. The radius of curvature was 130 mm. For rigid 3D-shaped touch devices, film insert molding

Table 4 Specular and diffuse reflection results for CNB and ITO GFF optical demonstrators with AR coating [62]. Copyright 2014 Society for Information Display

Direct-bonded touch module	Specular reflection (%)	Diffuse reflection (%)	Total reflection (%)
CNB AR/GFF	1.85	0.36	2.21
ITO AR/GFF	2.91	0.47	3.38

breakdown of the reflection values in the touch display structure. The CNB sensor stack showed no inherent reflections, hence the 1.8% specular reflection for the GFF stack originated from the glass–antireflection (AR) coating–air interface and from the display (Fig. 8). For the ITO sensor stack, despite complex index-matching layers, 1% specular reflection from the ITO layers was still observed. By better optimizing the AR coating, using a less reflective display, and optimizing the direct bonding materials, < 1% specular reflection is feasible with CNB GFF sensors.

Demonstrators of touch and display devices have therefore been successfully produced, indicating that CNB films are now a commercially viable option for high-volume applications and for high-quality flat, flexible, and 3D-formed touch sensors for use in mobile phones, tablets, phablets, laptops, smart watches, digital cameras, automotive consoles, and white goods.

8 Summary and Outlook

This review has described recent developments in SWNT thin films fabricated by dry methods based on FCCVD, including SWNT synthesis and film fabrication, properties, and applications as TCFs. As an emerging class of materials, SWNT thin films possess unique optical transparency and superior electric properties and mechanical flexibility, resulting from not only the incorporation of individual SWNTs but also their collective behavior, with additional properties arising from tube–tube interactions. Among these promising candidate materials, CNT TCFs exhibit great potential because of their chemical stability, high stretchability, color neutrality and less haze, wider spectral range, etc. [56, 59, 67]. Compared with liquid-phase processing, which involves various time- and resource-consuming steps, dry FCCVD methods without dispersion in solution are more direct and simpler. By avoiding the tradeoff between CNT length and solubility during film fabrication, the dry FCCVD method enables production of films that contain longer CNTs and exhibit excellent optoelectronic properties. Films based on SWNTs produced by the dry FCCVD method are already commercially available for application in touch and display devices. However, the transparent and conductive properties of these CNT films must be further improved to expand their application scope, e.g., to include solar cells.

In the dry FCCVD method, control of the CNT morphology and chirality is critical to improve the film performance. Increasing the bundle length and reducing the diameter, down to individual tube level, can effectively improve the film conductivity. The length of the SWNTs or bundles depends on the growth time and

growth rate during the synthesis. Limiting the number concentration of CNTs in gas phase prevents nanotube collision and bundle formation. With increasing aspect ratio of CNTs and bundles, it becomes very important to maintain a stable laminar gas flow, to prevent formation of CNT and bundle loops, which would greatly reduce the effect of greater CNT length. Controlled synthesis of CNTs is still in the development stage, with further research efforts needed. Although there are some papers on direct or posttreatment methods to synthesize or separate pure metallic or semiconducting CNTs [31, 49, 52, 111, 112], scalable and reliable methods are still desired for further commercialization in CNT applications. Separation of tubes based on their electric conductivity would benefit applications in transparent conductors and thin-film transistors [113], another major application for CNT films. Considering the difficulty of obtaining high-purity semiconducting CNTs [112], CNT film transistor technology remains at an earlier stage compared with transparent conductors. In addition to the neat material, extensive investigations on numerous dopants for CNTs have been carried out. The effectiveness of doping for improving the conductance of CNT films has been demonstrated. However, stability issues and the effects of functional groups and residual dopant on device performance have been less well studied and evaluated [114, 115], being critical for actual device applications and commercial use.

Research on the dry FCCVD method for fabrication of SWNT films could advance the development of not only industrial applications but also the fundamental science of related nanostructured materials and nanodevices. Except for transparent electrodes and thin-film transistors, SWNT films produced by the dry FCCVD method also have great potential for use in several other high-impact applications, including sensors [116–118], ultrafast femtosecond lasers [30, 119–121], thermoacoustic loudspeakers [122], energy storage [123–125], etc. We believe that SWNT films produced by the dry FCCVD method will soon be an essential component in commercial device applications, because of not only their unique properties and low cost but also promising research results.

Acknowledgements We acknowledge financial support from the European Union Seventh Framework Programme (FP7/2007–2013) under Grant Agreement No. 604472 (IRENA project), the Aalto Energy Efficiency (AEF) Research Program through the MOPPI project, TEKES of Finland via CNT-PV project, and Academy of Finland via projects 286546 and 292600.

References

1. de Volder MFL, Tawfik SH, Baughman RH, Hart AJ (2013) Carbon nanotubes: present and future commercial applications. *Science* 339:535–539
2. Iijima S, Ichihashi T (1993) Single-shell carbon nanotubes of 1-nm diameter. *Nature* 363:603–605
3. Iijima S (1991) Helical microtubules of graphitic carbon. *Nature* 354:56–58
4. Dresselhaus MS, Dresselhaus G, Saito R (1995) Physics of carbon nanotubes. *Carbon* N. Y. 33:883–891
5. Saito R et al (2001) Chirality-dependent G-band Raman intensity of carbon nanotubes. *Phys Rev B* 64:853121–853127
6. Cheng HM, Li F, Sun X, Brown SDM, Pimenta MA, Marucci A, Dresselhaus G, Dresselhaus MS (1998) Bulk morphology and diameter distribution of single-walled carbon nanotubes synthesized by catalytic decomposition of hydrocarbons. *Chem Phys Lett* 289:602–610

36. Bronikowski MJ, Willis PA, Colbert DT, Smith KA, Smalley RE (2001) Gas-phase production of carbon single-walled nanotubes from carbon monoxide via the HiPco process: a parametric study. *J Vac Sci Technol* 19:1800–1805
37. Li Y-L (2004) Direct spinning of carbon nanotube fibers from chemical vapor deposition synthesis. *Science* 304:276–278
38. Gui X et al (2010) Soft, highly conductive nanotube sponges and composites with controlled compressibility. *ACS Nano* 4:2320–2326
39. Lamouroux E, Serp P, Kalck P (2007) Catalytic routes towards single wall carbon nanotubes. *Catal Rev* 49:341–405
40. Barnard JS, Paukner C, Koziol KK (2016) The role of carbon precursor on carbon nanotube chirality in floating catalyst chemical vapour deposition. *Nanoscale* 8:17262–17270
41. Moisala A, Nasibulin AG, Kauppinen EI (2003) The role of metal nanoparticles in the catalytic production of single-walled carbon nanotubes. *J Phys Condens Matter* 15(42):3011
42. Mustonen K et al (2015) Gas phase synthesis of non-bundled, small diameter single-walled carbon nanotubes with near-armchair chiralities. *Appl Phys Lett* 107:013106
43. Cheng HM et al (1998) Large-scale and low-cost synthesis of single-walled carbon nanotubes by the catalytic pyrolysis of hydrocarbons. *Appl Phys Lett* 72:3282–3284
44. Li Y-L, Zhang L-H, Zhong X-H, Windle AH (2007) Synthesis of high purity single-walled carbon nanotubes from ethanol by catalytic gas flow CVD reactions. *Nanotechnology* 18:225604
45. Chen Z et al (2004) An enhanced CVD approach to extensive nanotube networks with directionality. *Carbon N Y* 12:275504
46. He M, Jiang H, Kauppinen EI, Lehtonen J (2012) Diameter and chiral angle distribution dependencies on the carbon precursors in surface-grown single-walled carbon nanotubes. *Nanoscale* 4:7394
47. Harutyunyan AR et al (2009) Preferential growth of single-walled carbon nanotubes with metallic conductivity. *Science* 326:116–120
48. Vilatela JJ, Windle AH (2010) Yarn-like carbon nanotube fibers. *Adv Mater* 22:4959–4963
49. Hou PX et al (2014) Preparation of metallic single-wall carbon nanotubes by selective etching. *ACS Nano* 8:7156–7162
50. Piao Y et al (2016) Intensity ratio of resonant Raman modes for (*n*, *m*) enriched semiconducting carbon nanotubes. *ACS Nano* 10:5252–5259
51. Jiang H, Nasibulin AG, Brown DP, Kauppinen EI (2007) Unambiguous atomic structural determination of single-walled carbon nanotubes by electron diffraction. *Carbon N Y* 45:662–667
52. He M et al (2013) Chiral-selective growth of single-walled carbon nanotubes on lattice-mismatched epitaxial cobalt nanoparticles. *Sci Rep* 3:1460
53. Nasibulin AG et al (2006) An essential role of CO₂ and H₂O during single-walled CNT synthesis from carbon monoxide. *Chem Phys Lett* 417:179–184
54. Moisala A et al (2006) Single-walled carbon nanotube synthesis using ferrocene and iron pentacarbonyl in a laminar flow reactor. *Chem Eng Sci* 61:4393–4402
55. Nasibulin AG et al (2007) A novel hybrid carbon material. *Nat Nanotechnol* 2:156–161
56. Hecht DS, Hu L, Irvin G (2011) Emerging transparent electrodes based on thin films of carbon nanotubes, graphene, and metallic nanostructures. *Adv Mater* 23:1482–1513
57. Ellmer K (2012) Past achievements and future challenges in the development of optically transparent electrodes. *Nat Photon* 6:809–817
58. Chang DS, Lai ST (2015) Implementation of cross-generation automation transportation system in the TFT-LCD industry. *Int J Adv Manuf Technol* 78:753–763
59. Du J, Pei S, Ma L, Cheng HM (2014) 25th anniversary article: carbon nanotube- and graphene-based transparent conductive films for optoelectronic devices. *Adv Mater* 26:1958–1991
60. Feldman D et al. (2015) Shared solar: current landscape, market potential, and the impact of federal securities regulation (No. NREL/TP-6A20-63892). National Renewable Energy Lab.(NREL), Golden, CO (United States)
61. Hecht DS et al (2009) Carbon-nanotube film on plastic as transparent electrode for resistive touch screens. *J Soc Inf Disp* 17:941
62. Anisimov AS, Brown DP, Mikladal BF, Liam Ó (2014) Printed touch sensors using carbon NanoBud material. *Soc. Inf. Disp. Tech. Dig.* 1–8
63. Garnett EC et al (2012) Self-limited plasmonic welding of silver nanowire junctions. *Nat Mater* 11:241–249
64. Lee JY, Connor ST, Cui Y, Peumans P (2008) Solution-processed metal nanowire mesh transparent electrodes. *Nano Lett* 8:689–692

65. Li X et al (2009) Large-area synthesis of high quality and uniform graphene films on copper foils. *Science* 324:1312–1314
66. Fukaya N et al (2014) One-step sub-10 μm patterning of carbon-nanotube thin films for transparent conductor applications. *ACS Nano* 8:3285–3293
67. Sun D-M et al (2013) Mouldable all-carbon integrated circuits. *Nat Commun* 4:1–8
68. Zhou W, Zhang Q, Wang Y, Xie S (2014) Ultrathin carbon nanotube film and preparation method and device thereof. U.S. Patent Application No. 14/889,753
69. Gonzalez D et al (2005) A new thermophoretic precipitator for collection of nanometer-sized aerosol particles. *Aerosol Sci Technol* 39:1064–1071
70. Yu L, Shearer C, Shapter J (2016) Recent development of carbon nanotube transparent conductive films. *Chem Rev*. <https://doi.org/10.1021/acs.chemrev.6b00179>
71. Dionigi C et al (2007) Carbon nanotube networks patterned from aqueous solutions of latex bead carriers. *J Mater Chem* 17:3681
72. Castro MRS, Lasagni AF, Schmidt HK, Mücklich F (2008) Direct laser interference patterning of multi-walled carbon nanotube-based transparent conductive coatings. *Appl Surf Sci* 254:5874–5878
73. Fukaya N, Kim DY, Kishimoto S, Noda S, Ohno Y (2014) One-step sub-10 μm patterning of carbon-nanotube thin films for transparent conductor applications. *ACS Nano* 8:3285–3293
74. Zhou W et al (2004) Single wall carbon nanotube fibers extruded from super-acid suspensions: preferred orientation, electrical, and thermal transport. *J Appl Phys* 95:649–655
75. Dan B, Irvin GC, Pasquali M (2009) Continuous and scalable fabrication of transparent conducting carbon nanotube films. *ACS Nano* 3:835–843
76. Hu L, Hecht DS, Grüner G (2004) Percolation in transparent and conducting carbon nanotube networks. *Nano Lett* 4:2513–2517
77. Ruzicka B, Degiorgi L (2000) Optical and dc conductivity study of potassium-doped single-walled carbon nanotube films. *Phys Rev B* 61:R2468–R2471
78. Bergin SD et al (2008) Towards solutions of single-walled carbon nanotubes in common solvents. *Adv Mater* 20:1876–1881
79. Tian Y et al (2010) Analysis of the size distribution of single-walled carbon nanotubes using optical absorption spectroscopy. *J Phys Chem Lett* 1:1143–1148
80. King PJ, Higgins TM, De S, Nicoloso N, Coleman JN (2012) Percolation effects in supercapacitors with thin, transparent carbon nanotube electrodes. *ACS Nano* 6:1732–1741
81. De S, King PJ, Lyons PE, Khan U, Coleman JN (2010) Size effects and the problem with percolation in nanostructured transparent conductors. *ACS Nano* 4:7064–7072
82. De S, Coleman JN (2011) The effects of percolation in nanostructured transparent conductors. *MRS Bull* 36:774–781
83. Harris JM et al (2012) Electronic durability of flexible transparent films from type-specific single-wall carbon nanotubes. *ACS Nano* 6:881–887
84. Timmermans MY et al (2012) Effect of carbon nanotube network morphology on thin film transistor performance. *Nano Res* 5:307–319
85. Znidarsic A et al (2013) Spatially resolved transport properties of pristine and doped single-walled carbon nanotube networks. *J Phys Chem C* 117:13324–13330
86. Farajian AA, Esfarjani K, Kawazoe Y (1999) Nonlinear coherent transport through doped nanotube junctions. *Phys Rev Lett* 82:5084–5087
87. Shin D-W et al (2009) A role of HNO_3 on transparent conducting film with single-walled carbon nanotubes. *Nanotechnology* 20:475703
88. Susi T et al (2011) Nitrogen-doped single-walled carbon nanotube thin films exhibiting anomalous sheet resistances. *Chem Mater* 23:2201–2208
89. Geng H-Z et al (2007) Effect of acid treatment on carbon nanotube-based flexible transparent conducting films. *J Am Chem Soc* 129:7758–7759
90. Lyons PE et al (2008) The relationship between network morphology and conductivity in nanotube films. *J Appl Phys* 104:044302
91. Hecht D, Hu L, Grüner G (2006) Conductivity scaling with bundle length and diameter in single walled carbon nanotube networks. *Appl Phys Lett* 89:133112
92. Anoshkin IV et al (2014) Hybrid carbon source for single-walled carbon nanotube synthesis by aerosol CVD method. *Carbon N Y* 78:130–136
93. Reynaud O et al (2014) Aerosol feeding of catalyst precursor for CNT synthesis and highly conductive and transparent film fabrication. *Chem Eng J* 255:134–140

94. Hata K et al (2004) Water-assisted highly efficient synthesis of impurity-free single-walled carbon nanotubes. *Science* 306:1362–1364
95. Shin DH, Shim HC, Song JW, Kim S, Han CS (2009) Conductivity of films made from single-walled carbon nanotubes in terms of bundle diameter. *Ser Mater* 60:607–610
96. Han J-H, Strano MS (2014) Room temperature carrier transport through large diameter bundles of semiconducting single-walled carbon nanotube. *Mater Res Bull* 58:1–5
97. Nirmalraj PN, Lyons PE, De S, Coleman JN, Boland JJ (2009) Electrical connectivity in single-walled carbon nanotube networks. *Nano Lett* 9:3890–3895
98. Mustonen K et al (2015) Uncovering the ultimate performance of single-walled carbon nanotube films as transparent conductors. *Appl Phys Lett* 107:1–6
99. Blackburn JL et al (2008) Transparent conductive single-walled carbon nanotube networks with precisely tunable ratios of semiconducting and metallic nanotubes. *ACS Nano* 2:1266–1274
100. Rother M, Schießl SP, Zakharko Y, Gannott F, Zaumseil J (2016) Understanding charge transport in mixed networks of semiconducting carbon nanotubes. *ACS Appl Mater Interfaces* 8:5571–5579
101. Zhang WJ, Zhang QF, Chai Y, Shen X, Wu JL (2007) Carbon nanotube intramolecular junctions. *Nanotechnology* 18:395205
102. Ouyang M (2001) Atomically resolved single-walled carbon nanotube intramolecular junctions. *Science* 291:97–100
103. Stadermann M et al (2004) Nanoscale study of conduction through carbon nanotube networks. *Phys Rev B* 69:201402
104. Topinka MA, Rowell MW, Goldhaber-gordon D, Mcgehee MD, Gruner G (2009) Charge transport in interpenetrating networks of semiconducting and metallic carbon nanotubes. *Nano Lett* 9:2–4
105. Hayes RA, Feenstra BJ (2003) Video-speed electronic paper based on electrowetting. *Nature* 425:383–385
106. Park Y, Hu L, Gruner G, Irvin G, Drzaic P (2008) 37.4: late-news paper : integration of carbon nanotube transparent electrodes into display applications. *Sid Dig.* <https://doi.org/10.1889/1.3069721>
107. Zhang D et al (2006) Transparent, conductive, and flexible carbon nanotube films and their application in organic light-emitting diodes. *Nano Lett* 6:1880–1886
108. Li J et al (2006) Organic light-emitting diodes having carbon nanotube anodes. *Nano Lett* 6:2472–2477
109. Trancik JE, Barton SC, Hone J (2008) Transparent and catalytic carbon nanotube films. *Nano Lett* 8:982–987
110. Park J-U et al (2007) High-resolution electrohydrodynamic jet printing. *Nat Mater* 6:782–789
111. Yang F et al (2014) Chirality-specific growth of single-walled carbon nanotubes on solid alloy catalysts. *Nature* 510:522–524
112. Krupke R, Hennrich F, Löhneysen HV, Kappes MM (2003) Separation of metallic from semi-conducting single-walled carbon nanotubes. *Science* 301:344–347
113. Park S, Vosguerichian M, Bao Z (2013) A review of fabrication and applications of carbon nanotube film-based flexible electronics. *Nanoscale* 5:1727
114. Jackson R, Domercq B, Jain R, Kippelen B, Graham S (2008) Stability of doped transparent carbon nanotube electrodes. *Adv Funct Mater* 18:2548–2554
115. Doherty EM et al (2009) The spatial uniformity and electromechanical stability of transparent, conductive films of single walled nanotubes. *Carbon N Y* 47:2466–2473
116. Lipomi DJ et al (2011) Skin-like pressure and strain sensors based on transparent elastic films of carbon nanotubes. *Nat Nanotechnol* 6:788–792
117. Cai L et al (2012) Highly transparent and conductive stretchable conductors based on hierarchical reticulate single-walled carbon nanotube architecture. *Adv Funct Mater* 22:5238–5244
118. Kim SN, Rusling JF, Papadimitrakopoulos F (2007) Carbon nanotubes for electronic and electro-chemical detection of biomolecules. *Adv Mater* 19:3214–3228
119. Avouris P, Freitag M, Perebeinos V (2008) Carbon-nanotube photonics and optoelectronics. *Nat Photon* 2:341–350
120. Kivistö S et al (2009) Carbon nanotube films for ultrafast broadband technology. *Opt Express* 17:2358
121. Rotermund F et al (2012) Mode-locking of solid-state lasers by single-walled carbon-nanotube based saturable absorbers. *Quantum Electron* 42:663–670
122. Xiao L et al (2008) Flexible, stretchable, transparent carbon nanotube thin film loudspeakers. *Nano Lett* 8:4539–4545

123. Niu Z et al (2011) Compact-designed supercapacitors using free-standing single-walled carbon nanotube films. *Energy Environ Sci* 4:1440
124. Niu Z et al (2013) Highly stretchable, integrated supercapacitors based on single-walled carbon nanotube films with continuous reticulate architecture. *Adv Mater* 25:1058–1064
125. Liu C, Li F, Ma LP, Cheng HM (2010) Advanced materials for energy storage. *Adv Mater* 22:E28
126. Mustonen K et al (2012) Influence of the diameter of single-walled carbon nanotube bundles on the optoelectronic performance of dry-deposited thin films. *Beilstein J Nanotechnol* 3:692–702

Sorting Carbon Nanotubes

Ming Zheng¹ 

Abstract

Keywords

Chapter 5 was originally published as Zheng, M. *Top Curr Chem (Z)* (2017) 375: 13. DOI 10.1007/s41061-016-0098-z.

&

1 Introduction

1.1 Separation in Nature and in Human Technologies

盘古

1.2 The CNT Sorting Problem

$n \ m$

$n \ m \quad m \ n$

$n \ m$

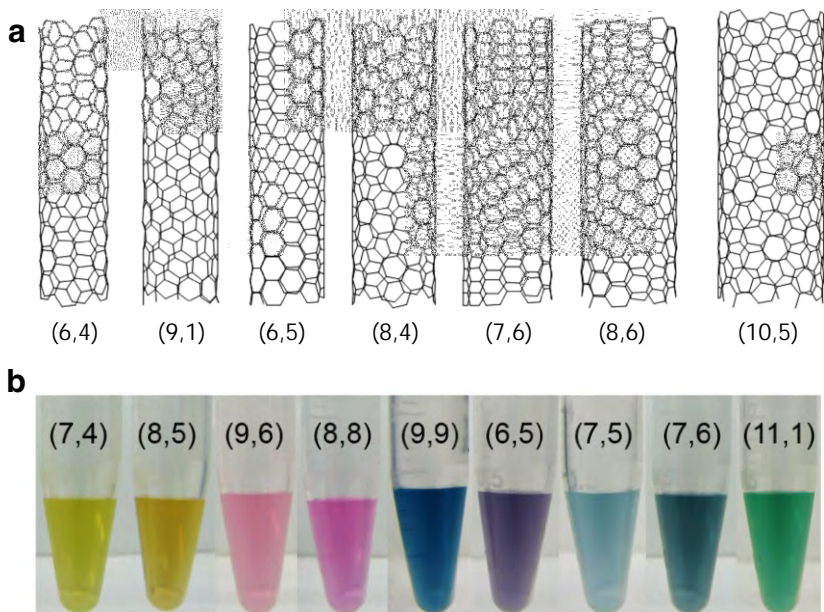


Fig. 1 a

b

(n, m)

θ)

d

$$\begin{aligned}
 & \frac{n}{m} \approx \frac{m}{n} \approx \frac{1}{2} \\
 & \frac{n}{m} \approx \frac{m}{n} \approx \frac{1}{2} \quad ; \quad \frac{n}{m} \approx \frac{m}{n} \approx \frac{1}{2} \\
 & \frac{n}{m} \approx \frac{m}{n} \approx \frac{1}{2} \quad ; \quad \frac{n}{m} \approx \frac{m}{n} \approx \frac{1}{2} \\
 & \frac{n}{m} \approx \frac{m}{n} \approx \frac{1}{2} \quad ; \quad \frac{n}{m} \approx \frac{m}{n} \approx \frac{1}{2}
 \end{aligned}$$

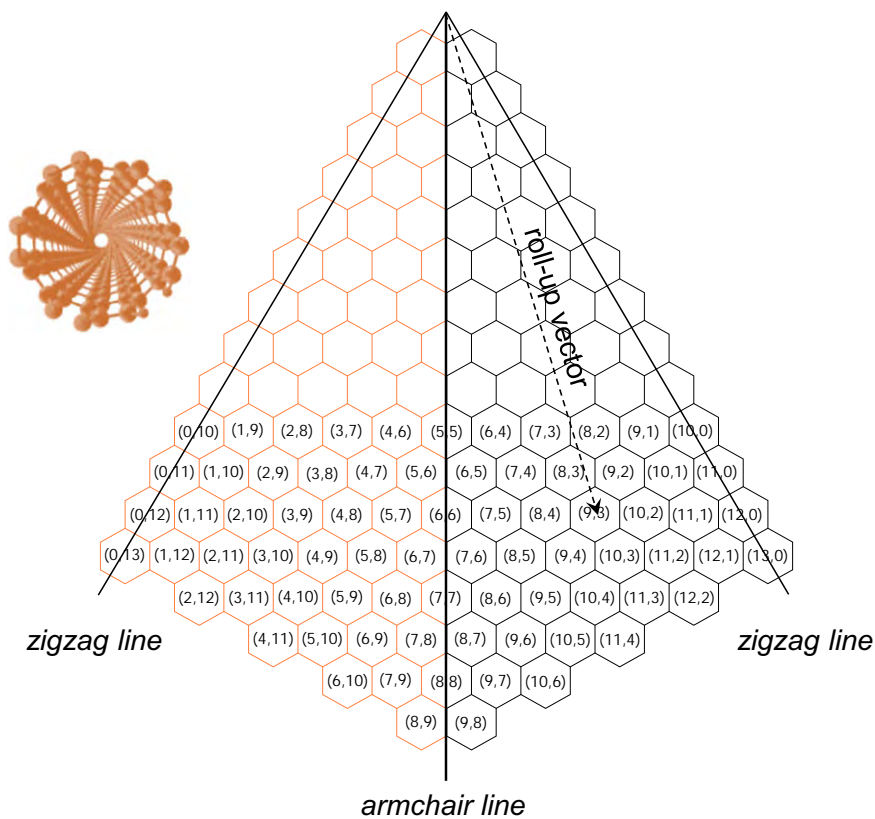


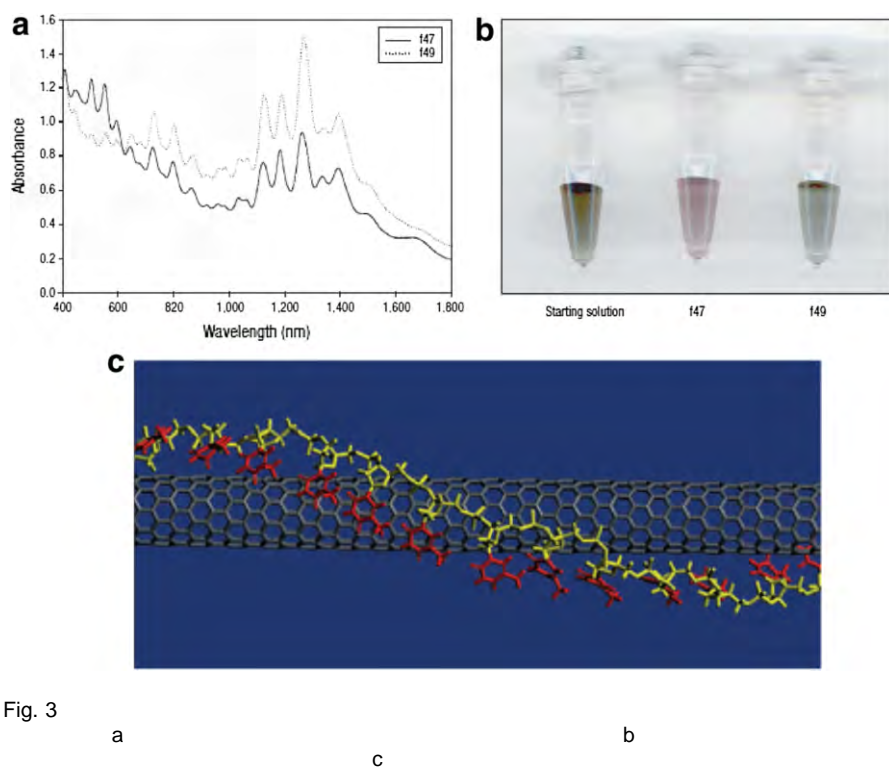
Fig. 2

1.3 Special Challenges in CNT Sorting

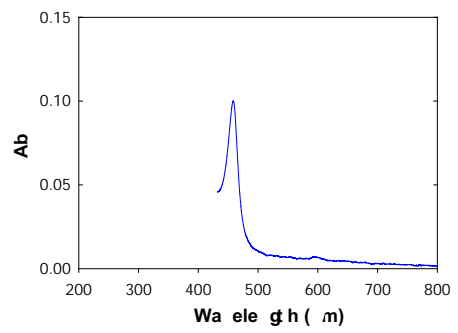
~

2 A Brief Account of the CNT Sorting Methodologies

2.1 Ion Exchange Chromatography (IEX) Separation of DNA- and Surfactant-Coated CNTs



n m



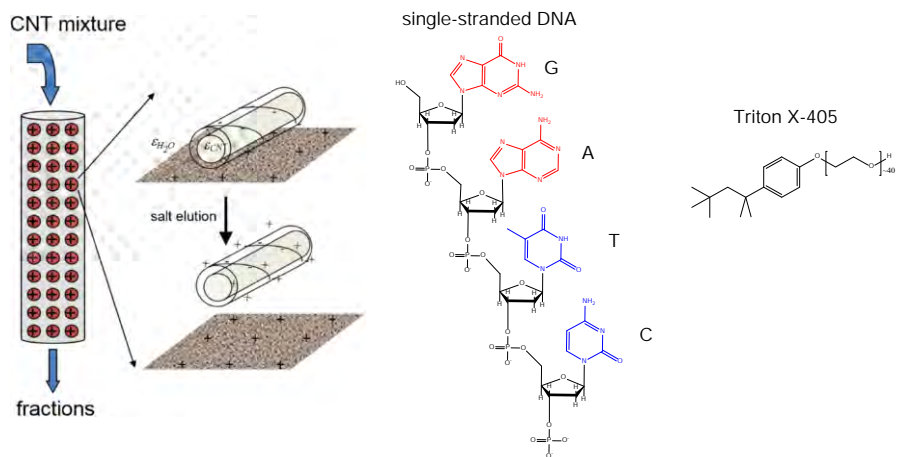


Fig. 5

2.2 Density Gradient Ultracentrifugation (DGU)

2.3 Selective Extraction in Organic Solvents by Conjugated Polymers and Small Molecules

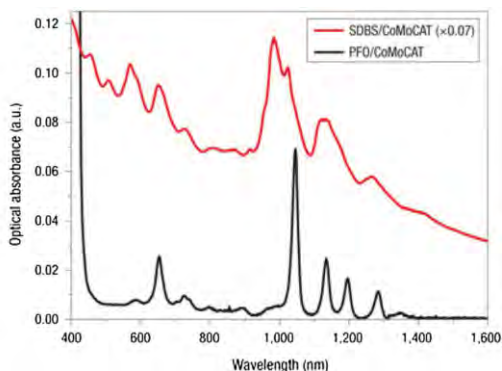
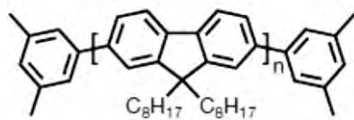


Fig. 7

black trace

b
red trace

Fig. 8

alt co 0 0

co

2.4 Gel Chromatography

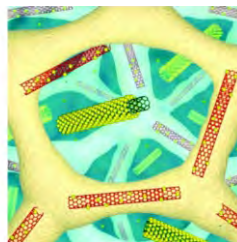
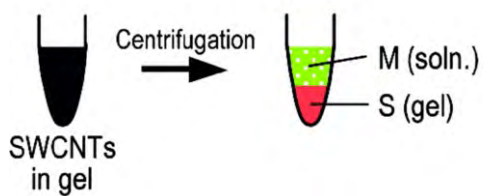


Fig. 9

2.5 Aqueous Two-Phase (ATP) Extraction

Fig. 10

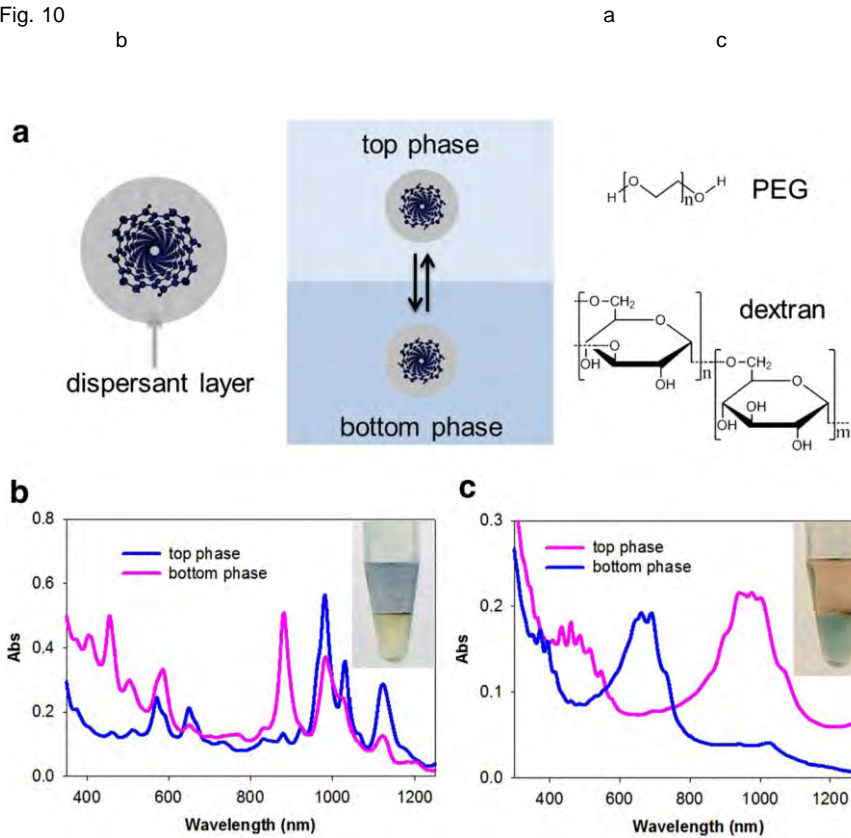


Fig. 11

a b c

Fig. 12

b

a

3 Sorting Mechanisms

n m

3.1 Solvation Structure, Solvation Energy and its Distribution

$$\begin{aligned} kT &= kT \\ k &= k \\ T &= T \\ &\approx kT \\ kT &= kT \end{aligned}$$

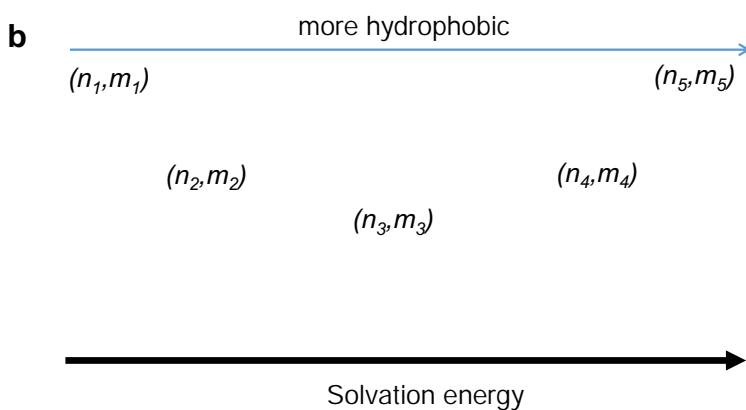
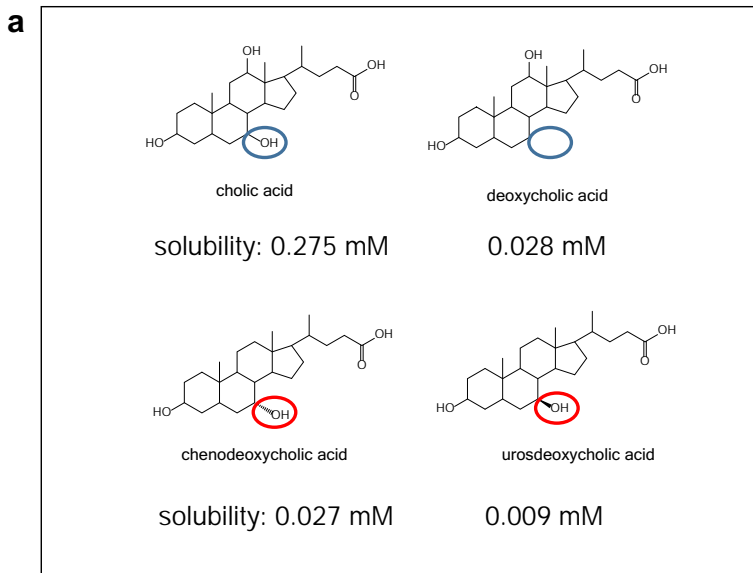


Fig. 13

a
b
n m

3.2 Electronic-Structure-Based Sorting via Redox Tuning

3.2.1 Redox Chemistry of CNTs

Fig. 14

3.2.2 Evidence for the Role of Redox in Bandgap-Based Sorting

d θ d θ

Fig. 15

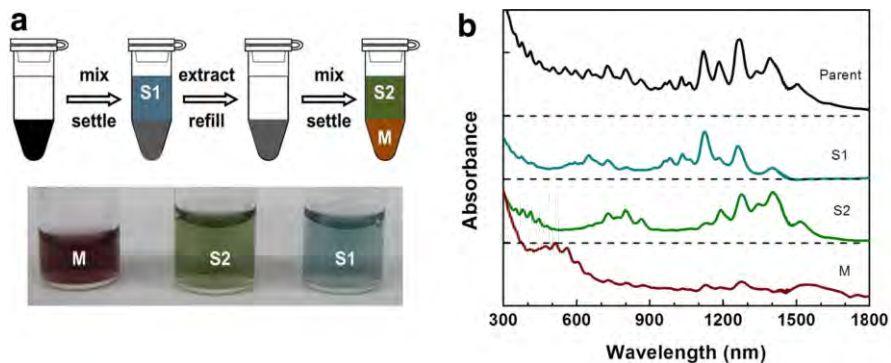


Fig. 16

b

a

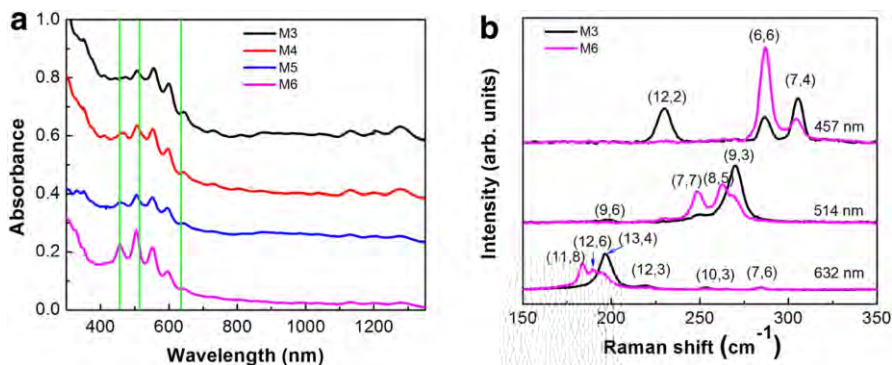
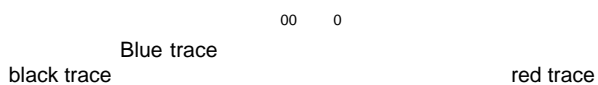


Fig. 17

a

b

Fig. 18



3.2.3 Molecular Mechanism of Redox Sorting

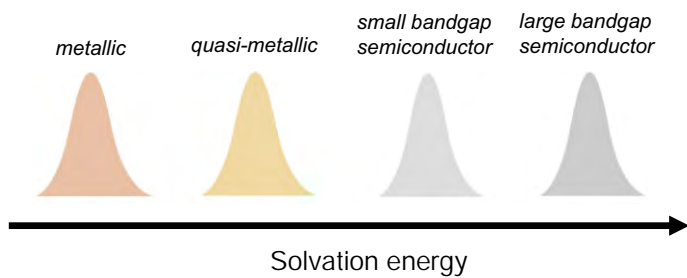


Fig. 19

3.3 Atomic-Structure-Based Sorting via Ordered Coating Structure Formation

n m

n m

Fig. 20



3.4 Nanotube Length Effect on Atomic- and Electronic-Structure-Based Separation

3.5 Resolution Limit of Atomic-Structure-Based Separation

$$\leq$$

$$kT$$

3.6 Evolvability of DNA-Based Sorting

<

n m

4 Future Directions

K

4.1 Sorting Other Types of Nanotubes

4.2 Quantifying Solvation Interactions

N

>

(unpublished results)

0

+

-



Electronic and optical properties of carbon nanotubes and quantum dots

R. Saito¹ · A. R. T. Nugraha · E. H. Hasdeo · N. T. Hung · W. Izumida

Received: 21 September 2016 / Accepted: 10 December 2016 / Published online: 28 December 2016
© Springer International Publishing Switzerland 2016

Abstract In this article, we overview our recent theoretical works on electronic and optical properties of carbon nanotubes by going from the background to the perspectives. Electronic Raman spectra of metallic carbon nanotubes give a new picture of Raman processes. Thermoelectricity of semiconducting nanotubes gives a general concept of the confinement effect on the thermoelectric power factor. Selective excitation of only a single phonon mode is proposed by the pulsed train technique of coherent phonon spectroscopy. Occurrence of both two and four fold degeneracy in the carbon nanotube quantum dot is explained by difference group velocities and the intra/inter valley scattering near the hexagonal corner of the Brillouin zone.

Keywords Carbon nanotubes · Quantum dots · Coherent phonon · Electric Raman spectroscopy · Thermoelectric power · Intervalley scattering

1 Introduction

A single wall carbon nanotube (SWNT) is a graphene sheet rolled up into a cylinder. An SWNT is either metallic or semiconducting [1–3] depending on the geometrical structure that is specified by two integers, (n, m) , which is known as chirality. Since SWNTs were found in 1993, the experimental techniques of synthesis and purification have been improving for 25 years. Recently, SWNTs samples in mass production can be commercially obtained for general purposes, while in the

Chapter 6 was originally published as Saito, R., Nugraha, A. R. T., Hasdeo, E. H., Hung, N. T. & Izumida, W. Top Curr Chem (Z) 375: 7. DOI 10.1007/s41061-016-0095-2.

✉ R. Saito
rsaito@flex.phys.tohoku.ac.jp

¹ Department of Physics, Tohoku University, Sendai 980-8578, Japan

laboratory, the purified, single chirality samples are also available, which makes it possible to observe the physical properties of SWNTs as a function of (n, m) . Then, selecting the optimum (n, m) for specific design of properties is now required in which we need supporting theoretical calculations that predict a perspective on the future of SWNT researches.

In this article, we present four subjects about physical properties of SWNTs as a function of (n, m) : (1) electronic Raman spectra of metallic SWNTs (m-SWNTs), (2) thermoelectric power of semiconducting SWNTs (s-SWNTs), (3) single phonon generation of SWNT by fast optics, and (4) transport of quantum dots made of semiconducting SWNTs. Here, we briefly mention each problem of the four subjects discussed in this article.

It is known in metallic SWNTs that not only phonon Raman spectra but also electronic Raman spectra (ERS) appear at the energy position of the van Hove singularity E_{ii} [4]. The origin of ERS are the excitation of an electron–hole pair near the Fermi energy by an exciton through the Coulomb interaction [5]. The interference effect of phonon Raman and ERS can be explained by changing the Fermi energy, which is known as gated modulated Raman spectroscopy [6].

In thermoelectricity, many attempts for finding the optimum low-dimensional materials to get a high efficiency for thermoelectricity have been investigated, especially after the Hicks and Dresselhaus paper published in 1993 [7, 8]. They showed that the confinement effect of one- or two dimensional (1-D, 2-D) semiconductors is an important factor for obtaining high figure-of-merit (ZT) values. Since 1993, many new nanomaterials show the high ZT values [9]. However, it is also known that some materials with small confinement length do not show a large thermoelectric power factor [10]. We show that the thermoelectric power factor is enhanced only when the confinement length is smaller than the so-called thermal de Broglie length [11].

In nanomechanics, the selective excitation of a single vibrational mode in the THz region is useful for possible applications [12]. In coherent spectroscopy, it is known that the pulse train of laser selectively excites a RBM mode of the specified (n, m) SWNT if the pulse repetition rate is selected for the frequency of the RBM mode [13]. Using the same technique, we propose that other phonon modes such as the G band phonon mode can be excited while the other phonon modes are suppressed.

In the quantum dot of finite length SWNT, we can observe discrete energy levels with a two or four fold degeneracy as a function of the gate voltage [14]. The appearance of the two kinds of degeneracies is partially related to the anisotropic group velocity in the k space [15]. Another important fact is that the edge states affect the energy levels near the Fermi energy. However, since the edge states of a SWNT depend on the shape at the edge of a SWNT, it is not easy to discuss in general the number of edge states and their electronic structure as a function of the edge shape of SWNTs. In this article, we discuss that the topological nature of specific properties is essential to explain the number of the edge states [16].

In the following sections, we discuss each subject and a perspective for the SWNT research at the end of each section.

2 El R a y al a

2.1 B Fa a a C a

lineshape appears in many metallic nanocarbon materials such as m-SWNTs [17, 20, 24], graphite intercalation compounds [25, 26], and graphene [27], origin of the continuous spectrum in m-SWNTs was not clear for 30 years. It was discussed that either single particle electron excitation [28, 29] or collective excitation (plasmon) [17, 30–32] were relevant to the continuous spectrum.

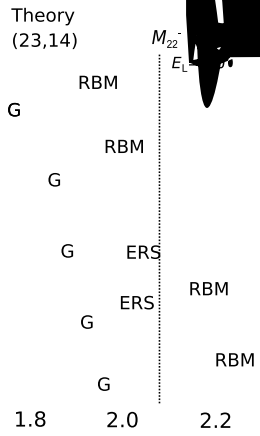
A breakthrough for understanding the origin of the continuous spectra has emerged by the observation of the electronic Raman spectra (ERS) in m-SWNTs by Farhat et al. [4]. In Fig. 2a, we can see the ERS with well-defined peak and broad spectral width ($\sim 500 \text{ cm}^{-1}$) between the radial breathing mode (RBM) and the G band for a (23,14) m-SWNT [4]. The ERS peak appears when scattered photon energy E_s matches to $M_{22}^- = 2.08 \text{ eV}$. With $E_L = 2.14 \text{ eV}$, the Raman shift of ERS at $M_{22}^- = 2.08 \text{ eV}$ corresponds to $E_L - M_{22}^- = 500 \text{ cm}^{-1}$ or 60 meV. Because of the broad spectral width of ERS, the G band and RBM lineshapes become asymmetric in m-SWNTs by interference between the ERS and phonon peaks. In Fig. 2b, on the other hand, no ERS appears in (25,8) s-SWNT indicating that the ERS originates from the linear energy band, which is absent in s-SWNTs. Farhat et al. can observe the ERS in m-SWNTs since the spectral width of ERS is smaller than that of the background spectra [4].

In order to study the origin of ERS, Farhat et al. further measured the ERS by changing the Fermi energy E_F [4]. In Fig. 2c, relative ERS intensity to the G band intensity is plotted as a function of E_F , which shows a maximum at $E_F = 0$ (Dirac

point). When $E_F < 0$, some parts of the energy bands are suppressed due to the presence of Fig. 2d). When $E_F > 0$, interband transitions occur because electrons in the final states are occupied (see the right panel of Fig. 2d). From this experimental observation, it can be seen that the ERS originates from electron–hole excitation near the linear bands. We can rule out the contribution of the surface plasmon because the spectral function of plasmon is proportional to $|E_F|$, while the experimental results show that the ERS is independent of electro-magnetic wave (transverse wave) except for the surface plasmon.

The electron–hole pair can be excited by the electron–phonon interaction which gives rise to phonon-assisted Raman scattering in m-SWNTs [33]. In order to check the origin of the ERS, Farhat et al. measured the E_L dependence of the Raman spectra [4]. Figure 3 shows the calculated and experimental Raman spectra as a function of scattered photon energy E_L . The RBM and G bands have fixed Raman shifts so that their positions do not change. The E_s appear at $E_L - \hbar\omega_0$. However, the ERS peak always appears at $E_L - \hbar\omega_0$ which is independent of E_L . These results indicate that the ERS originates from the electron–electron interaction between the photo-excited carrier at the linear band and the electron at the linear band. Hereafter, we will present the theoretical analysis of the ERS spectra from the theoretical calculations.

The electron–phonon interaction gives rise to phonon-assisted Raman scattering in m-SWNTs [33]. In order to check the origin of the ERS, Farhat et al. measured the E_L dependence of the Raman spectra [4]. Figure 3 shows the calculated and experimental Raman spectra as a function of scattered photon energy E_L . The RBM and G bands have fixed Raman shifts so that their positions do not change. The E_s appear at $E_L - \hbar\omega_0$. However, the ERS peak always appears at $E_L - \hbar\omega_0$ which is independent of E_L . These results indicate that the ERS originates from the electron–electron interaction between the photo-excited carrier at the linear band and the electron at the linear band. Hereafter, we will present the theoretical analysis of the ERS spectra from the theoretical calculations.



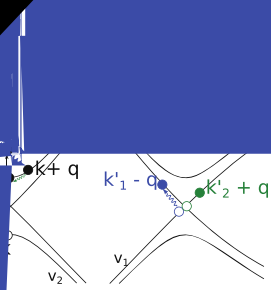
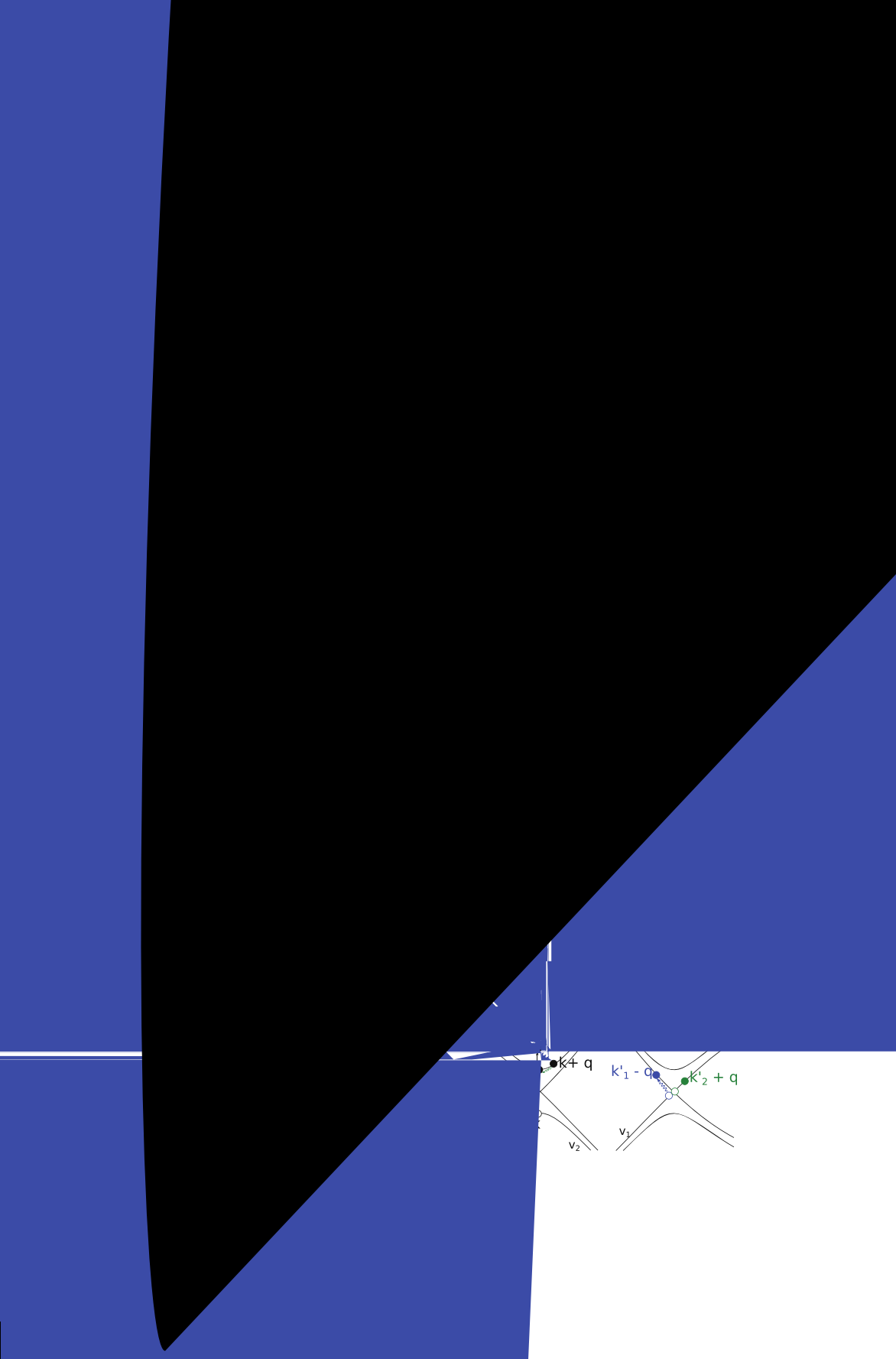


Fig. 5 **a** Calculated Raman spectra for a (23,14) SWNT with $E_L = 2.14$ eV. The total intensity shown is represented by the *solid line*. The *dashed lines* show contributions from the RBM and G modes, while the *dotted line* is the contribution from the ERS. Each *line shape* for the RBM, the G modes, and the ERS are Lorentzian. *Inset* shows the G band spectra after subtracted by the ERS spectrum. *Dots* are calculated results and the *solid line* shows the BWF fitting (Eq. (1)). Asymmetric factor ($1/q_{\text{BWF}}$) as a function of resonance condition ($E_L - M_{22}^-$). The *circles* and *squares* denote calculated results and experimental results, respectively [4]

$|A_{\text{iTO}}|^2$ or $|A_{\text{LO}}|^2$ (dashed line). As shown in the inset of Fig. 5a, the asymmetric line shape of the G band is obtained after subtracting the ERS contribution which reproduce the experimental spectra (*dots*). In Fig. 5b, the asymmetric factor $1/q_{\text{BWF}}$ is plotted as a function of $E_L - M_{22}^-$ in which the calculated $1/q_{\text{BWF}}$ gives a “V” shape as a function of $E_L - M_{22}^-$. Though the calculated $1/q_{\text{BWF}}$ values are of the same order with the experimental result, the E_L dependence of $1/q_{\text{BWF}}$ does not explain the experimental results, which should be clarified in the future.

In order to understand the origin of asymmetric lineshape, we consider phase difference of amplitudes between the ERS and G (or RBM) phonon spectrum, which is given by

$$I = |A_{\text{ERS}}|^2 + |A_v|^2 + 2|A_{\text{ERS}}||A_v|\cos(\varphi_{\text{ERS}} - \varphi_v), \quad (v = \text{G, RBM}), \quad (3)$$

where φ_v is a phase for the v -th phonon mode ($v = \text{ERS, G band, and RBM}$). The phase difference between the ERS and phonon spectra in Eq. (3) gives the quantum interference effect.

In Fig. 6a, we show φ_v of the RBM, ERS, and G (LO and iTO) modes as a function of Raman shift for $E_L = M_{22}^- = 2.1$ eV. Phase shift at the phonon energies (RBM or G) or ERS energy from $-\pi/2 \rightarrow \pi/2$ appears at each peak of the Raman spectra. Since the phase of ERS keeps constant at the resonance frequency that phonon spectra exhibit phase shifts, the interference term in Eq. (3) changes their sign as shown in Fig. 6b, c which is the origin of asymmetric lineshape. In fact, the sign change from negative (positive) to positive (negative) correspond to positive (negative) $1/q_{\text{BWF}}$ because of the phase shift position of ERS is at the right (left) of the RBM (G mode). It is important to note that the $|1/q|$ value for the RBM is larger than that of the G band when $E_L = M_{22}^-$. The reason why we get the large value of $|1/q|$ for RBM is a strong resonant condition at $E_L = M_{22}^-$ which makes the ERS peak closer to the RBM peak than to the G band peak. However, since RBM spectra are too sharp ($\sim 5\text{cm}^{-1}$), it might be difficult for experimentalists to observe the

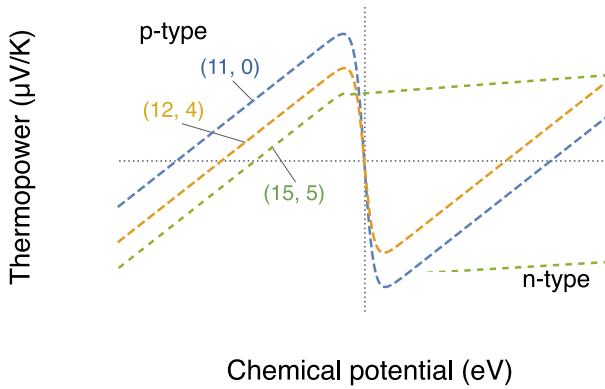
asymmetry of RBM. Theoretically, the BWF lineshape appears in any phonon modes as long as the ERS overlaps the phonon spectra, which should be observed by experiments in the future.

Recently, using single chirality SWNT samples, multiple ERS features originating from M_{ii}^- and M_{ii}^+ give either positive or negative values of $1/q_{\text{BWF}}$

We employ both numerical and analytical methods to calculate S from Eq. (4). In the numerical calculation, we adopt the BoltzTraP code [41], which is a widely-used package to calculate thermoelectric properties, such as the S and electrical conductivity, σ . An input data for the BoltzTraP code is the electronic energy dispersion $E(\mathbf{k})$ for all energy bands. We calculate the energy dispersion $E(\mathbf{k})$ of SWNTs within the extended tight-binding (ETB) model [42]. The ETB model takes into account long-range interactions up to the 20th nearest neighbors, SWNT curvature effects, and geometrical structure optimization, which are sufficient to reproduce the experimentally observed energy band gaps of the SWNTs [42, 43]. In the BoltzTraP calculation, we use a $20\text{nm} \times 20\text{nm} \times |\mathbf{a}|$ supercell, where $|\mathbf{a}|$ (in nm) is the length of the translational vector of a SWNT [1]. A larger supercell length (20nm) in the x - and y -directions is chosen so as to guarantee the one-dimensionality of the SWNT. Although S in the BoltzTraP code is expressed in terms of a tensor [41], we only consider the zz component of S , S_{zz} , which is the thermopower along the tube axis direction z . Hereafter, we denote S for S_{zz} .

3.3 Characterization of thermopower in s-SWNTs

In Fig. 8, we plot the thermopower as a function of chemical potential for three different s-SWNT chiralities: (11, 0), (12, 4), and (15, 5), at $T = 300\text{ K}$ [44]. The solid lines in Fig. 8 represent the numerical results, while dashed lines are analytical ones as shown below. For each chirality, the optimum value of the thermopower, indicated by a maximum (minimum) along the negative (positive) axis of the chemical potential, arises due to the p-type (n-type) s-SWNTs, which is consistent with a recent experimental observation [38]. The dependence of the thermopower on the chemical potential implies that it is possible to tune the thermoelectric properties of the s-SWNTs by applying gate voltages on the p-type and n-type s-SWNTs.



In order to understand the numerical results of thermopower, we have derived an analytical formula for the thermopower from Eq. (4) for the valence and the conduction bands closest to the Fermi level, known as the two-band model [40, 45]. It is noted that the thermopower is a linear function with the chemical potential if we only consider only one band. Thus, the contribution of two bands (valence and conduction bands) essential to get the optimum of the thermopower for the s-SWNTs. The thermopower for s-SWNTs, S_{CNT} , based on the two-band model and constant RTA, are given as a function of μ by [44]:

$$S_{\text{CNT}}(\mu) = \frac{k_B}{e} \left(\frac{\mu}{k_B T} - \frac{E_g}{2k_B T} - \frac{3}{2} + \frac{E_g/k_B T + 3}{e^{2\mu/k_B T} + 1} \right). \quad (5)$$

is the energy gap E_g . In Fig. 8, we show analytical results of Eq. (5) in the lines using the values of E_g from the ETB calculation. The analytical results deviate from the numerical results for large $|\mu|$ because the two-band model is no longer valid at a higher doping level. To describe the optimum thermopower of s-SWNTs which appear near $\mu = 0$.

We can determine a chemical potential μ_{opt} by taking $dS_{\text{CNT}}(\mu)/d\mu = 0$ for Eq. 5 as follows

$$\mu_{\text{opt}} = \frac{k_B T}{2} \ln \left(\frac{E_g}{k_B T} + 2 \pm \sqrt{\left(\frac{E_g}{k_B T} + 2 \right)^2 - 1} \right)$$

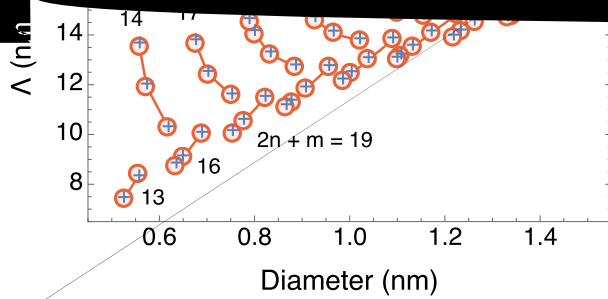
μ_{opt} values will move away from $\mu = 0$ as E_g becomes larger than $k_B T$. However, due to the presence of the logarithmic function, μ_{opt} is a slowly increasing function of E_g when E_g is much larger than $k_B T$. For example, for the range of d_t of 0.5–1.5 nm, the s-SWNTs have E_g values 0.46–1.58 eV. In this case, the E_g values are much larger than $k_B T$ for $T = 300$ K. For those E_g values, we obtain $0.046 < |\mu_{\text{opt}}| < 0.062$ eV for $T = 300$ K, which implies that the change in μ_{opt} (~ 16 meV) can be negligibly small compared with the width of $S(\mu)$ (~ 50 meV) as shown in Fig. 8. Thus at the room temperature, controlling the doping level or the chemical potential is important to obtain the optimum S for the even bundled s-SWNTs.

3.4 Calculating the optimum thermopower

Using both the numerical calculation by BoltzTraP and our analytical formula $S_{\text{CNT}}^{\text{opt}} \equiv S_{\text{CNT}}(\mu = \mu_{\text{opt}})$ as a function of d_t for s-SWNTs. In Fig. 9, we plot (a) $S_{\text{CNT}}^{\text{opt}}$ and (b) energy gap E_g as a function of d_t for $0.5 \leq d_t \leq 1.5$ nm. In Fig. 9a, we plot $S_{\text{CNT}}^{\text{opt}}$ calculated by both numerical BoltzTraP results (denoted by circles) and the analytical formula (plus symbols), from which we can see that the two methods give almost the same values of S . Thus, we will adopt the analytical formula for discussing the chirality dependence of S by

with decreasing d_i or with increasing family number [22] $2n + 1$. The power can reach a value much larger than those found in [46–49]. Thus, we can consider the

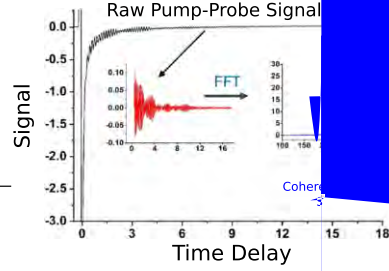
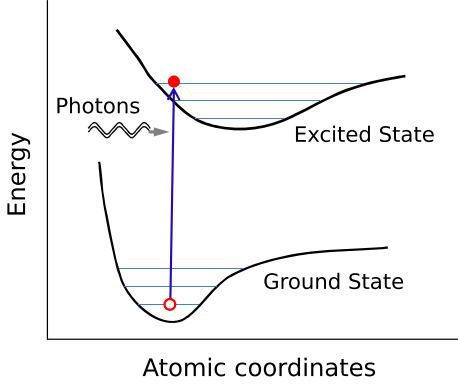
fact that $E_g \propto 1/d_i$ [22]. This also enhances the power of the NTs as a



Ultra-fast pump-probe spectroscopy is a useful tool for studying carrier and lattice dynamics in materials, since we can probe the physical properties on the same time scale as the relevant relaxation process. When ultra-short pump pulse of light is applied to a SWNT sample with a time duration less than a period of a phonon mode of the SWNT, all phonons start to oscillate with the same phase, which are known as the coherent phonon (CP) [51–55]. The CP is explained quantum mechanically in terms of coherent states, in which the amplitude-phase uncertainty reaches its minimum value [56–59]. Due to the coherent oscillations of phonons, macroscopic optical properties such as the reflectance R , transmittance T , or absorption coefficient α is modulated as a function of the time of the probe light, which is measured in CP spectroscopy.

Recently, by using sub-10-fs laser pulses, more than ten CP modes with frequency around $100\text{--}3000\text{ cm}^{-1}$ could be observed in a (6, 5) enriched SWNT sample [60]. This measurement has opened up possibilities to utilize a particular CP mode of the SWNT for ultra-sensitive, mechanical detection [61], as well as quantum information science [62, 63] in the THz region. However, we have to excite a single phonon mode coherently while suppressing other phonon modes, which is not possible to achieve by using only a single laser pulse.

One possible technique to selectively excite a particular phonon mode is by using repeated pulses of pump light in pump-probe spectroscopy. Kim et al. have shown that multiple pulses with different repetition rates can be generated by a pulse shaping technique to excite a radial breathing mode (RBM) of a specific SWNT in a bundled SWNT sample [13]. The bundled SWNT sample consists of several $(n, m$



$\Delta T/T$ from the monotonically changing term, we take the Fourier transform of $\Delta T/T$ to obtain the power spectrum, which is called the CP spectra.

In order to start all phonon oscillations at the same time with the same phase, it is necessary for the pulse width τ_p in time to be sufficiently short compared with a phonon period. For example, to generate coherent RBM phonons (5 THz), τ_p should be shorter than 200 fs. As for the G band (~ 47 THz), the τ_p should be shorter than 20 fs. It is the reason why they used a sub-10-fs pump to observe the G band and even the G' band (2700 cm^{-1}) [60].

The coherent phonons amplitude Q_m satisfies a driven oscillator equation defined by [12]

$$\frac{\partial^2 Q_v(t)}{\partial t^2} + \omega_v^2 Q_v(t) = S_m(t), \quad (9)$$

where v denotes the phonon mode and ω_v is frequency of the v -th phonon mode at phonon wavevector $q = 0$. The right hand side of Eq. 9 is the force generated by photoexcited carriers, which is given by

$$S_v(t) = -\frac{2\omega_v}{\hbar} \sum_{nk} \mathcal{M}_n^v(k) [f_n(k, t) - f_n^0(k)], \quad (10)$$

where $f_n(k, t)$ and $f_n^0(k)$ are, respectively, the time-dependent and the initial equilibrium Fermi distribution function for electrons. Here n labels an electronic state, and k gives the electron wavevector. $\mathcal{M}_n^v(k)$ denotes the electron-phonon matrix element within in the ETB model [65]. When we consider the pulse train, the right

side of Eq. (9) becomes a sum of S_ν of each pulse with the delays of the repetition time.

In the calculation of CP spectra, we calculate the absorption coefficient $\alpha(E_{\text{probe}}, \Delta t)$ as a function of the probe energy E_{probe} and Δt and the square of $\alpha(E_{\text{probe}}, \Delta t)$ is equivalent to $\Delta R/R$ or $\Delta T/T$ in the experiment. We can calculate $\alpha(E_L, \Delta t)$ using Fermi's golden rule [66] in which we take account of the time variation of the band structure within adiabatic approximation for given Q_m and carrier distribution functions in the ETB model [12, 67]. The modulation of absorption coefficient observed by the probe is given by

$$\Delta\alpha(E_{\text{probe}}, \Delta t) = -[\alpha(E_{\text{probe}}, \Delta t) - \alpha(E_{\text{probe}}, -\infty)], \quad (11)$$

where $t = -\infty$ denotes the condition when pump pulse is absent. Taking the Fourier transform of



important for understanding the alternating degeneracy of energy levels in a SWNT quantum dot, which is the subject of this subsection.

Figure 13a, b show the calculated energy bands near the K and K' valleys, respectively, for four different chiralities of m-SWNTs [15], in which the curvature induced energy gap are seen except for (4, 4) and (6, 6) armchair SWNTs. In particular, it is important to note that the absolute value of two slopes for linear energy bands (or the group velocities) for left- and right-going waves in the same valley are different from each other for the (4, 4) armchair nanotube, while the slopes are the same for the (9, 0) zigzag nanotube. The group velocities in the τ valley ($\tau = K, K'$) are defined by

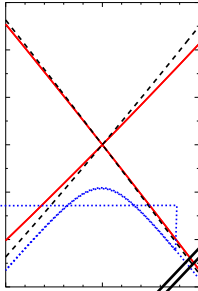
$$v_L^{(\tau)} = -\frac{1}{\hbar} \frac{\partial \varepsilon_L^{(\tau)}}{\partial k} (> 0), \quad v_R^{(\tau)} = \frac{1}{\hbar} \frac{\partial \varepsilon_R^{(\tau)}}{\partial k} (> 0), \quad (12)$$

where $\varepsilon_L^{(\tau)}$ ($\varepsilon_R^{(\tau)}$) is the energy as a function of the wavenumber k of the left-going (right-going) wave in the τ valley, which has negative (positive) slope. It is noted that the relation $v_L^{(\tau)} = v_R^{(-\tau)}$ holds because of the time reversal symmetry. Hereafter, we put an integer value for $\tau = 1$ (-1) for K (K') for convenience. The velocities estimated in the linear dispersion region are plotted in Fig. 13c, d. The velocity difference between the left- and right-going waves becomes larger for the smaller diameter and near the armchair chirality. Using a perturbation theory with respect to the curvature, we fitted the group velocities to the following expressions [15],

$$v_L^{(\tau)} = v_{av} - \tau \Delta v, \quad v_R^{(\tau)} = v_{av} + \tau \Delta v, \quad (13)$$

where

$$v_{av} = v_0 + \frac{c_2 + c_4 \cos 6\theta}{d_t^2}, \quad \Delta v = \frac{c_3 \sin 3\theta}{d_t^2}, \quad (14)$$



with $c_2 = -2.46$, $c_4 = 1.27$ and $c_6 = -2.45$ in units of 10^4 (m/s)·nm² and $v_0 = 8.32 \times 10^5$ m/s for the diameter region of $0.6 < d_t < 2.0$ nm.

Since the electrons are confined in the direction of the nanotube axis for a finite length SWNT (or simply called SWNT quantum dot), the discrete energy levels represent the standing wave consisting of left and right going waves. There are two possible couplings of left and right going waves, that is, left and right going waves within the same valley or in different valleys in the k space, which we call intravalley or intervalley coupling, respectively (see Fig. 14c). In the case of the intervalley coupling, in which the standing wave as the eigenstate are formed from the left-going wave at one valley and the right-going wave at *another valley*, there exist two inequivalent series of equispaced discrete energy levels, whose separations are given by $\hbar v_L^{(K)} \pi / L_{\text{NT}}$ and $\hbar v_R^{(K)} \pi / L_{\text{NT}}$, reflecting the asymmetric velocities (see Fig. 14a, c). However, the conventional picture only adopts the intravalley scattering, in which the standing wave is made of the left- and right-going waves in the *same valley* (see Fig. 14b, c) which gives two identical series of energy levels. The conventional picture explains the observation of the four fold degeneracy of the energy levels, reflecting the two valley states with two spin states, with a small lift of degeneracy by the spin-orbit interaction. However, recent experiments show oscillating behavior of the two fold and four fold degeneracies within the same SWNT [75–80] as a function of energy, which suggests that we must consider the intervalley scattering at both ends.

In order to consider the intervalley interaction, let us assume that both ends of a finite-length SWNT do not break the rotational symmetry C_d of SWNTs around the nanotube axis where d is the greatest common divisor, $d = \text{gcd}(n, m)$. Then we can use the conservation of angular momentum along the nanotube axis, L_μ . When the energy states belong to different L_μ 's, they are not coupled to each other, whereas the states with the same angular momentum are coupled with each other. It is known that a 1-D cutting line (or 1-D Brillouin zone) in the k -space corresponds to a L_μ [1, 81]. As far as we discuss the angular momentum from $L_\mu = 0$ to $d - 1$, it is convenient to adopt the long cutting lines [81], in which there are d ($L_\mu = 0, \dots, d - 1$) cutting lines, instead of the conventional N short cutting lines [1]. When we classified all (n, m) SWNTs, 80% of the SWNTs are classified

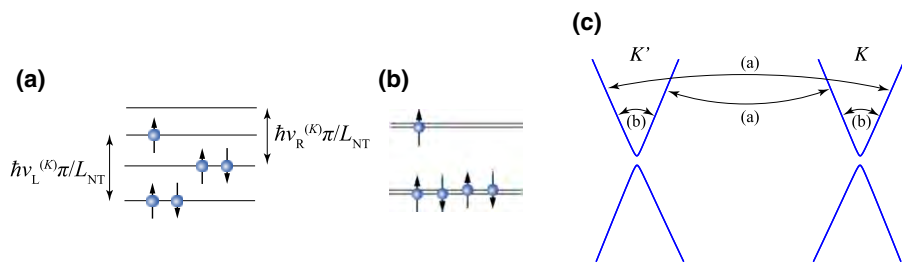


Fig. 14 Schematics of energy levels for two different cases, **a** strong coupling of two valleys (intervalley couplings), and **b** decoupling of two valleys (intravalley coupling). Two different combinations of traveling waves in the standing waves for the cases of **a** intervalley and **b** intravalley couplings

into either metal-2 m-SWNT [82] or $d = 1$ and $d = 2$ s-SWNTs. The intervalley coupling occurs when the K and K' valley states belong to the same L_μ , which corresponds to the cases of (1) $L_\mu = 0$ for metal-2 and $d = 1$ s-SWNTs, and (2) $L_\mu = 1$ for $d = 2$ s-SWNTs [16]

It should be mentioned that this behavior was considered as extrinsic factors such as impurities and defects, which might induce the intervalley valley coupling, too.

In Fig. 15d we show slightly modified the boundary shape from Fig. 15a, by removing the Klein edged carbon atom at the foot of z axis. The corresponding energy levels have nearly four fold degeneracy as shown in Fig. 15e, f, which is completely different behavior than (b) and (c) by removing just one atom. The four fold degeneracy occurs by the weakened intervalley coupling by the edge shape effect. Thus the shapes of edges are very sensitive to the occurrence of degeneracy, which makes the problem difficult.

In order to study the edge effect microscopically, it is useful to project total Hamiltonian to subHamiltonian with the angular momentum [83]. The Hamiltonian is decomposed into a projected Hamiltonian for L_μ -th angular momentum, L_μ , $H = \sum_{L_\mu} H_{L_\mu}$. By extracting a relevant H_{L_μ} , one gets an effective 1-D lattice model, whose detail is given in the reference [83]. The calculated results show that, in the low energy region near the Fermi energy, H_{L_μ} contains the evanescent modes of wavefunction for the edge state in which the wavefunctions of the edge state are localized at either the left or the right ends and either at the A sublattice or the B sublattice. The numbers of these modes are given as a function of (n, m) [16, 83, 84]. For example, the number of evanescent modes at the left boundary localized at either the A or B sublattice is given by $N_A^{\text{ev}} = 5$ and $N_B^{\text{ev}} = 4$ for (7, 4) nanotubes. Combining with the two delocalized states at K or K' valleys for each sublattice, there exist $N_A^{\text{ev}} + 2$ and $N_B^{\text{ev}} + 2$ independent modes for the A and B sublattices, respectively.

The eigenfunction of each sublattice is given by the linear combination of these modes. If the number of the boundary condition for $P = \text{A or B}$ sublattice, N_P^{bc} , is equal to or larger than that of the independent modes, all the coefficients in the eigenfunction should be zero. For this case, we have the fixed boundary condition for the envelope function $g_{P\tau}(\ell) \propto \sin(k\ell)$, which corresponds to the conventional standing wave. Since $1/|k|$ is much longer than the lattice constant, the standing wave is formed within the same valley. Strictly speaking, the localized modes at the A sublattice have a non-zero amplitude at the B sublattice, which makes the weak intervalley coupling. This corresponds to the case of the Fig. 15d, in which the number of boundary conditions for A sublattice $N_A^{\text{bc}} = 7$, which is the number of empty site in A sublattice in Fig. 15d, is equal to that of the independent mode number, $N_A^{\text{ev}} + 2$. On the other hand, for the case of Fig. 15a, there is no fixed boundary condition for the envelope functions since $N_P^{\text{ev}} + 2 = N_P^{\text{bc}} + 1 > N_P^{\text{bc}}$. Furthermore, it is shown that the strong intervalley coupling occurs to construct the standing wave in the region of linear energy dispersion [16, 83].

Finally, let us briefly discuss the edge states in the energy gap region, which are indicated by the red lines in Fig. 15b, e. It is straightforward to apply the above analysis to count the number of edge states, by subtracting the number of boundary conditions from the number of independent evanescent modes [83]. For the case of Fig. 15a, as an example, the number of evanescent modes and that of the boundary conditions for the B sublattice are given by $N_B^{\text{ev}} = 6$ (in the energy gap region) and $N_B^{\text{bc}} = 5$, respectively. Therefore, the number of edge states per spin and per

boundary is given by $N_B^{\text{edge}} = 1$, which is consistent with the numerical result shown in Fig. 15b.

It is interesting and surprising for us to show that the winding number w_{L_μ} as a topological invariant defined in the bulk materials is equal to the number of edge states [16]. The winding number is an integer to count the phase integration divided by 2π in the k -space for the off-diagonal part of the Hamiltonian matrix defined by,

$$w_{L_\mu} = \frac{1}{2\pi} \int_0^{2\pi} dk \frac{\partial \arg \langle AkL_\mu | H_{L_\mu} | BkL_\mu \rangle}{\partial k}. \quad (15)$$

where $|PkL_\mu\rangle$ is the Bloch state of the P sublattice. By using the theorem known as Cauchy's argument principle in the complex analysis, the number of edge states is the same as the winding number, which is proven in our recent work [16]. The winding number in the bulk materials is redefined to consider the orthogonal boundary condition, which gives the number of edge states in the finite size [16]. The bulk-edge correspondence reveals another new concept of SWNTs as topological materials. In future experiments, it would be required to measure the electronic states not only by tunneling spectroscopy with contacting electrodes but also by the scanning tunneling spectroscopy for detecting the evanescent wave of the wavefunction without disturbing the edge shape of SWNT.

A w l m R.S. acknowledges JSPS KAKENHI Grant Numbers JP25286005 and JP225107005. W.I. acknowledges JSPS KAKENHI Grant Numbers JP15K05118, JP16H01046 and JP15KK0147. A.R.T.N. and N.T.H. acknowledges the Interdepartmental Doctoral Degree Program for Material Science Leaders at Tohoku University. E.H.H. acknowledges the MEXT scholarship.

R


1. Saito R, Dresselhaus G, Dresselhaus MS (1998) Physical properties of carbon nanotubes. Imperial College Press, London
2. Saito R, Fujita M, Dresselhaus G, Dresselhaus MS (1992) Phys Rev B 46:1804
3. Saito R, Fujita M, Dresselhaus G, Dresselhaus MS (1992) Appl Phys Lett 60:2204
4. Farhat H, Berciaud S, Kalbac M, Saito R, Heinz TF, Dresselhaus MS, Kong J (2011) Phys Rev Lett 107:157401
5. Hasdeo EH, Nugraha ART, Sato K, Dresselhaus MS, Saito R (2013) Phys Rev B 88:115107
6. Saito R, Sato K, Araujo P, Mafra D, Dresselhaus M (2013) Solid State Commun 175–176:18
7. Hicks LD, Dresselhaus MS (1993) Phys Rev B 47:12727
8. Hicks LD, Dresselhaus MS (1993) Phys Rev B 47:16631
9. Dresselhaus MS, Chen G, Tang MY, Yang RG, Lee H, Wang DZ, Ren ZF, Fleurial JP, Gogna P (2007) Adv Mater 19:1043
10. Boukai AI, Bunimovich Y, Tahir-Kheli J, Yu J, Goddard WA III, Heath JR (2008) Nature 451:168
11. Hung NT, Hasdeo EH, Nugraha ART, Dresselhaus MS, Saito R (2016) Phys Rev Lett 117:036602
12. Kim JH, Nugraha ART, Booshehri LG, Haroz EH, Sato K, Sanders GD, Yee KJ, Lim YS, Stanton CJ, Saito R, Kono J (2013) Chem Phys 413:55
13. Kim JH, Han KJ, Kim NJ, Yee KJ, Lim YS, Sanders GD, Stanton CJ, Booshehri LG, Házor EH, Kono J (2009) Phys Rev Lett 102:037402
14. Laird EA, Kuemmeth F, Steele GA, Grove-Rasmussen K, Nygård J, Flensberg K, Kouwenhoven LP (2015) Rev Mod Phys 87:703
15. Izumida W, Vikström A, Saito R (2012) Phys Rev B 85:165430
16. Izumida W, Okuyama R, Yamakage A, Saito R (2016) Phys Rev B 93:195442

17. Brown SDM, Jorio A, Corio P, Dresselhaus MS, Dresselhaus G, Saito R, Kneipp K (2001) *Phys Rev B* 63:155414
18. Rao AM, Eklund PC, Bandow S, Thess A, Smalley RE (1997) *Nature (London)* 388:257
19. Pimenta MA, Marucci A, Empedocles S, Bawendi M, Hanlon EB, Rao AM, Eklund PC, Smalley RE, Dresselhaus G, Dresselhaus MS (1998) *Phys Rev B Rapid* 58:R16016
20. Kataura H, Kumazawa Y, Maniwa Y, Umezū I, Suzuki S, Ohtsuka Y, Achiba Y (1999) *Synth Metals* 103:2555
21. Alvarez L, Righi A, Rols S, Anglaret E, Sauvajol JL (2000) *Chem Phys Lett* 320:441
22. Saito R, Dresselhaus G, Dresselhaus MS (2000) *Phys Rev B* 61:2981
23. Fano U (1961) *Phys Rev* 124:1866
24. Alvarez L, Righi A, Guillard T, Rols S, Anglaret E, Laplaze D, Sauvajol J (2000) *Chem Phys Lett* 316:186
25. Eklund PC, Dresselhaus G, Dresselhaus MS, Fischer JE (1977) *Phys Rev B* 16:3330
26. Solin S (1977) *Mater Sci Eng* 31:153
27. Yoon D, Jeong D, Lee H, Saito R, Son Y, Lee H, Cheong H (2013) *Carbon* 61:373
28. Lazzeri M, Piscanec S, Mauri F, Ferrari AC, Robertson J (2006) *Phys Rev B* 73:155426
29. Wu Y, Maultzsch J, Knoesel E, Chandra B, Huang M, Sfeir MY, Brus LE, Hone J, Heinz TF (2007) *Phys Rev Lett* 99:027402
30. Bose SM, Gayen S, Behera SN (2005) *Phys Rev B* 72:153402
31. Jiang C, Kempa K, Zhao J, Schlecht U, Kolb U, Basché T, Burghard M, Mews A (2002) *Phys Rev B* 66:161404
32. Kempa K (2002) *Phys Rev B* 66:195406
33. Ando T (2008) *J Phys Soc Japan* 77:014707
34. Zhang D, Yang J, Hasdeo EH, Liu C, Liu K, Saito R, Li Y (2016) *Phys Rev B* 93:245428
35. Zhang D, Yang J, Li M, Li Y (2016) *ACS Nano* 10(12):10789. doi:[10.1021/acsnano.6b04453](https://doi.org/10.1021/acsnano.6b04453)
36. Hone J, Ellwood I, Munro M, Mizel A, Cohen ML, Zettl A, Rinzler AG, Smalley RE (1998) *Phys Rev Lett* 80:1042
37. Hone J, Llaguno MC, Nemes NM, Johnson AT, Fischer JE, Walters DA, Casavant MJ, Schmidt J, Smalley RE (2000) *Appl Phys Lett* 77:666
38. Yanagi K, Kanda S, Oshima Y, Kitamura Y, Kawai H, Yamamoto T, Takenobu T, Nakai Y, Maniwa Y (2014) *Nano Lett* 14:6437
39. Romero HE, Sumanasekera GU, Mahan GD, Eklund PC (2002) *Phys Rev B* 65:205410
40. Goldsmid HJ, Sharp JW (1999) *J Electron Mater* 28:869
41. Madsen GKH, Singh DJ (2006) *Comput Phys Commun* 175:67
42. Samsonidze GG, Saito R, Kobayashi N, Grüneis A, Jiang J, Jorio A, Chou SG, Dresselhaus G, Dresselhaus MS (2004) *Appl Phys Lett* 85:5703
43. Popov VN (2004) *New J Phys* 6:17
44. Hung NT, Nugraha ART, Hasdeo EH, Dresselhaus MS, Saito R (2015) *Phys Rev B* 92(16):165426
45. Goldsmid HJ (2010) *Introduction to thermoelectricity*. Springer, Berlin
46. Boukai AI, Bunimovich Y, Tahir-Kheli J, Yu JK, Goddard Iii WA, Heath JR (2008) *Nature* 451:168
47. Hochbaum AI, Chen R, Delgado RD, Liang W, Garnett EC, Najarian M, Majumdar A, Yang P (2008) *Nature* 451:163
48. Poudel B, Hao Q, Ma Y, Lan Y, Minnich A, Yu B, Yan X, Wang D, Muto A, Vashaee D, Chen X, Liu J, Dresselhaus MS, Chen G, Ren Z (2008) *Science* 320:634
49. Pei Y, Shi X, LaLonde A, Wang H, Chen L, Snyder GJ (2011) *Nature* 473:66
50. Weisman RB, Bachilo SM (2003) *Nano Lett* 3:1235
51. Dumitrică T, Garcia ME, Jeschke HO, Yakobson BI (2004) *Phys Rev Lett* 92:117401
52. Gambetta A, Manzoni C, Menna E, Meneghetti M, Cerullo G, Lanzani G, Tretiak S, Piryatinski A, Saxena A, Martin RL, Bishop AR (2006) *Nat Phys* 2:515
53. Lim YS, Yee KJ, Kim JH, Haroz EH, Shaver J, Kono J, Doorn SK, Hauge RH, Smalley RE (2006) *Nano Lett* 6:2696
54. Lüer L, Gadermaier C, Crochet J, Hertel T, Brida D, Lanzani G (2009) *Phys Rev Lett* 102:127401
55. Makino K, Hirano A, Shiraki K, Maeda Y, Hase M (2009) *Phys Rev B* 80:245428
56. Zeiger HJ, Vidal J, Cheng TK, Ippen EP, Dresselhaus G, Dresselhaus MS (1992) *Phys Rev B* 45:768
57. Kuznetsov AV, Stanton CJ (1994) *Phys Rev Lett* 73:3243
58. Hu X, Nori F (1996) *Phys Rev B* 53:2419
59. Merlin R (1997) *Solid State Commun* 102:207

60. Lim YS, Nugraha ART, Cho SJ, Noh MY, Yoon EJ, Liu H, Kim JH, Telg H, Hroz EH, Sanders GD, Baik SH, Kataura H, Doorn SK, Stanton CJ, Saito R, Kono J, Joo T (2014) *Nano Lett* 14:1426
61. Eichler A, Moser J, Chaste J, Zdrojek M, Wilson-Rae I, Bachtold A (2011) *Nat Nanotechnol* 6:339
62. Ruskov R, Tahan C (2012) *JPCS* 398:012011
63. Li JJ, Zhu KD (2012) *Sci Rep* 2:903
64. Saito R, Takeya T, Kimura T, Dresselhaus G, Dresselhaus MS (1998) *Phys Rev B* 57:4145
65. Jiang J, Saito R, Samsonidze GG, Chou SG, Jorio A, Dresselhaus G, Dresselhaus MS (2005) *Phys Rev B* 72:235408
66. Chuang SL (1995) *Physics of optoelectronic devices*. Wiley, New York
67. Nugraha ART, Hasdeo EH, Sanders GD, Stanton CJ, Saito R (2015) *Phys Rev B* 91:045406
68. Hamada N, Sawada SI, Oshiyama A (1992) *Phys Rev Lett* 68:1579
69. Kane CL, Mele EJ (1997) *Phys Rev Lett* 78:1932
70. Ando T (2000) *J Phys Soc Japan* 69:1757
71. Chico L, Lopez-Sancho MP, Munoz MC (2004) *Phys Rev Lett* 93:176402
72. Izumida W, Sato K, Saito R (2009) *J Phys Soc Japan* 78:074707
73. Chico L, López-Sancho MP, Muñoz MC (2009) *Phys Rev B* 79(23):235423
74. Jeong JS, Lee HW (2009) *Phys Rev B* 80(7):075409
75. Maki H, Ishiwata Y, Suzuki M, Ishibashi K (2005) *Jpn J Appl Phys* 44:4269
76. Makarovski A, An L, Liu J, Finkelstein G (2006) *Phys Rev B* 74:155431
77. Moriyama S, Fuse T, Ishibashi K (2007) *Phys Stat Sol B* 244:2371
78. Holm JV, Jørgensen HI, Grove-Rasmussen K, Paaske J, Flensberg K, Lindelof PE (2008) *Phys Rev B* 77:161406(R)
79. Schmid DR, Smirnov S, Margańska M, Dirnaichner A, Stiller PL, Grifoni M, Hüttel AK, Strunk C (2015) *Phys Rev B* 91:155435
80. Ferrier M, Arakawa T, Hata T, Fujiwara R, Delagrangé R, Weil R, Deblock R, Sakano R, Oguri A, Kobayashi K (2016) *Nat Phys* 12(3):230
81. White CT, Robertson DH, Mintmire JW (1993) *Phys Rev B* 47:5485
82. Saito R, Sato K, Oyama Y, Jiang J, Samsonidze GG, Dresselhaus G, Dresselhaus MS (2005) *Phys Rev B* 72:153413
83. Izumida W, Okuyama R, Saito R (2015) *Phys Rev B* 91:235442
84. Akhmerov AR, Beenakker CWJ (2008) *Phys Rev B* 77:085423



Review of Electronics Based on Single-Walled Carbon Nanotubes

Yu Cao¹ · Sen Cong¹ · Xuan Cao² · Fanqi Wu² · Qingzhou Liu² · Moh. R. Amer^{3,4} · Chongwu Zhou¹ 

Received: 6 March 2017 / Accepted: 11 July 2017 / Published online: 14 August 2017
Springer International Publishing AG 2017

Abstract Single-walled carbon nanotubes (SWNTs) are extremely promising materials for building next-generation electronics due to their unique physical and electronic properties. In this article, we will review the research efforts and achievements of SWNTs in three electronic fields, namely analog radio-frequency electronics, digital electronics, and macroelectronics. In each SWNT-based electronic field, we will present the major challenges, the evolutions of the methods to overcome these challenges, and the state-of-the-art of the achievements. At last, we will discuss future directions which could lead to the broad applications of SWNTs. We hope this review could inspire more research on SWNT-based electronics, and accelerate the applications of SWNTs.

Keywords Single-walled carbon nanotubes · Radio-frequency electronics · Digital electronics · Macroelectronics

Chapter 7 was originally published as Cao, Y., Cong, S. Cao, X., Wu, F. Liu, Q., Amer, M. R. & Zhou, C. Top Curr Chem (Z) (2017) 375: 75. DOI 10.1007/s41061-017-0160-5.

✉ Chongwu Zhou
chongwuz@usc.edu

¹ Department of Electrical Engineering, University of Southern California, Los Angeles, CA 90089, USA

² Department of Chemical Engineering and Materials Science, University of Southern California, Los Angeles, CA 90089, USA

³ Center of Excellence for Green Nanotechnologies, Joint Centers of Excellence Program, King Abdulaziz City for Science and Technology, P. O. Box 6086, Riyadh 11442, Saudi Arabia

⁴ Department of Electrical Engineering, University of California, Los Angeles, 420 Westwood Plaza, 5412 Boelter Hall, Los Angeles, CA 90095, USA

1 Introduction

In the past one and a half decades, continued downscaling of complementary metal–oxide–semiconductor (CMOS) technology toward nanoscale dimensions (e.g. sub-14-nm technology nodes) has been enabled by tremendous research breakthroughs and engineering innovations, such as the introduction of strained silicon channels, implementing high- κ /metal-gate dielectric stacks, and the use of non-planar transistor structures such as double-gate and fin field-effect transistors (FinFETs). Scaling beyond the silicon roadmap has generated much interest in the research of low-dimensional [i.e. one-dimensional (1D) and two-dimensional (2D)] electronic systems, the synthesis of nanomaterials, and the fabrication of nanoscale electronic devices. Low-dimensional nanomaterials have the desired scaling potential and also provide access to novel physical phenomena that results in unique electronic properties with exceptional transport characteristics that can enable future high-speed and low-power applications. In addition, low-dimensional materials bring new opportunities for flexible and portable electronics due to their ultrathin thickness. Single-walled carbon nanotubes (SWNTs) are the most prominent representatives of 1D nanomaterials. SWNTs, with diameters ranging between 1 and 3 nm, have chirality-dependent properties. Of particular interest, semiconducting SWNTs have shown to exhibit high mobility, high current-carrying capability, small intrinsic capacitance, and extraordinary thermal and mechanical properties [1–5]. Owing to their unique properties, SWNTs have been widely investigated as the channel materials for radio-frequency (RF) electronics, digital electronics, and macroelectronics.

In the application of RF electronics, researchers have devoted a majority of their efforts to improving the RF performance of SWNT transistors [6–18]. Different device structures, channel length scaling, and key SWNT parameters, such as diameter, semiconducting purity, and alignment, have all been investigated. The milestone came in 2016 when SWNT RF transistors with cut-off frequencies greater than 70 GHz were reported [11]. In addition, the linearity performance of these SWNT RF transistors has also been characterized [8, 11, 13, 14, 17–20]. Moreover, circuits (e.g. mixers and frequency doublers) [14, 16, 21] and systems (e.g. radio receivers) [4, 22, 23] based on SWNT RF transistors have also been demonstrated by several research groups.

In the application of digital electronics, significant progress has been achieved experimentally. SWNT-based digital systems are theoretically proven to have more than one order of magnitude higher energy-delay product in comparison with Si-based complementary metal–oxide–semiconductor (CMOS) technologies [24]. Field-effect transistors (FETs) based on a single nanotube [2, 5, 25–31] and aligned nanotube arrays [32–35] have all been fabricated and characterized, showing the tremendous potential for building future energy-efficient digital systems. SWNT FETs have also been further optimized in regard to nanotube alignment, dielectrics, and metal contact, and the channel length scaling of these transistors has been investigated systematically. Moreover, various methods to achieve n-type SWNT FETs have been developed, and complementary operations of SWNT FETs have

been demonstrated [36–43]. With the advancement in the transistor performance, both SWNT digital circuits and systems, e.g. central processing units (CPUs), have been demonstrated [35], and three-dimensional (3D) integration of SWNT digital electronics to achieve higher transistor density and more logic functions per area have been under active investigation [44–47].

In the application of macroelectronics, SWNT networks are considered as excellent materials for thin-film transistors (TFTs) due to their superior electrical performance, reliability, flexibility, and transparency [48–61]. A variety of methods to achieve pure, high-density, high-semiconducting, and highly uniform SWNT networks have been developed [48–50, 52, 54, 56, 62–73]. TFTs have been fabricated based on these SWNT networks on both rigid and flexible substrates and have been demonstrated to drive various displays and sensors [55–57, 74–76], and even to work as building blocks for digital circuits and systems [33, 48, 53, 68, 71, 77–82]. In addition, the application of SWNTs has extended into printed electronics due to their printability, and has generated great impacts in achieving large-scale and low-cost macroelectronics [49, 83–89].

In this review, we will discuss all the significant progress in the development of SWNT-based electronics, including SWNT-based RF electronics, SWNT-based digital electronics, and SWNT-based macroelectronics, including printed electronics. In the last part, further development of SWNT-based electronics will be discussed.

2 SWNT RF Electronics

The extraordinary properties of SWNTs, such as nanoscale size, high mobility, small intrinsic capacitance, and high current-carrying capability, make SWNTs one of the excellent materials for RF electronics [1–5]. In this research field, the majority of the efforts are devoted to improving the current gain cut-off frequency (f_t) and the maximum oscillation frequency (f_{max}) of SWNT RF transistors which are important for future circuit-level applications [6–18]. Recently, the RF performance of SWNT transistors has been advanced to 70 GHz which is ready for practical applications [11].

2.1 SWNT RF Transistors Based on CVD-Aligned Nanotubes

Arrays of aligned SWNTs are one existing form of the nanotubes used as the channel materials for RF transistors [10, 14–16]. Chemical vapor deposition (CVD) is a widely used method to produce aligned SWNT arrays [10, 90–92]. The density of such aligned nanotube arrays can be as high as 130 nanotubes/ μm by carefully engineering the catalyst and controlling the synthesis conditions [10]. The CVD-synthesized SWNT arrays are a mixture of semiconducting and metallic nanotubes, and the semiconducting purity of such CVD-aligned SWNT with high density is usually $\sim 60\%$. However, these nanotube arrays can be directly used for RF transistors. Unlike digital electronics which require an extremely high current on/off ratio, a high current on/off ratio is not a necessity for RF electronics.

Kocabas et al. are one group of pioneers who reported SWNT RF transistors based on CVD-aligned SWNTs [15]. Figure 1a presents their schematic cross-sectional illustration of the SWNT RF transistor layout. The density of the CVD-aligned SWNTs is 2–5 nanotubes/ μm , and the channel length (L) is 700 nm. Their device layout, which utilizes a double-channel configuration (two gate electrodes and two drain electrodes surrounding a drain electrode), is one of the two commonly used device structures for SWNT RF electronics. However, the drawback of this device structure is that there exist either un-gated channel regions or overlapped gate-to-source/drain regions which adversely affect the RF performance. Figure 1b

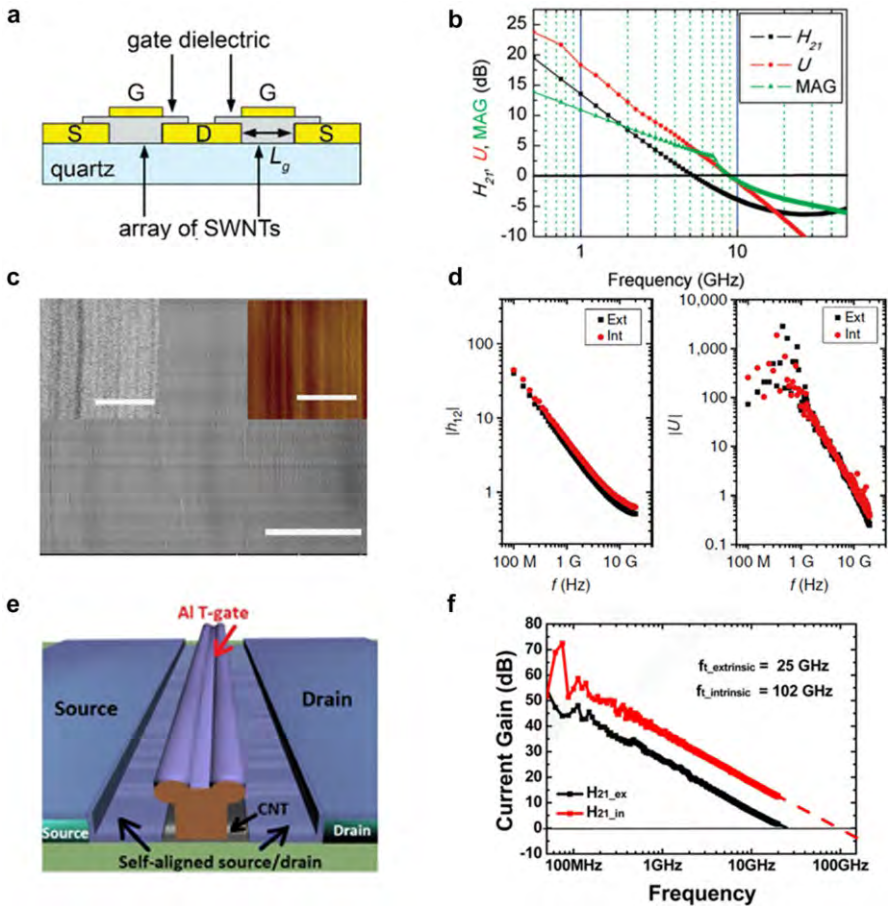


Fig. 1 a, b Schematic cross-sectional illustration of the SWNT RF transistors, and the corresponding frequency response, respectively. Adapted with permission from Ref. [15]. Copyright (2009) American Chemical Society. c, d SEM and AFM images of the high-density SWNT arrays on a sapphire surface, and the corresponding frequency response of the transistors based on these high-density aligned SWNTs, respectively. Adapted with permission from Ref. [10]. Copyright (2015) Nature Publishing Group. e, f Schematic of the CVD-aligned SWNT RF transistor with the self-aligned, self-oxidized, aluminum,

shows the RF performance of their SWNT RF transistor. According to the current gain (H_{21}), unilateral power gain (U), and maximum available gain (MAG) frequency response between 0.5 and 50 GHz, the f_t , which is the unity current gain frequency, and the f_{\max} , which is the unity power gain frequency, are ~ 5 and ~ 9 GHz, respectively.

One method to improve the RF transistors based on CVD-aligned SWNTs is to increase the SWNT density. Hu et al. successfully achieved SWNT arrays with a density of 130 nanotubes/ μm by using a Trojan catalyst [10]. Figure 1c shows SEM and AFM images of the as-grown high-density SWNT arrays on a sapphire surface. The RF performance of a typical SWNT transistor based on the high-density nanotube arrays with $L = 1200$ nm is shown in Fig. 1d. The extrinsic f_t and f_{\max} are 5 and 11 GHz, respectively. The intrinsic f_t and f_{\max} after device de-embedding, which would remove only the parasitics from the bonding pads without removing the capacitances associated with the gate, and reveal the performance of RF transistors achievable for practical applications, is 7 and 14 GHz, respectively. These RF transistors have similar device structure and RF performance as those reported by Kocabas et al. [15] but with a much larger channel length, indicating that one can achieve better RF performance by increasing the aligned nanotube density.

Another method to improve the RF transistors based on CVD-aligned SWNTs is to use a self-aligned gate structure. A self-aligned, self-oxidized, aluminum, T-shaped gate structure has been developed, as is shown in Fig. 1e [14]. This self-aligned, self-oxidized, aluminum, T-shaped gate structure has the advantages of reducing the gate parasitic capacitance, decreasing the gate resistance, scaling down the channel length, and offering optimized gate control. With this gate structure, the channel length of SWNT RF transistors has been scaled down to ~ 140 nm, and the thickness of the gate dielectric (self-oxidized Al_2O_3) has been reduced to 2–4 nm. The RF performance of these CVD-aligned SWNT transistors with a nanotube density of ~ 5 nanotubes/ μm is shown in Fig. 1f. The extrinsic f_t is as high as 25 GHz, and the intrinsic f_t after intrinsic de-embedding, which would remove the parasitics from both the bonding pads and the fringe capacitances associated with

diameter distribution of SWNTs could also be engineered to achieve the optimal diameter range for RF transistors. However, unlike aligned SWNT arrays where the charge transport is electrically continuous and has an independent pathway, the charge transport in SWNT networks is based on percolation transportation. The tube-to-tube junctions will limit the maximum carrier mobility achievable, which limits both the f_t and f_{\max} of RF transistors. However, SWNT networks still provide an important platform to investigate the RF performance of SWNTs, and researchers have demonstrated RF transistors based on SWNT networks [7, 8, 13, 17, 18].

The effects of SWNT semiconducting purity and diameter distribution on the performance of RF transistors based on SWNT networks have been investigated systematically [17, 18]. Cao et al. applied the excellent self-aligned, self-oxidized, aluminum, T-shaped gate structure to a variety of SWNT networks for the investigations, as schematically shown in Fig. 2a. Figure 2b, c shows the extrinsic and intrinsic current gain frequency response and power gain frequency response of RF transistors based on SWNTs with 99.99% semiconducting purity, respectively [17]. The extrinsic f_t and f_{\max} are 22 and 19 GHz, respectively, and after device de-embedding, the intrinsic f_t and f_{\max} are 28 and 25 GHz, respectively. The RF performance is better than that based on SWNT networks with lower semiconducting purity, indicating the importance of achieving ultrahigh semiconducting purity separation of SWNTs for RF applications. In addition, Cao et al. also investigated the effects of diameter distribution [18]. Figure 2d shows the diameter-separated SWNT solution which has a tight diameter distribution and an average diameter of ~ 1.6 nm. The RF performance of these transistors based on the diameter-separated SWNTs are shown in Fig. 2e, f. The f_t and f_{\max} are 23 and

Fig. 2 **a** Schematic of the RF transistors based on SWNT networks. Adapted with permission from Ref. [18]. Copyright (2016) American Institute of Physics. **b, c** Current gain frequency response and power gain frequency response of RF transistors based on ultrahigh-purity semiconducting SWNTs, respectively. Adapted with permission from Ref. [17]. Copyright (2016) Springer. **d–f** Optical absorbance spectrum of the diameter-separated SWNTs, the current gain frequency response, and the power gain frequency response, respectively. Adapted with permission from Ref. [18]. Copyright (2016) American Institute of Physics

20 GHz before de-embedding, and are 65 and 35 GHz after intrinsic de-embedding, respectively. The RF performance is similar to that based on 99.99% ultrahigh-purity semiconducting SWNTs, indicating the necessity to achieve diameter separation for SWNT RF electronics.

We note that the superior RF performance achieved with SWNT networks even outperforms the best RF transistors based on CVD-aligned SWNTs, suggesting that SWNT networks are a valuable platform for nanotube RF electronics.

2.3 SWNT RF Transistors Based on Aligned Pre-separated SWNTs

Based on the discussions above, CVD-aligned SWNTs have the advantages of free tube-to-tube junctions and high-density while suffering from low semiconducting purity and degraded output resistance. In comparison, SWNT networks have the advantages of high semiconducting purity and engineered diameter distribution, while having the disadvantages of tube-to-tube junctions and low density. The best platform for SWNT RF transistors is to use SWNTs which go through the process of post-synthesis sorting and assembly, combining the advantages of CVD-aligned SWNTs and SWNT networks together.

Le Louarn et al. reported using a dielectrophoresis (DEP) assembly method to achieve aligned SWNTs for the RF transistors [12]. The transconductance increased by a factor of 2.5 compared with their previous work using SWNT networks, and the de-embedded f_t was 30 GHz. However, their SWNTs still suffered from a low semiconducting purity. Steiner et al. used SWNTs with a much higher semiconducting purity ($\sim 99.6\%$), and also achieved aligned SWNTs using the DEP assembly method [9]. Their RF transistors showed a big improvement for SWNT RF electronics. With a channel length of 100 nm, the extrinsic f_t and f_{\max} were 7 and 15 GHz, respectively. The intrinsic f_t and f_{\max} were 153 and 30 GHz, respectively, using an intrinsic de-embedding structure. However, the f_{\max} of the RF transistors is still far below the f_t , which limits the highest frequency of their SWNT RF transistors in practical applications since a power gain is needed for real applications.

Recently, significantly improvement of the SWNT RF transistors has been achieved by the combined use of well-aligned, ultrahigh-purity semiconducting ($>99.99\%$), high-density SWNTs and our self-aligned, self-oxidized, aluminum, T-shaped gate structure [11]. The well-aligned, ultrahigh-purity semiconducting, high-density SWNTs are achieved by dose-controlled, floating evaporative self-assembly (DFES) of poly[(9,9-dioctylfluorenyl-2,7-diyl)-*alt-co*-(6,60-(2,20-bipyridine))] (PFO-BPy) separated SWNTs. Figure 3a shows the SEM image of one channel region of a typical SWNT RF transistor. The T-shaped gate, self-aligned source and drain electrodes, and aligned PFO-BPy-sorted SWNTs underneath are clearly demonstrated. The RF performance of these SWNT RF transistors are shown in Fig. 3b, c. The extrinsic f_t and f_{\max} of these transistors are both ~ 40 GHz. The intrinsic f_t and f_{\max} are 80 GHz and 70 GHz with device de-embedding, and 100 GHz and 70 GHz with intrinsic de-embedding, respectively. The RF performance exceeds all previously reported SWNT RF transistors, especially for the f_{\max} , which is at least twice that of the best previously reported results. The SWNT RF

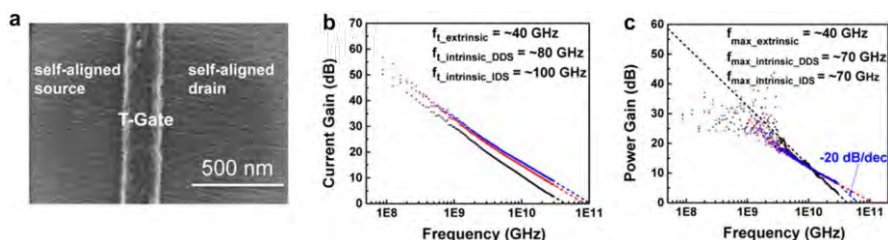


Fig. 3 **a** SEM image of a channel region of the RF transistor based on PFO-BPy-separated aligned SWNTs. The T-shape gate, self-aligned source and drain, and aligned polyfluorene-sorted SWNTs underneath are clearly demonstrated. **b**, **c** Current gain frequency response, and power gain frequency response, respectively. Adapted with permission from Ref. [11]. Copyright (2016) American Chemical Society

transistor advances the state-of-the-art of SWNT RF electronics, and may find broad applications for signal amplifications, wireless communications, and future flexible/wearable electronics.

2.4 Linearity Performance of SWNT RF Transistors

One great advantage of SWNT RF transistors is their linearity. Baumgardner et al. theoretically predicted that a carbon nanotube (CNT)-based field-effect transistor with ohmic contacts, quantum capacitance, and ballistic single-subband transport is inherently linear [19]. However, achieving the above conditions are difficult in realistic devices. Mothes et al. later used simulations to show that the requirements for high-linearity SWNT transistors could be relaxed with a moderate Schottky barrier at the source contact [20].

In addition to the simulation efforts, the linearity performance of SWNT RF transistors can be measured using single-tone and two-tone tests. Cao et al. have measured the linearity performance of the best SWNT RF transistors based on aligned PFO-BPy-separated SWNTs [11]. Figure 4a shows the schematic of the measurement setup commonly used for single-tone and two-tone tests [17]. In the single-tone test, they apply an RF single of a fixed frequency to one input of the measurement setup with various powers, and measure the power of the fixed frequency component at the output. A 1-dB gain compression point ($P_{1\text{ dB}}$), which defines the power level that causes the gain to drop by 1 dB from its small signal value, can be used to characterize the linearity. Figure 4b shows the results of the single-tone test. The $P_{1\text{ dB}}$ is 13–14 dBm. In the two-tone test, they apply two RF singles with a small frequency difference to the two inputs of the measurement setup, and measure the powers of the fundamental frequency term and the third-order frequency term at the output. Input third-order intercept point (IIP_3) is defined as the input power level which causes the fundamental frequency term and the third-order frequency term to have the same output power level. Figure 4c shows the results of the two-tone test. IIP_3 is ~ 22 dBm at a frequency of 8 GHz. Further improvement of the linearity performance of SWNT RF transistors can be achieved by carefully engineering the gate dielectric and source/drain contacts.

Fig. 4 **a** Schematic of the measurement setup for single-tone and two-tone tests. Adapted with permission from Ref. [17]. Copyright (2016) Springer. **b, c**

2.5 Circuit Applications Based on SWNT RF Transistors

In addition to transistor-level investigation of SWNT RF transistors, research groups have integrated SWNT RF transistors into circuits for realistic applications [4, 14, 16, 21–23].

Kocabas et al. demonstrated a radio which utilized four SWNT RF transistors [22]. The circuit schematic, images, and frequency response are shown in Fig. 5a–c.

The radio could record a commercial broadcast of a traffic report. Rutherglen et al. and Jensen et al. also demonstrated components in a receiver built with SWNT RF transistors [4, 23]. These receivers represent the most complex circuits so far built with SWNT RF transistors. With the advancement of SWNT RF transistors, circuits and systems with more complex functions and higher operation frequencies are

3 SWNT Nanoelectronics

SWNTs, due to their exceptional intrinsic carrier mobility [5], high saturation velocity [94], and quasi-1D structure, may offer various advantages for future digital electronics. Furthermore, the quasi-ballistic transport property of SWNTs enables a lower energy delay product predicted to outperform silicon-based complementary metal–oxide–semiconductor (CMOS) technologies [24]. During the past few years, SWNT-based devices and circuits have been making progress in various aspects under intense research.

3.1 Single SWNT Transistor

With the progress in nanotube synthesis, researchers have the material platform and are making further steps to gain better comprehension of the electrical transport properties of the SWNT FETs. Due to the fact that the properties of individual nanotubes may vary strongly from one another, it is indispensable to fabricate a transistor with a single nanotube present in the channel to fully understand the transport properties of each nanotube. Since the report of the first individual SWNT FETs [25], the high current-carrying capacity in the quantum ballistic regime [2], the high carrier mobility in the diffusive regime [5], and the low leakage current [26] have all been investigated. Furthermore, researchers have also worked extensively to improve the device performance by carefully studying the ohmic contacts between SWNTs and the contact metal, optimizing the device structures, and scaling down the device dimensions.

Up to now, the superior intrinsic properties of SWNTs have been confirmed by single nanotube FETs. Javey and coworkers did pioneering work by demonstrating high-performance ballistic SWNT FETs using palladium (Pd) contacts, with the room-temperature conductance near the ballistic transport limit of $G_0 = 4e^2/h$ and the high current-carrying capability of 25 μA per tube [2]. Kim and co-workers developed a method to deduce the mean free path by studying the channel length dependence of the channel resistance, where they confirmed that the long mean free path of SWNTs is on the order of a millimeter [27]. To study the diffusive transport, Durkop et al. fabricated semiconducting SWNT FETs with ultralong channel lengths larger than 300 microns, and estimated the intrinsic SWNT mobility to be $10,000 \text{ cm}^2 \text{ V}^{-1} \text{ s}^{-1}$ at room temperature, which was the highest value for all known semiconductors at the time of study [5]. Weitz and coworkers demonstrated that transistors based on individual CNTs can achieve large transconductance (5 μS), small subthreshold swing (68 mV/dec), large on/off ratio (10^7), and good reliability of performance under ambient conditions simultaneously [28].

For future high-performance SWNT circuits, the scaling of SWNT FETs is inevitable to pack more transistors on the chip. Of all the scaling parameters, two dimensions are critical, i.e., the channel length (L_{ch}) and the contact length (L_{c}). Understanding the scaling behavior of both L_{ch} and L_{c} are crucial for the integration of SWNT FETs. The IBM group fabricated a series of transistors with channel length scaled from 3 μm to 15 nm on the same SWNT, and demonstrated that these

nanotube transistors maintained their performance without the presence of short-channel effects [29]. When L_{ch} is aggressively scaled, the on state performance improves significantly, potentially leading to a high-speed circuit. The SEM image, transfer ($I_{\text{D}}-V_{\text{L BG}}$), and output ($I_{\text{D}}-V_{\text{DS}}$) characteristics of these devices are shown in Fig. 6a–c. The 15-nm device has the shortest channel length and highest room-temperature conductance ($0.7 G_0$) and transconductance ($40 \mu\text{S}$). In a separate work, the same group further pushed the L_{ch} scaling, and demonstrated a sub-10-nm SWNT transistor [30]. The transistor outperforms the best competing silicon devices with more than four times the diameter-normalized current density ($2.41 \text{ mA}/\mu\text{m}$) at a low operating voltage of 0.5 V. In terms of contact length scaling, for large contact lengths ($>100 \text{ nm}$), some studies have suggested that sharp needle-like contacts are ideal, since transport between a metal and a nanotube occurs only at the contact edge [95, 96]. On the contrary, for contact length less than 100 nm, the IBM group applied the same strategy as in the L_{ch} scaling study, i.e., with multiple devices located on the same nanotube, to study the contact length scaling from 20 to 100 nm, and showed that L_{c} scaling affects the on state far more dramatically than the off state of a device [29]. Figure 6d–f shows the contact length dependence of the SWNT FET performance. To tackle the short contact length scaling effects, Cao et al. developed an end-bonded contact scheme that allows scaling the contacts to 10 nm and beyond without increasing contact resistance [31]. The molybdenum film acts as the source and drain for the FETs and reacts with the CNT to form a carbide contact. Figure 6g shows the schematic of such carbide contact. Figure 6h shows a false-colored SEM image of a set of transistors with such carbide contact, and Fig. 6i shows the corresponding transfer characteristics. The molybdenum nanotube end-bonded contact exhibited no Schottky barrier. Using the bonded contact

Fig. 6 Single nanotube transistor. **a–c** Effects of channel length scaling on nanotube transistor performance **a** SEM image of a set of transistors on the same nanotube with different channel lengths. **b** Subthreshold I_D – V_{LBG} curve from devices with channel lengths of ~ 15 nm, 300 nm, and 3 μm . **c** Output I_D – V_{DS} characteristics of devices in **(b)**. **d–f** Effects of contact length scaling on nanotube transistor performance. **d** SEM image of a set of transistors on the same nanotube with different contact lengths. **e** Subthreshold I_D – V_{LBG} curve from devices with contact lengths of 100, 70, 50, 30, and 20 nm. *Inset* shows the dependence of g_m on L_c . **f** Output I_D – V_{DS} characteristics of devices in **(e)**. Adapted with permission from Ref. [29]. Copyright (2010) Nature Publishing Group. **(g–i)** Mo end-contacted SWNT transistors. **g** SEM image of the device. **h** Subthreshold I_D – V_{LBG} curve. **i** Output I_D – V_{DS} characteristics.

the toms5 from thecv

from 20 300 nm.

investigated, including gadolinium [36], yttrium [37], scandium [38], and erbium [39]. Ding et al. used yttrium as the source and drain contacts for top-gate FETs

with a single SWNT as the channel, and demonstrated n-type transistors with subthreshold swing (SS) of 73 mV/dec and drain-induced barrier lowering (DIBL) of 105 mV/V, as shown in Fig. 7a, b [37]. Shahrjerdi et al. performed a thorough experimental study of n-type contacts for SWNT FETs based on erbium (Er,

Fig. 7 N-type transistors from Ref. [37, 39–41, 43]. Schematic (a, c, e, g, i) and characteristics (b, d, f, h, j) of low work function metal, low work function metal aligned SWNT array, gate dielectric doping, and chemical doping N-type transistors, respectively. a, b Adapted with permission from Ref. [37]. Copyright (2009) American Chemical Society. c, d Adapted with permission from Ref. [39]. Copyright (2013) American Chemical Society. e, f Adapted with permission from Ref. [40]. Copyright (2011) American Chemical Society. g, h Adapted with permission from Ref. [41]. Copyright (2014) American Chemical Society. i, j Adapted with permission from Ref. [43]. Copyright (2016) American Chemical Society

$\Phi_M = 3.0$ eV), lanthanum (La, $\Phi_M = 3.5$ eV), and yttrium (Y, $\Phi_M = 3.1$ eV) [39]. Figure 7c shows the schematic of the bottom gate SWNT n-type FET (n-FET) and the corresponding high-resolution TEM image, which gives details of the Er contact with the oxidation layer and the Al encapsulation layer. The results suggest that by employing Er contacts, significant improvements in device characteristics can be achieved. Figure 7d shows the effect of partial oxidation of Er (left) and Y (right) electrodes on device performance. Due to rapid oxidation, the device performance degrades with increasing contact layer thickness. Controlling process parameters such as low base pressure and high deposition rate can help mitigate the oxidation effects. The electrical characteristics of n-FET devices with Er electrodes were shown to remain stable upon storage in air by employing a hydrophobic polymer deposited at 150 °C. It is worthwhile to note that the technique of applying low work function metal to achieve n-type transistors can be applied to both a single nanotube and also an array of aligned tubes. A small work function metal gadolinium (Gd) with a work function of ~ 3.1 eV has been used by Wang et al. in aligned nanotube transistors [40]. Figure 7e shows the schematic of Gd used as n-type contact in air-stable, n-type, aligned nanotube transistors. The transistor transfer characteristics are shown in Fig. 7f, and the linear output characteristics indicate good ohmic contacts between SWNTs and the Gd contacts.

Another approach is to take advantage of the gate dielectric to give rise to n-type doping in SWNTs. Liyanage et al. applied low work function metal oxides (Y_2O_3) as the gate dielectrics to SWNT FETs [41]. This novel and very-large-scale-integrated (VLSI)-compatible doping technique enables wafer-scale fabrication of high performance n-type SWNT transistors. The partially oxidized yttrium gives rise to n-type doping in SWNTs. Figure 7g shows the schematic of the Y_2O_3 gate dielectric SWNT FETs. From Fig. 7h, we can see the transistors demonstrate good n-type behavior with high performance of a large on current, high on/off ratio, and small subthreshold voltage swing.

The third approach is to apply chemical and electrostatic doping methods to provide excess electrons to promote electron tunneling and conduction [42]. Recently, Geier et al. reported the controlled n-type doping of SWNT thin-film transistors with a solution-processed pentamethylrhodocene dimer $[(RhCp^*Cp)_2]$ [43]. Its molecular-scale thickness enables large-area arrays of top-gated, high-yield, n-type SWNT transistors, as shown in Fig. 7i. Figure 7j shows the transfer curves for the top-gated SWNT TFTs for different exposure times, which shows the conversion of the top-gated SWNT TFTs into n-types under 10-min dopant exposure. The air-stable n-type dopant study will thus facilitate ongoing efforts to realize high-density SWNT integrated circuits.

3.3 Transistors and Digital Circuits Based on Aligned SWNTs

In spite of the great potential of SWNTs demonstrated by single SWNT transistors, in terms of commercial applications, the device-to-device variation can undermine their benefits. Different factors can contribute to the variations, such as chirality, oxygen adsorption, and defects. Multiple aligned SWNTs within the same device channel can average out the SWNT properties and greatly reduce device variation. Another advantage of aligned nanotube arrays is the simultaneous contribution to the device current by multiple SWNTs, which can multiply the device conductance. CVD-grown SWNTs on crystalline substrates like quartz and sapphire can yield highly aligned nanotubes. Using the massive aligned nanotube arrays grown by CVD on sapphire, our group reported a high yield and registration-free nanotube-on-insulator approach, analogous to the silicon-on-insulator approach adopted by the semiconductor industry [32]. To overcome the drawbacks of small sample size, large millimeter-scale channel length, and unavailability of controlled doping, our group reported a full-wafer scale CMOS analogous fabrication with SWNT transistors feature size down to $0.5\ \mu\text{m}$ [33]. After nanotube synthesis and transfer, the SWNT transistors employ the top-gate structure, and the metallic nanotubes inside the channel regions are removed by electrical breakdown to improve the current on/off ratio. P-type SWNT transistors are converted to n-type by potassium and electrostatic doping. Combining all the advantages, CMOS inverters, NAND, and NOR gates based on aligned SWNT array transistors are demonstrated in Fig. 8a. To demonstrate the feasibility of SWNT FET circuits at a highly scaled

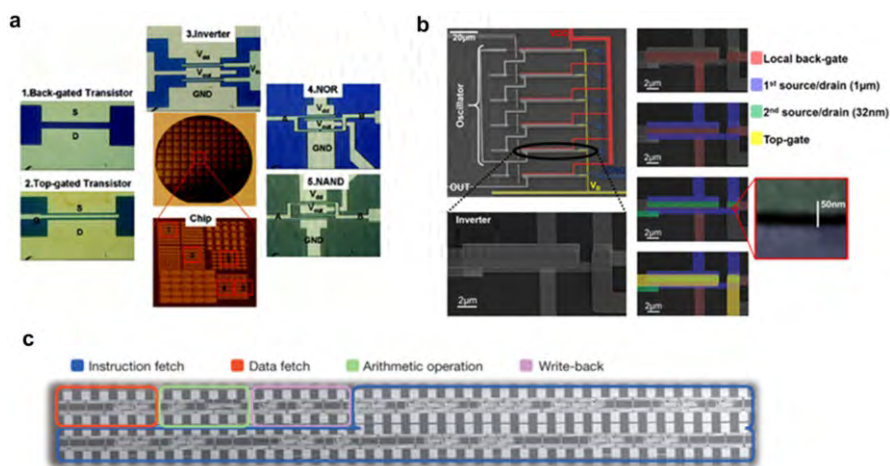


Fig. 8 Transistors and digital circuits based on aligned nanotubes. **a** Optical images of SWNT transistors and circuits built on a 4-inch Si/SiO₂ wafer: 1 back-gated transistor; 2 top-gated transistor; 3 CMOS inverter; 4 NOR logic gate; 5 NAND logic gate. Adapted with permission from Ref. [33]. Copyright (2009) American Chemical Society. **b** SEM of an integrated SWNT FET IR sensor and interface circuit (left), along with processing steps (right). Adapted with permission from Ref. [34]. Copyright (2014) American Chemical Society. **c** SEM of the SWNT computer. Adapted with permission from Ref. [35]. Copyright (2013) American Association for the Advancement of Science

technological node, Shulaker et al. at Stanford reported the first VLSI-compatible approach for SWNT FETs with devices as small as sub-20-nm channel lengths [34]. They demonstrated inverters functioning at 1 MHz and a fully integrated SWNT FET infrared (IR) light sensor and interface circuit at 32-nm channel length. The SEM images of the integrated SWNT FET IR sensor and interface circuit are shown in Fig. 8b. This demonstration is one step closer to highly scaled SWNT FET circuits as a digital VLSI technology.

In terms of the circuit complexity, the first SWNT computer has been demonstrated by the same Stanford group as an important milestone in the practical application of SWNT digital electronics [35]. The SWNT computer runs an operating system and achieves multitasking of counting and integer sorting simultaneously. The SEM of the computer comprising of instruction fetch, data fetch, arithmetic operation, and write back system is shown in Fig. 8c. Despite the fact that the first computer still has many aspects to improve, such as the PMOS-only logic and the low clock speed, the experimental demonstration of a SWNT computer is a breakthrough in the next generation of SWNT-based, highly energy-efficient electronic systems.

3.4 Large-scale Assembly of SWNTs

The materials challenges in the alignment and placement of SWNTs, as well as in the removal of metallic SWNTs, have prevented SWNTs from fully achieving their exceptional electronic properties. Joo et al. reported a novel yet simple method to deposit aligned semiconducting SWNTs on substrates via a dose-controlled, floating evaporative self-assembly (FESA) method [99]. The process starts from sorted SWNT solution with semiconducting purity of more than 99.9%. When dropping the solvent with semiconducting SWNT solution at a certain dose onto the water surface, the dose-covered air/water interface will spread out and reach the substrate. The solvent of the SWNT solution will evaporate, and SWNTs will stay on the substrate and align with the air/water interface. Repeatedly applying the solution dose and pulling out the receiving substrate at optimized speeds can give stripes of aligned nanotubes on the substrate. The FESA method can give high-density, aligned SWNTs with high semiconducting purity and few defects. The FESA steps are illustrated in Fig. 9a. The density of the assembled aligned tubes can be as high as 40–50 tubes/ μm . Based on the FESA platform, Grady et al. studied superior back-gated FET performance fabricated from these SWNT arrays, and achieved high on-conductance and a high on/off ratio simultaneously [100]. The schematic of the gate structure and the SEM image of the device channel area are shown in Fig. 9b, c, respectively. For a channel length (L_{ch}) of 240 nm, the on-conductance (G_{on}) per width and an on/off ratio ($G_{\text{on}}/G_{\text{off}}$) are as high as 261 $\mu\text{S}/\mu\text{m}$ and 2×10^5 , respectively (Fig. 9d), and for an L_{ch} of 1 μm , the corresponding performances are 116 $\mu\text{S}/\mu\text{m}$ and 1×10^6 , respectively (Fig. 9e).

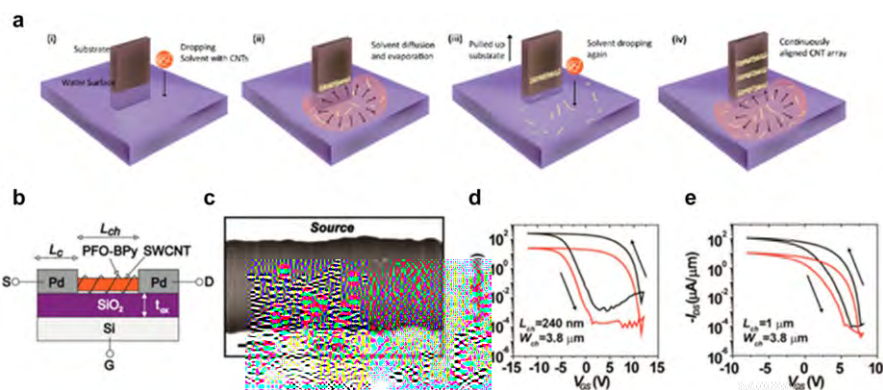


Fig. 9 Large-scale assembling of CNTs. **a** Schematic illustration of the iterative (FESA) process used to fabricate aligned nanotubes-SWNTs driven by the spreading and evaporation of controlled doses of organic solvent at the air/water interface. Adapted with permission from Ref. [99]. Copyright (2014) American Chemical Society. **b** Schematic of SWNT FET architecture. **c** Top-down SEM image of SWNT spanning Pd electrodes of a 240-nm L_{ch} SWNT FET (scale bar 100 nm). **d**, **e** Transfer characteristics at $V_{DS} = -1$ V (black) and -0.1 V (red) for a champion SWNT FET of $L_{ch} = 240$ nm and $W_{ch} = 3.8$ μm in (**d**) and $L_{ch} = 1070$ nm and $W_{ch} = 3.8$ μm in (**e**). Adapted with permission from Ref. [100]. Copyright (2014) American Chemical Society

3.5 3D Integration and Novel Structures of SWNT Transistors

In order to increase the transistor density and/or improve the SWNT FET performance, different integration methods and gate structures have been proposed and demonstrated. Wei et al. reported a scalable integration process for monolithic 3D integrated circuits (3D ICs) using SWNT FETs [44]. In their approach, SWNT FETs with high I_{ON}/I_{OFF} can be flexibly placed on arbitrary layers of monolithic 3D ICs, and connected using conventional vias to build fully complementary monolithic 3D logic gates and multi-stage logic circuits. The monolithic 3D logic gates can operate correctly over a range of supply voltages from 3 to 0.2 V, which shows the robustness of the method.

Constructing ICs along a single SWNT is another novel idea to minimize the effect of variation in different nanotubes and shows SWNT FETs can be used as a building block for electronics [101–104]. In 2001, Derycke et al. reported both p- and n-type transistors on the same nanotube for the first complementary nanotube-based inverter logic gate [102]. In 2006, Chen et al. demonstrated a CMOS 5-stage ring oscillator built entirely on a single 18-μm-long SWNT [103]. Later in 2014, Pei et al. reported an innovative modularized construction of ICs on individual CNTs [104]. In their work, pass-transistor-logic style 8-transistor (8-T) units were built and used as multifunctional function generators. The units have good tolerance to inhomogeneity in the CNTs and were used as building blocks for general ICs. An 8-bits BUS system used to transfer data between different systems in a computer was constructed.

Other possible novel SWNT gate structures with potential performance advantages at the circuit level including FinFETs [45] and gates all around [46]

have also been analyzed and studied. Furthermore, combining SWNT FETs with other semiconductors such as silicon to achieve CMOS integration [47] shows the promising future for high-performance digital logic applications.

4 SWNT Macroelectronics

4.1 Fabricated SWNT TFTs

The use of SWNT networks present a highly promising path for the realization of high-performance TFTs for macro and flexible electronic applications. Using SWNT random networks for TFTs has many significant advantages: SWNT thin films are mechanically flexible, optically transparent, and can be prepared using solution-based room-temperature processing, all of which cannot be provided by amorphous and polysilicon technologies [48–61]. The most common assembly methods for random nanotube networks including direct CVD growth [48, 62], dry filtration [54], evaporation assembly [63], spin coating [64–66], drop coating [56, 67–71], and printing [49, 50, 52, 72, 73].

4.1.1 Gaseous Phase-Based SWNT TFTs

As-grown nanotube networks usually contain both metallic and semiconducting nanotubes [105, 106], which leads to a trade-off between charge carrier mobility (which increases with greater metallic tube content) and on/off ratio (which decreases with greater metallic tube content). Many research efforts have been devoted to the successful realization of high-performance FETs comprised of semiconducting-enriched SWNT random networks based on CVD synthesis [48, 53, 90, 107]. Medium-scale SWNT thin-film integrated circuits on flexible substrates have been demonstrated by Rogers' group [48]. For this method, growth substrates decorated with metal catalysts (Fe particles or ferritin) were placed in a furnace at elevated temperatures (>800 °C). Then, a precursor containing carbon feedstock, such as methane, ethylene, isopropyl alcohol, etc., was introduced into the growth chamber for the dissociation of hydrocarbon molecule from the feedstock. The hydrocarbon molecules then facilitated the growth of the CNTs on the catalysts [48, 90]. Although the flexible SWNT TFTs and circuits shows promising electrical performance, the existence of metallic nanotubes degrades the on/off ratio of the devices.

Ohno's group introduced a floating catalyst CVD technique with monoxide (CO) as the carbon source, and achieved high-performance flexible nanotube TFTs and D-flip-flop circuits [54]. In Fig. 10a, the nanotubes grown by plasma-enhanced CVD were collected through a simple gas phase filtration process [53, 54, 108]. The density of the nanotubes can be easily controlled by the collection time. The SWNTs were subsequently transferred onto the device substrate by dissolving the filter in acetone. The transferred CNT film has a network morphology consisting of rather straight and long nanotubes, ~10 μm in length, as shown in the SEM images in Fig. 10b. The advantage of utilizing as-grown SWNTs directly for fabrication of

devices is that there are more Y-type junctions between the nanotubes than the X-junctions, which can result in a higher mobility of the transistors [54]. Figure 10c shows the transfer and output characteristics of a bottom-gate TFT device. The device showed p-type characteristics with a high on/off ratio (6×10^6) and an

◀ **Fig. 10** **a** Schematic diagram showing CNT growth, collection by filter, transfer, and patterning. **b** SEM images of a CNT network on a Si/SiO₂ substrate after transfer. **c** Transfer and output characteristics of fabricated bottom-gate TFT based on the nanotube network shown in (b). **a–c** Adapted with permission from Ref. [54]. Copyright (2011) Nature Publishing Group. **d** Schematic diagram showing the configuration of a CNT TFT in which the CNT network is deposited using separated semiconducting nanotube solution. **e** SEM images of an SWNT random network captured at different regions of a wafer after SWNT deposition. **f** Output characteristics of an SWNT TFT. **g** Statistical study of on-state current density and threshold voltage of as-fabricated SWNT TFTs. **d–g** Adapted with permission from Ref. [56]. Copyright (2009) American Chemical Society

effective device mobility of $35 \text{ cm}^2 \text{ V}^{-1} \text{ s}^{-1}$. The transfer process of the CVD grown SWNTs is carried out at room temperature, which is desirable for the fabrication of flexible electronics.

4.1.2 Solution-Based SWNT TFTs

In addition to CVD-based SWNT random network electronics, there are many approaches in the area of solution-based SWNT electronics [55–57, 68, 70, 71, 109]. About one third of the as-grown SWNTs are metallic nanotubes [110], which can cause significant leakage of current when the transistors are in the off state and result in a low on/off ratio [111–114]. Thus, the metallic nanotubes should be selectively removed, and high-purity semiconducting nanotubes are desired for high-performance transistors. Separation between metallic and semiconducting tubes, and even separation of single chirality nanotubes have been achieved by a variety of methods, such as density gradient ultracentrifugation (DGU) [110, 113], gel chromatography [115], and DNA-based chromatographic purification [116].

SWNT networks can be obtained by spin coating/dropping the nanotube solution onto a spinning substrate [64]. The drawback with this method is scalability because the deposited SWNTs often align along different orientations depending on the location on the substrate, which leads to wafer-scale fabrication with low uniformity. Drop coating is found to be a more promising solution-based SWNT assembly method for large-scale applications of nanotube TFTs. In this method, the substrates are first functionalized with amine-containing molecules, which are effective adhesives for SWNTs. By simply immersing the substrate into the nanotube solution, highly uniform nanotube networks can be obtained throughout the wafer, enabling the fabrication of nanotube TFTs with high yield and small device-to-device variation [56, 68, 70, 71].

Many research groups have systematically studied electrical performance of SWNT TFTs based on the high-purity semiconducting SWNT solution [7, 56, 63, 68, 79, 109]. The device characteristics of SWNT TFTs are heavily dependent on the nanotube density [69, 70] and channel length [71, 117]. SWNT TFTs with mobility greater than $100 \text{ cm}^2 \text{ V}^{-1} \text{ s}^{-1}$ have been reported [117–119], which exceed the mobility of amorphous and organic FETs by at least two orders of magnitude. The fact that such high-mobility SWNT TFTs can be fabricated using a facile solution-based process and processed at room temperature makes the nanotube TFTs ideal for a wide range of applications.

We are among the first few research groups to demonstrate SWNT TFTs comprised of an enriched semiconducting SWNT random network. Figure 10d illustrates a common back-gated TFT based on a random network of separated SWNT solution [56]. The SWNT solution was uniformly deposited onto the device substrate by first functionalizing with aminopropyltriethoxy to terminate the surface of the substrate with a layer of amino groups, which enhances the attraction between the SWNTs and the surface [65]. As can be observed in Fig. 10e, the SWNT thin film can be deposited invariantly over the entire surface of a 3-inch Si/SiO₂ wafer, as shown by the SEM images captured at different regions of the wafer after SWNT deposition. This proves that the deposition process is scalable, and can be used in industrial-scale fabrication. The geometry of the channel of the transistors can be defined by standard photolithography, followed by O₂ plasma etching of the SWNT film in the region outside the channel. This technique eliminates the issue of assembly of the nanotubes. The transistors fabricated with the 98% enriched SWNT solution exhibited ideal p-type behavior with mobility as high as 52 cm² V⁻¹ s⁻¹, while maintaining a current on/off ratio of 10⁴. Although the mobility of the devices is not as high as that exhibited by silicon transistors, it is still an invaluable thin film material for applications such as drivers for display, or flexible electronics [120]. The output characteristic of the SWNT TFTs is exhibited in Fig. 10f. As can be observed in the plot, the output curves can be fully saturated. The uniformity of the devices is illustrated in Fig. 10g. The normalized on current (I_{on}/W) and threshold voltage (V_{th}) of 10 SWNT TFTs were delineated in the figure. The results provided evidence for the applicability to implement the separated CNT thin films in large-scale fabrication processes.

4.2 Printed SWNT TFTs

SWNTs, which are intrinsically printable at room temperature, show its great advantage over amorphous silicon and polysilicon for printed electronics [49, 83]. Compared with other printable organic materials, SWNTs have much higher mobility and are chemically stable in ambient [58, 86, 121]. Thanks to the great progress made in SWNT separation [122, 123], semiconducting SWNT-enriched solution has been realized, which leads to feasibility of printing high-performance SWNT TFTs for macro and display electronic applications [49, 84–89].

To realize fully printed high-performance SWNT TFTs, selection of materials for electrodes and gate dielectrics is critical. In terms of electrodes, silver and gold based nanoparticle inks are mostly selected for their system because of their high conductivity and the formation of Ohmic contact between electrodes and SWNTs [84, 124, 125]. Although nanomaterials such as metallic SWNTs have been used as electrodes [126], the performance was rather moderate and therefore hard to be applied for macro and display electronics. For printing gate dielectrics, mixtures composed of high- κ metal oxide nanoparticles and organic binders are commonly used to achieve relatively high capacitance [86, 125], which can reduce the operation voltage of printed TFTs. Another group of dielectric materials is electrolyte, which have been reported by Frisbie and Hersam's groups [50, 88]. The most important advantage of employing electrolyte as the gate dielectric is the high

capacitance regardless of its rather large physical thickness. As a result, the performance of such printed electrolyte-gated SWNT TFT is superior in terms of on-state current density, on–off ratio and low operation voltage [127].

Multiple printing technologies reported for fabricating SWNT TFTs can be mainly divided into two groups [86]. The first one is of high registration accuracy represented by aerosol-jet printing and inkjet printing. The second one is of high scalability and throughput represented by gravure printing and flexographic printing. On one hand, for printing SWNTs as channel materials, ink-jet and aerosol-jet printing are main-stream technologies using relatively low viscosity inks to pattern an ultrathin and uniform film. On the other hand, ink-jet printing, aerosol-jet printing, screen printing, gravure printing and flexographic printing have all been employed for patterning gate dielectric and electrodes to achieve fully printed SWNT TFTs. Up until now, the fully-printed high-performance SWNT TFT has been used for macro, display, and sensor electronics. Our group made great efforts to developing fully printed SWNT TFTs for OLED driving using ink-jet printing (Fig. 11a) and screen printing (Fig. 11b) [49, 86]. Javey and Cho's groups pioneered in gravure printed SWNT electronics (Fig. 11c), realizing D flip-flop [52], full adder [51], and fully printed backplane for electronic skin [76]. Hersam's group reported high-performance printed ring oscillators using aerosol-jet printing [85, 128, 129]. Ohno's group made great efforts on developing fully flexographic printed SWNT TFTs with CVD grown nanotubes (Fig. 11d) [130]. Overall, such

Fig. 11 **a** Schematic diagram showing the process of fully ink-jet printed SWNT TFTs 1 printing first silver electrodes. 2 Printing SWNT network. 3 Printing second layer of silver electrodes. 4 Printing ionic gel as dielectric material. Adapted with permission from Ref. [49]. Copyright (2011) American Chemical Society. **b** Schematic diagram of screen printer and an optical image of screen printed SWNT TFT array on a PET substrate. Adapted with permission from Ref. [86]. Copyright (2014) American Chemical Society. **c** Schematic diagram outlining gravure printing process of SWNT TFTs and images of printed TFT and nanotube network on a PET substrate. Adapted with permission from Ref. [125]. Copyright (2013) American Chemical Society. **d** Schematic diagram of flexographic printing and an optical image of flexographic printed CNT TFT electronics on a PET substrate. Adapted with permission from Ref. [130]. Copyright (2011) Japan Society of Applied Physics

cost-effective and solution-based printing technologies have been attracting more and more research interest and are promising for practical applications.

4.3 Applications Based on SWNT TFTs

SWNT TFTs show great potential in a wide range of applications, ranging from digital circuits, active-matrix backplanes for display electronics and sensors, to flexible electronics. Over the past years, tremendous efforts have been devoted into SWNT TFT research, trying to make it a real technology. Here, we will review the potential applications of SWNT TFTs, including (1) digital circuits, (2) active-matrix backplanes for display electronics and sensors, and (3) flexible electronics.

4.3.1 Digital Circuits

The extremely high intrinsic carrier mobility and current-carrying capacity make SWNTs a promising channel material for next-generation digital circuits. Many groups have made significant progress by successfully fabricating integrated circuits based on p-type SWNT TFT platforms [48, 53, 54, 68, 71, 131]. In 2008, Cao et al. successfully demonstrated the first medium-scale SWNT-based integrated digital circuits, a four-bit row decoder composing of 88 SWNT TFTs, on polyimide substrates [48]. Random SWNT networks were initially synthesized by CVD, and then transferred to polyimide substrate as the channel materials. Figure 12a shows the optical image of a flexible SWNT integrated circuit chip bonded to a curved surface and high-magnification photographic image of the fabricated four-bit row decoder consisting of 88 SWNT transistors. Moreover, Sun et al. successfully realized the fabrication of SWNT-based TFTs and logic circuits on flexible substrates, such as 21-stage ring oscillator and master–slave delay flip-flops, using a floating-catalyst CVD SWNT deposition method followed by gas phase filtration and a transfer process [54]. Based on the platform of gas phase-synthesized nanotube networks, they further demonstrated the first all-carbon XOR gates and 1-bit static random access memory (SRAM) [53]. Later on, instead of using CVD-synthesized SWNTs, Wang et al. used separated high-purity semiconducting-enriched SWNTs as the channel material for high-performance SWNT TFTs and demonstrated separated nanotube-based integrated logic gates, including an inverter, NAND, and NOR gates, serving as a good platform to bypass the issue of the coexistence of both metallic and semiconducting nanotubes in the as-synthesized SWNTs [68]. After that, solution-processed semiconducting SWNT thin films have drawn much more attention from researchers, because solution-processed separated SWNTs offer high electrical performance, good mechanical flexibility, relatively low cost, and ambient compatibility simultaneously. Wang et al. successfully demonstrated high-performance logic gates, including inverters, NAND, NOR gates, with superior bending stabilities [71]. A recent breakthrough was made by Chen et al. by realizing a 4-bit adder which consists of 140 p-type SWNT TFTs and a 2-bit multiplier for the first time [77]. Thanks to the high uniformity and desirable threshold voltage of the CNT TFTs, the integrated circuits based on these TFTs can be operated by a small voltage down to 2 V.

Fig. 12 **a** Optical image of a flexible SWNT integrated circuit chip bonded to a curved surface and high-magnification photographic image of the decoder consisting of 88 CNT transistors. Adapted with permission from Ref. [48]. Copyright (2008) Nature Publishing Group. **b** Optical micrograph, read margin measurement, folded read margin measurements, and hold operation of a fabricated SWNT CMOS SRAM cell. Adapted with permission from Ref. [81]. Copyright (2015) Nature Publishing Group. **c** Hybrid integration of IGZO TFT and SWNT TFT for a CMOS inverter. Adapted with permission from Ref. [82]. Copyright (2014) Nature Publishing Group

Large hysteresis, a commonly observed phenomenon in the transfer characteristics of SWNT TFTs, is highly undesired in the operation of transistors and integrated logic gates, because hysteresis often results in the shift of threshold voltage as the voltage sweeping direction and range changes. Multiple factors can cause hysteresis in a SWNT-based TFT, including interface-trapped charges and trapped charges induced by the absorption of water molecules inside the channel [78]. Therefore, hysteresis-free nanotube-based TFTs are highly desired for the stable operations of SWNT-based TFTs and digital circuits. Ha et al. developed a promising approach of using fluorocarbon polymer as the encapsulation layer for hysteresis-free SWNT devices, which showed great device stability in both air and water [78]. Thanks to the high hydrophobicity of this Teflon-like polymer, the water molecules absorbed in the nanotubes can be effectively removed, which yields hysteresis-free SWNT TFTs. Recently, Chen et al. discovered an alternative approach for hysteresis-free SWNT devices by using Y_2O_3 thin film as the gate dielectric layer, which was oxidized from e-beam-evaporated yttrium film [77]. Their results showed that Y_2O_3 can offer very high gate efficiency and high

uniformity for SWNT-based TFTs, which paves the way for large-scale integration of SWNT-based TFTs.

CMOS integrated circuits have many advantages, especially their low static power consumption. Over the past two decades, many groups including our group have devoted a lot of efforts into trying to convert p-type SWNT TFTs into air-stable n-type TFTs aiming for integrated CMOS logic gates. Here, we will review some recent progress in CMOS integrated circuits consisting of n-type and p-type SWNT TFTs as the NMOS and PMOS, respectively. Ryu et al. reported a fully integrated CMOS inverter and NAND and NOR gates by using chemical doping to convert p-type aligned nanotube transistors to n-types [33]. Later on, Zhang et al. developed a new approach of using a thin layer of high- κ oxide passivation layer, deposited by atomic layer deposition, to convert separated SWNT TFTs from p-type to air-stable n-type [79]. Interestingly, the converted n-type transistors and the p-type transistors show symmetric electrical performance, regarding device mobility, on-state current, and on/off ratio. They further demonstrated a CMOS inverter with rail-to-rail output, large noise margin, and symmetric input/output behavior. Recently, Ha et al. reported a novel strategy of achieving air-stable n-doping SWNTs with SiN_x thin films deposited by plasma-enhanced chemical vapor deposition [80]. The n-type nanotube transistors are highly air-stable and show very good uniformity over large areas, which is an important factor for integrated circuit applications. In 2015, a great breakthrough was achieved by Geier et al. whom demonstrated the first solution-processed SWNT thin film-complementary SRAM [81] (Fig. 12b). The uniform and stable electronic performance of the complementary p-type and n-type SWNT TFTs is attributed to the well-controlled adsorbed atmospheric dopants and robust encapsulation layers. Recently, Yang et al. reported CMOS ICs by using Sc or Pd as the source/drain contacts to selectively inject carriers into the CNT network channels for NMOS and PMOS, respectively [132]. They demonstrated a 4-bit full adders consisting of 132 CMOS TFTs with 100% yield, showing the potential of medium-scale CNT network film-based ICs.

Considering metal oxide semiconductors have gradually emerged as a mature technology platform for n-type TFTs, Chen et al. demonstrated the first large-scale hybrid integration of p-type CNT and n-type indium–gallium–zinc–oxide thin-film transistors to realize 501-stage ring oscillators, consisting of more than 1000 transistors, on both rigid and flexible substrates (Fig. 12c) [82]. In this hybrid integration approach, the strength of the p-type nanotube and n-type indium–gallium–zinc–oxide are successfully combined together to achieve high uniformity and high yield.

4.3.2 Active-Matrix Backplanes for Display Electronics and Sensors

Separated semiconducting-enriched SWNT thin films possess great potential for TFTs and active-matrix backplanes for display electronics and sensors, due to their high semiconducting purity, high mobility, and room-temperature processing compatibility. As early as 2009, Wang et al. made the first conceptual demonstration of an organic light-emitting diode (OLED) control circuit with a nanotube TFT,

with the output light intensity exceeding 10^4 , which paves the way for using nanotube TFTs for display electronics [56]. Active-matrix organic light-emitting diode (AMOLED) display exhibits great potential as a competitive candidate for next-generation display technologies due to its high light efficiency, light weight, high flexibility, and low-temperature processing compatibility. Later, Zhang et al. further successfully demonstrated monolithically integrated AMOLED display elements, consisting of 500 pixels driven by 1000 nanotube TFTs [57]. The optical image of an AMOLED substrate containing 7 AMOLED elements, each with 20×25 pixels, is shown in Fig. 13a. Figure 13b is a photograph showing the pixels on an integrated AMOLED. The electrical characteristics of the OLED controlled by a single pixel circuit is shown in Fig. 13c. Figure 13d shows the plot of the current through the OLED (I_{OLED} ; red line) and OLED light intensity (green line) versus V_{DATA} with $V_{\text{DD}} = 8$ V. This approach may serve as a critical foundation for using separated CNT thin-film transistors for display applications in the future. Later on, inkjet-printed [49] and screen-printed [86] OLED control circuits were demonstrated, showing a low-cost approach to realize OLED driving capability. Recently, Zou et al. reported first CVD-grown SWNT network-based TFT driver

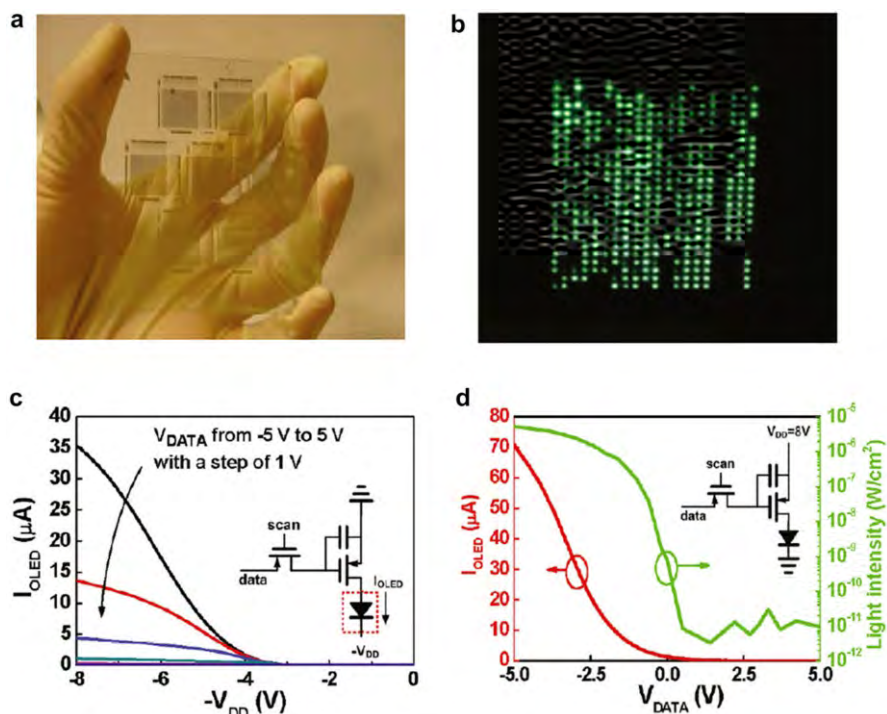


Fig. 13 AMOLED using SWNT TFTs. **a** Optical image of an AMOLED substrate containing 7 AMOLED elements, each with 20×25 pixels. **b** Photograph showing the pixels on an integrated AMOLED. **c** Characteristics of the OLED controlled by a single pixel circuit. **d** Plot of the current through the OLED (I_{OLED} ; red line) and OLED light intensity (green line) versus V_{DATA} with $V_{\text{DD}} = 8$ V. Adapted with permission from Ref. [57]. Copyright (2011) American Chemical Society

circuits for both static and dynamic 6×6 AMOLED displays, which further proved the suitability and capability of SWNT-TFTs for future OLED applications [74].

Additional great progress in this field was made by Wang et al. by demonstrating the first user-interactive electronic skin which can give simultaneously spatial-pressure mapping and visual response through a built-in AMOLED controlled by an SWNT-TFT-based active matrix (Fig. 14) [55]. In this system, the OLED arrays can be turned on locally at the location where there is pressure applied, and the intensity

Fig. 14 User-interactive electronic skin based on SWNT TFTs. **a, b** Schematic diagrams showing the configuration of a pixel, consisting of a nanotube TFT, an OLED, and a pressure sensor (PSR) integrated vertically on a polyimide substrate. **c** Circuit schematic of the e-skin matrix. **d** Photograph of a fabricated device (16×16 pixels). **e** *Green, blue, and red color* interactive e-skins are used to spatially map and display the pressure applied with C- (*left*), A- (*center*), and L- (*right*) shaped PDMS slabs, respectively. Adapted with permission from Ref. [55]. Copyright (2013) Nature Publishing Group

of the emission light can be used to quantify the pressure applied to the surface. This work represents a successful large-scale demonstration of three different electronic components, including nanotube TFTs, pressure sensors, and OLED arrays, which are monolithically integrated over large areas on plastic substrates. This electronic skin has great potential to be used for a range of applications, such as medical monitoring devices, interactive input/output devices, etc.

As early as 2011, Takahashi et al. reported fabrication of SWNT thin-film-based 12×8 active-matrix backplanes for pressure mapping with a pressure sensitive rubber as the active sensor element [70]. After that, they further demonstrated a flexible nanotube active-matrix backplane for visible light and X-ray imagers [75]. Recently, they realized large-area pressure mapping by the large-scale integration of a printed SWNT active-matrix backplane with tactile sensor arrays, indicating a scalable, low-cost approach towards electronic skin applications using CNT TFTs [76].

4.3.3 Flexible Electronics

Recently, flexible electronics have been widely explored for new applications which are impossible to be realized using the conventional rigid substrates. Due to the intrinsic flexibility of SWNTs, nanotube TFTs have attracted many people's attention and emerged as a promising technology platform for flexible electronics. To achieve good flexibility, a very thin layer of high-quality dielectric on plastic substrate is highly desired. Here, we will review some recent progress achieved in nanotube-TFT-based flexible electronics.

As early as 2006, Cao et al. reported mechanically flexible, optically transparent "all-tube" TFT on flexible substrates fabricated using layer-by-layer transfer printing of CVD-grown SWNT networks as both electrodes and channel materials [133]. Elastomeric dielectrics and flexible substrates were used to achieve high flexibility. In 2012, Wang et al. demonstrated extremely bendable, high-performance integrated inverters, NAND, and NOR logic gates, analog, and radio frequency applications using semiconducting-enriched SWNTs [71]. Later, Lau et al. further reported fully printed SWNT-based TFTs on flexible substrates, and the devices showed no measurable change in electrical performance under a bending radius as small as 1 mm [125]. Afterwards, all-carbon integrated circuits were demonstrated by Sun et al. for the first time [53]. The devices were entirely composed of carbon-based materials with active channels and passive elements fabricated using stretchable and thermostable assemblies of SWNTs, plastic polymer dielectric layers, and plastic substrates. Surprisingly, functional integrated circuits have also been successfully made into a 3D dome. Another interesting progress was reported by Chae et al. demonstrating a highly stretchable and transparent FET which combined graphene/SWNT hybrid electrodes and an SWNT network channel with a wrinkled Al_2O_3 dielectric layer [134]. The authors claimed that the wrinkled Al_2O_3 layer contained effective built-in air gaps, offering a gate leakage current as small as 10^{-13} A. Thanks to the wrinkled dielectric layer, the devices retained their good performance under strains as large as 20% without noticeable leakage current increases or performance degradations. Furthermore, the

devices showed no significant degradation after over 1000 cycles of stretch-release process. Recently, Cao et al. successfully demonstrated ultraflexible and imperceptible p-type nanotube transistors and integrated circuits with a bending radius down to 40 μm [131]. The as-fabricated ultralight-weight ($<3 \text{ g/m}^2$) nanotube transistors showed high mechanical robustness which can accommodate severe crumpling and compressive strain of 67%. Moreover, the nanotube circuits remained properly functional under 33% compressive strain, showing great potential as indispensable components for ultraflexible complementary electronics.

5 Summary and Outlook

In summary, SWNTs are highly promising for future RF electronics, digital electronics, and macroelectronics applications due to their excellent electrical, mechanical, and thermal properties. In regard to RF electronics, RF performance of SWNT transistors ready for some practical applications have been achieved, and RF circuits and systems based on SWNTs have been demonstrated [11, 23]. For SWNT-based nanoelectronics, ballistic SWNT transistors provide a good platform for further pushing forward Moore's law [2]. For macroelectronics, SWNT random network TFTs have been demonstrated in various applications, including digital circuits, active-matrix backplanes for display electronics and sensors, as well as flexible electronics. In spite of the significant progress achieved, several further developments are needed before SWNTs can be adopted by industry. First, it is of key importance to achieve 332 SWNT arrays with both high density (150–200 tubes/ μm) and ultrahigh-purity semiconducting ($>99.9999\%$) for SWNT RF and digital electronics. With the advancement in the nanotube 332ent technologies, multiple transfer of high-density and ultrahigh-purity semiconducting a332 SWNT arrays provides a promising way to reach the goal. Second, for all applications, hysteresis can be an issue compromising SWNT performance. Further optimization of dielectric materials for SWNT transistors to achieve hysteresis-free operations while maintaining excellent transistor performance is also necessary. In addition, passivation, integration, and stability of SWNT transistors require systematic investigations to cooperate with other functional parts. Moreover, developing reliable and small-area metal contacts for both p-type and n-type SWNT FETs in a sub-10- channel length also requires great research efforts to achieve energy-efficient digital electronics. With the advancement in the above developments, SWNT electronics will finally become an indispensable part of future electronics.

References

1. Saito R, Dresselhaus G, Dresselhaus MS (1998) Physical properties of carbon nanotubes. Imperial College Press, London, p 1 ([online resource](#))

2. Javey A, Guo J, Wang Q, Lundstrom M, Dai H (2003) Ballistic carbon nanotube field-effect transistors. *Nature* 424:654–657
3. Zhou X, Park JY, Huang S, Liu J, McEuen PL (2005) Band structure, phonon scattering, and the performance limit of single-walled carbon nanotube transistors. *Phys Rev Lett* 95:146805
4. Rutherglen C, Jain D, Burke P (2009) Nanotube electronics for radiofrequency applications. *Nat Nanotechnol* 4:811–819
5. Durkop T, Getty SA, Cobas E, Fuhrer MS (2004) Extraordinary mobility in semiconducting carbon nanotubes. *Nano Lett* 4:35–39
6. Li SD, Yu Z, Yen SF, Tang WC, Burke PJ (2004) Carbon nanotube transistor operation at 2.6 GHz. *Nano Lett* 4:753–756
7. Nougaret L, Happy H, Dambrine G, Derycke V, Bourgoin JP, Green AA, Hersam MC (2009) 80 GHz field-effect transistors produced using high purity semiconducting single-walled carbon nanotubes. *Appl Phys Lett* 94:243505
8. Wang C, Badmaev A, Jooyaie A, Bao M, Wang KL, Galatsis K, Zhou C (2011) Radio frequency and linearity performance of transistors using high-purity semiconducting carbon nanotubes. *ACS Nano* 5:4169–4176
9. Steiner M, Engel M, Lin YM, Wu YQ, Jenkins K, Farmer DB, Humes JJ, Yoder NL, Seo JWT, Green AA, Hersam MC, Krupke R, Avouris P (2012) High-frequency performance of scaled carbon nanotube array field-effect transistors. *Appl Phys Lett* 101:053123
10. Hu Y, Kang L, Zhao Q, Zhong H, Zhang S, Yang L, Wang Z, Lin J, Li Q, Zhang Z, Peng L, Liu Z, Zhang J (2015) Growth of high-density horizontally aligned SWNT arrays using Trojan catalysts. *Nat Commun* 6:6099
11. Cao Y, Brady GJ, Gui H, Rutherglen C, Arnold MS, Zhou C (2016) Radio frequency transistors using aligned semiconducting carbon nanotubes with current-gain cutoff frequency and maximum oscillation frequency simultaneously greater than 70 GHz. *ACS Nano* 10:6782–6790
12. Le Louarn A, Kapche F, Bethoux JM, Happy H, Dambrine G, Derycke V, Chenevier P, Izard N, Goffman MF, Bourgoin JP (2007) Intrinsic current gain cutoff frequency of 30 GHz with carbon nanotube transistors. *Appl Phys Lett* 90:233108
13. Che Y, Badmaev A, Jooyaie A, Wu T, Zhang J, Wang C, Galatsis K, Enaya HA, Zhou C (2012) Self-aligned T-gate high-purity semiconducting carbon nanotube RF transistors operated in quasi-ballistic transport and quantum capacitance regime. *ACS Nano* 6:6936–6943
14. Che Y, Lin YC, Kim P, Zhou C (2013) T-gate aligned nanotube radio frequency transistors and circuits with superior performance. *ACS Nano* 7:4343–4350
15. Kocabas C, Dunham S, Cao Q, Cimino K, Ho X, Kim HS, Dawson D, Payne J, Stuenkel M, Zhang H, Banks T, Feng M, Rotkin SV, Rogers JA (2009) High-frequency performance of submicrometer transistors that use aligned arrays of single-walled carbon nanotubes. *Nano Lett* 9:1937–1943
16. Wang Z, Liang S, Zhang Z, Liu H, Zhong H, Ye LH, Wang S, Zhou W, Liu J, Chen Y, Zhang J, Peng LM (2014) Scalable fabrication of ambipolar transistors and radio-frequency circuits using aligned carbon nanotube arrays. *Adv Mater* 26:645–652
17. Cao Y, Che YC, Gui H, Cao X, Zhou CW (2016) Radio frequency transistors based on ultra-high purity semiconducting carbon nanotubes with superior extrinsic maximum oscillation frequency. *Nano Res* 9:363–371
18. Cao Y, Che YC, Seo JWT, Gui H, Hersam MC, Zhou CW (2016) High-performance radio frequency transistors based on diameter-separated semiconducting carbon nanotubes. *Appl Phys Lett* 108:233105. doi:[10.1063/1.4953074](https://doi.org/10.1063/1.4953074)
19. Baumgardner JE, Pesetski AA, Murduck JM, Przybysz JX, Adam JD, Zhang H (2007) Inherent linearity in carbon nanotube field-effect transistors. *Appl Phys Lett* 91:052107. doi:[10.1063/1.2760159](https://doi.org/10.1063/1.2760159)
20. Mothes S, Claus M, Schroter M (2015) Toward linearity in Schottky barrier CNTFETs. *IEEE Trans Nanotechnol* 14:372–378
21. Wang Z, Ding L, Pei T, Zhang Z, Wang S, Yu T, Ye X, Peng F, Li Y, Peng LM (2010) Large signal operation of small band-gap carbon nanotube-based ambipolar transistor: a high-performance frequency doubler. *Nano Lett* 10:3648–3655
22. Kocabas C, Kim HS, Banks T, Rogers JA, Pesetski AA, Baumgardner JE, Krishnaswamy SV, Zhang H (2008) Radio frequency analog electronics based on carbon nanotube transistors. *Proc Natl Acad Sci USA* 105:1405–1409
23. Jensen K, Weldon J, Garcia H, Zettl A (2007) Nanotube radio. *Nano Lett* 7:3508–3511

24. Nikonov DE, Young IA (2012) Uniform methodology for benchmarking beyond-CMOS logic devices. In: 2012 IEEE international electron devices meeting (IEDM), San Francisco, CA, USA
25. Tans SJ, Verschueren ARM, Dekker C (1998) Room-temperature transistor based on a single carbon nanotube. *Nature* 393:49–52
26. Qiu C, Zhang Z, Zhong D, Si J, Yang Y, Peng LM (2015) Carbon nanotube feedback-gate field-effect transistor: suppressing current leakage and increasing on/off ratio. *ACS Nano* 9:969–977
27. Purewal MS, Hong BH, Ravi A, Chandra B, Hone J, Kim P (2007) Scaling of resistance and electron mean free path of single-walled carbon nanotubes. *Phys Rev Lett* 98:186808
28. Weitz RT, Zschieschang U, Forment-Aliaga A, Kalblein D, Burghard M, Kern K, Klauk H (2009) Highly reliable carbon nanotube transistors with patterned gates and molecular gate dielectric. *Nano Lett* 9:1335–1340
29. Franklin AD, Chen Z (2010) Length scaling of carbon nanotube transistors. *Nat Nanotechnol* 5:858–862
30. Franklin AD, Luisier M, Han SJ, Tulevski G, Breslin CM, Gignac L, Lundstrom MS, Haensch W (2012) Sub-10 nm carbon nanotube transistor. *Nano Lett* 12:758–762
31. Cao Q, Han SJ, Tersoff J, Franklin AD, Zhu Y, Zhang Z, Tulevski GS, Tang J, Haensch W (2015) End-bonded contacts for carbon nanotube transistors with low, size-independent resistance. *Science* 350:68–72
32. Liu X, Han S, Zhou C (2006) Novel nanotube-on-insulator (NOI) approach toward single-walled carbon nanotube devices. *Nano Lett* 6:34–39
33. Ryu K, Badmaev A, Wang C, Lin A, Patil N, Gomez L, Kumar A, Mitra S, Wong HS, Zhou C (2009) CMOS-analogous wafer-scale nanotube-on-insulator approach for submicrometer devices and integrated circuits using aligned nanotubes. *Nano Lett* 9:189–197
34. Shulaker MM, Van Rethy J, Wu TF, Liyanage LS, Wei H, Li Z, Pop E, Gielen G, Wong HS, Mitra S (2014) Carbon nanotube circuit integration up to sub-20 nm channel lengths. *ACS Nano* 8:3434–3443
35. Shulaker MM, Hills G, Patil N, Wei H, Chen HY, Wong HS, Mitra S (2013) Carbon nanotube computer. *Nature* 501:526–530
36. Kim HS, Jeon EK, Kim JJ, So HM, Chang H, Lee JO, Park N (2008) Air-stable n-type operation of Gd-contacted carbon nanotube field effect transistors. *Appl Phys Lett* 93:123106. doi:[10.1063/1.2990642](https://doi.org/10.1063/1.2990642)
37. Ding L, Wang S, Zhang Z, Zeng Q, Wang Z, Pei T, Yang L, Liang X, Shen J, Chen Q, Cui R, Li Y, Peng LM (2009) Y-contacted high-performance n-type single-walled carbon nanotube field-effect transistors: scaling and comparison with Sc-contacted devices. *Nano Lett* 9:4209–4214
38. Zhang ZY, Liang XL, Wang S, Yao K, Hu YF, Zhu YZ, Chen Q, Zhou WW, Li Y, Yao YG, Zhang J, Peng LM (2007) Doping-free fabrication of carbon nanotube based ballistic CMOS devices and circuits. *Nano Lett* 7:3603–3607
39. Shahrjerdi D, Franklin AD, Oida S, Ott JA, Tulevski GS, Haensch W (2013) High-performance air-stable n-type carbon nanotube transistors with erbium contacts. *ACS Nano* 7:8303–8308
40. Wang C, Ryu K, Badmaev A, Zhang J, Zhou C (2011) Metal contact engineering and registration-free fabrication of complementary metal-oxide semiconductor integrated circuits using aligned carbon nanotubes. *ACS Nano* 5:1147–1153
41. Suriyasena Liyanage L, Xu X, Pitner G, Bao Z, Wong HS (2014) VLSI-compatible carbon nanotube doping technique with low work-function metal oxides. *Nano Lett* 14:1884–1890
42. Javey A, Tu R, Farmer DB, Guo J, Gordon RG, Dai H (2005) High performance n-type carbon nanotube field-effect transistors with chemically doped contacts. *Nano Lett* 5:345–348
43. Geier ML, Moudgil K, Barlow S, Marder SR, Hersam MC (2016) Controlled n-type doping of carbon nanotubes by an organorhodium dimer. *Nano Lett* 16:4329–4334
44. Wei H, Shulaker M, Wong HSP, Mitra S (2013) Monolithic three-dimensional integration of carbon nanotube FET complementary logic circuits. 2013 IEEE international electron devices meeting (IEDM), San Francisco, CA, USA
45. Zhang PP, Qiu CG, Zhang ZY, Ding L, Chen BY, Peng LM (2016) Performance projections for ballistic carbon nanotube FinFET at circuit level. *Nano Res* 9:1785–1794
46. Franklin AD, Koswatta SO, Farmer DB, Smith JT, Gignac L, Breslin CM, Han SJ, Tulevski GS, Miyazoe H, Haensch W, Tersoff J (2013) Carbon nanotube complementary wrap-gate transistors. *Nano Lett* 13:2490–2495

47. Shulaker MM, Saraswat K, Wong HSP, Mitra S (2014) Monolithic three-dimensional integration of carbon nanotube FETs with silicon CMOS. In: VLSI technology (VLSI-technology): digest of technical papers, 2014 Symposium on VLSI Technology and Circuits, Honolulu, HI, USA
48. Cao Q, Kim HS, Pimparkar N, Kulkarni JP, Wang C, Shim M, Roy K, Alam MA, Rogers JA (2008) Medium-scale carbon nanotube thin-film integrated circuits on flexible plastic substrates. *Nature* 454:495–500
49. Chen P, Fu Y, Aminirad R, Wang C, Zhang J, Wang K, Galatsis K, Zhou C (2011) Fully printed separated carbon nanotube thin film transistor circuits and its application in organic light emitting diode control. *Nano Lett* 11:5301–5308
50. Ha M, Xia Y, Green AA, Zhang W, Renn MJ, Kim CH, Hersam MC, Frisbie CD (2010) Printed, sub-3 V digital circuits on plastic from aqueous carbon nanotube inks. *ACS Nano* 4:4388–4395
51. Noh J, Jung K, Kim J, Kim S, Cho S, Cho G (2012) Fully gravure-printed flexible full adder using SWNT-based TFTs. *IEEE Electron Device Lett* 33:1574–1576
52. Noh J, Jung M, Jung K, Lee G, Kim J, Lim S, Kim D, Choi Y, Kim Y, Subramanian V, Cho G (2011) Fully gravure-printed D flip-flop on plastic foils using single-walled carbon-nanotube-based TFTs. *IEEE Electron Device Lett* 32:638–640
53. Sun DM, Timmermans MY, Kaskela A, Nasibulin AG, Kishimoto S, Mizutani T, Kauppinen EI, Ohno Y (2013) Mouldable all-carbon integrated circuits. *Nat Commun* 4:2302
54. Sun DM, Timmermans MY, Tian Y, Nasibulin AG, Kauppinen EI, Kishimoto S, Mizutani T, Ohno Y (2011) Flexible high-performance carbon nanotube integrated circuits. *Nat Nanotechnol* 6:156–161
55. Wang C, Hwang D, Yu Z, Takei K, Park J, Chen T, Ma B, Javey A (2013) User-interactive electronic skin for instantaneous pressure visualization. *Nat Mater* 12:899–904
56. Wang C, Zhang J, Ryu K, Badmaev A, De Arco LG, Zhou C (2009) Wafer-scale fabrication of separated carbon nanotube thin-film transistors for display applications. *Nano Lett* 9:4285–4291
57. Zhang J, Fu Y, Wang C, Chen PC, Liu Z, Wei W, Wu C, Thompson ME, Zhou C (2011) Separated carbon nanotube macroelectronics for active matrix organic light-emitting diode displays. *Nano Lett* 11:4852–4858
58. Forrest SR (2004) The path to ubiquitous and low-cost organic electronic appliances on plastic. *Nature* 428:911–918
59. Sekitani T, Zschieschang U, Klauk H, Someya T (2010) Flexible organic transistors and circuits with extreme bending stability. *Nat Mater* 9:1015–1022
60. Cong S, Cao Y, Fang X, Wang YF, Liu QZ, Gui H, Shen CF, Cao X, Kim ES, Zhou CW (2016) Carbon nanotube macroelectronics for active matrix polymer-dispersed liquid crystal displays. *ACS Nano* 10:10068–10074
61. Street R (2000) Introduction. In: Street R (ed) *Technology and applications of amorphous silicon*. Springer, New York, pp 1–6
62. Snow ES, Novak JP, Campbell PM, Park D (2003) Random networks of carbon nanotubes as an electronic material. *Appl Phys Lett* 82:2145–2147
63. Engel M, Small JP, Steiner M, Freitag M, Green AA, Hersam MC, Avouris P (2008) Thin film nanotube transistors based on self-assembled, aligned, semiconducting carbon nanotube arrays. *ACS Nano* 2:2445–2452
64. Meitl MA, Zhou YX, Gaur A, Jeon S, Usrey ML, Strano MS, Rogers JA (2004) Solution casting and transfer printing single-walled carbon nanotube films. *Nano Lett* 4:1643–1647
65. LeMieux MC, Roberts M, Barman S, Jin YW, Kim JM, Bao Z (2008) Self-sorted, aligned nanotube networks for thin-film transistors. *Science* 321:101–104
66. Vosgueritchian M, LeMieux MC, Dodge D, Bao Z (2010) Effect of surface chemistry on electronic properties of carbon nanotube network thin film transistors. *ACS Nano* 4:6137–6145
67. Snow ES, Campbell PM, Ancona MG, Novak JP (2005) High-mobility carbon-nanotube thin-film transistors on a polymeric substrate. *Appl Phys Lett* 86:033105
68. Wang C, Zhang J, Zhou C (2010) Macroelectronic integrated circuits using high-performance separated carbon nanotube thin-film transistors. *ACS Nano* 4:7123–7132
69. Rouhi N, Jain D, Zand K, Burke PJ (2011) Fundamental limits on the mobility of nanotube-based semiconducting inks. *Adv Mater* 23:94–99
70. Takahashi T, Takei K, Gillies AG, Fearing RS, Javey A (2011) Carbon nanotube active-matrix backplanes for conformal electronics and sensors. *Nano Lett* 11:5408–5413

71. Wang C, Chien JC, Takei K, Takahashi T, Nah J, Niknejad AM, Javey A (2012) Extremely bendable, high-performance integrated circuits using semiconducting carbon nanotube networks for digital, analog, and radio-frequency applications. *Nano Lett* 12:1527–1533
72. Jung M, Kim J, Noh J, Lim N, Lim C, Lee G, Kim J, Kang H, Jung K, Leonard AD, Tour JM, Cho G (2010) All-printed and roll-to-roll-printable 13.56-MHz-operated 1-bit RF tag on plastic foils. *IEEE Trans Electron Devices* 57:571–580
73. Noh J, Kim S, Jung K, Kim J, Cho S, Cho G (2011) Fully gravure printed half adder on plastic foils. *IEEE Electron Device Lett* 32:1555–1557
74. Zou J, Zhang K, Li J, Zhao Y, Wang Y, Pillai SK, Volkan Demir H, Sun X, Chan-Park MB, Zhang Q (2015) Carbon nanotube driver circuit for 6×6 organic light emitting diode display. *Sci Rep* 5:11755
75. Takahashi T, Yu Z, Chen K, Kiriya D, Wang C, Takei K, Shiraki H, Chen T, Ma B, Javey A (2013) Carbon nanotube active-matrix backplanes for mechanically flexible visible light and X-ray imagers. *Nano Lett* 13:5425–5430
76. Yeom C, Chen K, Kiriya D, Yu Z, Cho G, Javey A (2015) Large-area compliant tactile sensors using printed carbon nanotube active-matrix backplanes. *Adv Mater* 27:1561–1566
77. Chen B, Zhang P, Ding L, Han J, Qiu S, Li Q, Zhang Z, Peng LM (2016) Highly uniform carbon nanotube field-effect transistors and medium scale integrated circuits. *Nano Lett* 16:5120–5128
78. Ha TJ, Kiriya D, Chen K, Javey A (2014) Highly stable hysteresis-free carbon nanotube thin-film transistors by fluorocarbon polymer encapsulation. *ACS Appl Mater Interfaces* 6:8441–8446
79. Zhang J, Wang C, Fu Y, Che Y, Zhou C (2011) Air-stable conversion of separated carbon nanotube thin-film transistors from p-type to n-type using atomic layer deposition of high-kappa oxide and its application in CMOS logic circuits. *ACS Nano* 5:3284–3292
80. Ha TJ, Chen K, Chuang S, Yu KM, Kiriya D, Javey A (2015) Highly uniform and stable n-type carbon nanotube transistors by using positively charged silicon nitride thin films. *Nano Lett* 15:392–397
81. Geier ML, McMorro JJ, Xu W, Zhu J, Kim CH, Marks TJ, Hersam MC (2015) Solution-processed carbon nanotube thin-film complementary static random access memory. *Nat Nanotechnol* 10:944–948
82. Chen H, Cao Y, Zhang J, Zhou C (2014) Large-scale complementary macroelectronics using hybrid integration of carbon nanotubes and IGZO thin-film transistors. *Nat Commun* 5:4097
83. Chen K, Gao W, Emaminejad S, Kiriya D, Ota H, Nyein HY, Takei K, Javey A (2016) Printed carbon nanotube electronics and sensor systems. *Adv Mater* 28:4397–4414
84. Cai L, Zhang SM, Miao JS, Yu ZB, Wang C (2015) Fully printed foldable integrated logic gates with tunable performance using semiconducting carbon nanotubes. *Adv Funct Mater* 25:5698–5705
85. Kim B, Jang S, Geier ML, Prabhumirashi PL, Hersam MC, Dodabalapur A (2014) High-speed, inkjet-printed carbon nanotube/zinc tin oxide hybrid complementary ring oscillators. *Nano Lett* 14:3683–3687
86. Cao X, Chen H, Gu X, Liu B, Wang W, Cao Y, Wu F, Zhou C (2014) Screen printing as a scalable and low-cost approach for rigid and flexible thin-film transistors using separated carbon nanotubes. *ACS Nano* 8:12769–12776
87. Xu W, Dou J, Zhao J, Tan H, Ye J, Tange M, Gao W, Xu W, Zhang X, Guo W, Ma C, Okazaki T, Zhang K, Cui Z (2016) Printed thin film transistors and CMOS inverters based on semiconducting carbon nanotube ink purified by a nonlinear conjugated copolymer. *Nanoscale* 8:4588–4598
88. Ha M, Seo JW, Prabhumirashi PL, Zhang W, Geier ML, Renn MJ, Kim CH, Hersam MC, Frisbie CD (2013) Aerosol jet printed, low voltage, electrolyte gated carbon nanotube ring oscillators with sub-5 μ s stage delays. *Nano Lett* 13:954–960
89. Vuttipittayamongkol P, Wu FQ, Chen HT, Cao X, Liu BL, Zhou CW (2015) Threshold voltage tuning and printed complementary transistors and inverters based on thin films of carbon nanotubes and indium zinc oxide. *Nano Res* 8:1159–1168
90. Che Y, Wang C, Liu J, Liu B, Lin X, Parker J, Beasley C, Wong HS, Zhou C (2012) Selective synthesis and device applications of semiconducting single-walled carbon nanotubes using isopropyl alcohol as feedstock. *ACS Nano* 6:7454–7462
91. Kocabas C, Hur SH, Gaur A, Meitl MA, Shim M, Rogers JA (2005) Guided growth of large-scale, horizontally aligned arrays of single-walled carbon nanotubes and their use in thin-film transistors. *Small* 1:1110–1116

92. Li J, Liu K, Liang S, Zhou W, Pierce M, Wang F, Peng L, Liu J (2014) Growth of high-density-aligned and semiconducting-enriched single-walled carbon nanotubes: decoupling the conflict between density and selectivity. *ACS Nano* 8:554–562
93. Ding L, Wang Z, Pei T, Zhang Z, Wang S, Xu H, Peng F, Li Y, Peng LM (2011) Self-aligned U-gate carbon nanotube field-effect transistor with extremely small parasitic capacitance and drain-induced barrier lowering. *ACS Nano* 5:2512–2519
94. Chen YF, Fuhrer MS (2005) Electric-field-dependent charge-carrier velocity in semiconducting carbon nanotubes. *Phys Rev Lett* 95:236803
95. Clifford JP, John DL, Castro LC, Pulfrey DL (2004) Electrostatics of partially gated carbon nanotube FETs. *IEEE Trans Nanotechnol* 3:281–286
96. Heinze S, Tersoff J, Martel R, Derycke V, Appenzeller J, Avouris P (2002) Carbon nanotubes as schottky barrier transistors. *Phys Rev Lett* 89:106801
97. Qiu CG, Zhang ZY, Xiao MM, Yang YJ, Zhong DL, Peng LM (2017) Scaling carbon nanotube complementary transistors to 5-nm gate lengths. *Science* 355:271–276
98. Kang D, Park N, Ko JH, Bae E, Park W (2005) Oxygen-induced p-type doping of a long individual single-walled carbon nanotube. *Nanotechnology* 16:1048–1052
99. Joo Y, Brady GJ, Arnold MS, Gopalan P (2014) Dose-controlled, floating evaporative self-assembly and alignment of semiconducting carbon nanotubes from organic solvents. *Langmuir ACS J Surf Colloids* 30:3460–3466
100. Brady GJ, Joo Y, Wu MY, Shea MJ, Gopalan P, Arnold MS (2014) Polyfluorene-sorted, carbon nanotube array field-effect transistors with increased current density and high on/off ratio. *ACS Nano* 8:11614–11621
101. Javey A, Kim H, Brink M, Wang Q, Ural A, Guo J, McIntyre P, McEuen P, Lundstrom M, Dai HJ (2002) High-kappa dielectrics for advanced carbon-nanotube transistors and logic gates. *Nat Mater* 1:241–246
102. Derycke V, Martel R, Appenzeller J, Avouris P (2001) Carbon nanotube inter- and intramolecular logic gates. *Nano Lett* 1:453–456
103. Chen ZH, Appenzeller J, Lin YM, Sippel-Oakley J, Rinzler AG, Tang JY, Wind SJ, Solomon PM, Avouris P (2006) An integrated logic circuit assembled on a single carbon nanotube. *Science* 311:1735
104. Pei T, Zhang PP, Zhang ZY, Qiu CG, Liang SB, Yang YJ, Wang S, Peng LM (2014) Modularized construction of general integrated circuits on individual carbon nanotubes. *Nano Lett* 14:3102–3109
105. Javey A, Kong J (2009) Carbon nanotube electronics. Springer Science & Business Media, New York
106. Odom TW, Huang J-L, Kim P, Lieber CM (1998) Atomic structure and electronic properties of single-walled carbon nanotubes. *Nature* 391:62–64
107. Zou Y, Li Q, Liu J, Jin Y, Qian Q, Jiang K, Fan S (2013) Fabrication of all-carbon nanotube electronic devices on flexible substrates through CVD and transfer methods. *Adv Mater* 25:6050–6056
108. Moiala A, Nasibulin AG, Brown DP, Jiang H, Khriachtchev L, Kauppinen EI (2006) Single-walled carbon nanotube synthesis using ferrocene and iron pentacarbonyl in a laminar flow reactor. *Chem Eng Sci* 61:4393–4402
109. Zhang JL, Wang C, Zhou CW (2012) Rigid/flexible transparent electronics based on separated carbon nanotube thin-film transistors and their application in display electronics. *ACS Nano* 6:7412–7419
110. Arnold MS, Green AA, Hulvat JF, Stupp SI, Hersam MC (2006) Sorting carbon nanotubes by electronic structure using density differentiation. *Nat Nanotechnol* 1:60–65
111. Cao Q, Rogers JA (2009) Ultrathin films of single-walled carbon nanotubes for electronics and sensors: a review of fundamental and applied aspects. *Adv Mater* 21:29–53
112. Rouhi N, Jain D, Burke PJ (2011) High-performance semiconducting nanotube inks: progress and prospects. *ACS Nano* 5:8471–8487
113. Arnold MS, Stupp SI, Hersam MC (2005) Enrichment of single-walled carbon nanotubes by diameter in density gradients. *Nano Lett* 5:713–718
114. Green AA, Hersam MC (2011) Nearly single-chirality single-walled carbon nanotubes produced via orthogonal iterative density gradient ultracentrifugation. *Adv Mater* 23:2185–2190
115. Liu H, Nishide D, Tanaka T, Kataura H (2011) Large-scale single-chirality separation of single-wall carbon nanotubes by simple gel chromatography. *Nat Commun* 2:309

116. Tu X, Manohar S, Jagota A, Zheng M (2009) DNA sequence motifs for structure-specific recognition and separation of carbon nanotubes. *Nature* 460:250–253
117. Sangwan VK, Ortiz RP, Alaboson JMP, Emery JD, Bedzyk MJ, Lauhon LJ, Marks TJ, Hersam MC (2012) Fundamental performance limits of carbon nanotube thin-film transistors achieved using hybrid molecular dielectrics. *ACS Nano* 6:7480–7488
118. Choi SJ, Wang C, Lo CC, Bennett P, Javey A, Bokor J (2012) Comparative study of solution-processed carbon nanotube network transistors. *Appl Phys Lett* 101:112104
119. Miyata Y, Shiozawa K, Asada Y, Ohno Y, Kitaura R, Mizutani T, Shinohara H (2011) Length-sorted semiconducting carbon nanotubes for high-mobility thin film transistors. *Nano Res* 4:963–970
120. Sze SM, Ng KK (2006) *Physics of semiconductor devices*. Wiley, Hoboken
121. Che YC, Chen HT, Gui H, Liu J, Liu BL, Zhou CW (2014) Review of carbon nanotube nano-electronics and macroelectronics. *Semicond Sci Technol* 29:073001
122. Ding J, Li Z, Lefebvre J, Cheng F, Dubey G, Zou S, Finnie P, Hrdina A, Scoles L, Lopinski GP, Kingston CT, Simard B, Malenfant PR (2014) Enrichment of large-diameter semiconducting SWCNTs by polyfluorene extraction for high network density thin film transistors. *Nanoscale* 6:2328–2339
123. Xu W, Zhao J, Qian L, Han X, Wu L, Wu W, Song M, Zhou L, Su W, Wang C, Nie S, Cui Z (2014) Sorting of large-diameter semiconducting carbon nanotube and printed flexible driving circuit for organic light emitting diode (OLED). *Nanoscale* 6:1589–1595
124. Cao C, Andrews JB, Kumar A, Franklin AD (2016) Improving contact interfaces in fully printed carbon nanotube thin-film transistors. *ACS Nano* 10:5221–5229
125. Lau PH, Takei K, Wang C, Ju Y, Kim J, Yu Z, Takahashi T, Cho G, Javey A (2013) Fully printed, high performance carbon nanotube thin-film transistors on flexible substrates. *Nano Lett* 13:3864–3869
126. Sajed F, Rutherglen C (2013) All-printed and transparent single walled carbon nanotube thin film transistor devices. *Appl Phys Lett* 103:143303. doi:[10.1063/1.4824475](https://doi.org/10.1063/1.4824475)
127. Kim SH, Hong K, Xie W, Lee KH, Zhang S, Lodge TP, Frisbie CD (2013) Electrolyte-gated transistors for organic and printed electronics. *Adv Mater* 25:1822–1846
128. Kim B, Park J, Geier ML, Hersam MC, Dodabalapur A (2015) Voltage-controlled ring oscillators based on inkjet printed carbon nanotubes and zinc tin oxide. *ACS Appl Mater Interfaces* 7:12009–12014
129. Kim B, Geier ML, Hersam MC, Dodabalapur A (2014) Complementary D flip-flops based on inkjet printed single-walled carbon nanotubes and zinc tin oxide. *IEEE Electron Device Lett* 35:1245–1247
130. Higuchi K, Kishimoto S, Nakajima Y, Tomura T, Takesue M, Hata K, Kauppinen EI, Ohno Y (2013) High-mobility, flexible carbon nanotube thin-film transistors fabricated by transfer and high-speed flexographic printing techniques. *Appl Phys Express* 6:085101
131. Cao X, Cao Y, Zhou C (2016) Imperceptible and ultraflexible p-type transistors and macroelectronics based on carbon nanotubes. *ACS Nano* 10:199–206
132. Yang YJ, Ding L, Han J, Zhang ZY, Peng LM (2017) High-performance complementary transistors and medium-scale integrated circuits based on carbon nanotube thin films. *ACS Nano* 11:4124–4132
133. Cao Q, Hur SH, Zhu ZT, Sun YG, Wang CJ, Meitl MA, Shim M, Rogers JA (2006) Highly bendable, transparent thin-film transistors that use carbon-nanotube-based conductors and semiconductors with elastomeric dielectrics. *Adv Mater* 18:304–309
134. Chae SH, Yu WJ, Bae JJ, Duong DL, Perello D, Jeong HY, Ta QH, Ly TH, Vu QA, Yun M, Duan X, Lee YH (2013) Transferred wrinkled Al_2O_3 for highly stretchable and transparent graphene-carbon nanotube transistors. *Nat Mater* 12:403–409

Carbon Nanotube Thin Film Transistors for Flat Panel Display Application

Xuelel Liang¹ · Jiye Xia¹ · Guodong Dong¹ ·
Boyuan Tian¹ · lianmao Peng¹

Received: 22 August 2016 / Accepted: 5 November 2016 / Published online: 21 November 2016
© Springer International Publishing Switzerland 2016

Abstract Carbon nanotubes (CNTs) are promising materials for both high performance transistors for high speed computing and thin film transistors for macroelectronics, which can provide more functions at low cost. Among macroelectronics applications, carbon nanotube thin film transistors (CNT-TFT) are expected to be used soon for backplanes in flat panel displays (FPDs) due to their superior performance. In this paper, we review the challenges of CNT-TFT technology. 8.61.7(for)-373.7(FPD of CNT-TF(s)-0111.1(and)2974.3(urrmens)-030.2-TFTs are critical

ureors in the

1 Introduction

Since its discovery nearly two-and-a-half decades ago, the carbon nanotube (CNT) remains of great interest as an emerging material in nano-science and technology [1, 2]. Because of its unique structure and superb electronic properties [3], single-walled CNTs (SWCNTs) are envisioned as the most promising candidate for information processing technologies beyond CMOS [4]. To compete with Si-based high performance transistors for computational devices, ideal carbon nanotube field-effect transistors (CNT-FETs) should be fabricated on well-aligned high-density semiconducting CNTs with controllable location, inter-tube spacing, and chirality on a 300-mm wafer scale [5, 6]. However, it is still a great challenge for such high standard SWCNT material production. In addition to the material challenge, the device fabrication technology is also far from ready for manufacturing, though some complicated CNT-FET circuits have been demonstrated [7–10]. The fabrication processes should be compatible or can be integrated with the highly developed Si-based chip fabrication technology, and the performance of the devices must be uniform around the wafer scale. Therefore, it is hard to predict whether the CNT-based high performance transistor technology will be ready at the time node around 2020, when the Si-based CMOS will reach its absolute performance limits [11].

In parallel to the high performance transistors for computational devices, such as microprocessor, thin film transistors (TFTs) are widely used for macroelectronics. The performance of the transistors required for the macroelectronics are not as high as those for the computational devices, while the costs and functions are critical concerns for the macroelectronics [11]. The channel materials for the thin film transistor are, therefore, not necessarily single crystal semiconductor material. Amorphous and polycrystalline semiconductors can be employed as the channel material, such as amorphous Si (a-Si), poly-Si, metal oxide, and organic semiconductors [12]. Nevertheless, performance uniformity is still strictly required for TFTs on large area substrates up to meters scale and even larger. The channel size of TFTs are usually several to hundreds of micrometers. Thus, the non-uniformity due to the channel material may be smoothed out in the large channel area and uniform performance on large area substrates is obtainable.

In recent years carbon nanotube thin film transistors (CNT-TFTs) have drawn more and more attentions. In CNT-TFTs, the channel layer is random network or partially aligned CNT films composed of numerous SWCNTs. Many methods have been reported for producing SWCNT thin film at low cost on large area substrates. In some aspects the reported performances of the CNT-TFTs are superior to those fabricated by the current TFT manufacturing technologies [13–25]. These make CNT-TFTs strong competitors in the field of macroelectronics [17–19] for products such as displays, flexible electronics, bio-chemical sensors, and solar cells.

Flat panel display (FPD), an industry with a total value of hundreds of billions of U.S. dollars [26], is undoubtedly one of the most important macroelectronic products. A backplane with TFT array is a necessary component of each FPD, which is used for pixel addressing. Actually, the development of FPDs burgeoned only when a-Si TFTs became available [12]. As FPDs develop to larger size, ultra-

high resolution, low power, high frame rate, and flexibility, the current TFT technologies are difficult to meet all these demands. Therefore, new materials and technologies for TFTs are demanded to keep the FPD industry growing.

As an emerging TFT technology, CNT-TFTs have shown high mobility, high on/off ratio, and high on-current [27, 28], the performance of which can surpass the current TFT technologies potentially. Moreover, the fabrication process is regarded as facile, reliable, scalable to large area, and compatible with the current TFT manufacturing process [29]. Therefore, CNT-TFT technology is very promising for the future FPD industry. Research on using CNT-TFTs for pixel-driving circuits for displays has been performed in many groups [24, 30, 31]. Active matrix organic light-emitting diode (AMOLED) displays driven by CNT-TFTs have been demonstrated in the laboratory [13, 32], though with limited yields.

Much of the effort on the application of CNT-TFTs for backplane FPD electronics has been in research laboratories previously, and now it is at a critical status of being transferred from lab to industry. Two-and-a-half decades have passed since the discovery of CNT; however, almost no electronic products of CNT-FETs have been commercialized. Since research on CNT-TFTs is progressing rapidly in recent years, we have good reasons to believe that FPD products integrated with CNT-TFT technology are possible in the near future.

In this paper, we review the progress on CNT-TFTs from the point of FPD manufacturing. This review is organized as follows. In Sect. 2, we briefly introduce the structure of the FPD. Herein, we show how to address pixels using a TFT array. In Sect. 3, we discuss the trends of the FPD products and their requirements for TFT technologies, and elucidate why CNT-TFTs are promising for future FPDs. In Sect. 4, we discuss the challenges of the CNT-TFT technology for display applications. The challenges are discussed from the aspects of materials, fabrication process, device performance, stability, and uniformity. Finally, in Sect. 5, we conclude the review and future prospect of CNT-TFT technology.

2 Flat Panel Displays and TFTs

A flat panel display comprises many pixels arranged in arrays, which compose an image. There is an element in each pixel that has an electro-optical effect, and this effect can be switched on and off for displaying an image. It is not an easy task to deliver picture data to each pixel of a FPD with millions of pixels. To deliver image data to the electro-optical element in each pixel correctly, an addressing circuit is needed for a FPD so that each pixel can be addressed individually. All of today's high quality displays use active matrix addressing, where there is at least one TFT in each pixel. The TFTs in each pixel are used as switching devices to set image data of the pixel in a short addressing time and to store it until the next refresh signal is obtained.

For a principle demo, as illustrated in Fig. 1, the TFT matrix is connected in rows and columns, with a common connection to the gate electrodes in each row, and a common connection to the drain terminals in each column (n-type FET). The source of each TFT is connected to the element for electro-optical effect. The image signal

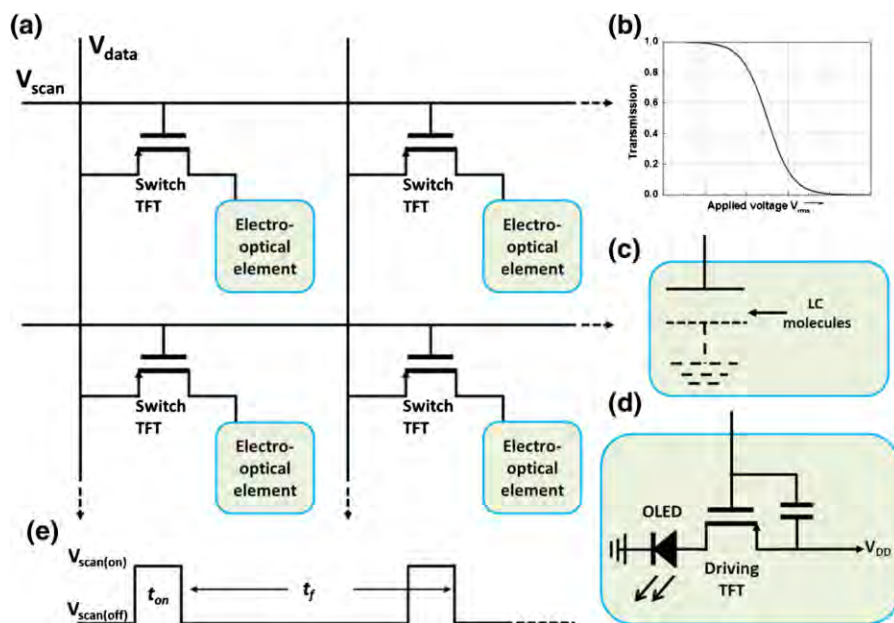


Fig. 1 **a** Active matrix layout. **b** Illustration of typical transmission versus voltage curve of LC. **c** Diagram of the electro-optical element based on LC and **d** OLED. **e** Row timing signal wave form

is fed into the pixel array in a serial row-by-row mode, by sequentially switching on each row of TFTs ($V_{scan} = V_{on}$), whilst holding the others in the off-state ($V_{scan} = V_{off}$). During the time interval of a row was switching on (t_{on}), the signal voltages (V_{data}) on the column electrodes of the display are applied in parallel to the common drains of TFTs. However, the signal will be sent to only the one row of the electro-optical effect elements connected to the row of TFTs, which has been turned on. At the end of t_{on} , that row is deselected (by switching the gate bias to V_{off}), and the adjacent row is switched on, and the process described above is repeated. In this way, the image information is loaded row by row during a frame time (t_f), and signals need to be maintained. Then the whole process is repeated with the next frame of image information.

The representatives of the electro-optical elements are realized using liquid crystal (LC) molecules or organic light emission diodes (OLED). In the liquid crystal display (LCD), the LC molecules work as the dielectrics of the capacitor in each pixel (Fig. 1c). When the capacitor is charged by V_{data} , the LC molecule will turn in the electric field, and the transmission of the ambient illumination is modulated in this way (shown in Fig. 1b). In the active matrix OLED (AMOLED) display, an OLED in the pixel gives emission of light when switched on. In addition to the addressing TFT, another driving TFT and a capacitor are needed, composing the 2T1C driving circuits for AMOLED (Fig. 1d). When the addressing TFT (switch transistor) is switched on by V_{scan} , V_{data} is sent to the pixel. Then the driving TFT is turned on and current flows through the OLED, which emits light. During the

time period of t_{on} , the capacitor is also charged, which can supply a voltage to keep the driving TFT on during t_f when the addressing TFT is off.

From the above discussion, we know the TFTs are crucial for a FPD. Actually,

a-Si. Also, the fabrication cost of IGZO TFTs is lower than LTPS. Though the mobility of a-IGZO is higher than a-Si, it is lower than that for LTPS [37], which limits its application in ultra-high resolution FPDs. More importantly, the narrow process window and poor long term stability are still challenges for the MO TFTs [36].

The current trends of FPDs products are large panel size, ultra-high resolution, low power, high frame rate, flexibility, and transparency. New materials and technologies for high performance TFTs are in high demand to keep the FPD industry growing. There are continuous efforts in searching for new types of TFTs to improve performance or to lower the production cost of TFTs. CNT-TFTs are promising candidates, which may comply with the requirements of the above trends.

Single-wall CNT (SWCNT) can be regarded as a seamless cylinder rolled by graphene. Though it is only one atomic thick, there are no dangling bonds in the surface. Owing to its perfect structure and quasi-one-dimensional quantum confinement effects, the carrier scattering in SWCNT was greatly reduced. The mean free path of carriers in SWCNT is up to micrometer, thus ballistic transport is easily obtained. The mobility of SWCNT can be high up to $100,000 \text{ cm}^2/\text{Vs}$ [11]. High performance CNT-TFTs with mobility ranging from tens to hundreds of cm^2/Vs have been reported by many research groups [15, 16, 38–41]. These results make CNT-TFTs very attractive for pixel driving circuits of display. The atomic thin body results in excellent gate control of the channel even in extremely scaled CNT-FETs. The strong carbon–carbon bond and the high thermal conductance allow it to carry high current up to 10^9 A/cm^2 . SWCNT is one of the most strong and flexible known materials. CNT thin film is transparent, making it suitable for transparent and flexible electronics. Moreover, CNT thin film can be fabricated at room temperature

Fig. 3 Demonstration of AMOLED display driven by CNT-TFTs. Optical microscope images of the single pixel circuit (**a**) and **b** 7 AMOLED arrays, each with 20×25 pixels. **c** Photograph showing the AMOLED array was turned on. Reprinted with permission from [13] (Copyright 2011 American Chemical Society). **d** A schematic cross-sectional perspective view of the single AMOLED pixel. **e** Photograph of the 6×6 pixel array. **f–i** Turn on image of the AMOLED array. Reprinted with permission from [32] (Copyright 2015 Nature Publishing Group)

4 Challenges of CNT-TFT Technology for Display

The components of a CNT-TFT includes a CNT thin film channel, electrodes (source, drain, and gate), and an insulating layer for gate dielectrics. For display application, the CNT-TFTs are fabricated in arrays on the backplane glass. The performance of the CNT-TFTs must comply with those requirements for pixel addressing and picture quality. The fabrication process must be facile, reliable, and scalable to large area. Low cost and compatibility to current TFT fabrication processes are also required. In the following, we discuss the challenges of the materials for CNT-TFTs (including the CNT thin film, the electrodes, and gate dielectrics), the device fabrication process, and the device performance.

4.1 SWCNT Materials and Thin Film Fabrication

The channel of CNT-TFTs is a two-dimensional film composed of numerous SWCNTs. Undoubtedly, high quality CNT thin film is critical to the performance of CNT-TFTs. The techniques for SWCNT thin films production can be divided into

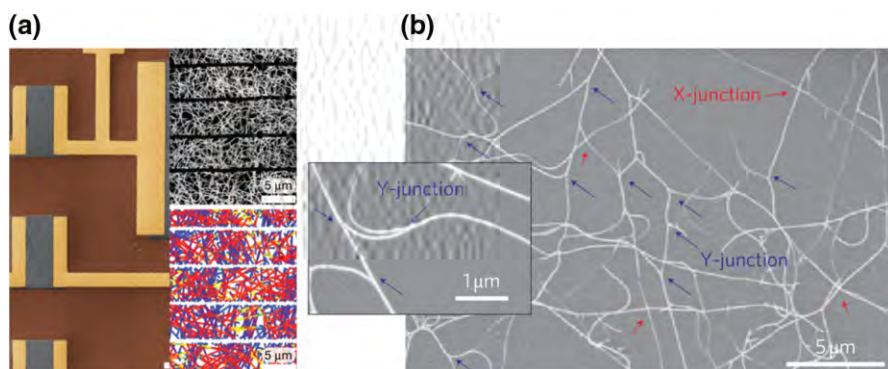


Fig. 4 Increasing the on/off ratio of the CNT-TFT. **a** Stripping high density SWCNT thin film. Reprinted with permission from [20] (Copyright 2008 Nature Publishing Group). **b** Using low density SWCNT thin film. Reprinted with permission from [41] (Copyright 2011 Nature Publishing Group)

with longer channel lengths results in very low on-current density [41]. To obtain high enough current for pixel driving, the channel width of the CNT-TFT has to be enlarged meanwhile. Thus, the size of such CNT-TFT is pretty large, which limits the application of this strategy for high pixel density displays. Moreover, CVD growth on substrates is included in both of the two CNT thin film fabrication techniques, which is a relatively low productivity process. Whether the CVD growth of CNT is scalable to large area substrates, e.g. the size of backplane glasses, is not known. Therefore, neither the direct growth on target substrates method and the growth and transfer to target substrates method are suitable for mass production of CNT-TFT backplanes.

SWCNTs can be generated in powder form by several methods, and the products can be dissolved in solutions [29]. Then CNT thin films can be produced by solution deposition. The high temperature CNT growth processes are separated by the thin film fabrication processes in this route, which enables the thin film to be fabricated at room temperature on arbitrary substrates. Although the as-produced CNTs are a mixture of both semiconducting and metallic types, a variety of post-production sorting techniques have been developed to enrich semiconducting SWCNTs in the solution. Some of these techniques include DNA-assisted sorting [48, 49], conjugated polymer-assisted sorting [50, 51], porphyrin-assisted sorting [52], sorting using copolymers [53], gel chromatography [54, 55], aqueous two-phase extraction [56], and density gradient ultracentrifugation (DGU) [57]. A high purity of separated semiconducting SWCNTs up to 99.9%, measured by electrical testing, has been reported [58]. Although still not meeting the purity requirement of 99.9999% [5] for high performance FETs, it does satisfy CNT-TFTs. A benefit of these research progresses is that SWCNT solutions with semiconducting purity above 99% are now commercially available [59, 60]. Currently the sorted SWCNT solution is pretty expensive, e.g., several hundreds of U.S. dollars per milligram, which is an obstacle for mass production of CNT-TFT backplanes. However, this is mostly due to the relatively small quantity of market demand presently. If production of the sorted SWCNT material is scaled up, the cost will be reduced greatly.

Once high purity semiconducting SWCNT solutions are obtained, industrially well-established solution deposition methods such as ink-jet/aerosol printing [24, 61, 62] can be used to deposit SCWNTs onto the large size backplane glasses or flexible substrates with high throughput and low cost. More importantly, fabrication of the SWCNT films is compatible with the existing TFT backplane manufacturing process. Therefore, solution processed SWCNTs are the best choice for CNT-TFT backplane electronics. Hereafter, we focus our discussions on the solution processed SWCNTs.

Many methods have been reported for SWCNT thin film fabrication from SWCNT solutions. Among these methods, the most used is direct solution deposition [15, 21, 38]. In this method, a piece of substrate is immersed into the SWCNT solution for certain time, and then the SWCNTs are deposited onto the substrate, which forms a thin film. The film density can be controlled by the solution concentration and soaking time. This method is very simple; however, the throughput is low because the deposition usually takes hours to even several days to obtain a film with the desired density [21, 38]. To improve the SWCNT deposition, the surface of the substrate is commonly functionalized with a self-assembling monolayer by using aminopropyltriethoxysilane (APTES) [15], poly-L-lysine (PLL) [63–65], or HMDS [16, 39, 66]. Thus, pretty uniform SWCNT films are obtained in relatively short time. However, the short range uniformity of the film is usually worse than long range [13, 15, 67], which leads to higher performance fluctuation when the TFTs are scaled down for high pixel density displays.

In addition to the direct deposition method, the well-established ink-jet or aerosol printing methods amenable to solution processed SWCNTs [24, 30, 61], as mentioned before. These thin film fabrication technologies are high throughput and scalable to large area. Printing is also an “additive” lithographic technique, which can avoid the wasting of material and the use of photolithography or other expensive lithographic tools, potentially reducing the fabrication cost. An OLED driving circuit composed of fully printed CNT-TFTs on Si wafers controlled the OLED successfully and was demonstrated by Chen et al. [24]. Similar circuits for OLED driving on flexible substrate was reported by Xu et al. [30]. These works demonstrate the significant potential of printed CNT-TFTs for display backplane applications.

The uniformity of the printed CNT films is usually worse than those of direct solution deposited, especially at the rim of the printed patterns, due to the coffee ring effect. Many more contaminants are easily observed in the as-fabricated SWCNT films by printing methods than solution deposition. There are usually excessive surfactants and/or other species in the CNT solution, which are used for CNT dispersion and sorting. In the printing process, all of these species are left on the substrate, which contaminates the CNT thin film. Therefore, a thorough washing step is needed to clean these contaminants [24, 30, 68, 69]. Meanwhile, in the solution deposition processes, the deposition is assisted by the electrostatic interaction between the functionalized substrate and the SWCNTs in solution [70, 71] so that less contaminants were observed.

SWCNT thin films, generated by either solution deposition or printing, are random networks, which include numerous inter-tube junctions. These junctions

limit the charge transport through the μm . The number of the junctions can be reduced by aligning the tubes, thus improving the mobility of the μm . Densely aligned SWCNT μms can be obtained in self-assembly processes by tuning the interaction at the interface of the three phases, i.e. CNT solution, air, and the solid substrate [66, 72–74]. Figure 5 depicts some self-assembled SWCNT stripes with aligned tubes. However, the critical disadvantages of the self-assembly processes are the low throughput and difficult to scale up to large area. Otherwise, the self-assembly process is not easy to control, e.g. the positions (or the starting position of the first stripe) and the spacing between these self-assembled stripes shown in Fig. 5 are not strictly controlled. Therefore, such μms are not suitable for TFT array fabrication.

External forces can also be employed to align SWCNTs. A notable alignment method is ac-dielectrophoresis (DEP), where ac-voltage is applied between two

Fig. 5 Densely aligned SWCNT thin μm obtained by self-assembly method. **a–c** Evaporation self-assembly. Reprinted with permission from [72] (Copyright 2008 American Chemical Society). **d–f** Dose-controlled coating evaporation method. Reprinted with permission from [66] (Copyright 2014 American Chemical Society)

electrodes to align SWCNTs, as shown in Fig. 6 [75, 76]. Highly aligned SWNTs with controllable density can be obtained by tuning the solution concentration or the ac-voltage frequency. The advantages of DEP are scalable, location selective and high efficiency, wherein the CNT assembly can be finished in several minutes or even seconds [77]. However, DEP preferentially assemble metallic SWCNT, which results in low on/off ratios of the TFTs unless extremely high purity semiconducting SWCNT solution was used [78].

Table 2 compared the above methods for SWCNT thin film fabrication using solution processed materials. The direct solution deposition and printing methods are more promising; however, they are still under-developed for mass production of CNT-TFT backplanes. More efforts are needed to develop the techniques of CNT thin film fabrication. It should be noted that CNT-TFTs fabricated on glass substrates that are being used for current TFT backplanes are seldom reported (as shown in Table 3). Though might be a trivial issue, it should be confirmed before the CNT-TFTs go out of the laboratory to manufacturing.

Fig. 6 SWCNTs assembled by DEP. **a–c** Fringing field DEP method Reprinted with permission from [76] (Copyright 2014 Nature Publishing Group). **d–g** Normal co-planar DEP method. Reprinted with permission from [75] (Copyright 2011 American Chemical Society). **h–i** Two step fringing field DEP method. Reprinted with permission from [99] (Copyright 2016 Science China Press). **a** shows the experimental set-up for fringing field DEP, while **d** for normal co-planar DEP. **c** Simulated space distribution of the fringing electric field. **e–d** Control the assembled SWCNT density by simply tuning the concentration of the solution while keeping all other DEP parameters fixed. **h** Two SWCNT arrays were assembled at the source and drain electrodes sequentially which form a cascade structure for reducing the possibility of percolating metallic pathways and the inter-tube junctions in each path

Table 2 Comparison of the SWCNT thin film fabrication methods

	Direct solution deposition	Printing (ink jet/aerosol)	Self-assembly	DEP
CNT geometry	Random network	Random network	Aligned	Aligned
Contamination	Low	High (cleaning needed)	Low	Low
Throughput	High	High	Low	High
Scalability	Good	Good	Poor	Good
Cost	Low	Low	Low	High (pattern electrodes for DEP)
Uniformity	Good	Poor	Medium	Medium
Compatibility to current TFTs manufacturing process	Good	To be determined	Poor	Poor
Process complexity	Low	Medium	High	High

4.2 The Fabrication Process of CNT-TFTs

The investment of a display production line is huge, e.g. billions of U.S. dollars for a line of generation 8 (G8). If the fabrication process of CNT-TFTs can accommodate the existing backplane manufacturing process, the production cost will be greatly reduced. In this section, we discuss the reported CNT-TFT fabrication processes in the laboratory and the requirements for mass production now in industry.

We have discussed the CNT thin film fabrication in the previous section. After depositing the CNT film on substrates, photolithography is used to pattern the channel of the CNT-TFTs. The channel area is protected by a photoresist and the unwanted areas are removed by oxygen plasma reactive ion etching (RIE). For the fully printed fabrication processes, the photolithography patterning step can be avoided [24, 79]. However, the performances of fully printed CNT-TFTs are relatively low, and the device sizes are relatively big. In those non-fully printed fabrication processes, photolithography is needed for patterning the gate insulator, the source/drain and gate electrodes [61, 80].

Almost all of the reported photolithography processes for CNT-TFT fabrication are lift-off (shown in Fig. 7). In the lift-off process, the photoresist was first patterned, and then the targeted material was deposited over the whole surface of the substrate, and the unwanted area was lifted off using solvents. On the contrary, in the industry of TFT backplane manufacturing, almost every pattern transfer step was combined photolithography and etching processes, either dry or wet. In lift-off process, the un-wanted area of the deposited film was lifted off into the solvents. However, debris may be left on the substrate, which results in device or circuit failure. This problem can be more easily controlled in the etching process. Thus, etching processes are preferred due to production control. Furthermore, there are photoresist patterns on the substrates in the thin film deposition steps in the lift-off process (as shown in Fig. 7). However, the photoresist is not allowed to enter

Table 3 Performance metrics of reported solution processed CNT-TFTs

Ref	CNT separation	Thin fabrication	Im	L (μm)	W (μm)	Ion ($\mu\text{A}/\mu\text{m}$)	I_{off} (A)	On/off	Mobility (cm^2/Vs)	SS (V/dec)	Hysteresis	Substrate
[123]	No	Spray coating		100	2000	0.15 @2 V			6.7	0.26		(PEI-TiO ₂) ₁₅ /SiO ₂ /Si
[124]	No	Self-sorting/aligned		50	1000	~0.001 @0.1–1 V	$>10^{-10}$	10^2 – 10^5	0.01–3			SiO ₂ /Si, APTES
[125]	Yes	Drop-casting		20	500	~0.02 @–1 V		10^3 – 10^5	0.4–1.3	>1	Yes	SiO ₂ /Si, APTES
[126]	Yes	Drop-casting		25	25	<0.1 @1 V		10^3 – 10^7	0.3–10	>10		SiO ₂ /Si
[127]	No	Self-sorting/spin coating		50	1000	<0.01 @–1 V	10^{-11}	10^5	<2			SiO ₂ /Si, APTES
[128]	No	Self-sorting/spin coating		50	1000	<0.05 @–0.5 V		10^4	<5		Yes	
[129]	Yes	Ink-jet printing		125	13	<0.001 @1 V		10^2	0.327			SiO ₂ /Si
[130]	Yes	Direct deposition		50–200	500	<0.03	10^{-11}	10^5 – 10^6	<5		Yes (<1 V)	SiO ₂ /Si, APTES
[131]	Yes	Direct deposition		50	500	<0.03 @10 V	10^{-13}	10^6 – 10^7	<1			SiO ₂ /Si, functionalized SiO ₂ /Si
[132]	Yes	Drop and blow		40	200	~2 @–1 V	10^{-10}	10^6	164			
[133]	Yes	Direct deposition		5–100	10–200	<0.1 @1 V	10^{-11}	10^6	<15			SiO ₂ /Si, APTES
[134]	Yes	Direct deposition		4–100	10–200	<1 @1 V	10^{-11}	10^4 – 10^5	20–30			
[135]	Yes	Spray coating		60–180	50	<0.2 @2 V	10^{-10}	10^5	4–23		Yes	SiO ₂

Table 3 continued

Ref	CNT separation	Thin Im fabrication	L (μm)	W (μm)	Ion (μA/μm)	I _{off} (A)	On/off	Mobility (cm ² /Vs)	SS (V/dec)	Hysteresis	Substrate
[136]	Yes	Inkjet printing	140	60	<0.1 @0.5 V		10 ⁴ –10 ⁵	~40		Yes (0.5–2.5 V)	HfO ₂ /PET
[137]	Yes	Direct deposition	0.8–3	2–30	~1.2 @–0.5 V	10 ^{–13} –10 ^{–12}	10 ⁵	73			SiO ₂ /Si, PLL
[79]	Yes	Direct deposition	~85	~1250	<0.03 @–5 V	10 ^{–10}	10 ⁴ –10 ⁵ @–5 V	~2–8		Yes (<1 V)	BTO/PET, PLL
[138]	Yes	DEP	8	22–80	<3 @–1 V		10 ³ –10 ⁵	0.1–20		Yes (>30 V)	Al ₂ O ₃ /glass
[139]	Yes	Direct deposition	25	100	<1 @1 V		10 ⁵ –10 ⁷	5–25		Yes	SiO ₂ /Si, PLL
[140]	Yes	Direct deposition	40	500	~0.02 @–1 V	10 ^{–12}	10 ⁵ –10 ⁷	1–10			SiO ₂ /Si, APTES
[141]	Yes	Drop casting	300–900	500	<0.01 @1 V	10 ^{–12}	10 ⁵ –10 ⁶	~1			Al ₂ O ₃ /paper
[142]	Yes	Direct deposition	40	40	<0.03 @2 V	10 ^{–13}	10 ⁵	10–20			PET/SiO ₂ , APTES, MgO + Al ₂ O ₃
[106]	Yes	Direct deposition	5	80	0.01–0.1 @1 V		10 ⁴ –10 ⁵	16–20	0.2 (avg.), 0.09 (min.)		HfO, PLL
[143]	Yes	Direct deposition	4–100	200–2000	<0.01 @0.5 V	10 ^{–11}	10 ⁴ –10 ⁷	1–27			SiO ₂ /Si
[144]	Yes	Aerosol jet printing	100	160	0.1 @–2 V	10 ^{–12}	10 ⁶	5.3			SiO ₂ /Si, PLL
[145]	Yes	Direct deposition	4	400	<3 @–5 V		10 ⁵ –10 ⁷	15–20		Yes	SiO ₂ /Si, PLL
[15]	Yes		4–100	10–200	~10 @1 V		>10 ⁴	~52			SiO ₂ /Si, APTES

Table 3 continued

Ref	CNT separation	Thin Im fabrication	L (μm)	W (μm)	Ion (μA/μm)	I _{off} (A)	On/off	Mobility (cm ² /Vs)	SS (V/dec)	Hysteresis	Substrate
[65]	Yes	Direct deposition	105	1000	<0.01 @-1 V	10 ⁻¹⁰	10 ⁴ -10 ⁵	7.67		Yes (minimal)	SiO ₂ , PET + PLL
[24]	Yes	Printing	10-200	100-500	<0.1 @1 V		10 ⁴ -10 ⁷	9-30			SiO ₂ /Si
[13]	Yes	Direct deposition	20	100	~0.8 @1 V		>10 ⁴	31.65			Glass; Al ₂ O ₃ /SiO ₂ /APTES;
[67]	Yes	Direct deposition	100	100	<0.1 @1 V	10 ⁻¹⁰	10 ³ -10 ⁴	4.47	0.8		Glass, - exible, Al ₂ O ₃ , APTES
[105]	Yes	Drop cast	50	1000	~0.1 @-5 V	10 ⁻¹² @-5 V	~ 10 ⁵	17.26 ± 4.77	0.28 ± 0.04	0 ± 0.09 V	SiO ₂ /Si, PLL

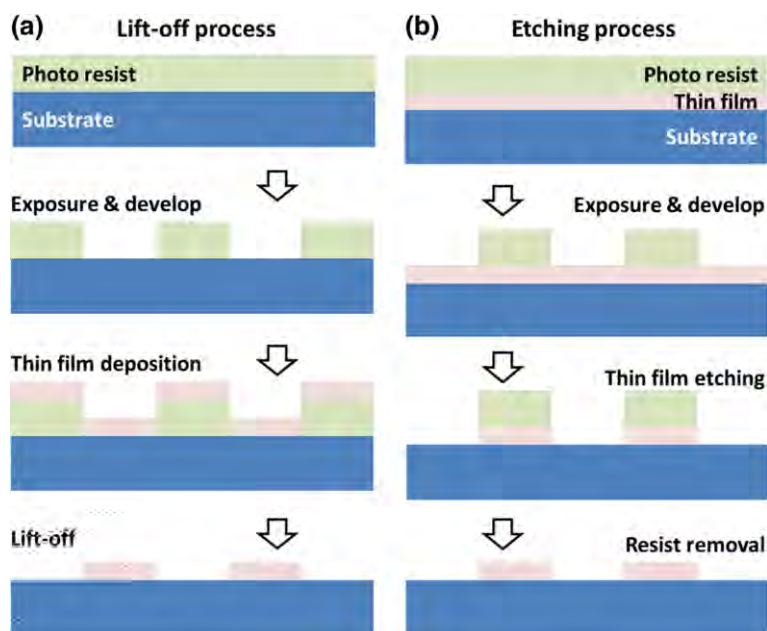


Fig. 7 Diagram depiction of the lift-off and etching processes

industrial vacuum instruments with plasma process, e.g. PVD or PECVD, otherwise the instruments may be damaged by discharge generated by the photoresist.

In the etching process, the fabrication of metal contact to the CNTs is more complicated than lift-off. Source/drain metal electrodes may be fabricated through wet etching and then depositing the SWCNT 1m and pattern the channel by RIE. In the RIE step, the metal leads unprotected by the photoresist are exposed to the oxygen plasma, which may be oxidized. Moreover, the CNTs lie on the electrode, and the contact is built on van de Waals interaction between the CNTs and the metal in this way. Such contacts are high resistance, and the geometry of metal deposited on CNTs is preferred for lowering the contact resistance according to the experiences of FETs on individual CNT [28, 81]. For this geometry, the metal is deposited over the substrate, and then the source/drain electrodes are defined by photolithography and wet etching. In this way, the SWCNT 1m channel area is covered by the metal 1m first and then exposed by wet etching of the metal. In manufacturing, the metal 1ms are usually deposited by PVD process due to its high throughput, instead of thermal or e-beam evaporations used in the literature [15]. The atomic thin SWCNTs in the channel area are bombarded by the high energy particles in the PVD process, which may damage the SWCNTs. In the following metal wet etching, the SWCNT 1m is exposed to the metal etchants. How the metal etching residues and the contamination of the wet chemical etchants affect the devices performance are not known. In the metal PVD deposition step, an insulating layer may be used to protect the SWCNT 1m from being bombarded, just as the etching stop layer in the fabrication of a-IGZO TFTs [36, 82]. However, windows

for metal contacts must be opened in this layer by photo lithography and wet etch only, otherwise the SWCNTs below will be damaged by dry etch. Then the metal is deposited and the source/drain patterned by another photo lithography step. Thus, one more photolithography step is needed, which increases the fabrication cost. Also, how insulator etchant contamination and insulating residues on the SWCNTs affect the contact is waiting for study [83, 84].

4.3 The Electrodes and Dielectric Materials

It is known that the Fermi level pinning effect in SWCNT is negligible due to its quasi-one-dimensional structure [85]. Thus, one can choose a metal with an appropriate work function to obtain Ohmic contact with the semiconducting SWCNTs [27, 28, 86]. In addition to the work function, the wettability between the metal and the SWCNT also affects the contact properties significantly [87]. Among the many existing metal materials, p-type Ohmic contact is obtained by using Pd [28], while n-type by using Sc [27] or Y [86]. Pd, Sc, and Y are the mostly used contact metals for high performance carbon-based nanoelectronics, including CNT and graphene in the literature. Also, the deposition method is mainly e-beam evaporation, instead of the widely used PVD method in industry. These metals have never been used in the TFT backplane manufacturing. The currently used metal is Al due to its high chemical stability, low resistivity, and low cost. Though Schottky barriers form at the contact of these metals to SWCNTs [27, 28, 88], the corresponding etching processes of these metals are well-established for mass production. If changing the metals to Pd or Sc in the production line, PVD deposition and the corresponding wet etching processes should be developed and verified, which are nontrivial matters. For example, the hillock formation problems of the metal films are resolvable for the metals in manufacturing [36, 89, 90]. However, Pd is found not stick to the substrate well, so that a very thin layer of Ti was employed to improve the adhesion to substrates [91]. Moreover, the cost of Pd and Sc are much higher than those currently used metals for TFTs.

Besides the metal electrodes, the gate dielectrics also impact the performance of the TFT greatly. CNT-TFTs fabricated on Si substrates with the thermally grown SiO_2 as gate dielectrics have been reported. In addition to the thermally grown SiO_2 , other materials such as HfO_2 and Al_2O_3 grown by atomic layer deposition (ALD) have been employed as gate dielectrics. Though high quality dielectrics are easily obtained by ALD, the cost is high. In the backplane manufacturing, the mostly used gate dielectric materials are Si_3N_4 or SiO_2 , which are grown by using PECVD. There are a few reports on CNT-TFT using PECVD grown gate dielectrics [32, 92]. However, fixed charges exist in the PECVD grown Si_3N_4

4.4 Performance of CNT-TFTs

The key device metrics for evaluating the performance of a TFT include on-state current (I_{on}), off-state current (I_{off}), the on/off current ratio ($I_{\text{on}}/I_{\text{off}}$), mobility (μ),

Figure 1b shows an illustration of typical transmission versus voltage curve of LC molecule. About 2 V is needed for the transparency of the LC molecule changes from 10 to 90% [95]. If these 2 V are divided into a 256 gray scale (8 bit), then ~ 8 mV is needed for one gray scale change. $C_{\text{pixel_charge}}$ is usually about 1 \sim 4 times of $C_{\text{pixel_leak}}$ [95], thus the required $I_{\text{on}}/I_{\text{off}} \sim 10^6$ for a 1024 line image with 60 Hz frame rate. If the frame rate is higher than 60 Hz, the on/off ratio is required to be higher than 10^6 . Moreover, higher on/off ratio makes easier design for the driving circuits and better control of picture quality.

I_{on} is not a problem for CNT-TFTs. Because of the excellent electrical properties of SWCNT, the current of an individual SWCNT can be higher than 20 μA [27, 28]. Though there are many inter-tube junctions, high I_{on} is easily obtained in the network type CNT-TFTs. The current density in the range of 1–10 $\mu\text{A}/\mu\text{m}$ is commonly reported for solution processed CNT-TFTs (as shown in Table 3). These current densities are much higher than that of the a-Si TFTs [12], and even higher than some of those reported a-IGZO [34] and LTPS TFTs [96]. The current density is greatly improved when the tubes in the channel are aligned [16, 39, 72]. The high I_{on} of CNT-TFTs not only meet the requirement of high resolution displays, but is also bene t for improving the aperture ratio.

Lower I_{off} and higher $I_{\text{on}}/I_{\text{off}}$ are preferred for low power consumption and better picture quality of FPDs. Both the semiconducting purity of the SWCNTs in the channel and the diameter (or band gap) affect the I_{off} and $I_{\text{on}}/I_{\text{off}}$ of the CNT-TFTs. In early studies, considerable metallic SWCNTs exist in the channel of the CNT-TFTs. Though high I_{on} and high mobility are easily obtained, the I_{off} is relatively high and the $I_{\text{on}}/I_{\text{off}}$ is very low [15]. To improve the $I_{\text{on}}/I_{\text{off}}$ and lower I_{off} , the CNT lm was stripped to suppress the possibility of the percolated metallic conducting paths that directly bridge the source to the drain [20, 31]. By tuning the ratio of the width and length of the CNT lm stripe, high $I_{\text{on}}/I_{\text{off}}$ up to 10^5 can be obtained. However, it is very difficult to obtain $I_{\text{on}}/I_{\text{off}}$ higher than 10^6 .

Bao's group developed a self-sorted technique for solution processed SWCNTs which can obtain high $I_{\text{on}}/I_{\text{off}}$ [70, 97]. The un-separated SWCNT solution was spin-coated to surface functionalized substrates, and semiconducting SWCNTs are preferred to be absorbed onto the substrates and partially aligned. In this way, $I_{\text{on}}/I_{\text{off}}$ of the fabricated CNT-TFTs can be high up to 10^5 – 10^6 due to the high semiconducting purity. Unfortunately, the tube density of the SWCNT lm is very low, which results in too low I_{on} .

As the development of the solution-based sorting techniques of semiconducting SWCNTs, high purity ($>99\%$) semiconducting SWCNT solutions are commercialized, and even with certain chirality [59, 60]. By using the separated SWCNT solutions, the metallic percolation paths was suppressed greatly and the obtained $I_{\text{on}}/I_{\text{off}}$ of the CNT-TFTs can be up to 10^5 – 10^7 , which meet the requirements for display application.

It should be noted that the reported high $I_{\text{on}}/I_{\text{off}}$ values are mostly obtained in relatively long channel CNT-TFTs (usually >10 μm) and at low source/drain bias (usually <1 V as shown in Table 3). The reason is large channel length to tube length ratio is bene t to suppress the metallic percolating paths, and hence high $I_{\text{on}}/I_{\text{off}}$ is obtainable according to the percolation theory [46, 47]. However, to maintain

high I_{on} , the channel width should be increased meanwhile for long channel length devices. Thus, the size of the CNT-TFTs increases, which lowers the aperture ratio, and limits their application in high pixel density (e.g. ~ 1000 ppi) FPDs.

To obtain high $I_{\text{on}}/I_{\text{off}}$ in CNT-TFTs with relatively short channel length (or small size device), the purity of the SWCNT material should be further enhanced and/or decreasing the average length of the SWCNTs. Usually, high power sonication is used to shorten the SWCNTs in solution, which also introduces more defects [98] and degrades the mobility of the fabricated CNT-TFTs. Thus, we need to balance the $I_{\text{on}}/I_{\text{off}}$ and the mobility. Recently, Liang et al. [99] used a two-step fringing field dielectrophoretic method to fabricate short channel CNT-TFTs with high $I_{\text{on}}/I_{\text{off}}$ (shown in Fig. 6h, i). Densely aligned SWCNT arrays were assembled at the source and drain electrodes sequentially which form a cascade structure of the aligned SWCNT arrays. The cascade structure reduces the possibility of percolating metallic pathways in the channel. In this way, both high $I_{\text{on}}/I_{\text{off}}$ (up to 10^7) and high I_{on} ($8.5 \mu\text{A}/\mu\text{m}$) were obtained in CNT-TFTs with short channel length ($1\text{--}2.5 \mu\text{m}$). This work promises the application of CNT-TFTs in high pixel density FPDs.

The band gap of the SWCNT also impacts the I_{off} , and hence the on/off ratio critically. Ambipolar transport is more likely observed in small band gap (large diameter) SWCNTs [100]. The pronounced ambipolar behavior results in higher leakage current, and hence lower $I_{\text{on}}/I_{\text{off}}$, especially at high source/drain bias. The reported high $I_{\text{on}}/I_{\text{off}}$ values are mostly obtained at relatively low bias (<1 V). However, the bias on the TFTs can be as high as $2V_{\text{data}}$ (~ 10 V for LCD) during t_{f} , as mentioned before. Therefore, the $I_{\text{on}}/I_{\text{off}}$ of the CNT-TFTs should be $\sim 10^6$ even at such high bias. In industrial backplane manufacturing, the I_{off} and $I_{\text{on}}/I_{\text{off}}$ of a TFT is measured at pretty high bias (\sim up to over 10 V) and wide gate voltage sweep range (can be up to -30 V $\sim +30$ V). However, high $I_{\text{on}}/I_{\text{off}}$ at such high bias of CNT-TFTs is seldom reported.

To suppress the ambipolar transport, larger band gap (small diameter) SWCNTs are preferred. The diameter distribution of the SWCNT depend on the production methods. For solution based sorting, the SWCNT source materials are mainly produced by arc-discharge, HiPCO, plasma, and CoMoCAT. The corresponding diameter distributions are listed in Table 4. Obviously, the HiPCO and CoMoCAT SWCNTs are more preferred for low I_{off} and high $I_{\text{on}}/I_{\text{off}}$ [101]. However, the cost of the HiPCO CNT is much higher than other methods, which is an obstacle for its application in TFT backplanes.

In addition to choosing smaller diameter SWCNTs, the ambipolar transport can be suppressed by engineering the device structure. Lin et al. [100] used an asymmetric gate structure with respect to the source and drain electrodes (Fig. 8a,

Table 4 Diameter distribution of SWCNTs produced by various methods

	Diameter (nm)	Ref.
Arc-discharge	1.55 ± 0.1	[146]
HiPCO	$0.8\text{--}1.2$	[59]
CoMoCAT	$0.7\text{--}1.4$	[147]
Plasma	$0.9\text{--}1.9$	[59]

Fig. 8 Suppress the ambipolar transport behavior of SWCNT by device structure engineering. **a** Partially gated structure by Lin et al. and their results (**b**). Reprinted with permission from [100] (Copyright 2011 American Chemical Society) **c** Feedback gate structure by Qiu et al. and **d** comparison of the transfer curves of normal (*red*) and feedback gate CNT-FETs. Reprinted with permission from [102] (Copyright 2015 American Chemical Society)

b). Qiu et al. [102] proposed a feedback gate structure FET, where an additional gate was introduced at the drain end of the FETs (Fig. 8c, d). Both strategies suppressed the ambipolar behavior of the SWCNT effectively; however, the feedback gate structure is more facile for fabrication. It should be noted those strategies are proposed in individual CNT devices. Whether it can be generalized to the CNT-TFTs should be verified, though it is very possible in principle.

4.4.2 Sub-threshold Swing (*SS*)

Lower *SS* value indicates the TFT can be switched from off- to on-state quickly, which is required for high resolution FPDs due to the short t_{on} . Typical *SS* value for

a-Si TFT is ~ 1 V/dec, while those for LTPS and a-IGZO TFTs are $0.3 \sim 0.5$ V/dec. The SS value nearly 60 mV/dec has been reported in CNT-FETs [103], and values lower than 0.1 V/dec are routinely obtained [102, 104]. For CNT-TFTs, the SS down to 0.15 V/dec was reported by Sangwan et al. [93] by using the hybrid molecular dielectrics (V-sand). These low SS values are obtained in devices, either CNT-FETs or CNT-TFTs, with high quality and relatively thin gate dielectrics. The gate dielectrics of the CNT-TFTs for backplane electronics cannot be very thin. It must be thick enough to minimize the gate leakage current at high bias and wide gate voltage range. Thicker dielectrics will degrade the gate control of the channel and hence increase the SS values of the CNT-TFTs. SS of CNT-TFTs is seldom measured at high bias [105]; however, typical values of $0.1 \sim 0.3$ V/dec were reported [105, 106]. Owing to its thin body, it is expected that the SS value of CNT-TFTs can be further optimized to surpass those of LTPS and oxide TFTs.

4.4.3 Threshold Voltage (V_{th})

The V_{th} of the TFTs in backplanes are required to be near 0 V stably. The reported V_{th} values of the CNT-TFTs are somewhat deviated [38]. Furthermore, large hysteresis is usually observed in CNT-TFTs [15, 24, 69], which is believed to be due to the charge trapping induced by the absorbed water and hydroxyl groups at the substrate surface and mobile charges in the gate dielectrics [105, 107, 108]. It is meaningless to talk about tuning V_{th} before fully suppressing the hysteresis. The hysteresis in CNT-FETs can be suppressed by many methods, such as passivation by using PMMA [107], HMDS [109], or suspending the SWCNTs [107, 110]. These methods work pretty well at relatively low bias and/or small gate sweep ranges. However, the situation is more complicated in CNT-TFTs. In addition to the absorbed water molecules and surface hydroxyl groups, many dangling bonds at the tube ends and spices binding to the tube surface which are used for sorting the SWCNTs exist in the channel. These results in more trap centers, which makes fully suppressing the hysteresis of CNT-TFTs more difficult. Lefebvre et al. [111] used hydrophobic dielectrics for CNT-TFTs, and the hysteresis was suppressed effectively (Fig. 9a, b). However, the device fabrication process needs to be optimized to be compatible with the TFT backplane fabrication process. Ha et al. [105] encapsulated the CNT-TFTs by using a fluorocarbon polymer. The hydrophobic fluoropolymers remove the absorbed water molecules from the vicinity of CNTs efficiently and provide effective screening of the charge carriers in nanotubes from various trap states in the substrate. The hysteresis is suppressed even when the device is biased at 5 V and gate voltage sweep from -10 V to $+10$ V, as shown in Fig. 9c, d. More importantly, the device fabrication is compatible with the TFT backplane production. Once the hysteresis is suppressed, consistent V_{th} is obtainable, and it can be tuned to targeted values, e.g. by doping [112, 113], engineering the work function of the gate [114], or dual gate device structure [105].

When the above problems are solved, the gate bias stress (GBS) stability would be a critical concern for CNT-TFTs. It has been reported that a variation in V_{th} of only ± 0.1 V leads to the luminance of OLED changes by 16% [34]. Poor GBS stability results in V_{th} shift subject to prolonged gate-source bias, and hence device malfunction. In conventional TFTs, the GBS instability usually correlates with the

Fig. 9 Hysteresis-free CNT-TFTs using hydrophobic dielectrics of PVP-pMSSQ (**a**) and Te. on-AF (**b**). Reprinted with permission from [111] (Copyright 2015 AIP Publishing LLC). Fluorocarbon polymer encapsulation of CNT-TFTs (**c**) and the resulting hysteresis-free transfer curves (**d**). Reprinted with permission from [105] (Copyright 2014 American Chemical Society)

hysteresis problem. Factors that lead to hysteresis may also contribute to GBS instability. However, not enough attentions have been paid to the GBS stability of the CNT-TFTs. Lee et al. studied GBS stabilities of solution processed CNT-TFTs [115, 116], as shown in Fig. 10. Obviously, the GBS stabilities of CNT-TFTs need to be further improved.

4.4.4 Mobility

As discussed in Sect. 3, high mobility is one of the biggest advantages of the CNT-TFTs over other TFT technologies. The mobility is closely related to the quality of

Fig. 10 Positive GBS (a)–(d) and negative GBS (e)–(h) measurements of CNT-TFTs, which were fabricated on SiO₂/Si substrates with (a), e Al₂O₃, b, c, f, g PVA, d, h HfO₂ passivation layer. Reprinted with permission from [115] (Copyright 2014 AIP Publishing LLC)

the channel material. For CNT-TFTs, electrons are scattered within the individual tubes and at the inter-tube junctions as well. Lower structural defect density in the individual tubes and less inter-tube junctions are preferred to obtain higher mobility. The structural defect density in the solution processed SWCNTs are relatively high due to additional defects introduced during the solution processing. Cao et al. [98] have evaluated the mobility of the solution processed SWCNTs. The mobility of an individual SWCNT was measured in the range of 200–600 cm²/Vs. We believe the mobility can be further improved by optimizing the solution processing, and higher values up to ~1000 cm²/Vs of an individual tube are expected. Since inter-tube scattering at the junctions deteriorate the mobility, the mobility of the CNT-TFTs would be much lower than those of the individual solution processed SWCNTs intuitively. However, the situation may not be that bad. The mobility of a material depends on the scattering rate of the electrons. If there is no scattering at the inter-tube junctions, the mobility of the CNT 1m will be almost equal to that of the average value of the individual SWCNTs, which is expected to be several hundred to a thousand cm²/Vs. When considering the inter-tube junctions, the junctions between two semiconducting tubes are overwhelming in the channel due to the high purity semiconducting SWCNT solution used. The junction conductance between two semiconducting tubes is very high, as reported experimentally [117]. Theoretical studies predicted that the transmission coefficient between two CNTs can be very high [118]. These results indicate the scattering at the junction can be very low if intimate contact between these tubes is realized [119]. Considering the density of the inter-tube junction in the 1m is much lower than that of the structural defects, the mobility of the CNT 1ms may be expected close to those of the

individual tubes. Mobility higher than $100 \text{ cm}^2/\text{Vs}$ in the CNT-network has been reported by several groups [16, 120, 121]. When the tubes are aligned, the number of inter-tube junctions are further reduced, which is a benefit for mobility enhancing, and mobility in the range $200\text{--}380 \text{ cm}^2/\text{Vs}$ has been reported in aligned SWCNT films [16]. These results indicate that even higher mobility for CNT-TFTs is very possible.

4.4.5 Stability and Uniformity

Stability and uniformity are prior requirements of any developed TFT technologies for real production. For the backplane electronics application, the stability of environment, temperature, UV irradiation, and GBS for CNT-TFTs should be investigated thoroughly. However, such investigations are still lacking, just as the GBS stability, which was discussed in the Sect 4.4.3.

There are some reports on the device uniformity statistics [38, 79]. However, most results are obtained from devices on relatively small pieces of substrate. Although a few results on 4-inch wafer scale are reported, the device performance uniformity does not meet the requirements for practical production [21, 22, 38]. These substrate sizes are much smaller than the backplane glass, even those of the generation 2.5 ($370 \text{ mm} \times 470 \text{ mm}$). Much effort is needed to improve the uniformity of the SWCNT thin film over a large area, hence improving the device performance uniformity.

5 Conclusions and Outlook

So far, we have discussed the application of the CNT-TFTs in FPD products from the viewpoint of backplane manufacturing. We reviewed the progress of CNT-TFTs, which were fabricated by solution processed SWCNT materials, which is the most promising route for mass production. When examining the key performance metrics of the individual CNT-TFTs, we found that they meet the requirements for pixel addressing in backplanes of a FPD, and strategies for improving each metric exist. Some prototype displays have been demonstrated in laboratories. These progresses give us more confidence of the CNT-TFTs technology for future FPD industry. However, there is not yet a report on CNT-TFTs for which performance metrics comply with all those required for displays. The fabrication process is also needed to be optimized to integrate with the existing TFT manufacturing technologies. The current research on CNT-TFTs for display is mainly carried out in research institutes. Now it is time for close collaboration between the research institutes and FPD manufacturers. In this way, the challenges for CNT-TFTs we discussed in this paper will be overcome earlier. Although we focus on our discussion on using CNT-TFTs for the pixel addressing array, we must point out that CNT-TFTs are capable of much more than that. For example, high performance CNT-TFT CMOS circuits are demonstrated [122], providing more possibility for the application of CNT-TFTs in future high-end FPDs, such as the peripheral circuits on the backplane. Owing to the rapid development of the FPD industry,

nowadays lifestyle has been changed greatly. After two-and-a-half decades of the discovery of CNT, a FPD with CNT-TFT backplane is now expectable in the near term. Low power consumption, light-weight, fully transparent, and flexible displays are also enabled by CNT-TFTs, and the CNT-TFTs technology will impact the FPD industry profoundly.

Acknowledgements This work was supported by the National Natural Science Foundation of China (Grant No. 61321001), National Key Research and Development program (Grant No. 2016YFA0201902), and BOE Technology Group, Co., Ltd.

References

1. Iijima S (1991) *Nature* 354:56. doi:[10.1038/354056a0](https://doi.org/10.1038/354056a0)
2. Iijima S, Ichihashi T (1993) *Nature* 363:603. doi:[10.1038/363603a0](https://doi.org/10.1038/363603a0)
3. Saito R, Dresselhaus G, Dresselhaus MS (1998) Physical properties of carbon nanotubes. Imperial College Press, UK
4. International technology roadmap for semiconductors www.itrs.net
5. Franklin AD (2013) *Nature* 498:443. doi:[10.1038/498443a](https://doi.org/10.1038/498443a)
6. Tulevski GS, Franklin AD, Frank D, Lobe JM, Cao Q, Park H, Afzali A, Han S-J, Hannon JB, Haensch W (2014) *ACS Nano* 8:8730. doi:[10.1021/nn503627h](https://doi.org/10.1021/nn503627h)
7. Pei T, Zhang PP, Zhang ZY, Qiu CG, Liang SB, Yang YJ, Wang S, Peng LM (2014) *Nano Lett* 14:3102. doi:[10.1021/nl5001604](https://doi.org/10.1021/nl5001604)
8. Ding L, Zhang ZY, Liang SB, Pei T, Wang S, Li Y, Zhou WW, Liu J, Peng LM (2012) *Nature Communications* 3. doi:[10.1038/ncomms1682](https://doi.org/10.1038/ncomms1682)
9. Shulaker MM, Hills G, Patil N, Wei H, Chen HY, PhilipWong HS, Mitra S (2013) *Nature* 501:526. doi:[10.1038/nature12502](https://doi.org/10.1038/nature12502)
10. Chen B, Zhang P, Ding L, Han J, Qiu S, Li Q, Zhang Z, Peng L-M (2016) *Nano Lett* 16:5120. doi:[10.1021/acs.nanolett.6b02046](https://doi.org/10.1021/acs.nanolett.6b02046)
11. Waldrop MM (2016) *Nature* 530:144. doi:[10.1038/530144a](https://doi.org/10.1038/530144a)
12. Brotherton SD (2013) Introduction to thin film transistors—physics and technology of TFTs. Springer, New York
13. Zhang J, Fu Y, Wang C, Chen PC, Liu Z, Wei W, Wu C, Thompson ME, Zhou C (2011) *Nano Lett* 11:4852. doi:[10.1021/nl202695v](https://doi.org/10.1021/nl202695v)
14. Ishikawa FN, Chang HK, Ryu K, Chen PC, Badmaev A, De Arco LG, Shen GZ, Zhou CW (2009) *ACS Nano* 3:73. doi:[10.1021/nn800434d](https://doi.org/10.1021/nn800434d)
15. Wang C, Zhang JL, Ryu KM, Badmaev A, De Arco LG, Zhou CW (2009) *Nano Lett* 9:4285. doi:[10.1021/nl902522f](https://doi.org/10.1021/nl902522f)
16. Brady GJ, Joo Y, Wu MY, Shea MJ, Gopalan P, Arnold MS (2014) *ACS Nano* 8:11614. doi:[10.1021/nn5048734](https://doi.org/10.1021/nn5048734)
17. Sun DM, Liu C, Ren WC, Cheng HM (2013) *Small* 9:1188. doi:[10.1002/sml.201203154](https://doi.org/10.1002/sml.201203154)
18. Wang C, Takei K, Takahashi T, Javey A (2013) *Chem Soc Rev* 42:2592. doi:[10.1039/c2cs35325c](https://doi.org/10.1039/c2cs35325c)
19. Park S, Vosguerichian M, Bao Z (2013) *Nanoscale* 5:1727. doi:[10.1039/c3nr33560g](https://doi.org/10.1039/c3nr33560g)
20. Cao Q, Kim HS, Pimparkar N, Kulkarni JP, Wang CJ, Shim M, Roy K, Alam MA, Rogers JA (2008) *Nature* 454:495. doi:[10.1038/nature07110](https://doi.org/10.1038/nature07110)
21. Liyanage LS, Lee H, Patil N, Park S, Mitra S, Bao Z, Wong HS (2012) *ACS Nano* 6:451. doi:[10.1021/nn203771u](https://doi.org/10.1021/nn203771u)
22. Kim J, Hong D, Lee H, Shin Y, Park S, Khang Y, Lee M, Hong S (2013) *The Journal of Physical Chemistry C* 117
23. Lau PH, Takei K, Wang C, Ju Y, Kim J, Yu ZB, Takahashi T, Cho G, Javey A (2013) *Nano Lett* 13:3864. doi:[10.1021/nl401934a](https://doi.org/10.1021/nl401934a)
24. Chen P, Fu Y, Amini-rad R, Wang C, Zhang J, Wang K, Galatsis K, Zhou C (2011) *Nano Lett* 11:5301. doi:[10.1021/nl202765b](https://doi.org/10.1021/nl202765b)

27. Zhang ZY, Liang XL, Wang S, Yao K, Hu YF, Zhu YZ, Chen Q, Zhou WW, Li Y, Yao YG, Zhang J, Peng LM (2007) *Nano Lett* 7:3603. doi:[10.1021/nl0717107](https://doi.org/10.1021/nl0717107)
28. Javey A, Guo J, Wang Q, Lundstrom M, Dai H (2003) *Nature* 424. doi:[10.1038/nature01797](https://doi.org/10.1038/nature01797)
29. Park S, Vosguerichian M, Bao Z (2013) *Nanoscale* 5:1727. doi:[10.1039/c3nr33560g](https://doi.org/10.1039/c3nr33560g)
30. Xu W, Zhao J, Qian L, Han X, Wu L, Wu W, Song M, Zhou L, Su W, Wang C, Nie S, Cui Z (2014) *Nanoscale* 6:1589. doi:[10.1039/c3nr04870e](https://doi.org/10.1039/c3nr04870e)
31. Kim S, Kim S, Park J, Ju S, Mohammadi S (2010) *ACS Nano* 4:2994. doi:[10.1021/nn1006094](https://doi.org/10.1021/nn1006094)
32. Zou J, Zhang K, Li J, Zhao Y, Wang Y, Pillai SKR, Volkan Demir H, Sun X, Chan-Park MB, Zhang Q (2015) *Sci Rep* 5:11755. doi:[10.1038/srep11755](https://doi.org/10.1038/srep11755)
33. Matsueda Y (2010) *Digest of Int. Transistor Conf.* 2010 Hyogo, Japan p 314
34. Toshio K, Kenji N, Hideo H (2010) *Sci Technol Adv Mater* 11:044305
35. Ohshima H (2014) *SID Symp Digest Techn Pap* 45:75. doi:[10.1002/j.2168-0159.2014.tb00021.x](https://doi.org/10.1002/j.2168-0159.2014.tb00021.x)
36. Wang L, Xu M, Lan L, Zou J, Tao H, Xu H, Li M, Luo D, Peng J (2013) *Sci Sin Chim* 43:1383. doi:[10.1360/032013-293](https://doi.org/10.1360/032013-293)
37. Cunningham KL (2014) *Nanochip Fab Solut* 9:24
38. Tian B, Liang X, Yan Q, Zhang H, Xia J, Dong G, Peng L, Xie S (2016) *J Appl Phys* 120:034501. doi:[10.1063/1.4958850](https://doi.org/10.1063/1.4958850)
39. Brady GJ, Joo Y, Singha Roy S, Gopalan P, Arnold MS (2014) *Appl Phys Lett* 104:083107. doi:[10.1063/1.4866577](https://doi.org/10.1063/1.4866577)
40. Sun DM, Timmermans MY, Kaskela A, Nasibulin AG, Kishimoto S, Mizutani T, Kauppinen EI, Ohno Y (2013) *Nat Commun* 4:2302. doi:[10.1038/ncomms3302](https://doi.org/10.1038/ncomms3302)
41. Sun DM, Timmermans MY, Tian Y, Nasibulin AG, Kauppinen EI, Kishimoto S, Mizutani T, Ohno Y (2011) *Nat Nanotechnol* 6:156. doi:[10.1038/Nnano.2011.1](https://doi.org/10.1038/Nnano.2011.1)
42. Kang SJ, Kocabas C, Ozel T, Shim M, Pimparkar N, Alam MA, Rotkin SV, Rogers JA (2007) *Nat Nanotechnol* 2:230. doi:[10.1038/nnano.2007.77](https://doi.org/10.1038/nnano.2007.77)
43. Dresselhaus MS, Dresselhaus G, Avouris P (eds) (2001) *Carbon nanotubes: synthesis, structure, properties, and applications*. Springer, Heidelberg
44. Choi YS, Yun JU, Park SE (2016) *J Non Cryst Solids* 431:2. doi:[10.1016/j.jnoncrysol.2015.05.007](https://doi.org/10.1016/j.jnoncrysol.2015.05.007)
45. Kang SJ, Kocabas C, Kim HS, Cao Q, Meitl MA, Khang DY, Rogers JA (2007) *Nano Lett* 7:3343. doi:[10.1021/nl071596s](https://doi.org/10.1021/nl071596s)
46. Kumar S, Murthy JY, Alam MA (2005) *Phys Rev Lett* 95:066802. doi:[10.1103/Physrevlett.95.066802](https://doi.org/10.1103/Physrevlett.95.066802)
47. Alam MA, Pimparkar N, Kumar S, Murthy J (2006) *MRS Bull* 31:466. doi:[10.1557/Mrs2006.120](https://doi.org/10.1557/Mrs2006.120)
48. Tu XM, Manohar S, Jagota A, Zheng M (2009) *Nature* 460:250. doi:[10.1038/nature08116](https://doi.org/10.1038/nature08116)
49. Zheng M, Jagota A, Semke ED, Diner BA, Mclean RS, Lustig SR, Richardson RE, Tassi NG (2003) *Nat Mater* 2:338. doi:[10.1038/nmat877](https://doi.org/10.1038/nmat877)
50. Nish A, Hwang J-Y, Doig J, Nicholas RJ (2007) *Nat Nano* 2:640. doi:[10.1038/nnano.2007.290](https://doi.org/10.1038/nnano.2007.290)
51. Lee HW, Yoon Y, Park S, Oh JH, Hong S, Liyanage LS, Wang H, Morishita S, Patil N, Park YJ, Park JJ, Spakowitz A, Galli G, Gygi F, Wong PHS, Tok JBH, Kim JM, Bao Z (2011) *Nat Commun* 2:541. doi:[10.1038/ncomms1545](https://doi.org/10.1038/ncomms1545)
52. Li H, Zhou B, Lin Y, Gu L, Wang W, Fernando KAS, Kumar S, Allard LF, Sun Y-P (2004) *J Am Chem Soc* 126:1014. doi:[10.1021/ja037142o](https://doi.org/10.1021/ja037142o)
53. Wang WZ, Li WF, Pan XY, Li CM, Li L-J, Mu YG, Rogers JA, Chan-Park MB (2011) *Adv Funct Mater* 21:1643. doi:[10.1002/adfm.201002278](https://doi.org/10.1002/adfm.201002278)
54. Liu H, Tanaka T, Urabe Y, Kataura H (2013) *Nano Lett* 13:1996. doi:[10.1021/nl400128m](https://doi.org/10.1021/nl400128m)
55. Liu H, Nishide D, Tanaka T, Kataura H (2011) *Nat Commun* 2:309. doi:[10.1038/ncomms1313](https://doi.org/10.1038/ncomms1313)
56. Khripin CY, Fagan JA, Zheng M (2013) *J Am Chem Soc* 135:6822. doi:[10.1021/ja402762e](https://doi.org/10.1021/ja402762e)
57. Arnold MS, Green AA, Hulvat JF, Stupp SI, Hersam MC (2006) *Nat Nano* 1:60. doi:[10.1038/nnano.2006.52](https://doi.org/10.1038/nnano.2006.52)
58. Tulevski GS, Franklin AD, Afzali A (2013) *ACS Nano* 7:2971. doi:[10.1021/nn400053k](https://doi.org/10.1021/nn400053k)
59. <http://www.nanointegris.com>
60. <http://www.atomnanoelectronics.com>
61. Ha M, Xia Y, Green AA, Zhang W, Renn MJ, Kim CH, Hersam MC, Frisbie CD (2010) *ACS Nano* 4:4388. doi:[10.1021/nn100966s](https://doi.org/10.1021/nn100966s)
62. Abdelhalim A, Abdellah A, Scarpa G, Lugli P (2014) *Nanotechnology* 25:055208. doi:[10.1088/0957-4484/25/5/055208](https://doi.org/10.1088/0957-4484/25/5/055208)
63. Takahashi T, Takei K, Gillies AG, Fearing RS, Javey A (2011) *Nano Lett* 11:5408. doi:[10.1021/nl203117h](https://doi.org/10.1021/nl203117h)

64. Wang C, Chien JC, Takei K, Takahashi T, Nah J, Niknejad AM, Javey A (2012) *Nano Lett* 12:1527. doi:[10.1021/nl2043375](https://doi.org/10.1021/nl2043375)
65. Cao X, Chen H, Gu X, Liu B, Wang W, Cao Y, Wu F, Zhou C (2014) *ACS Nano* 8:12769. doi:[10.1021/nn505979j](https://doi.org/10.1021/nn505979j)
66. Joo Y, Brady GJ, Arnold MS, Gopalan P (2014) *Langmuir* 30:3460. doi:[10.1021/la500162x](https://doi.org/10.1021/la500162x)
67. Zhang J, Wang C, Zhou C (2012) *ACS Nano* 6:7412. doi:[10.1021/nn3026172](https://doi.org/10.1021/nn3026172)
68. Qian L, Xu WY, Fan XF, Wang C, Zhang JH, Zhao JW, Cui Z (2013) *J Phys Chem C* 117:18243. doi:[10.1021/jp4055022](https://doi.org/10.1021/jp4055022)
69. Wang C, Qian L, Xu WY, Nie SH, Gu WB, Zhang JH, Zhao JW, Lin J, Chen Z, Cui Z (2013) *Nanoscale* 5:4156. doi:[10.1039/c3nr34304a](https://doi.org/10.1039/c3nr34304a)
70. LeMieux MC, Roberts M, Barman S, Jin YW, Kim JM, Bao Z (2008) *Science* 321:101. doi:[10.1126/science.1156588](https://doi.org/10.1126/science.1156588)
71. Opatkiewicz JP, LeMieux MC, Bao Z (2010) *ACS Nano* 4:1167. doi:[10.1021/nn901388v](https://doi.org/10.1021/nn901388v)
72. Engel M, Small JP, Steiner M, Freitag M, Green AA, Hersam MC, Avouris P (2008) *ACS Nano* 2:2445. doi:[10.1021/nn800708w](https://doi.org/10.1021/nn800708w)
73. Li X, Zhang L, Wang X, Shimoyama I, Sun X, Seo W-S, Dai H (2007) *J Am Chem Soc* 129:4890. doi:[10.1021/ja071114e](https://doi.org/10.1021/ja071114e)
74. Cao Q, Han SJ, Tulevski GS, Zhu Y, Lu DD, Haensch W (2013) *Nat Nanotechnol* 8:180. doi:[10.1038/Nnano.2012.257](https://doi.org/10.1038/Nnano.2012.257)
75. Shekhar S, Stokes S, Khondaker SI (2011) *ACS Nano* 5:1739. doi:[10.1021/nn102305z](https://doi.org/10.1021/nn102305z)
76. Cao Q, Han SJ, Tulevski GS (2014) *Nat Commun* 5:5071. doi:[10.1038/ncomms6071](https://doi.org/10.1038/ncomms6071)
77. Monica AH, Papadakis SJ, Osiander R, Paranjape M (2008) *Nanotechnology* 19:085303. doi:[10.1088/0957-4484/19/8/085303](https://doi.org/10.1088/0957-4484/19/8/085303)
78. Krupke R, Hennrich F, Löhneysen HV, Kappes MM (2003) *Science* 301: 344
79. Lau PH, Takei K, Wang C, Ju Y, Kim J, Yu Z, Takahashi T, Cho G, Javey A (2013) *Nano Lett* 13:3864. doi:[10.1021/nl401934a](https://doi.org/10.1021/nl401934a)
80. Xu W, Dou J, Zhao J, Tan H, Ye J, Tange M, Gao W, Xu W, Zhang X, Guo W, Ma C, Okazaki T, Zhang K, Cui Z (2016) *Nanoscale* 8:4588. doi:[10.1039/c6nr00015k](https://doi.org/10.1039/c6nr00015k)
81. Tans SJ, Verschueren ARM, Dekker C (1998) *Nature* 393:49
82. Zhu XM, Jiang CS, Yuan GC, Liu W, Li XY, Xin LB, Wang ML, Wang G (2015) *SID symposium digest of technical papers*, vol 46, p 1198. doi:[10.1002/sdtp.10057](https://doi.org/10.1002/sdtp.10057)
83. Li W, Liang YR, Yu DM, Peng LM, Pernstich KP, Shen T, Walker ARH, Cheng GJ, Hacker CA, Richter CA, Li QL, Gundlach DJ, Liang XL (2013) *Appl Phys Lett* 102. doi:[10.1063/1.4804643](https://doi.org/10.1063/1.4804643)
84. Li W, Hacker CA, Cheng GJ, Liang YR, Tian BY, Walker ARH, Richter CA, Gundlach DJ, Liang XL, Peng LM (2014) *J Appl Phys* 115. doi:[10.1063/1.4868897](https://doi.org/10.1063/1.4868897)
85. Leonard F, Tersoff J (2000) *Phys Rev Lett* 84:4693. doi:[10.1103/PhysRevLett.84.4693](https://doi.org/10.1103/PhysRevLett.84.4693)
86. Ding L, Wang S, Zhang ZY, Zeng QS, Wang ZX, Pei T, Yang LJ, Liang XL, Shen J, Chen Q, Cui RL, Li Y, Peng LM (2009) *Nano Lett* 9:4209. doi:[10.1021/nl9024243](https://doi.org/10.1021/nl9024243)
87. Zhang Y, Franklin NW, Chen RJ, Dai HJ (2000) *Chem Phys Lett* 331:35. doi:[10.1016/S0009-2614\(00\)01162-3](https://doi.org/10.1016/S0009-2614(00)01162-3)
88. Chen ZH, Appenzeller J, Knoch J, Lin YM, Avouris P (2005) *Nano Lett* 5:1497. doi:[10.1021/Nl0508624](https://doi.org/10.1021/Nl0508624)
89. Morrison NA, Stolley T, Hermanns U, Reus A, Deppisch T, Bolandi H, Melnik Y, Singh V, Grif th Cruz J (2015) *Proc IEEE* 103:518. doi:[10.1109/jproc.2015.2408052](https://doi.org/10.1109/jproc.2015.2408052)
90. Wang P, Hwang J, Chuang A, Huang F-S (2000) *Thin Solid Films* 358:292. doi:[10.1016/S0040-6090\(99\)00674-4](https://doi.org/10.1016/S0040-6090(99)00674-4)
91. Franklin AD, Farmer DB, Haensch W (2014) *ACS Nano* 8:7333. doi:[10.1021/nn5024363](https://doi.org/10.1021/nn5024363)
92. Wind SJ, Appenzeller J, Martel R, Derycke V, Avouris P (2002) *Appl Phys Lett* 80:3817. doi:[10.1063/1.1480877](https://doi.org/10.1063/1.1480877)
93. Sangwan VK, Ortiz RP, Alaboson JMP, Emery JD, Bedzyk MJ, Lauhon LJ, Marks TJ, Hersam MC (2012) *ACS Nano* 6:7480. doi:[10.1021/nn302768h](https://doi.org/10.1021/nn302768h)
94. Hur S-H, Yoon M-H, Gaur A, Shim M, Facchetti A, Marks TJ, Rogers JA (2005) *J Am Chem Soc* 127:13808. doi:[10.1021/ja0553203](https://doi.org/10.1021/ja0553203)
95. Dai YX (2010) *Design and operation of TFT LCD panels*. Tsinghua University Press, Beijing
96. Brotherton SD, Ayres JR, Young ND (1991) *Solid State Electron* 34:671. doi:[10.1016/0038-1101\(91\)90002-G](https://doi.org/10.1016/0038-1101(91)90002-G)
97. Opatkiewicz JP, LeMieux MC, Liu D, Vosgueritchian M, Barman SN, Elkins CM, Hedrick J, Bao Z (2012) *ACS Nano* 6:4845. doi:[10.1021/nn300124y](https://doi.org/10.1021/nn300124y)

98. Cao Q, Han SJ, Tulevski GS, Franklin AD, Haensch W (2012) ACS Nano 6:6471. doi:[10.1021/nn302185d](https://doi.org/10.1021/nn302185d)
99. Liang Y, Xia J, Liang X (2016) Sci Bull 61:794. doi:[10.1007/s11434-016-1075-1](https://doi.org/10.1007/s11434-016-1075-1)
100. Lin YM, Appenzeller J, Avouris P (2004) Nano Lett 4:947. doi:[10.1021/nl049745j](https://doi.org/10.1021/nl049745j)
101. Zhang J, Gui H, Liu B, Liu J, Zhou C (2013) Nano Res 6:906. doi:[10.1007/s12274-013-0368-9](https://doi.org/10.1007/s12274-013-0368-9)
102. Qiu C, Zhang Z, Zhong D, Si J, Yang Y, Peng L-M (2015) ACS Nano 9:969. doi:[10.1021/nn506806b](https://doi.org/10.1021/nn506806b)
103. Wang ZX, Xu HL, Zhang ZY, Wang S, Ding L, Zeng QS, Yang LJ, Pei TA, Liang XL, Gao M, Peng LM (2010) Nano Lett 10:2024. doi:[10.1021/nl100022u](https://doi.org/10.1021/nl100022u)
104. Javey A, Tu R, Farmer DB, Guo J, Gordon RG, Dai HJ (2005) Nano Lett 5:345. doi:[10.1021/nl047931j](https://doi.org/10.1021/nl047931j)
105. Ha TJ, Kiriya D, Chen K, Javey A (2014) Acs Appl Mater Interfaces 6:8441. doi:[10.1021/am5013326](https://doi.org/10.1021/am5013326)
106. Kim B, Franklin A, Nuckolls C, Haensch W, Tulevski GS (2014) Appl Phys Lett 105:063111. doi:[10.1063/1.4891335](https://doi.org/10.1063/1.4891335)
107. Kim W, Javey A, Vermesh O, Wang O, Li YM, Dai HJ (2003) Nano Lett 3:193. doi:[10.1021/nl0259232](https://doi.org/10.1021/nl0259232)
108. Park RS, Shulaker MM, Hills G, Suriyasena Liyanage L, Lee S, Tang A, Mitra S, Wong HSP (2016) ACS Nano 10:4599. doi:[10.1021/acsnano.6b00792](https://doi.org/10.1021/acsnano.6b00792)
109. Franklin AD, Tulevski GS, Han SJ, Shahrjerdi D, Cao Q, Chen HY, Wong HSP, Haensch W (2012) ACS Nano 6:1109. doi:[10.1021/nn203516z](https://doi.org/10.1021/nn203516z)
110. Shlafman M, Tabachnik T, Shtempluk O, Razin A, Kochetkov V, Yaish YE (2016) Appl Phys Lett 108:163104. doi:[10.1063/1.4947099](https://doi.org/10.1063/1.4947099)
111. Lefebvre J, Ding J, Li Z, Cheng F, Du N, Malenfant PRL (2015) Appl Phys Lett 107:243301. doi:[10.1063/1.4937223](https://doi.org/10.1063/1.4937223)
112. Ha TJ, Chen K, Chuang S, Yu KM, Kiriya D, Javey A (2015) Nano Lett 15:392. doi:[10.1021/nl5037098](https://doi.org/10.1021/nl5037098)
113. Seong N, Kim T, Kim H, Ha T-J, Hong Y (2015) Curr Appl Phys 15:S8. doi:[10.1016/j.cap.2015.03.009](https://doi.org/10.1016/j.cap.2015.03.009)
114. Zhang ZY, Wang S, Ding L, Liang XL, Pei T, Shen J, Xu HL, Chen O, Cui RL, Li Y, Peng LM (2008) Nano Lett 8:3696. doi:[10.1021/nl8018802](https://doi.org/10.1021/nl8018802)
115. Lee SW, Suh D, Lee SY, Lee YH (2014) Appl Phys Lett 104. doi:[10.1063/1.4873316](https://doi.org/10.1063/1.4873316)
116. Lee SW, Lee SY, Lim SC, Kwon Y-d, Yoon J-S, Uh K, Lee YH (2012) Appl Phys Lett 101:053504. doi:[10.1063/1.4740084](https://doi.org/10.1063/1.4740084)
117. Fuhrer MS, Nygard J, Shih L, Forero M, Yoon YG, Mazzone MSC, Choi HJ, Ihm J, Louie SG, Zettl A, McEuen PL (2000) Science 288:494. doi:[10.1126/science.288.5465.494](https://doi.org/10.1126/science.288.5465.494)
118. Liu Q, Luo G, Qin R, Li H, Yan X, Xu C, Lai L, Zhou J, Hou S, Wang E, Gao Z, Lu J (2011) Phys Rev B 83:155442. doi:[10.1103/PhysRevB.83.155442](https://doi.org/10.1103/PhysRevB.83.155442)
119. Pimparkar N, Alam MA (2008) Electron Device Lett IEEE 29:1037. doi:[10.1109/led.2008.2001259](https://doi.org/10.1109/led.2008.2001259)
120. Xia J, Dong G, Tian B, Yan Q, Zhang H, Liang X, Peng L (2016) Nanoscale 8:9988. doi:[10.1039/c6nr00876c](https://doi.org/10.1039/c6nr00876c)
121. Choi SJ, Bennett P, Takei K, Wang C, Lo CC, Javey A, Bokor J (2013) ACS Nano 7:798. doi:[10.1021/nn305277d](https://doi.org/10.1021/nn305277d)
122. Yang YJ, Ding L, Zhang ZY, Peng LM (2016) 4th carbon nanotube thin film electronics and applications satellite. In: Seventeenth international conference of the science and applications of nanotubes and low-dimensional materials, University of Vienna, Austria
123. Shin K, Jeon H, Park CE, Kim Y, Cho H, Lee G, Han JH (2010) Org Electron 11:1403. doi:[10.1016/j.orgel.2010.05.012](https://doi.org/10.1016/j.orgel.2010.05.012)
124. Barman SN, LeMieux MC, Baek J, Rivera R, Bao Z (2010) Acs Appl Mater Interfaces 2:2672. doi:[10.1021/am1005223](https://doi.org/10.1021/am1005223)
125. Asada Y, Miyata Y, Ohno Y, Kitauro R, Sugai T, Mizutani T, Shinohara H (2010) Adv Mater 22:2698. doi:[10.1002/adma.200904006](https://doi.org/10.1002/adma.200904006)
126. Lee CW, Han X, Chen F, Wei J, Chen Y, Chan-Park MB, Li L-J (2010) Adv Mater 22:1278. doi:[10.1002/adma.200902461](https://doi.org/10.1002/adma.200902461)
127. LeMieux MC, Sok S, Roberts ME, Opatkiewicz JP, Liu D, Barman SN, Patil N, Mitra S, Bao Z (2009) ACS Nano 3:4089. doi:[10.1021/nn900827v](https://doi.org/10.1021/nn900827v)
128. Vosgueritchian M, LeMieux MC, Dodge D, Bao Z (2010) Acs Nano 4:6137. doi:[10.1021/nn1012226](https://doi.org/10.1021/nn1012226)

129. Yuki N, Yuki T, Shota G, Satoki M, Kazuhiro Y, Taishi T (2012) *Jpn J Appl Phys* 51:06FD15
130. Ohmori S, Ihara K, Nihey F, Kuwahara Y, Saito T (2012) *Rsc Adv* 2:12408. doi:[10.1039/c2ra22272h](https://doi.org/10.1039/c2ra22272h)
131. Asada Y, Nihey F, Ohmori S, Shinohara H, Saito T (2011) *Adv Mater* 23:4631. doi:[10.1002/adma.201102806](https://doi.org/10.1002/adma.201102806)
132. Miyata Y, Shiozawa K, Asada Y, Ohno Y, Kitaura R, Mizutani T, Shinohara H (2011) *Nano Res* 4:963. doi:[10.1007/s12274-011-0152-7](https://doi.org/10.1007/s12274-011-0152-7)
133. Zhang J, Wang C, Fu Y, Che Y, Zhou C (2011) *Acs Nano* 5:3284. doi:[10.1021/nn2004298](https://doi.org/10.1021/nn2004298)
134. Wang C, Zhang J, Zhou C (2010) *Acs Nano* 4:7123. doi:[10.1021/nn1021378](https://doi.org/10.1021/nn1021378)
135. Raman Pillai SK, Chan-Park MB (2012) *Acs Applied Mater Interfaces* 4:7047. doi:[10.1021/am302431e](https://doi.org/10.1021/am302431e)
136. Lee CW, Raman Pillai SK, Luan X, Wang Y, Li CM, Chan-Park MB (2012) *Small* 8:2941. doi:[10.1002/smll.201200041](https://doi.org/10.1002/smll.201200041)
137. Lee D, Seol M-L, Moon D-I, Bennett P, Yoder N, Humes J, Bokor J, Choi Y-K, Choi S-J (2014) *Appl Phys Lett* 104:143508. doi:[10.1063/1.4871100](https://doi.org/10.1063/1.4871100)
138. Tatsuya T, Hiroshi F, Mamoru F (2013) *Jpn J Appl Phys* 52:03BB09
139. Li Z, Ding J, Lefebvre J, Malenfant PRL (2015) *Org Electron* 26:15. doi:[10.1016/j.orgel.2015.07.006](https://doi.org/10.1016/j.orgel.2015.07.006)
140. Yuki K, Fumiyuki N, Shigekazu O, Takeshi S (2015) *Appl Phys Express* 8:105101
141. Liu N, Yun KN, Yu H-Y, Shim JH, Lee CJ (2015) *Appl Phys Lett* 106:103106. doi:[10.1063/1.4914400](https://doi.org/10.1063/1.4914400)
142. Li G, Li Q, Jin Y, Zhao Y, Xiao X, Jiang K, Wang J, Fan S (2015) *Nanoscale* 7:17693. doi:[10.1039/c5nr05036g](https://doi.org/10.1039/c5nr05036g)
143. Wei L, Liu B, Wang X, Gui H, Yuan Y, Zhai S, Ng AK, Zhou C, Chen Y (2015) *Adv Electron Mater* 1:1500151. doi:[10.1002/aelm.201500151](https://doi.org/10.1002/aelm.201500151)
144. Cao C, Andrews JB, Kumar A, Franklin AD (2016) *Acs Nano* 10:5221. doi:[10.1021/acs.nano.6b00877](https://doi.org/10.1021/acs.nano.6b00877)
145. Gui H, Chen H, Khripin CY, Liu B, Fagan JA, Zhou C, Zheng M (2016) *Nanoscale* 8:3467. doi:[10.1039/c5nr07329d](https://doi.org/10.1039/c5nr07329d)
146. <http://www.carbonsolution.com/>
147. <http://www.sigmaaldrich.com/>

Carbon Nanotube Thin Films for High-Performance Flexible Electronics Applications

Jun Hirotani¹ · Yutaka Ohno^{1,2}

Received: 18 September 2018 / Accepted: 11 December 2018
© Springer Nature Switzerland AG 2019

Abstract

Carbon nanotube thin films have attracted considerable attention because of their potential use in flexible/stretchable electronics applications, such as flexible displays

trans parent conductors [19, 20], can be realized with CNT thin films. It should be emphasized that these functionalities can be achieved simultaneously with CNTs. The multi-functionalities and high performances are especially important requirements for wearable devices, where various functional devices must be integrated on a stretchable ultra-thin substrate. Another advantage of CNT thin films is processability. Simple room-temperature and nonvacuum processes can be adopted to form CNT thin films, such as the solution-based coating [21, 22], printing [23–27], and dry transfer [20, 28] processes. High-performance flexible devices can be manufactured by low-cost processes.

The greatest challenge for CNT electronics is the control of the structures of CNTs, i.e., the bandgap [29]. Recent progress on chirality-controlled growth and post-growth separation [30–33] will create new possibilities for the practical use of CNT devices. In particular, post-growth separation processes, such as density-gradient ultracentrifugation [30] and gel-column chromatography [34], have enabled the use of high-purity semiconducting CNTs in transistor applications. The formation of ultra-high-purity semiconducting CNTs with a purity of >99.9% was reported [35, 36].

However, to achieve the performance potentials of CNT materials, the formation of CNT thin films is a key issue. The current flows through multiple CNTs in the thin film. The conductivity of a CNT thin film is governed by the junctions between the CNTs, where a high junction resistance may exist. The junction resistances between the CNTs range from 100 k Ω to 10 M Ω , depending on the type of CNTs and the junction structure [37–39], which are much higher than the quantum resistances of one-dimensional ballistic conductors. Therefore, to obtain highly conductive CNT thin films, it is essential to reduce the number of tube-to-tube junctions in the current path by using long CNTs as well as maintaining clean tube surfaces to prevent increases in the junction resistance during the film formation process.

The alignment of the CNTs can also enhance the performance of thin film devices, especially for short channel field-effect transistors (FETs), in which the channel length is shorter than the length of the CNTs and each CNT is connected to electrodes directly. Highly aligned CNTs were grown on single-crystal oxide substrates, such as quartz and sapphire [40–43]. However, as-grown CNT arrays inevitably contain metallic CNTs, which significantly degrade the device performance.

The variability control in the device operation is also one of the most challenging issues to be addressed for CNT thin-film electronics. The variability is intrinsically caused by the randomness of the network structure of a CNT thin film, especially in the case of ultra-thin films for FET channels. The variability of the CNT thin film directly impacts the variability of the thin-film transistor (TFT) electrical performance, especially the current driving ability and gate capacitance. For logic circuits, the operation speed is limited by devices with low current driving abilities. Higher operation voltages are needed to secure a margin of error to account for the worst-case scenario, resulting in increased power consumption. For analogue circuits, such as amplifiers and analogue-to-digital converters for sensor applications, the transistor variability directly affects the circuit variability and performance. The accuracy of an analogue-to-digital converter is degraded by this variability, and a dedicated circuit design is necessary to compensate for the variability.

However, the experimentally observed variability is much larger than the intrinsic variability [44]. To date, the extrinsic origins of the characteristic variation are still unclear. There have been several numerical [45, 46] and experimental studies [44, 47] in which the characteristic variations of TFTs based on randomly dispersed CNT film were investigated. In the numerical simulations, two-dimensional percolation theory predicted that the characteristic variation would be reduced by increasing the number of CNTs in the channel, thereby increasing (averaging) the number of current paths [45]. This was observed experimentally by increasing the CNT number density with shortened CNTs [47]. The averaging method would be effective for solving the variability issue. However, other problems would arise, such as overlapping and bundling of CNTs, resulting in a degradation of the gate field effect due to the screening effect. For a bundle of CNTs, the gate field is screened by the outer CNTs, and the carrier densities of the inner CNTs are not significantly modified by the gate field. This results in a drain leakage current in the off state. For the variability issue, a film formation technique that provides a uniform monolayer film of individualized CNTs needs to be developed.

In this chapter, we review the recent progress on the above-mentioned issues of film formation technologies for CNT-based flexible electronics after reviewing the fundamental film formation processes.

2 Fundamental Film Formation Processes

CNTs are not typically grown directly on elastic substrates because of the large gap between the growth temperature of the CNTs and the glass transition point of the elastic substrate, and thus, the growth and deposition processes are separately carried out. There are two types of process for depositing a CNT thin film on an elastic substrate: solution and dry processes, as illustrated in Fig. 1. In the solution process, the raw soot of CNTs grown by chemical vapor deposition or other techniques is dispersed in a liquid, such as water or an organic solvent, to make an ink. Subsequently, a thin film is formed on an elastic substrate by printing or coating techniques. As a feature of the solution method, a separation process that yields high-purity semiconducting or metal CNTs by the previously mentioned method can be used after the dispersion process, based on the requirements of the application.

The key challenge of the solution process is the mono-dispersion of CNTs in the ink without damaging the CNTs. The degree of mono-dispersion directly impacts the purity and yield in the metal/semiconductor separation process. To achieve this, ultrasonication is applied in the dispersion process to de-bundle the CNTs in the raw soot. However, the CNTs are damaged and cut to shorter lengths by the sonication. This increases the number of junctions in the current path and degrades the carrier mobility and conductivity. In addition, a dispersant, such as a surfactant, and a polymer are added to the liquid to stabilize the dispersion of CNTs. The residual dispersant in the CNT film increases the contact resistance between the CNTs. Furthermore, some surfactants also cause unintentional carrier doping of the CNTs, making it difficult to control the threshold voltage of the transistors. A cleaning process

Fig. 1 Process flow chart from CNT thin film formation to device fabrication for solution and dry processes

must be developed to completely remove the surfactants and polymers used as the dispersant.

CNT thin films produced by the solution method exhibit much poorer performance than expected from the conductivity of individual CNTs in many cases. The typical lengths of CNTs range from 0.1 to 1.5 μm , depending on the sonication power and time [22, 48]. Recently, some efforts have been made to address these issues. Shirai et al. developed a selective dispersion–extraction process to overcome the trade-off between achieving sufficient dispersion and the lengths of the dispersed CNTs and obtained a highly conductive transparent conductive film based on the solution process [49]. This technique also overcomes the quality–quantity trade-off in the dispersion process, yielding long CNTs (10–20 μm) and short CNTs that were a few μm long for few-wall CNTs. The length-sorting technique based on gel-column chromatography developed by Miyata et al. is also effective for obtaining high-performance CNT thin films, though the yield is low [50]. The mean length of the length-sorted semiconducting CNTs was $\sim 1.5 \mu\text{m}$. A high carrier mobility of $164 \text{ cm}^2 \text{ V}^{-1} \text{ s}^{-1}$ was achieved in a CNT TFT. Toshimitsu et al. struggled with the residual dispersant issue and developed a removable solubilizer based on dynamic supramolecular coordination chemistry [51].

Another difficult issue to be addressed is the uniformity and bundling control of the CNT thin film in the deposition process. CNTs tend to agglomerate due to the surface tension of the liquid when the ink dries on the substrate, resulting in a non-uniform film. For transistor applications, the bundling of the CNTs should also be controlled. Recent progress regarding this issue will be presented further in the next section.

The main dry process for CNT film formation is a transfer process based on the floating-catalyst chemical vapor deposition technique [52]. In floating-catalyst chemical vapor deposition, the catalyst nanoparticles for CNT growth are not supported on a substrate but float in the carrier gas, and thus, individualized or bundled CNTs are obtained in aerosol form. A thin film can be easily obtained from the CNT aerosol by filtration [20] or direct deposition [53] methods. By the filtration method, the CNTs are collected by a membrane filter and a fairly uniform thin film of CNTs is obtained on the filter. The CNT thin film on the filter is transferable to various kinds of target substrates, such as plastic, glass, silicon, and metals [20]. For very thin CNT films for transistor applications, the thin films can be transferred by dissolving the nitrocellulose-based membrane filter with acetone after attaching the filter onto the target substrate [4]. Micro-attaching necessary for device applications is also possible in the filtration process by using a micro-attached filter [28]. In the direct deposition techniques, the CNTs are directly deposited on the plastic film by utilizing electrostatic forces [53] or temperature-gradient-induced thermophoresis [54–56] to attract the CNTs to the substrate. Alignment of the CNTs would also be possible by utilizing gas flow.

In dry processes, a thin film is directly formed by as-grown CNTs without dissolution in the liquid, unlike the solution process. Therefore, it is possible to obtain a uniform and high-performance thin film with long and contamination-free CNTs. The length of the single-walled CNTs ranges from 2 to 6 μm [57]. Aggregation of CNTs does not occur in the dry process. High-performance, transparent, conductive films with sheet resistances of $78 \Omega \text{ sq}^{-1}$ and optical transmittances of 90% were achieved [58]. The trade-off between the sheet resistance and optical transmittance can be overcome by aligning a microscale grid structure [28]. A roll-to-roll process for producing meter-scale transparent conductive films on a plastic film was recently developed by Wang et al. [59]. CNT TFTs with high-carrier mobilities of more than $1000 \text{ cm}^2 \text{ V}^{-1} \text{ s}^{-1}$ were also fabricated using the semi-dry process based on floating-catalyst chemical vapor deposition, where a CNT thin film was formed on a membrane filter and was subsequently transferred to a plastic substrate by dissolving the filter with acetone [4, 5]. The unique morphology of the long CNT network with Y-type tube-to-tube junctions rather than X-type junctions also contributed to the low contact resistance and high carrier mobility [4].

However, it is difficult to introduce a semiconductor/metal separation process, which is normally a solution-based process. The conduction ratio is controlled by the density and ratio of semiconducting/metallic CNTs. Semiconducting behavior can be obtained by using a network-like CNT thin film with a very low density near the percolation threshold. However, a short-circuit issue is likely to occur if it is a mixture of semiconducting and metallic CNTs. The probability of the short-circuit issue occurring increases with an increase in the density of the CNTs, and thus, there is a trade-off between uniformity and performance of the CNT TFTs. To overcome the trade-off, preferential growth of semiconducting CNTs and quality-controlled growth of particular CNT species may be possible solutions [60–62]. An alternate route is the selective removal of the metallic or semiconducting CNTs after the growth. The electrical breakdown technique by Joule heating is often used to selectively cut the metallic CNTs without damaging the other CNTs, exploiting the

Fig. 2 Effect of surfactant type on morphologies of CNT thin films formed by solution process. **a** AFM images and height profiles (the green line in the AFM image) of the typical CNT networks formed using (i) SDS, (ii) SDBS, (iii) SC, and (iv) DOC. Scale bar 1 μm . Inset in panels (iii) and (iv): magnified views of the thin film. Scale bar 400 nm. **b** Schematic images of the network with different attractive interactions in the solution just before removing it. More CNTs are aligned in a parallel fashion as the attractive interaction increases. (i) Aligned short bundles (SDS). (ii) Continuously connected bundles (SDBS). (iii) Locally aligned CNTs (SC). (iv) Random network of CNTs (DOC). (v, vi) Side-view images of the lateral calligraphy force, which is present when the substrate is dried. (v) The CNTs form bundles due to inhomogeneous lateral calligraphy forces (SDS, SDBS). (vi) The networks maintain a random network (SC, DOC) because the calligraphy forces cancel each other. Copyright 2013 American Chemical Society [78]

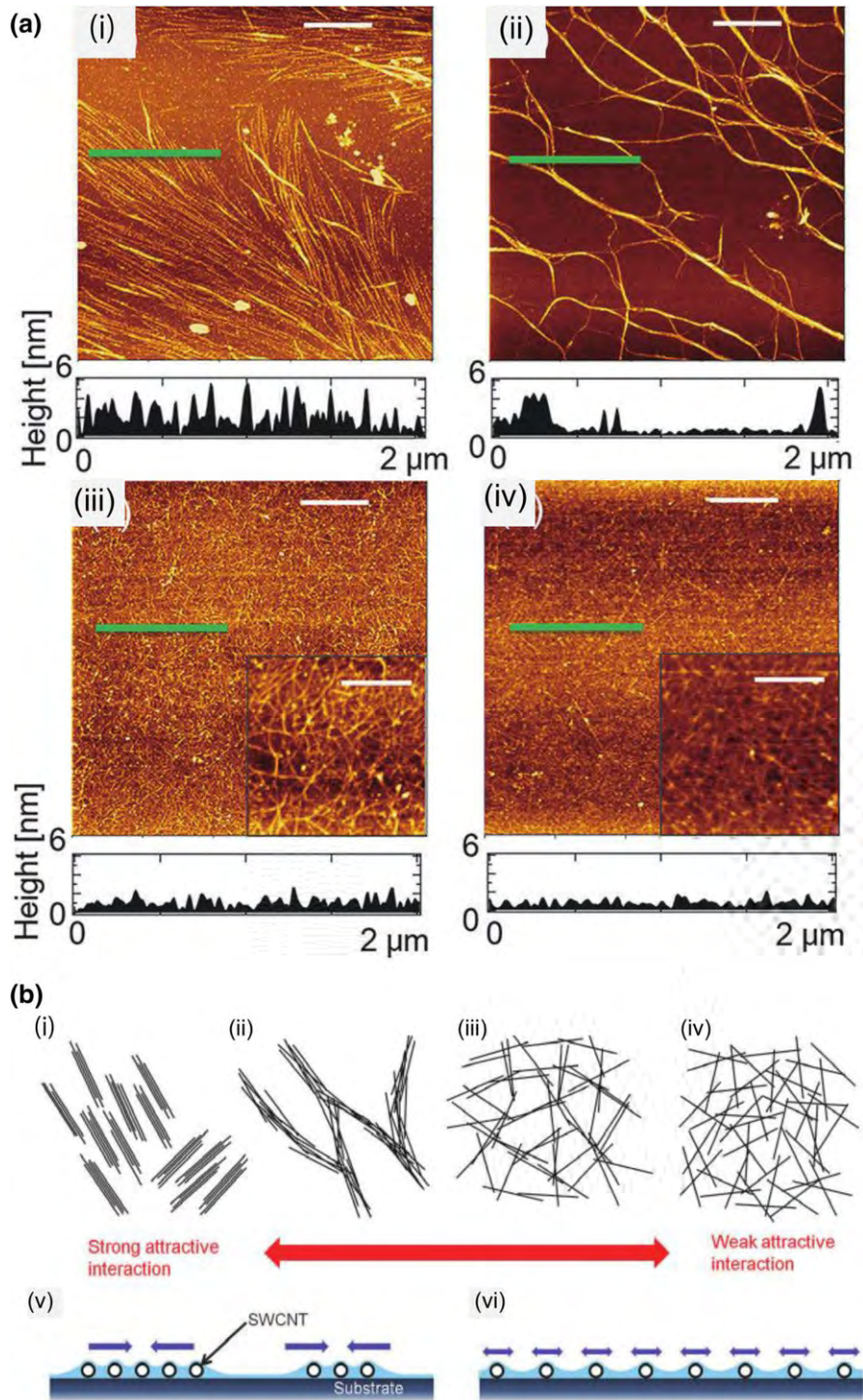
difference in the electrical transport properties of the two types of CNTs [63–66]. Polymer- and water-assisted electrical breakdown have been developed to burn metallic CNTs with large lengths [64, 67]. Chemical and electrochemical approaches [68–70] are scalable batch processes for the removal of metallic CNTs.

3 Thin-Film Formation for Semiconductor Applications

Solution-processed semiconducting CNTs can potentially be used to realize high-performance flexible transistors with high uniformity and yield. In this section, we focus on the recent progress in the deposition of semiconducting CNTs from suspensions onto substrates. By utilizing specific interactions between CNTs and functionalized surfaces [71, 72], the controlled deposition of CNT thin films, e.g., alignment, desired density, and micro-patterning, has been enabled.

Solution-based wet processes for random CNT network formation are mainly categorized as drop-casting [73], immersion-coating [74], spray-coating [75], filtration/transfer methods [19, 76], and dielectrophoretic assembly [77]. With a drop-casting technique, Shimizu et al. indicated that the surfactant type affects the morphology of CNT thin film and the TFT performance [78]. The network morphologies were highly dependent on the surfactant type, even though the CNT thin-films were fabricated from the same CNTs using the same process, as shown in Fig. 2. Sodium deoxycholate produced structures with the finest mesh sizes that comprised mostly individual CNTs. The performance of the TFTs was highly correlated with the morphology of the CNT network. The highest on/off ratio and mobility of 1×10^6 and $42 \text{ cm}^2 \text{ V}^{-1} \text{ s}^{-1}$ were obtained, respectively, for the TFT produced from sodium deoxycholate, due to the fine mesh structure. Designing surfactant–substrate interactions is important for assembling CNT networks. However, the mechanisms involved have not been clarified well.

Kiuya et al. investigated a CNT assembly with steroid- and alkyl-based surfactants [79]. They found that the steroid-based surfactants yielded highly dense CNT films. However, the alkyl surfactants prohibited CNT assembly due to formation of stacked alkyl layers of residual surfactants on the substrate surface that precluded surfactant-encapsulated CNTs, as illustrated in Fig. 3. Using this method, roll-to-roll assembly of CNTs on elastic substrates with high densities was achieved. Large-scale 4-in.-area CNT film formation was also reported by Tian et al. by covering the Si/SiO₂ surface with a CNT suspension, and wafer-scale



fabrication of TFTs was achieved with high yield on the entire surface of a Si substrate [80]. Using various geometries, 25,200 devices were fabricated on rigid and flexible substrates, and the structures exhibited relatively uniform characteristics. A similar technique was used to obtain TFTs that showed small threshold voltage distributions. Consequently, logic gates were able to achieve voltages as low as 2 V [81, 82].

Wet-filtration processes using a vacuum [76, 83] are also good candidates for obtaining large-scale and relatively uniform thin films.

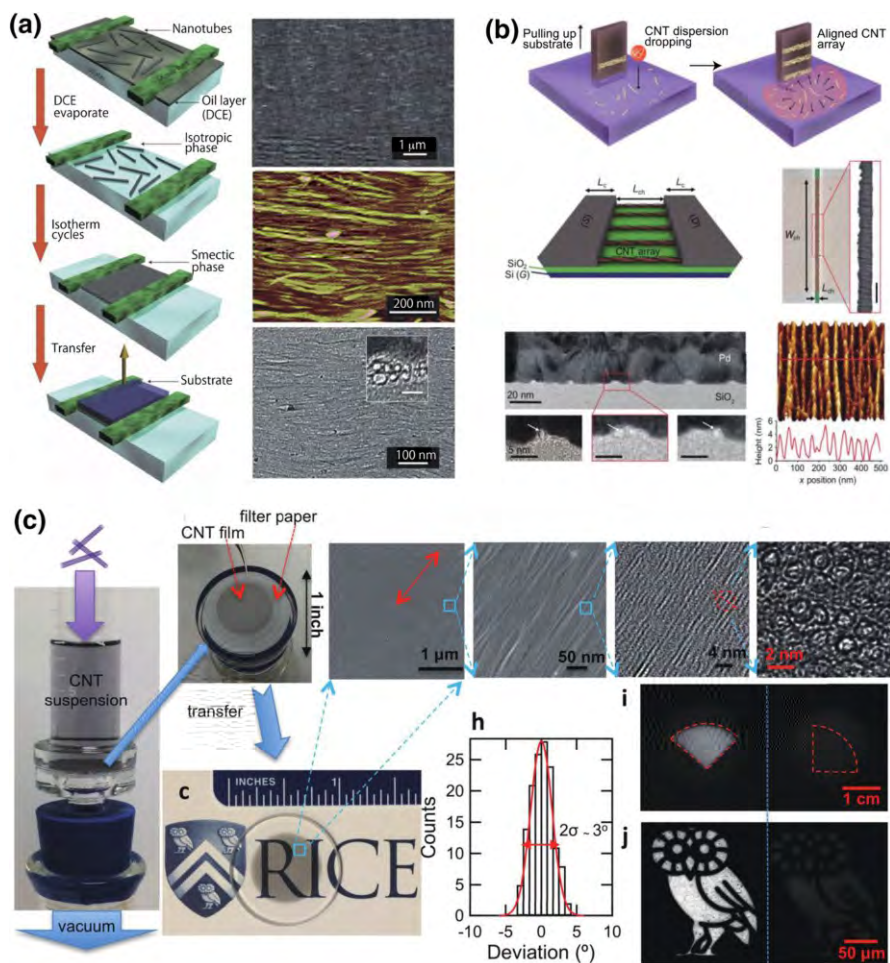


Fig. 4 Assembly of aligned CNT thin films. **a** Langmuir–Schaefer assembly process. SEM, AFM, and TEM images of the aligned CNT thin film. *Inset* of TEM image is the high-resolution cross-sectional TEM image (scale bar 5 nm). Copyright 2013 Macmillan Publishers Limited [85]. **b** The iterative process used to fabricate aligned CNTs given by the spreading and evaporation of controlled doses of organic solvent at the air/water interface. Copyright 2014 American Chemical Society [86]. FETs constructed from densely packed aligned semiconducting CNT arrays. Schematic of CNT array resting on a SiO₂/Si back gate with top Pd source and drain electrodes. False-colored SEM image of a representative FET with channel width W_{ch} of 4.1 μm and channel length L_{ch} of 150 nm. *Inset* SEM image (scale bar 200 nm) shows the CNT array, with 47 CNTs μm^{-1} and a high degree of alignment. Cross-sectional TEM image of Pd/CNT/SiO₂ electrode stack where the “humps” in the Pd cores correspond to CNTs in the array. High-resolution TEM images reveal individual CNTs beneath the Pd “humps” with diameters of 1.3–1.9 nm. AFM image of 30 nm of Pd coating a CNT array, showing the Pd conforming to the individual CNTs. Copyright 2016 American Association for the Advancement of Science [87]. **d** Slow filtration method for wafer-scale monodomain films of aligned CNTs. A CNT suspension passes slowly through a vacuum filtration system. A wafer-scale, uniform CNT film is formed on the filter membrane. The SEM and top-view TEM images show the strong alignment and high density of the film. A cross-sectional TEM image shows a high cross-sectional areal density of $\sim 10^9 \mu\text{m}^{-2}$. The angular distribution of CNTs with a standard deviation of 1.5° shows the high degree of alignment. The film is opaque to light polarized parallel to the CNT alignment direction and transparent to light polarized perpendicular to the alignment direction on a macroscopic scale. Copyright 2016 Science [90]

shown in Fig. 4a. The CVD method achieved semiconducting CNT arrays with high densities of more than $500 \text{ tubes } \mu\text{m}^{-1}$, and the transistor exhibited a high current density of 120 mA mm^{-1} and a transconductance greater than 40 mS mm^{-1} .

Floating evaporative self-assembly and alignment of semiconducting CNTs from organic solvents was achieved by Joo et al. The CNTs were highly aligned (within $\pm 14^\circ$), packed at a density of $\sim 50 \text{ tubes } \mu\text{m}^{-1}$, and formed a well-ordered monolayer, as shown in Fig. 4b [86]. The TFTs showed high performances with mobilities of $38 \text{ cm}^2 \text{ V}^{-1} \text{ s}^{-1}$ and on/off ratios of 2.2×10^6 for a channel size of $9 \text{ } \mu\text{m}$. The CNT FET with a channel length of 140 nm exhibited a current driving ability of 350 mA mm^{-1} .

circuits are indispensable for designing functional circuits, such as analogue–digital converters for wearable sensor applications.

References

1. Snow ES, Novak JP, Campbell PM, Pak D (2003) Random networks of carbon nanotubes as an electronic material. *Appl Phys Lett* 82:2145–2147
2. Cao Q et al (2008) Medium-scale carbon nanotube thin-film integrated circuits on flexible elastic substrates. *Nature* 454:495–502
3. Hu LB, Hecht DS, Greene G (2010) Carbon nanotube thin films: fabrication, properties, and applications. *Chem Rev* 110:5790–5844
4. Sun DM et al (2011) Flexible high-performance carbon nanotube integrated circuits. *Nat Nanotechnol* 6:156–161
5. Sun DM et al (2013) Mouldable all-carbon integrated circuits. *Nat. Commun.* 4:2302
6. Wu ZC et al (2004) Transparent, conductive carbon nanotube films. *Science* 305:1273–1276
7. Bradley K, Gabriel JCP, Greene G (2003) Flexible nanotube electronics. *Nano Lett* 3:1353–1355
8. McCee RL (2008) Advanced carbon electrode materials for molecular electrochemistry. *Chem Rev* 108:2646–2687
9. Choe S, McGuire K, Gothard N, Rao AM, Pham A (2003) Selective gas detection using a carbon nanotube sensor. *Appl Phys Lett* 83:2280–2282
10. Woo CS et al (2007) Fabrication of flexible and transparent single-wall carbon nanotube gas sensors by vacuum filtration and poly(dimethyl siloxane) mold transfer. *Micromol Eng* 84:1610–1613
11. Kim J, Yoo H, Ba VAP, Shin N, Hong S (2018) Dye-functionalized sol-gel matrix on carbon nanotubes for refreshable and flexible gas sensors. *Sci Rep* 8:11958
12. Ly SY (2008) Diagnosis of cations in vascular tissues using a fluorescence-doped carbon nanotube sensor. *Talanta* 74:1635–1641
13. Melzer K et al (2015) Flexible electrolyte-gated ion-selective sensors based on carbon nanotube networks. *IEEE Sens J* 15:3127–3134
14. Xuan X, Pak JY (2018) A miniaturized and flexible cadmium and lead ion detection sensor based on micro-attuned reduced graphene oxide/carbon nanotube/bismuth composite electrodes. *Sens. Actuators B* 255:1220–1227
15. Cai H, Cao XN, Jiang Y, He PG, Fang YZ (2003) Carbon nanotube-enhanced electrochemical DNA biosensor for DNA hybridization detection. *Anal Bioanal Chem* 375:287–293
16. Besteman K, Lee JO, Wiecz FGM, Heering HA, Dekker C (2003) Enzyme-coated carbon nanotubes as single-molecule biosensors. *Nano Lett* 3:727–730
17. Lauila T, Sainio S, Cao MA (2017) Hybrid carbon based nanomaterials for electrochemical detection of biomolecules. *Prog Mater Sci* 88:499–594
18. Sekitani T et al (2008) A rubber-like stretchable active matrix using elastic conductors. *Science* 321:1468–1472
19. Hu L, Hecht DS, Greene G (2004) Percolation in transparent and conducting carbon nanotube networks. *Nano Lett* 4:2513–2517
20. Kaskela A et al (2010) Aerosol-synthesized SWCNT networks with tunable conductivity and transparency by a dry transfer technique. *Nano Lett* 10:4349–4355
21. Wang HL et al (2010) High-performance field effect transistors from solution processed carbon nanotubes. *ACS Nano* 4:6659–6664
22. Asada Y et al (2010) High-performance thin-film transistors with DNA-assisted solution processing of isolated single-walled carbon nanotubes. *Adv Mater* 22:2698–2701
23. Lin YH, Lu F, Wang J (2004) Disposable carbon nanotube modified screen-printed biosensor for amperometric detection of organophosphorus pesticides and nerve agents. *Electroanal.* 16:145–149
24. Hu SH et al (2005) Printed thin-film transistors and complementary logic gates that use polymer-coated single-walled carbon nanotube networks. *J Appl Phys* 98:114302
25. Takenobu T et al (2009) Ink-jet printing of carbon nanotube thin-film transistors on flexible elastic substrates. *Appl Phys Express* 2:025005
26. Ha MJ et al (2010) Printed, sub-3 V digital circuits on elastic form aqueous carbon nanotube inks. *ACS Nano* 4:4388–4395

27. Cao X et al (2016) Fully screen-printed, large-area, and flexible active-matrix electrochromic displays using carbon nanotube thin-film transistors. *ACS Nano* 10:9816–9822
28. Fukaya N, Kim DY, Kishimoto S, Noda S, Ohno Y (2014) One-step sub-10 μm patterning of carbon-nanotube thin films for transparent conductive applications. *ACS Nano* 8:3285–3293
29. Saito R, Dresselhaus G, Dresselhaus MS (1998) Physical properties of carbon nanotubes. World Scientific Publishing Co. Pte. Ltd., Singapore
30. Arnold MS, Green AA, Hulvat JF, Stucky SL, Heath MC (2006) Sorting carbon nanotubes by electronic structure using density differentiation. *Nat Nanotechnol* 1:60–65
31. Tanaka T et al (2009) Simple and scalable gel-based separation of metallic and semiconducting carbon nanotubes. *Nano Lett* 9:1497–1500
32. Liu HP, Tanaka T, Uchibe Y, Kataura H (2013) High-efficiency single-chirality separation of carbon nanotubes using temperature-controlled gel chromatography. *Nano Lett* 13:1996–2003
33. Wu J et al (2012) Short channel field-effect transistors from highly enriched semiconducting carbon nanotubes. *Nano Res* 5:388–394
34. Tanaka T, Jin HH, Miyata Y, Kataura H (2008) High-yield separation of metallic and semiconducting single-wall carbon nanotubes by aqueous gel electrophoresis. *Appl Phys Express* 1:114001
35. Qiu S et al (2018) Solution-processing of high-purity semiconducting single-walled carbon nanotubes for electronics devices. *Adv Mater* 30:1800750
36. Lefebvre J et al (2017) High-purity semiconducting single-walled carbon nanotubes: a key enabling material in emerging electronics. *Acc Chem Res* 50:2479–2486
37. Fuhler MS et al (2000) Crossed nanotube junctions. *Science* 288:494–497
38. Nirmalraj PN, Lyons PE, De S, Coleman JN, Boland JJ (2009) Electrical connectivity in single-walled carbon nanotube networks. *Nano Lett* 9:3890–3895
39. Znidarsic A et al (2013) Spatially resolved transport properties of pristine and doped single-walled carbon nanotube networks. *J Phys Chem C* 117:13324–13330
40. Kocabas C et al (2007) Experimental and theoretical studies of transport through large scale, partially aligned arrays of single-walled carbon nanotubes in thin film type transistors. *Nano Lett* 7:1195–1202
41. Kang SJ et al (2007) High-performance electronics using dense, perfectly aligned arrays of single-walled carbon nanotubes. *Nat Nanotechnol* 2:230–236
42. Ago H et al (2005) Aligned growth of isolated single-walled carbon nanotubes programmed by atomic arrangement of substrate surface. *Chem Phys Lett* 408:433–438
43. Han S, Liu XL, Zhou CW (2005) Temperature-directional growth of single-walled carbon nanotubes on a- and c-plane surface. *J Am Chem Soc* 127:5294–5295
44. Hiotani J, Kishimoto S, Ohno Y (2018) Origins of the variability of the electrical characteristics of solution-processed carbon nanotube thin-film transistors and integrated circuits. *Nanoscale Adv.* <https://doi.org/10.1039/c1038na00184g>
45. Ishida M, Nihey F (2008) Estimating the yield and characteristics of random network carbon nanotube transistors. *Appl Phys Lett* 92:163507
46. Islam AE et al (2012) Effect of variations in diameter and density on the statistics of aligned array carbon-nanotube field effect transistors. *J Appl Phys* 111:054511
47. Ohmori S, Iha K, Nihey F, Kuwahara Y, Saito T (2012) Low variability with high performance in thin-film transistors of semiconducting carbon nanotubes achieved by shortening tube lengths. *RSC Adv* 2:12408
48. Asada Y et al (2011) Thin-film transistors with length-sorted DNA-walled single-wall carbon nanotubes. *J Phys Chem C* 115:270–273
49. Shihae H et al (2015) Overcoming the quality–quantity tradeoff in dispersion and printing of carbon nanotubes by a selective dispersion–extraction process. *Carbon* 91:20–29
50. Miyata Y et al (2011) Length-sorted semiconducting carbon nanotubes for high-mobility thin film transistors. *Nano Res* 4:963–970
51. Toshimitsu F, Nakashima N (2014) Semiconducting single-walled carbon nanotubes sorting with a removable solubilizer based on dynamic supramolecular coordination chemistry. *Nat Commun* 5:5041
52. Moissala A et al (2006) Single-walled carbon nanotube synthesis using ferrocene and ion-entacarbonyl in a laminar flow reactor. *Chem Eng Sci* 61:4393–4402
53. Zavodchikova MY et al (2009) Carbon nanotube thin film transistors based on aerosol methods. *Nanotechnology* 20:085201

54. Lefebvre J, Ding J (2017) Carbon nanotube thin film transistors by direct electrochemical synthesis. *Mater Today Commun* 10:72–79
55. Laiho P, Mustonen K, Ohno Y, Maeyama S, Kauranen EI (2017) Direct and directed deposition of aerosol-synthesized single-walled carbon nanotubes by thermal evaporation. *ACS Appl Mater Interfaces* 9:20738–20747
56. Laiho P et al (2018) Water-free thermal deposition of single-walled carbon nanotube thin films. *ACS Omega* 3:1322–1328
57. Kaskela A et al (2016) Highly individual SWCNTs for high performance thin film electronics. *Carbon* 103:228–234
58. Ding EX, Zhang Q, Wei N, Khan A, Kauranen EI (2018) High-performance single-walled carbon nanotube ambient conducting film fabricated by using low feeding rate of ethanol solution. *R Soc Open Sci* 5:180392
59. Wang BW et al (2018) Continuous fabrication of meter-scale single-wall carbon nanotube films and their use in flexible and ambient integrated circuits. *Adv Mater* 30:e1802057
60. Zhou WW, Zhan ST, Ding L, Liu J (2012) General rules for selective growth of enriched semi-conducting single walled carbon nanotubes with water vapor as in situ etchant. *J Am Chem Soc* 134:14019–14026
61. Yang F et al (2016) Templated synthesis of single-walled carbon nanotubes with specific structure. *Acc Chem Res* 49:606–615
62. Yang F et al (2014) Chirality-specific growth of single-walled carbon nanotubes on solid alloy catalysts. *Nature* 510:522–524
63. Li JH, Franklin AD, Liu J (2015) Gate-free electrical breakdown of metallic pathways in single-walled carbon nanotube crossbar networks. *Nano Lett* 15:6058–6065
64. Otsuka K, Inoue T, Chiashi S, Maeyama S (2014) Selective removal of metallic single-walled carbon nanotubes in full length by organic film-assisted electrical breakdown. *Nanoscale* 6:8831–8835
65. Collins PC, Avouris MS, Avouris P (2001) Engineering carbon nanotubes and nanotube circuits using electrical breakdown. *Science* 292:706–709
66. Otsuka K, Inoue T, Shimomura Y, Chiashi S, Maeyama S (2016) Field emission and anode etching during formation of length-controlled nanogaps in electrical breakdown of horizontally aligned single-walled carbon nanotubes. *Nanoscale* 8:16363–16370
67. Otsuka K, Inoue T, Shimomura Y, Chiashi S, Maeyama S (2017) Water-assisted self-sustained burning of metallic single-walled carbon nanotubes for scalable transistor fabrication. *Nano Res* 10:3248–3260
68. Yang CM et al (2005) Selective removal of metallic single-walled carbon nanotubes with small diameters by using nitric and sulfuric acids. *J Phys Chem B* 109:19242–19248
69. Zhang GY et al (2006) Selective etching of metallic carbon nanotubes by gas-phase reaction. *Science* 314:974–977
70. Wei DC et al (2009) Selective electrochemical etching of single-walled carbon nanotubes. *Adv Funct Mater* 19:3618–3624
71. LeMieux MC et al (2008) Self-sorted, aligned nanotube networks for thin-film transistors. *Science* 321:101–104
72. LeMieux MC et al (2009) Solution assembly of organized carbon nanotube networks for thin-film transistors. *ACS Nano* 3:4089–4097
73. Baedeker JA et al (2008) Directed assembly of single-walled carbon nanotubes via direct casting onto a UV-curable photosensitive monolayer. *J Am Chem Soc* 130:7226–7227
74. Shimizu M, Fujii S, Asano S, Tanaka T, Kataura H (2013) Fabrication of homogeneous thin films of semiconductor-enriched single-wall carbon nanotubes for uniform-quality transistors by using immersion coating. *Appl Phys Express* 6:105103
75. Jeong M, Lee K, Choi E, Kim A, Lee SB (2012) Spray-coated carbon nanotube thin-film transistors with stacked transport channels. *Nanotechnology* 23:505203
76. Maeda M et al (2015) Printed, short-channel, top-gate carbon nanotube thin-film transistors on flexible plastic film. *Appl Phys Express* 8:045102
77. Liang YR, Xia JY, Liang XL (2016) Short channel carbon nanotube thin film transistors with high on/off ratio fabricated by two-step firing field electro deposition. *Sci Bull* 61:794–800
78. Shimizu M, Fujii S, Tanaka T, Kataura H (2013) Effects of surfactants on the electronic transport properties of thin-film transistors of single-wall carbon nanotubes. *J Phys Chem C* 117:11744–11749
79. Kikuya D et al (2014) Design of surfactant-substrate interactions for roll-to-roll assembly of carbon nanotubes for thin-film transistors. *J Am Chem Soc* 136:11188–11194

80. Tian B et al (2016) Wafer-scale fabrication of carbon nanotube thin film transistors with high yield. *J Appl Phys* 120:034501
81. Chen BY et al (2016) Highly uniform carbon nanotube field-effect transistors and medium scale integrated circuits. *Nano Lett* 16:5120–5128
82. Xiang L et al (2018) Low-temperature carbon nanotube-based integrated circuits that can be transferred to biological surfaces. *Nat Electron* 1:237–245
83. Geier ML et al (2015) Solution-processed carbon nanotube thin-film complementary static random access memory. *Nat Nanotechnol* 10:944–948
84. Li XL et al (2007) Langmuir–Blodgett assembly of densely aligned single-walled carbon nanotubes from bulk materials. *J Am Chem Soc* 129:4890–4891
85. Cao Q et al (2013) Arrays of single-walled carbon nanotubes with full surface coverage for high-performance electronics. *Nat Nanotechnol* 8:180–186
86. Joo Y, Brady GJ, Arnold MS, Goalan P (2014) Dose-controlled, floating evaporative self-assembly and alignment of semiconducting carbon nanotubes from organic solvents. *Langmuir* 30:3460–3466
87. Brady GJ et al (2016) Quasi-ballistic carbon nanotube array transistors with current density exceeding Si and GaAs. *Sci Adv* 2:e1601240
88. Cao Y et al (2016) Radio frequency transistors using aligned semiconducting carbon nanotubes with current-gain cutoff frequency and maximum oscillation frequency simultaneously greater than 70 GHz. *ACS Nano* 10:6782–6790
89. Wu J, Antaris A, Gong M, Dai H (2014) Top-down patterning and self-assembly for regular arrays of semiconducting single-walled carbon nanotubes. *Adv Mater* 26:6151–6156
90. He XW et al (2016) Wafer-scale monodomain films of spontaneously aligned single-walled carbon nanotubes. *Nat Nanotechnol* 11:633–638

Publisher's Note Springer Nature remains neutral with regard to jurisdictional claims in published maps and institutional affiliations.



Single-Walled Carbon Nanotubes in Solar Cells

Il Jeon¹ · Yutaka Matsuo^{1,2} · Shigeo Maruyama^{1,3}

Received: 28 January 2017 / Accepted: 23 December 2017 / Published online: 22 January 2018
Springer International Publishing AG, part of Springer Nature 2018

Abstract Photovoltaic, more generally known as solar cell, are made from semiconductor materials that convert light into electricity. Solar cells have received much attention in recent years due to their promise as a clean and efficient light-harvesting device. Single-walled carbon nanotubes (SWNT) could play a crucial role in the device and have been the subject of much research, which continues to this day. SWNT are known to outperform multi-walled carbon nanotubes (MWNT) as a low-density, because of the difference in their optical transmittance for the same current density, which is the most important parameter in comparing SWNT and MWNT. SWNT have low semiconducting features, which make SWNT function as a active or charge-transporting material. This chapter, consisting of two sections, focuses on the use of SWNT in solar cells. In the first section, we discuss SWNT as a light harvester and charge transporter in the photovoltaic layer, which are reviewed chronologically to show the history of the research progress. In the second section, we discuss SWNT as a transparent conductive layer outside of the photovoltaic layer, which is relatively more actively researched. This section introduces SWNT application in silicon solar cell, organic solar cell, and perovskite solar cell each, from their prospective to recent results. As we go along, the science and progress of the application of solar cells will be discussed.

Chapter 10 was originally published as Jeon, I., Matsuo, Y. & Maruyama, S. Top Curr Chem (Z) (2018) 376: 4. <https://doi.org/10.1007/s41061-017-0181-0>.

✉ Shigeo Maruyama
maruyama@photon.ueo.ac.jp

¹ Department of Mechanical Engineering, The University of Tokyo, Tokyo 113-8656, Japan

² Hefei National Laboratory for Physical Science at Microscale, University of Science and Technology of China, Anhui 230026, China

³ Energy Nano Engineering Laboratory, National Institute of Advanced Industrial Science and Technology (AIST), Ibaraki 305-8564, Japan

Keywords Carbon nanotube · Silicon solar cell · Organic solar cell · Perovskite solar cell

1 Single-Walled Carbon Nanotubes as the Photoactive Material in Solar Cells

SWNT provide an ideal light-harvesting medium, which has a wide range of direct band gap [1], strong absorption within the solar spectrum [2–4], and high carrier mobility [5, 6] with the excellent chemical stability. Compared with carbon nanotube (CNT), organic compounds have inherently low carrier mobility and low stability. Organic semiconductors have carrier mobility that is a hundredth of inorganic materials. This creates a bottleneck in the performance of organic solar cells (OSC) [7–11]. Therefore, incorporating CNT in OSC can improve device performance greatly. In this section, we discuss the use of SWNT in the photoactive layer of photovoltaic devices, and review the demonstration of this technology in literature.

An individual SWNT can form a p-n junction diode, giving rise to the photovoltaic effect [12, 13]. Thus, SWNT exhibits high power conversion efficiency (PCE) under illumination. SWNT comprises semiconducting and metallic forms, generally in a 2:1 ratio. Semiconducting SWNT forms Schottky contacts with metallic objects, which are responsible for the ideal diode behavior, whereas metallic SWNT easily recombine electrons and holes [14]. It is therefore important that SWNT be purified according to their use. The difference in electronic structure between semiconducting and metallic SWNT originates from their chirality, and they can be chirality-specifically synthesized [15, 16] or sorted by various methods based on their diameter and electronic properties (Fig. 1). Well-known sorting methods are density gradient ultracentrifugation [17, 18]

only a slight barrier, but also a charge transporter in the photoactive layer. This means the SWNT provides the dual functionality of a light absorber and a charge-electric material.

Solar cell devices, in general, are mainly composed of an active layer, a charge-electric layer, and a charge-conductive layer. The active layer absorbs light and generates electron-hole pairs. The charge-electric layer separates the photo-generated electron-hole pairs and prevents recombination after excitation. The electrons are then followed by the conductive layer, which extracts the separated charge. A polymer material composed of conductive polymer, and SWNT allows efficient dissociation in a strong electric field, with the CNT functioning as the electron transporter [21]. An interesting donor-acceptor heterojunction achieves efficient charge separation and charge collection both for electron and hole transport toward their respective contacts through the polymer donor and CNT acceptor. Poly(3-hexylthiophene), or P3HT, and poly(3-octylthiophene), P3OT, are the most commonly used polymer donors and are generally mixed with SWNT in solution [22, 23].

1.1 CNT as Electron Acceptors/Transporters

In this line of research, CNT served as an electron acceptor. Prof. Sir. Richard Friend reported polymer- and CNT-based OSC using poly(*p*-phenylene vinylene), PPV, and MWNT (Table 1: report A for the first time on the basis of knowledge) [24]. Despite the electron transfer from PPV to the CNT, charge recombination within the CNT network limited the device performance. Moreover, poor dispersion of CNT in PPV resulted in severe aggregation of the CNT. Y. Maki and Amaraunga reported the OSC using SWNT, which were mixed with P3OT (Table 1: report B) [21, 25]. Although the PCE was low (0.04%), they successfully demonstrated the electron acceptor behavior of the SWNT with an open-circuit voltage (V_{OC}) of 0.9 V and fill factor (FF) of 0.4. The results revealed that photo-generated electron transfer occurred at the polymer/nanotube interface and showed the promise of conjugated polymer-SWNT composite. C_{60} -modified SWNT were mixed with P3HT to give a much-improved PCE of 0.57% (Table 1: report C) [26, 27]. SWNT and C_{60} were mixed in solution and irradiated with microwave, followed by addition of P3HT. Improved short-circuit current density (J_{SC}) was a direct result of higher electron mobility owing to the SWNT. Furthermore, a change of morphology increased FF as well.

Thermal post-treatment was also considered as a point, which enhances heating device beyond the glass transition temperature of the polymer donor. This treatment caused beneficial phase separation of the blend and improved the ordering of the polymeric chain, which improved charge transfer, transport, and collection. It was also reported that this treatment substantially increased the hole mobility of the polymer-CNT composite [28]. J. J. Li and colleagues reported SWNT, P3HT, and 1-(3-methoxycarbonyl)-propyl-1-phenyl[6,6]C61 (PCBM) nanocomposite have been prepared by a method using high dilution followed by concentration to control the ratio of CNT-to-P3HT/PCBM in the mixture and disperse the CNT

Table 1 Photochemical data of representative devices from literature, in which SWNT has been used as either a light harvester or charge transporter

S. No.	Structure	PCE (%)	Note
A	MWNT/PPV/Al	1.8	The effect of OSC using CNT in the active layer
B	ITO/P3OT:SWNT/Al	0.04	The effect of OSC using SWNT in the active layer
C	ITO/PEDOT/P3HT:C ₆₀ -SWNT/Al	0.57	C ₆₀ -SWNT composite were used
D	ITO/PEDOT/CNT:P3HT:PCBM/LiF/Al	2.0	Studied the effect of CNT content in composite
E	ITO/PEDOT:SWNT/P3HT:PCBM/Al	4.9	Incorporated positional effect of SWNT on PCE
F	ITO/PEDOT/SWNT:P3HT/BCP/Al	0.72	Using emiconducting SWNT coated with P3HT
G	ITO/SWNT:PCBM/C60/BCP/Ag	1.3	SWNT as electron donor and infrared absorber
H	ITO/PEDOT/SWNT:r-GO:C ₇₀ /C ₇₀ /Al	0.85	Incorporated reduced graphene oxide
I	ITO/PEDOT/TFB/PC ₇₁ BM:r-GO:SWNT/Al	1.3	Further improved PCE by using PC ₇₁ BM
J	ITO/PEDOT/SWNT/C ₆₀ /Ag	0.46	No SWNT composite, a simple full-carbon SC
K	ITO/ZnO NW/SWNT:PC ₇₁ BM/MoO ₃ /Ag	3.1	Application of ZnO NW
L	ITO/PEDOT/P3HT:PCBM:B-CNT/TiO ₂ /Al	4.1	B-, N-doped MWNT were used to enhance PCE
M	ITO/PEDOT/P3HT:ICBA:QD:N-CNT/TiO ₂ /Al	6.1	QD were used to enhance doping and dipole ion
N	ITO/PEDOT/PTB7:PC ₇₁ BM:N-CNT/Ca/Al	8.6	Low-band gap polymer, PTB7 was used
O	ITO/ZnO/P3HT:SWNT/MoS ₂ /PEDOT/Al	0.46	SWNT enabled a mixture of MoS ₂ and P3HT

homogeneous hydrophobic materials (Table 1: report D) [5]. A P3HT/PCBM (1:1) mixture with 0.1 wt % MWNT gave the highest PCE of 2.0%. Oskan and colleagues realized controlled placement of an SWNT monolayer network for different position in polymer fullerene solar cell and found that SWNT on the hole-collecting side of the active layer gave a high PCE of 4.9% (Table 1: report E; Fig. 2) [6]. They also demonstrated that SWNT on top of the active layer led to an increased device lifetime of P3HT. Dip coating from a hydrophilic suspension was used for this experiment. Gradedecak and co-workers researched SWNT as electron acceptor and demonstrated a PCE of 0.72% for SWNT/P3HT bulk heterojunction solar cell (Table 1: report F) [29]. A key point in his research was using pre-emiconducting SWNT coated with well-ordered P3HT by intercalation to enhance charge separation and transport. They found that the electrical characteristics of the device were strongly dependent on the SWNT loading. Modeling of the V_{OC} suggested that despite the large carrier mobility in SWNT, PCE was limited by carrier recombination.

Fig. 2 Illustration of a work reported in reference [6]. SWNT located either above or below the hole-transporting layer of OSC perform the best (the numbers indicate PCE obtained with different position of the SWNT layer)

1.2 CNT as Light Absorber and Electron Donor

Arnold and colleagues when further explored how an emiconducting SWNT can be used not only as an electron acceptor but also as a high-harvesting electron donor as well [30–32]. They formed an emiconducting SWNT/PCBM bulk heterojunction with a layer of bathophthalocyanine (BCP) and overcame the limited diffusion of emiconducting SWNT to produce near-infrared efficiency of 1.3% (Table 1: report G) [33]. A follow-up work [34] provided some mechanistic insight but did not produce a higher efficiency, particularly in the visible region of the solar spectrum. Higher efficiency was not realized until reduced graphene oxide (r-GO) was introduced as a cascade material connecting SWNT and fullerene acceptor. Both pristine CNT and graphene have low surface energy arising from natural C–C bonding [35, 36]. In contrast, chemically modified graphene, such as r-GO and nitrogen-doped GO, have higher surface energy due to their surface functional groups and doped heteroatoms with differing electronegativity [37–39]. With a moderate area and relatively high surface energy, chemically modified graphene adds a robust additional layer to be built upon in further nanoscale processing. The high thermal and chemical stability of chemically modified graphene is advantageous for direct nanoscale processing. Huang and colleagues achieved PCE of 0.21 and 0.85% using C₆₀ and C₇₀, respectively, in a system with emiconducting SWNT as the donor, fullerene as the acceptor, and r-GO as an energetically mediating species (Table 1: report H) [40, 41]. Ren and colleagues followed this theme by using r-GO and SWNT with [6]-phenyl C₇₁-biphenyl carboxylic acid methyl ester (PC₇₁BM). Also, poly[[9,9-dioctylfluorene-2,7-diyl)-co-(4,4'-bis(4-ethylphenyl)-2,5-dithienyl)] diphenylamine (TFB) was used as a hole-blocking layer, which is rather unusual. They achieved a PCE of 1.3% using a composition of PC₇₁BM (88–97%) / emiconducting-SWNT (1–10%) / r-GO (2%; Table 1: report I) [42]. Bao and colleagues reported an attempt at an all-carbon OSC, in which the anode, the active layer, and the cathode were all made up of carbon material. As a result, they optimized the active layer composed of a bilayer of oxygen- or ed emiconducting SWNT as the light absorber and donor and C₆₀ as the acceptor between indium tin oxide (ITO) and metal electrode. By optimizing the emiconducting SWNT dispersion and deposition condition and the C₆₀ layer thickness, they produced a PCE of 0.46% (Table 1: report J) [43, 44]. A new

ep, he replaced the ITO anode with r-GO lyer and the metallic cathode with an n-type SWNT film to achieve an all-carbon OSC. However, PCE were on the order of 0.1%. In 2014, Heram and colleagues reported a Na-ional Renewable Energy Laboratory-certified PCE of 2.5% and a higher PCE of 3.1% using emiconducting SWNT of aristic chirality as the hole-transporting and light-harvesting material (Table 1: report K) [45]. Compared with single-chirality emiconducting SWNT, multi-chirality emiconducting SWNT enabled a wider range of absorption from visible to near-infrared. Normal and inverted architectures were also fabricated and compared. An inverted architecture gave a higher efficiency owing to ZnO nano-wire (NW) penetrating the active lyer (Fig. 3).

1.3 CNT as Charge Transporter and Others

Despite considerable research efforts, the use of CNT as a charge transporter did not yield a substantial leap in PCE with the use of dopants and the introduction of inorganic materials, such as quantum dots (QD). Kim and co-workers addressed the intrinsic limitation imposed by the recombination effect and improved PCE by more than 30% through B and N doping (Table 1: report L) [46]. B- and N-doped CNT functioned as efficient charge-electron transport material with a benchmark effect. The low work function of N-doped CNT aligned well with the electron transport energy level, while the high work function of B-doped CNT aligned well with the hole transport level. Kama and colleagues studied the interaction between SWNT and light-harvesting CdS [47, 48]. Since then, Raelle and colleagues [49] demonstrated the incorporation of QD in a SWNT composite in 2005 and colloidal QD-decorated N-doped CNT were developed for synergistic charge separation and transport enhancement. Porey charged QD could directly attach a N-doped piece of CNT as an electrocatalytic interaction. Such an ideal hybrid structure with an adhesive lyer showed a synergistic effect, combining efficient electron and hole separation. Efficiency soared, reaching 4.7–6.11% (Table 1: report M) when using indene-C60 bisadditive (ICBA) as the electron acceptor [50], and climbed to 7.5–8.6% upon further development using different organic photoactive materials (Table 1: report N) [51]. With QD as an acceptor and doped CNT as an efficient

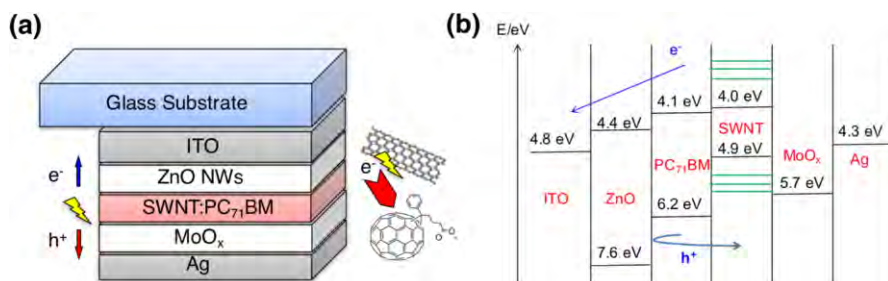


Fig. 3 Illustration of **a** an inverted solar cell where ZnO NW and SWNT:PC₇₁BM were used and **b** the energy level diagram

charge transport, the evidence demonstration has worked function-able chemically modified CNT has the potential to improve charge separation, transport, and recombination in SWNT-based OSC, which generally suffer from trapping and low transport of charge carrier in their organic acetylene and energy level mismatch interface.

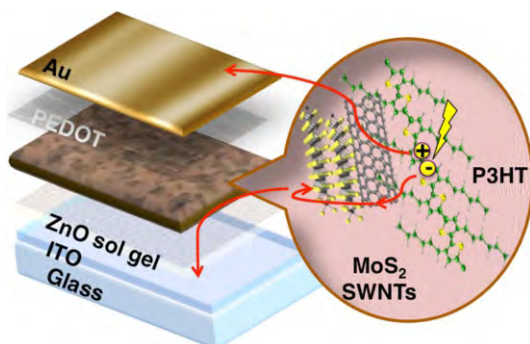
Other approaches have been taken to apply SWNT in the acetylene. We reported the use of modified MoS₂ on low-conductivity semiconducting SWNT as the electron acceptor in a bulk heterojunction with P3HT in inverted OSC (Fig. 4) [52]. MoS₂ is an inorganic material has intrinsically immiscible with organic compounds. However, we were able to disperse in organic matrix by exploiting the tendency of SWNT to intercalate with P3HT through interaction. The successful binding of MoS₂ on SWNT bundle and its photovoltaic effect was clearly evidenced by a PCE of 0.46% (Table 1: report O).

We have briefly reviewed the use of SWNT as the light harvest or charge transport in the photovoltaic layer of solar cell. Chirality, chemical doping, and dispersibility in solution were critical factors in achieving high performance. Various approaches have been introduced to improve SWNT application and the ongoing expanded the possibilities of CNT technology in solar cell. Yet, this is still the tip of the iceberg. Uniform blending of the electron-donating conjugated polymer and the electron-accepting CNT is one of the most challenging as well as a critical aspect in creating efficient photovoltaic collection in CNT-based OSC device. Therefore, research on using CNT in the photovoltaic layer of OSC device is still in the early stage and room remains for novel methods to take better advantage of the advantages proper use of CNT.

2 Single-Walled Carbon Nanotubes as a Transparent Electrode in Solar Cells

Many type of solar cell have been developed over the years: silicon solar cell, followed by OSC [53–55], and most recently perovskite solar cell (PSC), which have emerged as a focus of research. A critical aspect common to these device is their transparent electrode through which light travels before causing








Fig. 4 Illustration of MoS₂/SWNT:P3HT-based solar cell



electricity in the active layer. Conventionally, ITO has been used as the transparent electrode, and it is an essential component in almost all the device designs in the reaction. The high conductivity and transparency of ITO are unparalleled so far. There have been many attempts to replace ITO because of its high cost and limited earth-abundance. Other downside includes brittleness, which makes it unable to withstand cyclic electrolysis without breaking. An additional drawback is ITO's vulnerability to high temperatures. Therefore, borine-doped tin oxide (FTO), which can withstand higher temperatures than ITO, is sometimes used instead. Avoiding the elimination by using alternative transparent electrode material has therefore been the subject of intense research for many years [56, 57]. The difficulty has been the finding an alternative electrode that is not only robust and cheap, but also optically transparent and electrically conductive [58–60]. CNT has good optical transparency over a broad range from the visible to the near-infrared as well as high electrical conductivity [61–64]. In addition to this, the outstanding mechanical resilience of CNT not only exceeds that of ITO but also a order of magnitude of solar cell device. SWNT are effective for hole collection because their work function is in the range 4.8–5.0 eV, which is higher than that of ITO (about 4.8 eV) [64]. The cost of CNT fabrication has also been reported to be the same or lower than that of ITO [65]. Good performance of the resistance–optical transparency can be obtained by metal-based electrode such as metal grid transparent electrode [66] or silver (Ag) nanowire [67]. Comprehensive review of transparent electrode for device are available [68]. In Fig. 5, the resistance–optical transparency at 550 nm wavelength of the dry-deposited SWNT film [63] are compared with CVD graphene [69], DWNT [70], typical ITO, PET/ITO, FTO, and Ag nanowire [67]. Performance of SWNT film can be further enhanced by adequate doping [71]. In this section, we discuss the feasibility of SWNT as a transparent electrode in solar cell by reviewing application reported so far.

Fig. 5 Sheet resistance–transparency plot for various transparent conductors (Pristine SWNT [63], Doped SWNT [63], CVD graphene [69], CVD DWNT [70], ITO from K3rammo Co., Ltd., PET/ITO from Nippon Sheet Glass Co., Ltd., and Ag nanowire [67])

Table 2 Photo catalytic degradation of organic pollutants using SWNT, from literature

	CNT reagent	Si reagent	Silicon	PCE (%)	Note
A	SOCl ₂	n/a	Si/SWNT	1.3	The r SWNT-based silicon solar cell
B	SOCl ₂	n/a	Ag/Si/SWNT/Ag	4.5	Transferring a -gro ^W n SWNT on silicon
C	n/a	HF	Ag/Si/SWNT/Cr/ 	1.7	Synthesized CNT chirality and random orientation
D	n/a	Oxidation		10.9	Electrodeposition of graphene
E	HNO ₃ /NaCl	HF	Ti/Si/SWNT/ 	13.8	p doping of HNO ₃
F	HNO ₃	HF	Ti/Si/SWNT/ 	10.0	Encapsulation of the active area by PDMS
G	n/a	Oxidation		12.0	Grid line of SWNT on the small area of Si
H				2.4	(6,5) SWNT with high impedance
I	HNO ₃	HF	Al/Si/SiO ₂ /SWNT/Cr/ 	11.3	Keeping acid in the oxide layer of CNT
J	HNO ₃	HF	 /Si/SiO ₂ /SWNT/Cr/  (Al)	11.5	Superacid catalytic reaction
K	HNO ₃		P/Ti/n-Si/SWNT/P	10.0	Micro-honeycomb network CNT
L				14.9	SWNT and graphene comparison on Si
M			P/Ti/n-Si/SWNT/P	11	Application of a SWNT
N	MoO ₃	HF	In/Si/SWNT/MoO ₃ / 	17.0	Application of MoO ₃ doping.

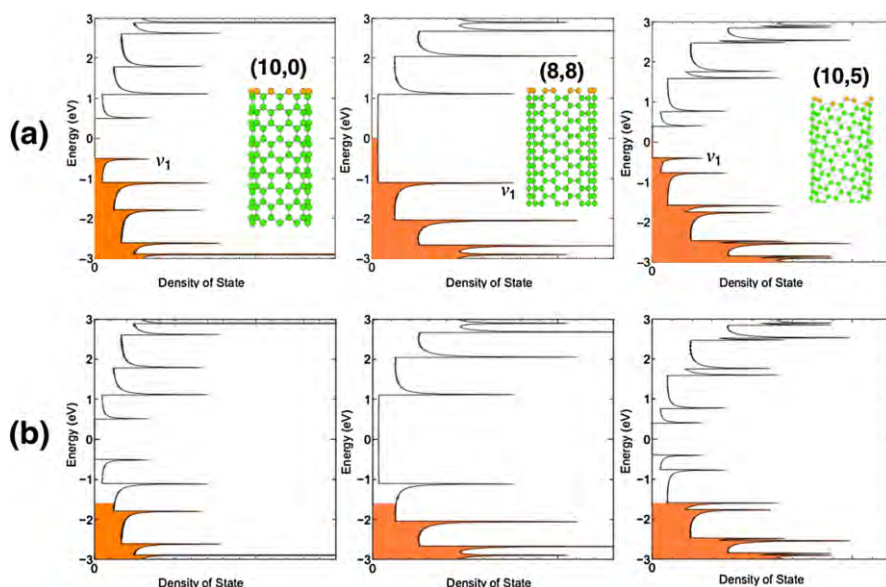


Fig. 7 **a** Density of state and v_1 of an armchair SWNT, a zigzag SWNT, and a chiral SWNT. **b** Density of state after p doping

of (6,5) SWNT (Table 2: report H) [91]. Regarding acid doping, an even higher PCE greater than 11.2% was achieved by Taylor and colleagues by keeping the acid inside the void space of CNT (Table 2: report I) [73]. They discovered the characteristic of dark for w and ac eren density with varying emperable and found a temperature-dependent ac eren rectification originally from thermally activated band-to-band transition of carrier in silicon and the SWNT thin film enabled a built-in potential for carrier separation/collect ion. In the same year, Taylor published another paper with a marginally improved PCE of 11.5%. A new superacid liquid casting method was used for the CNT fabrication (Table 2: report J) [92]. A PCE of 10.0% was also achieved by building micro-honeycomb CNT network in silicon SC (Table 2: report K) [93]. We reported vertically aligned SWNT treated with water to form a honeycomb network on n -Si substrate. CNT and graphene were combined with cylindrical silicon wafer to fabricate silicon solar cell. Solar cell with direct graphene-silicon contact exhibited better characteristics than did those with CNT-silicon contact, owing to improved junction quality and increased contact area. Using the composite film, the obtained SWNT/graphene/Si solar cell reached a PCE of 14.9% (Table 2: report L) [94]. A problem with weak acid doping is a high electron benching rate, which reduced the efficiency by employing aligned CNT, which shortened the transport distance. Moreover, the aligned CNT were in better contact with the silicon as evidenced by an increase in J_{SC} . Overall, the primary aerological SWNT with long bundle length to fabricate SWNT/Si solar cell [95]. A PCE approaching 11% was achieved by using a primary SWNT with many chemical reactions (Table 2: report M). More importantly, the solar cell were able for

a leave 10 months in air without any passivation. In fact, a slight increase in PCE was observed after storing in air, in contrast to previously reported in the literature. Li et al. [96] demonstrated an *n*-SWNT/*p*-Si photovoltaic system by joining SWNT from *p*-type to *n*-type through polyethyleneimine functionalization. Recently, Ma-Bada and colleagues studied metal oxide layer to prepare both *p*-SWNT/*n*-Si and *n*-SWNT/*p*-Si with significant improved PCE [97]. The metal oxide also serves as a both an antireflective layer and an efficient carrier dopant, leading to reduced loss of incident solar light and increased photocurrent, respectively. As a consequence, the photovoltaic performance of both *p*-SWNT/*n*-Si and *n*-SWNT/*p*-Si heterojunction solar cell using MoO₃ and ZnO layer was improved, resulting in very high PCE of 17.0 and 4.0%, respectively (Table 2: report N).

Since the early report of a PCE around 1%, CNT/Si solar cell has seen rapid performance gain up to around 17%. However, the mechanism is still unclear, as the Schottky metal oxide junction theory established by Jia et al. contradicts the *p*-*n* junction theory of Ong et al. [85]. However, the Schottky metal oxide junction theory seems to be more dominant for the time being. Although the polychirality of CNT further obscures this issue, pure CNT are becoming increasingly available, so we can anticipate a clearer understanding in the near future. Considering the decade of wide-ranging research in silicon solar cell, this is still a relatively small area of research and it is worthwhile to investigate the device further. The apparent early high PCE has been rapidly achieved by a limited number of research groups, including and beyond prompt further research.

2.2 Single-Walled Carbon Nanotubes as a Transparent Electrode in Organic Solar Cells

OSC has received focused attention in recent academic research [98–100] due to OSC providing flexibility and a lower cost than silicon solar cell cannot match. OSC built by conducting organic compounds as electron donor and electron-rich fullerene derivative as electron acceptor [55, 101]. Owing to their high absorption coefficient, low cost, and mechanical flexibility, OSC has been established as one of the important categories of solar cell research. Nevertheless, despite the considerable achievement in recent years, OSC are still faced with limitations including the reduced light absorption range of organic compounds, reduced hole mobility, and intrinsic instability [102]. Above all, the maximum PCE of OSC (ca. 10%) are lagging behind those of silicon solar cell (ca. 20%).

Early on, many studies were conducted having CNT as a light harvester in OSC, as discussed in the previous section of this chapter [21]. Nowadays, however, CNT in OSC are typically not responsible for electron generation upon light absorption. Instead, a more promising approach is to use CNT on either side of the device as a charge-collecting transparent electrode. In this section, we focus mainly on the use of SWNT as electrode in OSC. SWNT has been used mostly as the anode. For example, Gerner and colleagues reported the use of SWNT as a transparent anode and demonstrated efficient, flexible OSC with a structure of polyethylene terephthalate (PET)/SWNT/poly(3,4-ethylenedioxythiophene) (PEDOT)/

Table 3 Photochemical degradation of SWNT-OSC from literature

	Structure	PCE (%)	Note
A	SWNT/PEDOT/P3HT:PCBM/Al	2.5	Filtraion-ferred CNT anode on PET
B	PET/SWNT/ZnO NW/P3HT/Ag	0.6	Filtraion-ferred SWNT cathode on PET
C	SWNT/PEDOT/P3HT:PCBM/LiF/Al	2.3	Spin-coated SWNT anode
D	PEDOT-SWNT /P3HT:PCBM/Al	1.3	SWNT and PEDOT hybrid anode
E	SWNT/PEDOT/P3HT:PCBM/LiF/Al	2.0	Bimetallic SWNT anode
F	CNT/PEDOT/F8T2/C ₆₀ /Al	2.27	CNT ^W generated in erfacially in
G	MoO ₃ /SWNT/MoO ₃ /PEDOT/PTB7:PC ₇₁ BM/LiF/Al	6.04	Aerolytically generated SWNT film
H	ITO/ZnO/PTB7/PTB7:PC ₇₁ BM/MoO ₃ /SWNT	4.1	p-doped SWNT film as electrode

Fig. 8 Current density–voltage characteristics of the device from the report G

Fig. 9 Literature PCE values of SWNT-based OSCs compared to the work presented in reference [110]

From the results discussed above, we can see that SWNTs have been recommended as potential for use in OSCs. They can replace not only ITO as a hole electrode. Nevertheless, further study is needed, as the results do not completely

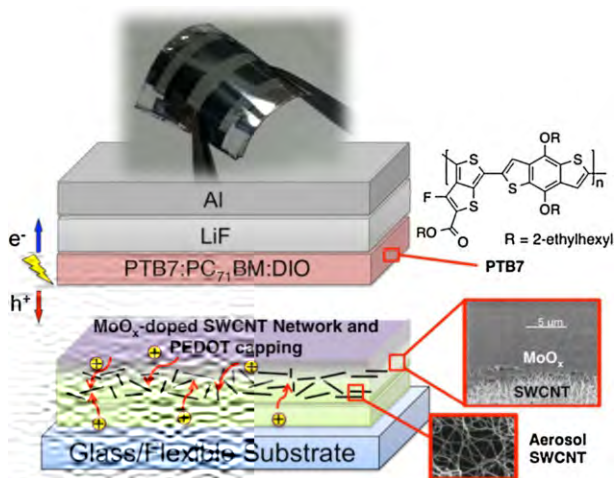


Fig. 10 Schematic of the device from the report [G]

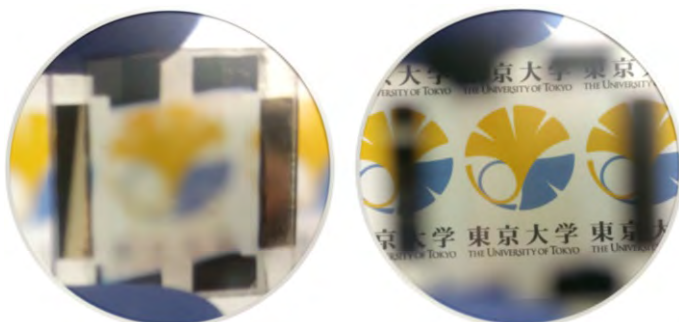


Fig. 11 Transparent OSC for window application

equal the performance of ITO. We will discuss how to go about addressing this issue and the conclusion of this chapter.

2.3 Single-Walled Carbon Nanotubes as a Transparent Electrode in Perovskite Solar Cells

2.3.1 DSSCs

To do this, PSC, the most promising type of energy-efficient solar cell (DSSC). Due to their simple fabrication and high efficiency, DSSC have attracted considerable interest from researchers around the world. Titanium dioxide nanoparticles have been widely used as the working electrode in DSSC because they provide higher efficiency and more robustness than any other metal oxide semiconductor in the field [115].

To search for an efficient counter-electrode in DSSC, Yanagida and co-workers examined different kinds of carbon materials [116]. A PCE of 4.5% was obtained when SWNT were used (Table 4: report A). This value was comparable to that of platinum-based borine-doped tin oxide-based DSSC. There had been several attempts at fabricating DSSC using a carbon material as the counter-electrode, but this work was the first to produce a fair PCE [117]. Later, Kim and colleagues investigated the effect of acid treatment of SWNT in a TiO_2 film with the dye anchored. Compared with an unmodified cell, DSSC using acid-treated SWNT as the TiO_2 /electrode interface had significantly improved photo-current density characteristics [118]. The modified cell showed a 25% increase in J_{SC} , which resulted from improved contact between the acid-treated SWNT and the TiO_2 particle and enhanced light scattering by TiO_2 cluster. For dye-linked, acid-treated SWNT anchored on the TiO_2 /electrode interface, V_{OC} increased by around 0.1 V, mainly due to the basicity of the TiO_2 surface from the NH group of ethylenediamine moiety in the anchored dye linked on the SWNT. Kama and co-workers reported the use of SWNT not only as an electrode but also as a charge transport layer [119]. SWNT exhibited a conducting channel in TiO_2 -based DSSC boosted PCE by a factor of 2 (Table 4: report B). Titanium dioxide nanoparticles were coated on an SWNT film to improve photo-induced charge separation and transport of carrier on the collecting electrode surface. An approximate 100-mV shift in the Fermi level of the SWNT/ TiO_2 system compared with the pristine TiO_2 indicated equilibration of the Fermi level between the two systems. The interplay between the TiO_2 and SWNT for achieving charge equilibration was an important factor in improving solar cell performance. Yoo and colleagues used the sol-gel method to prepare TiO_2 -coated MWNT for use as a DSSC electrode (Table 4: report C) [120]. CNT-coated with TiO_2 achieved better solar cell performance through a reduction in R_s . Compared with the conventional device, the TiO_2 -CNT (0.1 wt %) cell showed a 50% increase in PCE from 3.32 to 4.97%, which is attributed to the increase in J_{SC} due to improved interconnection between the TiO_2 particle and the TiO_2 -CNT in the porous TiO_2 film.

Table 4 Photochemical data of representative SWNT-DSSC and SWNT-PSC from literature

	Structure or research impact	PCE (%)
A	Membrane layer/SWNT/electrode/reduction layer/ TiO_2 /dye/FTO	4.5
B	TiO_2 particles were coated on SWNT to improve charge separation and transport	0.6
C	DSSC using the sol-gel method to obtain TiO_2 -coated MWNT	4.97
D	SWNT/PEDOT/ $\text{CH}_3\text{NH}_3\text{PbI}_3$ /PCBM/Al	6.32
E	FTO/ TiO_2 /mesoporous TiO_2 / $\text{CH}_3\text{NH}_3\text{PbI}_3$ /SWNT/ piro-MeOTAD	9.90
F	FTO/ TiO_2 /mesoporous TiO_2 /(FAPbI ₃) ₃ (MAPbBr ₃)/SWNT/ piro-MeOTAD	15.5
G	FTO/ TiO_2 /Al ₂ O ₃ / $\text{CH}_3\text{NH}_3\text{PbI}_3$ /P3HT/SWNT/PMMA/Ag	15.3
H	SWNT/MoO ₃ /PEDOT/ $\text{CH}_3\text{NH}_3\text{PbI}_3$ /C ₆₀ /BCP/Al	12.8
J	SWNT/P3HT/ $\text{CH}_3\text{NH}_3\text{PbI}_3$ /PCBM/SWNT	7.32

2.3.2 PSCs

The emergence of organic/inorganic halide PSC, which has a PCE of approximately 20%, has caused a paradigm shift from DSSC to PSC (Fig. 12) [121, 122], and within the 5-year period, PSC has been at the forefront of photovoltaic research. This enabled some of the researchers from the OSC field to join the PSC research. Initially, there was a confusion in coinage of the PSC. Generally, perovskite is normal and which is in error. A broad range of fabrication approaches and device concepts are being constantly developed and highly diverging progress has performance is still far from being fully optimized [123].

The application of an SWNT as an ITO replacement in PSC was demonstrated by our laboratory in 2015 [124]. Specifically, we examined the effect of SWNT subjected to acid treatment, wettability control, and MoO₃ doping. Different methods were employed to overcome the hydrophobicity of SWNT and doping in solar cell device, including modification of the wettability of PEDOT, MoO₃ thermal doping, and HNO₃ (aq) doping with various dilution from 15 to 70% (v/v) to minimize the inactivity and toxicity of the SWNT. We discovered that isopropanol-modified PEDOT worked better than surface-modified PEDOT as an electron-blocking layer on SWNT in PSC because of its superior wettability, whereas MoO₃ was incompatible due to energy level mismatch. A diluted HNO₃ (35% v/v)-doped SWNT-based device produced the highest PCE of 6.32% among the SWNT-based PSC, exceeding 70% of the PCE of an ITO-based device (9.05%). Furthermore, a flexible cell was prepared using a PET film and a PCE of 5.38% was realized (Table 4: report D; Fig. 13). By integrating the SWNT film could be deposited from above to replace the metal electrode. Mahalingam and co-workers reported a transparent PSC made by laminating aerogel on the PEDOT

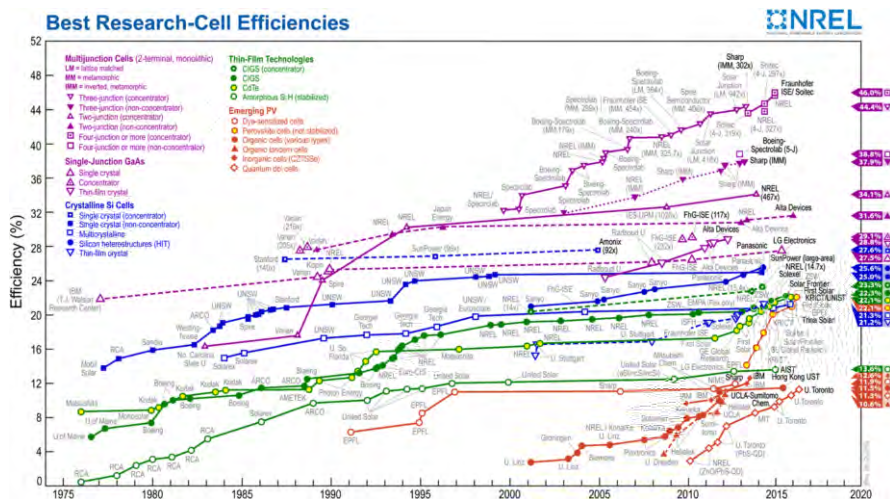


Fig. 12 Certified solar cell PCE chart of all types of solar cell. We can see the PCE of PSC in orange (<http://www.nrel.gov/pv>)

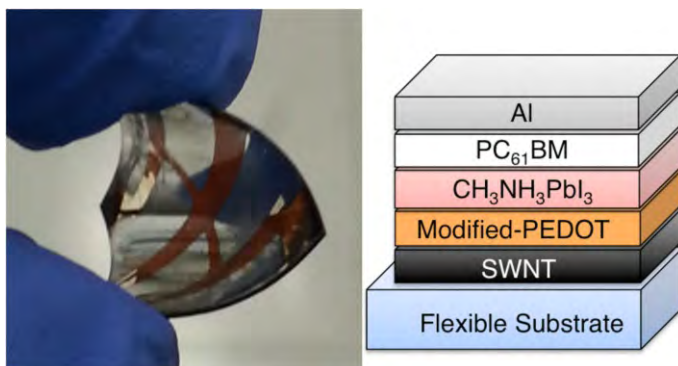


Fig. 13 Flexible SWNT-PSC device (right) and image (left)

Implementation of a $\text{CH}_3\text{NH}_3\text{PbI}_3$ layer, with the SWNT functioning as both a hole collector and electrode [125]. This enabled metal deposition, an energy-consuming additional process, to be bypassed. In the absence of an organic hole-transporting material and metal contact, $\text{CH}_3\text{NH}_3\text{PbI}_3$ and CNT formed a solar cell with an efficiency up to 6.87% (Table 4: report E). The $\text{CH}_3\text{NH}_3\text{PbI}_3/\text{CNT}$ solar cell was semi-transparent and produced photoelectric output under halide illumination because of the transparency of the CNT electrode. Interfacial charge transfer in solar cell was investigated through photoluminescence and impedance measurements. The flexible and transparent CNT network demonstrated great potential for realizing flexible and semi-transparent PSC. With the addition of 2,2,7,7-tetrakis(*N,N*-di-*p*-methoxyphenylamine)-9,9'-piroborene (piro-MeOTAD) on the CNT network, PCE improved from 6.87 to 9.90% as a result of enhanced hole extraction and reduced charge recombination. A similar approach was demonstrated by Wong and colleagues [126]. Ti foil-TiO₂ nanosheets with an organic-inorganic halide perovskite absorber and transparent CNT were adopted in PSC fabrication. Ti foil-TiO₂ nanosheets were formed by one-step anodization. The composition served as a deposition catalyst and electron conductor for the perovskite absorber. Later, a transparent conductive CNT film was laminated on top of perovskite and served as a hole transport layer as well as a transparent electrode for light illumination. A PCE of 8.31% was achieved, which is the highest among TiO₂ nanosheet-based flexible solar cells. The kind of PSC, in which CNT were used to replace the top metal electrode, reached their current peak in a study by Bochlou and co-workers [127]. They demonstrated highly efficient PSC with a hybrid hole-transporting counter-electrode based on aerogel in the presence of SWNT film and drop-cast piro-MeOTAD. An average PCE of 13.6% with a maximum of 15.5% was recorded, while the reference solar cell with piro-MeOTAD and a gold electrode showed an average of 17.7% (Table 4: report F). The results revealed the feasibility of high-efficiency PSC with carbon-based hole-transporting material. The SWNT functioned not only as a charge conductor or transport layer, but also as an encapsulating layer to protect the device from water intrusion. The ability of PSC using SWNT was addressed by Snail and colleagues (Table 4: report G) [128]. They demonstrated a method for

- of CNT are not comparable to those of ITO, which has the resistance of around $5 \times 10^{-4} \Omega$ and a transparency of more than 90%. Therefore, it is imperative to have more stable and ecofriendly devices.
- Fermi level:** To achieve high performance, especially at the cathode in OSC, CNT electrode must have a proper Fermi level to minimize energy barrier for charge transfer. Normally, carbon material has a Fermi level of 4.5–5 eV, similar to that of an ITO. In a work function of 4.6–4.8 eV. The Fermi level can be tuned for various electrodes [121–133]. Material like PEDOT are commonly used to increase the Fermi level for charge injection at the anode, whereas material like C_2CO_3 are used to reduce the Fermi level for electron collection at the cathode.
 - Wettability:** CNT are hydrophobic, so their device need to be made of hydrophilic or the material being deposited on top need to be hydrophobic. Even better would be deposition of the material by a method that is independent of the wettability, such as thermal evaporation. Many chemical reactions to increase hydrophilicity decrease conductivity by introducing oxygen-containing groups or defects. Thus, other methods are needed that do not undermine the properties of CNT while improving the wettability.
 - Surface roughness:** A rough surface of CNT creates a pathway within the device, which results in reduced performance. The reproducibility of SWNT-based OSC mainly hinge on their surface roughness. Therefore, much more attention should be paid to keeping the surface smooth and clean during the fabrication and processing of SWCNT.
 - Encapsulation:** Device stability under ambient condition is a crucial issue for practical application, especially for OSC and PSC. The photoactive material of the type of cell are rather unstable in air, and the barrier properties of plastic encapsulation are not good enough. Therefore, it is necessary to develop a reliable barrier that can passivate the device effectively. CNT have shown some promise in this regard, yet no much research has been conducted. Further work will help open a path to more industrially viable CNT-based solar cell.

References

- Abri P, Freitag M, Perebeino V (2008) Carbon nanotube photonic and optoelectronic. *Nat Photon* 2(6):341–350
- O'Connell MJ, Bachilo SM, Hsiao CB, Moore VC, Siano MS, Haro EH, Rialon KL, Bock PJ, Noon WH, Kirell C, Ma J, Hauge RH, Wei man RB, Smalley RE (2002) Band gap dependence from individual single-walled carbon nanotubes. *Science* 297(5581):593–596
- Lebedkin S, Hennrich F, Kido K, Kappe MM (2008) Photophysical properties of carbon nanotubes in organic polymer matrices: emission and excitation lifetime and relaxation pathways. *Phys Rev B* 77(16):165429
- Kakara H, Kamawa Y, Manawa Y, Umeda I, Sakaki S, Ohnaka Y, Achiba Y (1999) Optical properties of single-walled carbon nanotubes. *Synth Met* 103(1–3):2555–2558
- Beroun S, de Beghnie R, Bailly S, Billero S, Joulema B (2007) Elaboration of P3HT/CNT/PCBM composite for organic photovoltaic cell. *Adv Mater* 17(16):3363–3370

6. Chaudhary S, Bhunia H, Miller AM, Bardeen CJ, Oskan M (2007) Hierarchical placement and application of optoelectronic impact of carbon nanotube in polymer fullerene solar cell. *Nano Lett* 7(7):1973–1979
7. Ma BH, Yip H, Hwang F, Jen AK-Y, Ma H, Yip H, Hwang F, Jen AK-Y (2010) Interface engineering for organic electroluminescent. *Adv Mater* 20(9):1371–1388
8. Seim R, Kogler FR, Brabec CJ (2010) Interface material for organic solar cell. *J Mater Chem* 20(13):2499–2512
9. Li G, Shrotriya V, Hwang J, Yao Y, Moriarty T, Emery K, Yang Y (2005) High-efficiency photovoltaic power photovoltaic cell by self-organization of polymer blend. *Nature* 439(7105):864–868
10. Park SH, Roy A, Beaupre S, Cho S, Coates N, Moon JS, Mooney D, Leclerc M, Lee K, Heeger AJ (2009) Bulk heterojunction solar cells with internal quantum efficiency approaching 100%. *Nature Photon* 3(5):297–302
11. Huynh WU (2002) Hybrid nanorod-polymer solar cell. *Science* 295(5564):2425–2427
12. Lee JU (2005) Photovoltaic efficiency in ideal carbon nanotube diode. *Appl Phys Lett* 87(7):073101
13. Achari P, Freier AG, Perebeinos V (2008) Carbon-nanotube photonic and optoelectronic. *Nature Photon* 2(6):341–350
14. Hühner MS (2000) Crystalline nanotube photovoltaic. *Science* 288(5465):494–497
15. Yang F, Wang X, Zhang D, Yang J, Bao D, Wu Z, Wei J, Wang JQ, Wu Z, Peng F, Li X, Li R, Li Y, Li M, Bai X, Ding F, Li Y (2014) Chirality-specific growth of single-walled carbon nanotube on solid catalyst. *Nature* 510(7506):522–524
16. Yan Y, Karahan HE, Yildirim C, Wei L, Birer , Zhai S, Liao R, Chen Y (2016) Smart positioning of Co/SiO₂ catalyst by ligand for chirality-selective synthesis of (9,8) single-walled carbon nanotube. *Nanotechnology* 27:17705–17713
17. Arnold MS, Stupp SI, Heram MC (2005) Enrichment of single-walled carbon nanotube by diameter in density gradient. *Nature* 434(7044):713–718
18. Arnold MS, Green AA, Hsiao JF, Stupp SI, Heram MC (2006) Sorting carbon nanotube by electronic structure using density differential ion. *Nature Nanotechnol* 1(1):60–65
19. Bhunia H, Nishide D, Tanaka T, Kakei H (2011) Large-scale single-chirality separation of single-walled carbon nanotube by simple gel chromatography. *Nature Commun* 2:309
20. Fagan JA, Khripin CY, Silvestri BA, Simpson JR, Hsiao EH, High Walker AR, Zheng M (2014) Isolation of specific small-diameter single-walled carbon nanotube species via aqueous two-phase extraction. *Adv Mater* 26(18):2800–2804
21. Yumaki E, Andreucci J, Amaraunga GAJ (2003) High open-circuit voltage photovoltaic device from carbon nanotube polymer composite. *J Appl Phys* 93(3):1764
22. Landi BJ, Rasmussen RP, Carro SL, Bailey SG (2005) Single-walled carbon nanotube-polymer solar cell. *Prog Photovoltaic Res Appl* 13(2):165–172
23. Kakei S, Minami N, Nalini B, Kim Y, Hara K (2005) Near-infrared photovoltaic device and photovoltaic device using single-walled carbon nanotube in conductive polymer film. *J Appl Phys* 98(8):084314
24. Ago H, Perich K, Shafer MSP, Windle AH, Friend RH (1999) Composite of carbon nanotube and conjugated polymer for photovoltaic device. *Adv Mater* 11(15):1281–1285
25. Yumaki E, Amaraunga GAJ (2002) Single-walled carbon nanotube/conjugated polymer photovoltaic device. *Appl Phys Lett* 80(1):112
26. Pradhan B, Balyal SK, Pal AJ (2006) Functionally modified carbon nanotube in donor/acceptor-type photovoltaic device. *Appl Phys Lett* 88(9):093106
27. Li C, Chen Y, Wang Y, Iqbal Z, Chhawal MA, Mirza S (2007) A fullerene single-walled carbon nanotube composite for polymer bulk heterojunction photovoltaic cell. *J Mater Chem* 17(23):2406–2411
28. Chiriac D, Parikh J, Himmelen JC, Yakono V (2004) Influence of nanomorphology on the photovoltaic action of polymer fullerene composite. *Nanotechnology* 15(9):1317–1323
29. Ren S, Bernardi M, Binn RR, Belloic V, Grozman JC, Gradecek S (2011) Toward efficient carbon nanotube/P3HT solar cell: active layer morphology, electrical, and optical properties. *Nano Lett* 11(12):5316–5321
30. Bindl DJ, Safran NS, Arnold MS (2010) Diffusion and diffusion photogeneration in emitters using carbon nanotube as polymer photovoltaic heterojunction in interface. *ACS Nano* 4(10):5657–5664
31. Arnold MS, Zimmerman JD, Renhauser CK, Wu X, Binn RR, Binn CM, Forrester SR (2009) Broad spectral response using carbon nanotube/organic emitters or 60 photodiode. *Nano Lett* 9(9):3354–3358

32. Bindl DJ, Weber MY, Prehn FC, Arnold MS (2011) Efficiency enhancement from electronic transport in rolled emiconducting carbon nanotubes. *Nano Lett* 11(2):455–460
33. Bindl DJ, Brewer AS, Arnold MS (2011) Semiconducting carbon nanotube/polymer blended heterojunction for photochemical near-infrared photovoltaic energy. *Nano Res* 4(11):1174–1179
34. Jain RM, Hordden R, Traylor K, Shimoda S, Hilmer AJ, McNichols TP, Gleason KK, Stransky MS (2012) Polymer-free near-infrared photochemical with single chirality (6,5) emiconducting carbon nanotube arrays. *Adv Mater* 24(32):4436–4439
35. Raj R, Maroo SC, Wang EN (2013) Wettability of graphene. *Nano Lett* 13(4):1509–1515
36. Rabe J, Mi X, Gopalapalli H, Thomas AV, Yari F, Shi Y, Ajayan PM, Koros NA (2012) Wettability of graphene. *Nature Mater* 11(3):217–222
37. Wang SR, Zhang Y, Abidin N, Cabral L (2009) Wettability and surface free energy of graphene. *Langmuir* 25(18):11078–11081
38. Kim BH, Kim JY, Jeong SJ, Hwang JO, Lee DH, Shin DO, Choi SY, Kim SO (2010) Surface energy modification by pinning, large-area graphene film for block copolymer lithography. *ACS Nano* 4(9):5464–5470
39. Shin YJ, Wang Y, Hwang H, Kalon G, Wee ATS, Shen Z, Bhatia CS, Yang H (2010) Surface-energy engineering of graphene. *Langmuir* 26(6):3798–3802
40. Ding VC, Hwang J-HJ, Kim J, Smith AJ, Choe C-W, Hwang J-HJ (2012) Toward oxygen production in all-carbon solar cell: a perspective. *Energy Environ Sci* 5(7):7810
41. Ding VC, Hwang JH, Teo I, Kim F, Kim J, Choe CW, Sapp SI, Hwang J (2011) Surface-free water production from photochemical in all-carbon composite. *J Am Chem Soc* 133(13):4940–4947
42. Bernardi M, Lohrman J, Kumar PV, Kirkeminde A, Ferrali N, Groisman JC, Ren S (2012) Nanocarbon-based photochemical. *ACS Nano* 6(10):8896–8903
43. Ranby MP, Voisard M, Wei P, Wang C, Gao Y, Wu Y, Chen Y, Bao Z (2012) Enhancement of oxygen production in carbon-based electrode for all-carbon solar cell. *ACS Nano* 6(11):10384–10395
44. Wang H, Koleila GI, Lopez P, Jimenez-O G, Lai Y-C, Voisard M, Fang Y, Park S, Hock KN, Bao Z (2014) High yield of small-diameter carbon nanotubes for solar cell and radiation. *ACS Nano* 8(3):2609–2617
45. Gong M, Sha Y, Xie Y, Bernardi M, Jang D, Beck KA, Mark TJ, Groisman JC, Ren S, Heram MC (2014) Polychiral emiconducting carbon nanotube-polymer solar cell. *Nano Lett* 14(9):5308–5314
46. Lee JM, Park JS, Lee SH, Kim H, Yoo S, Kim SO (2011) Selective electron- or hole-transport enhancement in bulk-heterojunction organic solar cell with N- or B-doped carbon nanotubes. *Adv Mater* 23(5):629–633
47. Robel I, Bunker BA, Kumar PV (2005) Single-walled carbon nanotube-CdS nanocomposite as a light-harvesting assembly: photoinduced charge-transfer interaction. *Adv Mater* 17(20):2458–2463
48. Barak O, S, Ho chandani S, Vinodgopal K, Kumar PV (2004) Single-wall carbon nanotube film for photochemical generation. A prompt response to visible-light irradiation. *J Phys Chem B* 108(44):17015–17018
49. Landi BJ, Castro SL, Park HJ, Ekan CM, Bailey SG, Rabele RP (2005) CdSe quantum dot-single wall carbon nanotube composite for photovoltaic solar cell. *Sol Energy Mater Sol Cell* 87(1–4):733–746
50. Lee JM, Kwon B-HH, Park H, Kim H, Kim MG, Park JS, Kim ES, Yoo S, Jeon DY, Kim SO (2013) Electron dissociation and charge-transport enhancement in organic solar cell with functionalized N-doped CNT hybrid nanomaterial. *Adv Mater* 25(14):2011–2017
51. Li L, Li T, Chen W, Lee JM, Bao Z, Ding IH, Park H, Kim SO, Li L (2013) The role of N-doped nanotubes in all carbon nanotube in achieving highly efficient polymer bulk heterojunction solar cell. *Nano Lett* 13(6):2365–2369
52. Jeon I, Kim S, Wang D, Hahim Y, Yana T, Nagahama T, Shimada T, Ma Y (2015) Modified MoS₂ nanoscale band of carbon nanotube as electron acceptor in bulk heterojunction in organic solar cell. *Org Electron* 17:275–280
53. Thompson BC, Fréchet JMJ (2008) Polymer fullerene composite solar cell. *Angew Chemie Int Ed* 47(1):58–77
54. Nelson J (2011) Polymer: fullerene bulk heterojunction solar cell. *Mater Today* 14(10):462–470
55. Dennler G, Scharber MC, Brabec CJ (2009) Polymer fullerene bulk-heterojunction solar cell. *Adv Mater* 21(13):1323–1338

56. Zilberberg K, Gao F, Pagani R, Potwarka A, Behrend A, Trost S, Heiderhorst R, O'Brien P, Riedel T (2014) Highly robust, indium-free transparent conductive electrode based on composite of silver nanowire and conductive metal oxide. *Adv Mater* 24(12):1671–1678
57. Inagaki O (2011) Organic photoelectrode: a promising technology. *Nat Photon* 5(4):201–202
58. Yang M, Kim D, Jha H, Lee K, Park J, Schnitzler P (2011) Nb doping of TiO₂ nanowires for an enhanced efficiency of dye-sensitized solar cell. *Chem Commun* 47(7):2032–2034
59. Delacour C, Jeon I, Seo S, Nakagawa T, Kippelen B, Mauryama S, Maury Y (2017) Indium in oxide-free small molecule organic solar cell using single-walled carbon nanowire electrode. *ECS J. Solid State Sci. Technol.* 6(6):M3181–M3184
60. Sakaguchi T, Jeon I, Chiba T, Shalaby A, Xiang R, Chiahi S, Kippelen B, Park N-G, Maury Y, Mauryama S (2017) Single-walled carbon nanowire-based metal-free perovskite solar cell with improved stability and efficiency. *J Mater Chem A* (Submitted)
61. Wu Z, Chen Z, Du X, Logan JM, Sippel J, Nikolov M, Kamara K, Rynold JR, Tanner DB, Hebard AF, Rinkler AG (2004) Transparent, conductive carbon nanowire film. *Science* 305(5688):1273–1276
62. Lee YH, Kim SG, Tomazek D (1997) Catalytic growth of single-wall carbon nanowire: an ab initio study. *Phys Rev Lett* 78(12):2393–2396
63. Naitablin AG, Kalkela A, Mäkelä K, Animo AS, Räsänen V, Kivimäki S, Rakkola S, Timmerman MY, Rissanen M, Aichon B, Kippelen B, Brown DP, Okkonen OG, Kippelen B (2011) Multifunctional free-standing single-walled carbon nanowire film. *ACS Nano* 5(4):3214–3221
64. van de Lagemaat J, Barne TM, Rumble G, Shaheen SE, Cobble TJ, Week C, Leible I, Pelola J, Glavitski P (2006) Organic solar cell with carbon nanowire replacing In₂O₃: Sn as the transparent electrode. *Appl Phys Lett* 88(23):233503
65. Ahn N, Jeon I, Yoon J, Kippelen B, Mauryama S, Choi M (2018) Carbon- andwiched perovskite solar cell. *J Mater Chem A*. <https://doi.org/10.1039/C7TA09174E>
66. Schneider J, Rohner P, Tureja D, Schmid M, Galliker P, Polikakos D (2016) Electrolyte-dynamic nanodrip printing of high aspect ratio metal grid transparent electrode. *Adv Mater* 26:833–840
67. Langley D, Goh G, Myer C, Celle C, Belle D, Simona JP (2013) Flexible transparent conductive material based on silver nanowire network: a review. *Nanotechnology* 24(45):452001
68. Cao W, Li J, Chen H, Xie J (2014) Transparent electrode for organic photovoltaic device: a review. *J Photochem Energy* 4:040990
69. Bae S, Kim H, Lee Y, Xu X, Park JS, Zheng Y, Balakrishnan J, Lei T, Kim HR, Song YI, Kim YJ, Kim KS, Ohlman B, Ahn JH, Hong BH, Iijima S (2010) Roll-to-roll production of 30-inch graphene film for transparent electrode. *Nat Nanotechnol* 5:574–578
70. Han PX, Yu B, Song Y, Shi C, Zhang LL, Li C, Li SS, Du JH, Cheng HM (2014) Double-walled carbon nanowire transparent conductive film with excellent performance. *J Mater Chem A* 2:1159–1164
71. Hech DS, Heinke AM, Lee R, He L, Moore B, Ockler C, Rieker S (2011) High conductivity transparent carbon nanowire film deposited from superacid. *Nanotechnology* 22:075201
72. Bane DD, Flaifel BS, Kippelen R, Shaper JG (2012) Carbon nanowire-silicon solar cell. *Adv Energy Mater* 2(9):1043–1055
73. Ding Y, Li X, Rajan NK, Taylor AD, Reed MA (2013) Record high efficiency single-walled carbon nanowire/silicon photovoltaic solar cell. *Nano Lett* 13(1):95–99
74. Wei J, Jia Y, Shi Q, Chen Z, Wang K, Zhang D, Zhang G, Wang Z, Bao J, Cao A, Wu D (2007) Double-walled carbon nanowire solar cell. *Nano Lett* 7(8):2317–2321
75. Wenham SR, Green MA (1996) Silicon solar cell. *Prog Photovoltaics* 4(1):3–33
76. Song Y, Li X, Mackin C, Zhang X, Fang W, Palacio T, Zhi H, Kong J (2015) Role of interfacial oxide in high-efficiency graphene-silicon heterojunction solar cell. *Nano Lett* 15(3):2104–2110
77. Shi E, Zhang L, Li Z, Li P, Shang Y, Jia Y, Wei J, Wang K, Zhi H, Wu D, Zhang S, Cao A (2012) TiO₂-coated carbon nanowire-silicon solar cell with efficiency of 15%. *Sci Rep* 2:884
78. Anderson WA (1974) An 8% efficiency heterojunction solar cell. *J Appl Phys* 45(9):3913
79. Ding RT (2001) Recent advances in heterojunction barrier concept. *Mater Sci Eng R Rep* 35(1–3):1–138
80. Jia Y, Wei J, Wang K, Cao A, Shi Q, Chen X, Zhi H, Zhang D, Zhang G, Ma B, Wang L, Li W, Wang Z, Bao J, Wu D (2008) Nanowire heterojunction solar cell. *Adv Mater* 20(23):4594

81. Li Z, Kune VP, Saini V, Xu Y, Der i hi E, Salamo GJ, Biri AR, Biri AS (2008) SOCl_2 enhanced photochemical conversion of single-walled carbon nanotube/n-silicon heterojunction. *Appl Phys Lett* 93(24):243117
82. Li Z, Kune VP, Saini V, Xu Y, Der i hi E, Salamo GJ, Biri AR, Biri AS (2009) High-efficiency high density *p-n* junction single-walled carbon nanotube/*n*-silicon heterojunction. *ACS Nano* 3(6):1407–1414
83. Li Z, Jia Y, Wei J, Wang K, Shi Q, Gu X, Zhang H, Cao A, Wu D (2010) Large area, highly transparent carbon nanotube p-n junction for energy harvesting. *J Mater Chem* 20(34):7236
84. Blackburn JL, Barne TM, Beard MC, Kim Y-H, Tenen RC, McDonald TJ, To B, Cobble TJ, Heben MJ (2008) Transparent conductive single-walled carbon nanotube network with precise tunable ratio of emiconducting and metallic nanotubes. *ACS Nano* 2(6):1266–1274
85. Ong P-L, Butler WB, Leij IA (2010) Hybrid solar cell based on single-walled carbon nanotube/Si heterojunction. *Nanotechnology* 21(10):105203
86. Wadhwa P, Liu B, McCarthy MA, Wu Z, Rinkler AG (2010) Electronic junction control in a nanotube-emiconductor Schottky junction solar cell. *Nano Lett* 10(12):5001–5005
87. Jia Y, Cao A, Bai X, Li Z, Zhang L, Guo N, Wei J, Wang K, Zhang H, Wu D, Ajayan PM (2011) Achieving high efficiency silicon-carbon nanotube heterojunction solar cell by acid doping. *Nano Lett* 11(5):1901–1905
88. Jia Y, Li P, Gu X, Wei J, Wang K, Zhang H, Wu D, Zhang L, Cao A, Xu Y (2011) Encapsulated carbon nanotube-oxide-silicon solar cell with stable 10% efficiency. *Appl Phys Lett* 98(13):133115
89. Wadhwa P, Seol G, Peterson MK, Guo J, Rinkler AG (2011) Electronic-induced recombination in Schottky junction solar cell. *Nano Lett* 11(6):2419–2423
90. Chen W, Seol G, Rinkler AG, Guo J (2012) Carrier dynamic and degradation mechanism of electronic-induced recombination in carbon nanotube-silicon Schottky junction solar cell. *Appl Phys Lett* 100(10):103503
91. Kozawa D, Hiraoka K, Miyachi Y, Mori S, Maeda K (2012) Analysis of the photochemical properties of single-walled carbon nanotube/silicon heterojunction solar cell. *Appl Phys Express* 5(4):042304
92. Li X, Ling Y, Sakimoto K, Goh TH, Reed MA, Taylor AD (2013) Improved efficiency of monoheteroaligned single-walled carbon nanotube/silicon hybrid solar cell. *Energy Environ Sci* 6(3):879–887
93. Gu K, Chiba T, Omori S, Tsuraki Tere T, Zhao P, Fujii S, Katsura H, Einarsen E, Chiahi S, Mamiya S (2013) Self-Assembled microheterostructure of single-walled carbon nanotube for solar cell. *J Phys Chem Lett* 4(15):2571–2576
94. Xu W, Deng B, Shi E, Wu S, Zhang M, Yang L, Wei J, Peng H, Cao A (2015) Comparison of nanocarbon-silicon solar cell with nanotube Si or graphene Si contact. *ACS Appl Mater Interfaces* 7(31):17088–17094
95. Gu K, Animo AS, Chiba T, Fujii S, Katsura H, Naiklin AG, Chiahi S, Koppinen EI, Mamiya S (2014) Air-stable high-efficiency solar cell with dimerized single-walled carbon nanotube film. *J Mater Chem A* 2(29):11311–11318
96. Li Z, Saini V, Der i hi E, Kune VP, Zhang J, Xu Y, Biri AR, Salamo GJ, Biri AS (2010) Polymer functionalized *n-n* junction single-walled carbon nanotube photochemical device. *Appl Phys Lett* 96(3):033110
97. Wang F, Kozawa D, Miyachi Y, Hiraoka K, Mori S, Ohno Y, Maeda K (2015) Considerably improved photochemical performance of carbon nanotube-based solar cell using metal-oxide layer. *Nat Commun* 6:6305
98. Dong L, Yoo J, Yang J, Chen C, He Y, Mure S, Moriarty T, Emery K, Li G, Yang Y (2012) Tandem polymer solar cell featuring a peculiarly matched low-bandgap polymer. *Nat Photon* 6(3):180–185
99. Angmo D, Krebs FC (2013) Flexible ITO-free polymer solar cell. *J Appl Phys* 112(1):1–14
100. Jarzala D, Sangwan VK, Leshon LJ, Mark TJ, Heram MC (2013) Carbon nanomaterials for electronic, optoelectronic, photochemical, and sensing. *Chem Soc Rev* 42(7):2824–2860
101. Liu Y, Wan X, Wang F, Zhu J, Long G, Tian J, Yoo J, Yang Y, Chen Y (2011) Spin-coated multilayer for high performance solar cell. *Adv Energy Mater* 1(5):771–775
102. Li S-S, Chen C-W (2013) Polymer metal-oxide hybrid solar cell. *J Mater Chem A* 1(36):10574
103. Roedel MW, Topinka MA, McGehee MD, Prall H-J, Dennler G, Saricici NS, Halls L, Gruner G (2006) Organic solar cell with carbon nanotube network electrode. *Appl Phys Lett* 88(23):233506

104. De Gomes Arco L, Zhang Y, Schlenker CW, Bui K, Thompson ME, Zhou C (2010) Conductive, highly flexible, and transparent graphene-like chemical vapor deposition for organic photovoltaic. *ACS Nano* 4(5):2865–2873
105. Unalan HE, Hiralal P, Kuo D, Parekh B, Amaraunga G, Chhowalla M (2008) Flexible organic photovoltaic from zinc oxide nanowire grown on transparent and conducting single-walled carbon nanotube thin film. *J Mater Chem* 18(48):5909
106. Ymaki E, Klapich G, Kaddama E, Sraiki E, Kornilio N, Vidaki N, Franghiadaki Y (2006) Carbon nanotube/PEDOT:PSS electrode for organic photovoltaic. *Br Polym J Appl Polym* 36(3):257–259
107. Kim S, Yim J, Wang X, Bradley DDC, Lee S, DeMello JC (2010) Spin- and photodeposited single-walled carbon-nanotube electrode for organic solar cell. *Adv Mater* 20(14):2310–2316
108. Yler TP, Brock RE, Karmel HJ, Mark TJ, Heram MC (2011) Electrically monodisperse single-walled carbon nanotube thin film as transparent conducting anode in organic photovoltaic device. *Adv Energy Mater* 1(5):785–791
109. Salaserra RV, Calace CE, Roman LS, Zarbin AJG (2013) ITO-free and flexible organic photovoltaic device based on high transparent and conducting poly(aniline)/carbon nanotube thin film. *Adv Mater* 23(12):1490–1499
110. Jeon I, Bui K, Chiba T, Anzimo A, Naitillin AG, Kappinen EI, Manoma S, Ma Bo Y (2015) Direct and photodeposited single-walled carbon nanotube film doped with MoO₃ as electron-blocking transparent electrode for flexible organic solar cell. *J Am Chem Soc* 137(25):7982–7985
111. Hellrom SL, Voerichian M, Solenberg RM, Irfan I, Hammock M, Wang YB, Jia C, Cao X, Gao Y, Bao Z (2012) Strong and stable doping of carbon nanotube and graphene by MoO₃ for transparent electrode. *Nano Lett* 12(7):3574–3580
112. Shin D-W, Lee JH, Kim Y-H, Yoon SM, Park S-Y, Yoo J-B (2009) A role of HNO₃ on transparent conducting film with single-walled carbon nanotube. *Nanotechnology* 20(47):475703
113. Deb SK (1966) Optical properties and color-center formation in thin film of molybdenum trioxide. *J Appl Phys* 37(13):4818
114. Jeon I, Delacour C, Kalkela A, Kappinen IE, Manoma S, Ma Bo Y (2016) Metal-electrode-free window-like organic solar cell with p-doped carbon nanotube thin-film electrode. *Sci Rep* 6:31348
115. Chappel S, Chen S-G, Zaban A (2002) TiO₂-coated nanoporous SnO₂ electrode for dye-sensitized solar cell. *Langmuir* 18(8):3336–3342
116. Sasaki K, Yamaguchi M, Kamagai M, Yanagida S (2003) Application of carbon nanotube as counter electrode of dye-sensitized solar cell. *Chem Lett* 32(1):28–29
117. Ky A, Gratzel M (1996) Low cost photovoltaic module based on dye-sensitized nanocrystalline anatase dioxide and carbon powder. *Sol Energy Mater Sol Cells* 44(1):99–117
118. Jang S-R, Villar R, Kim K-J (2004) Incorporation of functionalized single-wall carbon nanotube in dye-sensitized TiO₂ solar cell. *Langmuir* 20(22):9807–9810
119. Kongkanand A, Manandom R, Kama PV (2007) Single-wall carbon nanotube catalyst for photoelectrochemical solar cell: capture and transport of photogenerated electron. *Nano Lett* 7(3):676–680
120. Lee TY, Alegaonkar PS, Yoo J-B (2007) Fabrication of dye-sensitized solar cell using TiO₂ coated carbon nanotube. *Thin Solid Films* 515(12):5131–5135
121. Snaihi HJ (2013) Peroxide: the emergence of a new era for low-cost, high-efficiency solar cell. *J Polym Chem Lett* 4(21):3623–3630
122. Green MA, Ho-Baillie A, Snaihi HJ (2014) The emergence of peroxide solar cell. *Nature Photon* 8(7):506–514
123. McGehee MD (2014) Peroxide solar cell: concluding oar. *Nature Mater* 13(9):845–846
124. Jeon I, Chiba T, Delacour C, Cao Y, Kalkela A, Ryndak O, Kappinen EI, Manoma S, Ma Bo Y (2015) Single-walled carbon nanotube film as electrode in indium-free planar heterojunction peroxide solar cell: in the integration of electron-blocking layer and dopant. *Nano Lett* 15(10):6665–6671
125. Li Z, Kulkarni SA, Bopp PP, Shi E, Cao A, Bui K, Balyal SK, Zhang J, Xiong Q, Wong LH, Maheshwari N, Mahalkar SG (2014) Laminated carbon nanotube network for metal electrode-free efficient peroxide solar cell. *ACS Nano* 8(7):6797–6804
126. Wang X, Li Z, Xiong W, Kulkarni SA, Balyal SK, Zhang S, Cao A, Wong LH (2015) TiO₂ nanotube array based flexible peroxide solar cell with transparent carbon nanotube electrode. *Nano Energy* 11:728–735

127. Airola K, Seintjens K, Correa-Baena J-P, Kakkela A, Abate A, Tian Y, Johansson EMJ, Grätzel M, Kippelen EI, Hagfeldt A, Bochlou G (2016) Carbon nanotube-based hybrid hole-transporting material and electrolyte for high efficiency perovskite solar cell. *Energy Environ Sci* 9(2):461–466
128. Habiringer SN, Leijon T, Eperon GE, Snares SD, Nicholas RJ, Snaihl HJ (2014) Carbon nanotube/polymer composite as a highly efficient hole collector layer in perovskite solar cell. *Nano Lett* 14(10):5561–5568
129. Jeon I, Yoon J, Ahn N, Ahn M, Delacour C, So A M, Kippelen EI, Choi M, Mauryama S, Ma Bo Y (2017) Carbon nanotube/graphene as a efficient recombination electrode in perovskite solar cell. *J Phys Chem Lett* 8:5395–5401
130. Jeon I, Seo S, So A Y, Delacour C, Senaga K, Kippelen EI, Mauryama S, Ma Bo Y (2017) Perovskite solar cell using carbon nanotube as a buffer layer and anode electrode. *J Phys Chem C* 21(46):25743–25749
131. Choe M, Lee BH, Jo G, Park J, Park W, Lee S, Hong WK, Seong MJ, Kahng YH, Lee K, Lee T (2010) Efficient bulk-heterojunction photovoltaic cell with intercalated layered graphene electrode. *Org Electron Phys Mater Appl* 11(11):1864–1869
132. Dai J, Pei S, Ma L, Cheng H-M (2014) 25th anniversary article: carbon nanotube- and graphene-based intercalated conductive film for optoelectronic device. *Adv Mater* 26(13):1958–1991
133. Jo G, Choe M, Lee S, Park W, Kahng YH, Lee T (2012) The application of graphene as an electrode in electrical and optical device. *Nanotechnology* 23(11):112001



Advances in Production and Applications of Carbon Nanotubes

Xilai Jia¹ · Fei Wei²

Received: 31 August 2016 / Accepted: 2 January 2017 / Published online: 30 January 2017
© Springer International Publishing Switzerland 2017

Abstract Recent decades have witnessed many breakthroughs in research on carbon nanotubes (CNTs), particularly regarding controllable synthesis, production scale-up, and application advances for this material. This sp^2 -bonded nanocarbon uniquely combines extreme mechanical strength, exceptionally high electrical conductivity, as well as many other superior properties, making it highly attractive for fundamental research and industrial applications. Synthesis and mass production form the solid basis for high-volume applications of CNTs. During recent decades, CNT production capacity has reached more than thousands of tons per year, greatly decreasing the price of CNTs. Although the unique physiochemical properties of an individual CNT are stated repeatedly, manifestation of such unique properties in a macroscopic material, e.g., realization of high-strength CNT fibers, remains a great challenge. If such challenges are solved, many critical applications will be enabled. Herein we review the critical progress in the development of synthesis and scaled-up production methods for CNTs, and discuss advances in their applications. Scientific problems and technological challenges are discussed together.

Keywords Carbon nanotube · Mass production · Application advances

Chapter 11 was originally published as Jia, X. & Wei, F. Top Curr Chem (Z) (2017) 375: 18. DOI 10.1007/s41061-017-0102-2.

& Fei Wei
wf-dce@tsinghua.edu.cn

¹ School of Materials Science and Engineering, University of Science and Technology Beijing, Beijing 100083, People's Republic of China

² Beijing Key Laboratory of Green Chemical Reaction Engineering and Technology, Department of Chemical Engineering, Tsinghua University, Beijing 100084, People's Republic of China

1 Introduction

Since being reported in 1991 by Sumio Iijima [1], carbon nanotubes (CNTs) have attracted great attention from researchers and industry. CNTs can be classified into single-walled CNTs (SWNTs), double-walled CNTs (DWNTs), and multiwalled CNTs (MWNTs) based on the number of graphitic layers. They are composed of sp^2 -bonded carbon atoms assembled into a cylindrical tube with length ranging from less than 100 nm to several centimeters. The diameter of SWNTs is typically 0.4–2 nm, while the diameter of MWNTs ranges from ~ 1.4 nm to nearly 100 nm, depending on the synthesis conditions.

CNTs are well known for their unique physicochemical properties, including extremely high tensile strength, high electrical conductivity, high ductility, and relative chemical inactivity. All these properties make CNT-based products attractive. Moreover, due to their low dimensionality, CNTs are also favored for use in nanocomposite engineering. In this context, CNTs open a new avenue in materials science and nanotechnology [2]. CNTs can be found in a wide range of applications, e.g., in electronics, polymer composites, energy storage materials, catalysis, gas storage materials, and sensors.

Since its discovery, there have been thousands of publications and patents aiming to explore the synthesis and applications of this material, and encouraging progress has been made by academic researchers and industry. Mass production of CNTs has become possible, offering more than thousands of tons of CNTs per year worldwide. In fact, production capacity could reach much higher than this if high-volume applications of CNTs could be found. Along with improved mass production, the cost of CNTs has been greatly reduced. The price of MWNTs has reached below US \$100 kg^{−1} and that of SWNTs below US \$2000 kg^{−1} in recent years [3].

A wide range of applications for CNTs have been reported in literature [4–6]. Rather than a detailed survey on CNTs, herein we pay more attention to the critical progress in terms of production scale-up and high-volume applications of CNTs, as well as technological challenges. We start with controllable synthesis of CNTs and scale-up techniques, then posttreatments such as purification, dispersion, and doping are also briefly introduced, since they are important for the following applications. Then, recent advances in critical applications, including macroscopic assembly of CNTs, composite materials, energy storage, catalysis materials, and environmental applications, are reviewed and analyzed. We hope this review will offer readers valuable opinions on advances in terms of CNT production and practical applications.

2 Synthesis and Production Scale-Up

2.1 Basic Principles of CNT Synthesis

For the wide range of applications of CNTs, synthesis and mass production with controlled structures is the first and critical step. Before the well-known report of CNTs in 1991 by Iijima, Endo reported synthesis of “vapor-grown carbon fiber,”

which actually contained MWNTs with diameter of tens of nanometers [7]. During development in recent years, a number of laboratory and scaled-up synthesis methods for CNTs have been reported, e.g., arc discharge, laser ablation, chemical vapor deposition (CVD), gas-phase pyrolysis, template methods, etc. [8], among which the CVD route has become dominant for mass production of CNTs. In particular, fluidized bed reactor-based CVD can produce CNTs with capacity of thousands of tons per year worldwide.

Before scale-up of CNT synthesis, their growth mechanism was widely studied in recent years. In a typical CVD process, hydrocarbon gas (e.g., methane, CH_4) is cracked into carbon atoms and hydrogen atoms on transition-metal (e.g., iron)

[catalytic the CVD process, hydrocarbon gas (e.g., methane, CH_4) is cracked into carbon atoms and hydrogen atoms on transition-metal (e.g., iron)

the catalyst in the form of an

nanometer (nm) scale (band) 1506.3ad

the growth mechanism of CNTs can be

10r [

reach 90–95% at optimized conditions [10, 11]. However, synthesis of SWNTs with controlled structure still faces challenges. Understanding of catalyst composition and growth conditions for SWNTs therefore remains an important theme. Recently, Li and coworkers proposed use of high-melting-point alloys as catalysts for controlled growth of SWNTs [12]. Due to their high melting point, such alloy catalyst nanoparticles remain in solid state, ensuring crystalline structure during CVD growth. As a result, the selectivity of metallic SWNTs has reached more than 99%.

Regarding macroscopic SWNT structures, Maruyama's group provided a breakthrough in synthesis of SWNT arrays [13] by uniformly depositing a dense layer of metal catalyst on a quartz plate to achieve vertical growth of SWNT arrays using alcohol as carbon source. Thereafter, a trace amount of water is introduced as a weak oxidant in the CNT growth process, strongly promoting the growth rate by maintaining the activity of the catalyst [14, 15]. Some other strategies for higher-quality SWNT arrays have also been studied, including feedstock optimization [16] among others. At present, scale-up techniques for reduced cost of SWNTs are required for their large-scale application. A high-pressure CO disproportionation (HiPco) process is one successful development to meet increasing demands for SWNTs [17]. CVD processes using a supported catalyst, e.g., the CoMoCAT[®] - process, which uses a fluidized bed reactor, also offer an effective approach to manufacture larger quantities of SWNTs [18]. The supported catalyst approach also offers the unique ability to provide a substantial degree of chirality control during synthesis.

2.3 Synthesis of MWNTs

In synthesis of CNTs, one important theme is growth of defect-free long CNTs. Wei's group pioneered growth of superlong defect-free CNTs [19, 20]. In this synthesis method, the catalyst nanoparticle is at the floating end of the CNT and keeps moving forward with its growth (Fig. 2a). By tuning the growth conditions to promote the activity of the iron catalyst nanoparticles, CNTs can grow up to 55 cm long (Fig. 2b). Raman and transmission electron microscopy (TEM) (Fig. 2c) characterization confirmed the perfect structure of such CNTs. The tensile strength of this kind of CNTs reaches ~ 140 GPa at strain of $\sim 15\%$ (Fig. 2d), which is nearly the theoretical value for MWNTs. Also, such defect-free CNTs were found to show superlubricity phenomena [21].

For vertically aligned MWNT arrays, one important method is to deposit catalyst nanoparticles on specially treated substrates (e.g., silicon wafer), which are then placed in a horizontal furnace [22]. Generally, a dense catalyst on the substrates is important for formation of CNT arrays. Such arrays represent an important platform material for subsequent CNT assembly, especially CNT fibers and films [23].

On the other hand, for large-scale and continuous production of aligned CNT arrays, millimeter-diameter spheres have been used as growth substrates by Wei's group [24], a method further developed by Noda's group by using ceramic beads in a fluidized bed reactor [25] and Bai's group by using alumina particles [26]. In most cases, the operation temperature of the CVD process ranges from 500 to 1200 °C.

The catalyst nanoparticles may easily aggregated if they are not well controlled. Wei's group developed use of layered vermiculite to stabilize the catalyst nanoparticles (Fig. 3a) [27]. Vertically aligned MWNTs approaching tens of microns can be produced in such vermiculite flakes (Fig. 3b). Moreover, layered double hydroxides (LDHs) have been developed as a catalyst for CNT growth [28]. As shown in Fig. 3

Fig. 3 **a** Formation of hybrid composites by intercalating vertically aligned CNT films into layered inorganic compounds. **b** Morphology of vermiculite–CNT composite after intercalation. Reprinted from Ref. [27]. Copyright 2009, Wiley–VCH, Weinheim, Germany. **c** Concept of chemical precursor-mediated catalyst synthesis. **d** Morphology of Fe NPs distributed on reduced Fe/Mg/Al layered double oxide (LDO) flake. Reproduced from Ref. [29], Copyright 2010, American Chemical Society. **e** Agglomerated S/DWCNTs grown on LDO with low catalyst density. Reproduced from Ref. [30], Copyright 2010, Wiley–VCH, Weinheim, Germany. **f** SEM and **g** TEM image of SWNT arrays grown on LDH with high catalyst density. Reproduced from Ref. [29]

2.4 Production Scale-Up of CNTs Using Fluidized-Bed CVD

CNTs are typically synthesized in a fixed horizontal furnace. For large-scale production, fluidized-bed CVD has been developed as an important technique for production of CNT powder worldwide, considering its advantages of uniform mass and heat transfer, sufficient growth space, and continuous operation [3, 31]. As shown in Fig. 4, this process operates with an input gas to achieve fluidization of catalyst particles. Although it is difficult to fluidize individual CNTs in such a reactor, the strong interactions between CNTs lead to formation of large-size aggregates in the gas, which can then be fluidized [32]. The growth ratio can reach more than 40-fold, resulting in product purity above 98%. Aligned CNTs can also be produced using fluidized CVD by tuning the catalyst structure; For example,

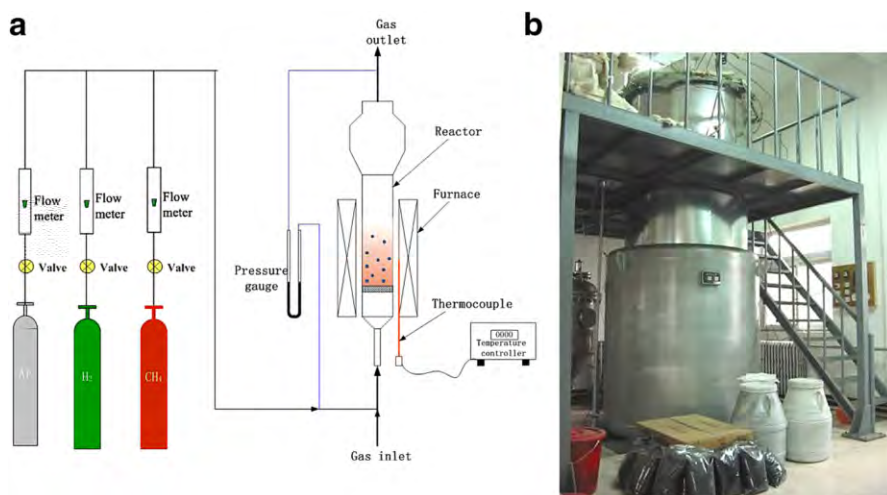


Fig. 4 **a** Scheme of typical fluidized-bed reactor system: a cylindrical fluidized-bed reactor is fixed inside a furnace with appropriate temperature, pressure, and gas flow controls. **b** A factory fluidized-bed reactor for producing CNT powder (images courtesy of Cnano Ltd.)

CNT arrays can be grown among the layers of vermiculite in a fluidized bed reactor [33]. By using LDHs as catalyst, SWNTs can be prepared in a fluidized bed reactor [34]. After further purification, the purity of such SWNTs can reach 99.5 wt%, offering high-quantity material for high-end applications [35]. This method can offer SWNT capacity of 1000 kg per year with price lower than US \$2000 kg⁻¹.

Note that scientific research and production scale-up of CNTs has also promoted development of other nanocarbons [36], such as graphene (G). The combination of CNTs and graphene may extend the applications of both [37–42]. As shown in Fig. 5a, by incorporating the catalysts of CNT and graphene together, SWNT/G hybrids or composites can be prepared based on catalytic growth on LDHs [37]. The morphology of the resulting structure (Fig. 5b, c) reveals a robust connection between the SWNTs and graphene, facilitating construction of a high-electrical-conductivity nanocarbon architecture. Moreover, catalyst residuals can be removed using a CO₂-oxidation-assisted purification method (Fig. 5d), leading to high carbon purity of 98.4 wt% [43]. Such nanocarbon architectures can combine high conductivity and high surface area, with important applications in energy storage and electrocatalysis [37–38].

3 Postprocessing of CNTs

3.1 CNT Purification and Dispersion

As discussed in “Synthesis of MWNTs” section, many as-produced MWNT materials are aggregated powders with a certain content of impurities and catalyst residue. For SWNTs, the problem of impurities is more serious. In some

Fig. 5 **a** Schematic illustration of catalytic CVD of G/SWNT hybrids on LDH flakes. **b** SEM and **c** TEM images of as-fabricated G/SWNT hybrids. Reprinted from Ref. [37]. American Chemical Society, copyright 2012. **d** G/SWNT hybrids after removal of residual impurities Reprinted from Ref. [43]. Elsevier, copyright 2013

applications, such as polymer composites, the problem of impurities and catalyst residues may be less critical; for example, MWNT powders with catalyst residues can still be directly mixed with polymer matrix [44]. Nevertheless, in most cases, catalyst residues and impurities must be removed, and CNT aggregates need to be dispersed before use. Therefore, purification and dispersion are important steps before CNT application. It is necessary to develop cost-effective and reliable processes for dispersion of CNTs for various applications.

As is well known, for CNT powders, the strong π - π interactions between CNTs and their structural entanglement make them difficult to disperse for applications. One direct method to disperse MWNTs is through mechanical treatment such as high-energy sand milling, high-speed liquid-phase shearing, etc. in industrial units. The solvent is typically nonaqueous. Aqueous solutions with a certain surfactant can also be used. Figure 6a shows that MWNTs made from fluidized-bed CVD can be uniformly dispersed into *N*-methyl-2-pyrrolidone by high-speed liquid-phase shearing. The dispersed CNTs easily form network structures due to their maintained lengths (Fig. 6b). Currently, manufacturers can produce MWNT dispersion, slurry, or paste, which may find a broad range of applications, e.g., in lithium (Li)-ion batteries, supercapacitors, printed electronics, electromagnetic shielding, coating materials, heat dissipation, etc. The largest application in China is as a conductive additive on the cathode side of Li-ion batteries to replace conductive

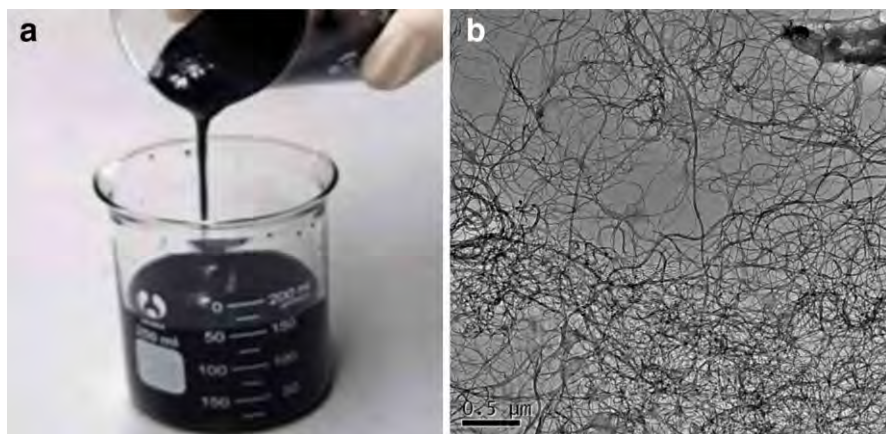


Fig. 6 **a** MWNTs dispersed in *N*-methyl-2-pyrrolidone at concentration of 1.0 mg mL^{-1} by high-speed liquid-phase shearing, displaying excellent dispersion. **b** Network structure of dispersed CNTs under TEM observation

carbon black for increased conductivity as well as cyclability. More than 10,000 t/a of CNT slurry have been used in Li-ion batteries for electric vehicles (EVs) and smartphones in China. It should be pointed out that high-energy mechanical treatments may destroy the structure of CNTs and decrease their length, thereby compromising their properties [45]. Also, the toxicity of the organic solvents used should be considered in manufacturing.

Alternatively, surface modifications, including noncovalent or covalent treatments, have been intensively investigated throughout the development of CNTs; progress in this regard has been summarized in many literature reports [46, 47]. Such strategies are still widely used for CNT treatments and applications. We only briefly introduce them here.

To preserve the structure and properties of CNTs, noncovalent treatment has been applied by adding a guest molecule for interfacial interaction. Typically, aromatic molecules can be appended to outer surfaces of CNTs by π - π interactions [48]. Groups emanating from these molecules interact with the surrounding solvent or matrix, making CNTs easier to disperse in a solvent or polymer matrix. Also, a certain structured polymer can be wrapped around CNTs via noncovalent interactions. This strategy has been utilized to harvest ultrahigh-purity SWNTs [49, 50], since separation of semiconducting and metallic SWNTs is challenging [51].

On the other hand, chemical modifications are also used to treat CNTs. Surface treatments of CNTs by acid oxidation seem to be a direct and powerful method [52] that can introduce carboxyl, hydroxyl, and ketone groups onto their surface. After such treatment, CNTs are much easier to disperse in solvents. In addition, CNTs can be grafted with other functional groups on their surface for various applications [53]. Unfortunately, chemical modifications create defects in the CNT structure, which may lower the electrical conductivity or compromise the mechanical properties to a certain degree.

Fig. 7 **a** Doping of CNTs by introducing heteroatoms into the carbon framework. **b** Elements reported to be suitable for heteroatom doping of CNTs, mainly including B, N, P, O, S, etc. Contact angles of CNTs **c** before and **d** after S doping Reprinted from Ref. [62]. Elsevier, copyright 2015

3.2 Heteroatom Doping

Introduction of heteroatoms into the carbon framework (Fig. 7a) of CNTs has been used to tailor the electronic and interfacial properties of this material. Figure 7b shows the most widely used elements for doping into the carbon skeleton. Boron (B), nitrogen (N), phosphorus (P), oxygen (O), sulfur (S), etc. have been solely or jointly utilized to dope CNTs and tune their structural properties [54–57]. Heteroatom doping strategies greatly change the properties of CNTs, extending their potential applications.

To date, much progress on heteroatom doping of CNTs has been made. The methods can mostly be categorized into in situ and posttreatment approaches. As their name implies, in situ approaches rely on introduction of heteroatom sources during the CNT synthesis process [58]. Posttreatment methods including wet chemical methods, thermal annealing of CNTs with heteroatom precursors, and plasma approaches have been developed in literature [59]. Precisely controlled heteroatom doping techniques are currently being developed for applications.

It is well known that pristine CNTs are quite chemically inert. Introduction of heteroatoms tailors the physicochemical properties of CNTs, which can result in catalyst activity; For example, N-doped CNTs can be used as electrode materials for fuel cells, with performance comparable to that of current platinum (Pt)-based catalyst [60, 61]. Theoretical and experimental investigations are being combined for more targeted doping of CNTs to achieve higher activity.

Additionally, CNTs display highly hydrophobic properties. Doping strategies may change this. Heteroatom doping enables CNTs to be much more easily dispersed, which is important for polymer composite and energy storage applications; For example, S-doped CNTs can be obtained by thermal annealing of pristine CNTs with sulfur compounds. Due to the sulfur doping, the contact angle of the CNTs is greatly reduced compared with pristine CNTs (Fig. 7c, d), suggesting effective modification of the CNT surfaces. The obtained S-doped CNTs can be stably dispersed in water [62]. When used in battery electrodes, higher capacity and rate performance can be achieved due to the improved dispersion due to construction of conductive networks.

4 Application Advances

4.1 Macroscopic Assemblies and Their Applications

The unique properties of CNTs have been measured for individual nanotubes. An important theme is to produce large-scale CNT architectures which also offer such properties [63, 64], although this still remains a big challenge. Generally, macroscopic CNT architectures can be fabricated by direct growth methods or by postprocessing of dispersed CNTs.

CNT arrays made by CVD are typical assemblies where CNTs are aligned on the substrate [23]. Many groups have reported synthesis of such structured CNTs for various applications. CNT films can be made by spinning aligned CNT arrays (Fig. 8a). Also, the CNT arrays can be continuously spun into macroscopic fibers (Fig. 8b). CNT films are believed to represent an alternative to indium tin oxide, since CNTs can make flexible displays [65]. Based on the CVD technique, Xie's group prepared nonwoven SWNT films (Fig. 8c, d) [66]. The SWNTs created Y-type junctions during synthesis, leading to the formation of a network structure. This unique structure can be easily handled for further study and use, e.g., in tough polymer composites [67], electrodes for flexible supercapacitors [68], etc. Recently, Kauppinen et al. developed an aerosol CVD method for fabrication of highly conductive and transparent free-standing SWNT films, where the products can be directly and continuously collected [69, 70]. For reduced formation of SWNT bundles, a spark generator-based floating catalyst CVD method was developed to produce nonbundled, small-diameter single-walled carbon nanotubes by feeding catalyst nanoparticles into a laminar flow chemical vapor deposition reactor [71, 72]. The resulting films exhibited outstanding properties that are desirable for touch panels, etc.

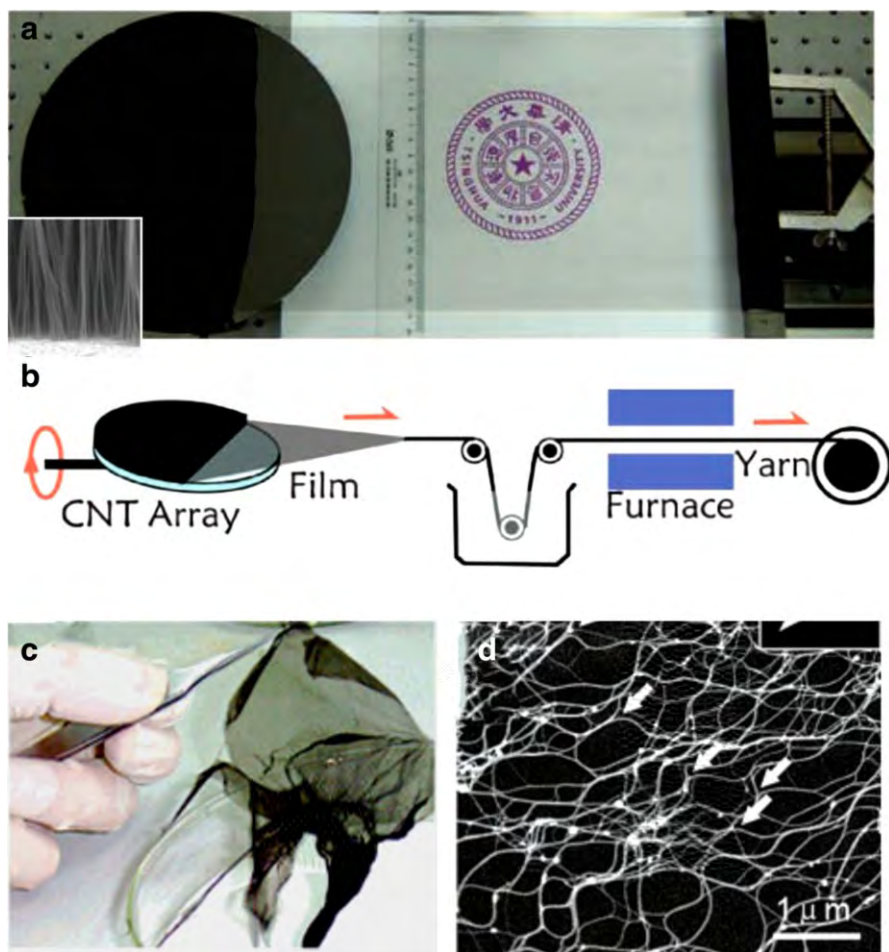


Fig. 8 **a** Drawing of a transparent conducting film of 8-inch superaligned CNT arrays (*inset* SEM structure). **b** Schematic illustration of process from superaligned CNT array to films and then shrunk yarns. Reprinted from Ref. [23]. Copyright 2011, Wiley-VCH, Weinheim, Germany. **c** As-grown 250-nm-thick SWNT film. **d** SEM image of SWNT network in a single layer; *white arrows* indicate Y-type junctions and flow direction Reprinted from Ref. [66]. American Chemical Society, copyright 2007

In terms of mechanical properties, most CNT fibers are reported to show tensile strength of 0.2–8.8 GPa [7]. To date, this strength value is still not competitive with that of traditional carbon fibers for actual applications. The critical factors affecting this need to be investigated. Commonly, condensation and alignment of CNTs, as well as interface engineering between CNTs, are important to increase the fiber strength. Recently, Wang's group continuously produced CNT macroscopic assemblies in the form of a hollow cylinder based on a floating catalyst approach (Fig. 9a) [7]. The hollow cylinder assembly was aligned, condensed, and deposited on a winding drum to form a CNT film (Fig. 9b). The prepared film displayed

Fig. 9 **a** Schematic illustration of fabrication of CNT film. Reaction solution is sprayed into a tube reactor and pyrolyzed to form a hollow CNT cylinder, which is then condensed and deposited on a winding drum. **b** Film removed from the substrate. **c** Stress versus strain curves, showing averaged tensile strength of 9.6 GPa. **d** Fracture surface visualized under SEM, displaying the aligned structure Reprinted from Ref. [74]. American Chemical Society, copyright 2016

tensile strength of 9.6 GPa (Fig. 9c, d), well above that of all other manmade films or fibers.

CNT foams/sponges with interconnected network structure can also be produced by the CVD method [76]. In this case, CNTs are randomly distributed in the sponge, rather than having aligned morphology. Such foams/sponges have been explored for energy and environmental applications. Moreover, Hata and coworkers developed a viscoelastic material from CNTs that is similar to silicone rubber, but maintains temperature-invariant viscoelasticity from -196 to 1000 °C in an oxygen-free environment [76]. This CNT material could find applications in extremely hot or cold environments.

On the other hand, stable CNT dispersions can be obtained based on gradually maturing dispersion techniques. As a one-dimensional nanocarbon material, CNT is attractive for engineering of large-scale architectures, including fibers, films, and aerogels/foams [63]. Similar to the important process used to produce industrial fibers, wet spinning of dispersions has enabled fabrication of SWNT and MWNT fibers [77–79]; For example, SWNTs dissolved in chlorosulfonic acid at weight concentrations of 0.5 wt% could be readily processed into macroscopic fibers or sheets to obtain functional materials [77]. Such functional fibers have conductivity comparable to copper wire but 1/8 of the density and several times the strength, enabling important engineering applications in the aerospace industry. In addition, three-dimensional aerogels/foams can be assembled from dispersed CNTs, showing highly porous structure. The high aspect ratio and strong interactions between CNTs are important for such porous structures. Gao's group described that CNTs can be

used as “ribs” to reinforce the framework of CNT/G aerogel [80]. The porous structure has porosity above 99.9%, yet structural flexibility and robustness.

4.2 Composite Materials

The elastic modulus of an individual MWNT is measured to approach 1 TPa, while the tensile strength exceeds 100 GPa [81]. This strength is over tenfold higher than any other fiber, even the well-known carbon fibers. Considering this high strength, it is believed that CNTs can be incorporated into another matrix for enhanced mechanical properties, including strength, toughness, and stiffness. Such polymer composites have been successfully prepared by adding CNTs and indeed offer excellent properties [82, 83]. These polymer composites have found a diverse range of applications such as automotive, tires, sports goods, aerospace, packaging, and even household goods.

Although individual CNTs show very good mechanical properties, transferring these unique properties to macroscopic composite materials remains a great challenge. If this issue is solved, many key applications will be enabled. When engineering polymer composites for load-bearing applications, the alignment, dispersion, diameter, and aspect ratio of the CNTs and their interfacial interactions with the matrix are critical for the final composite. Most CNTs obtained today are entangled powders. Commonly, when making CNT-based composites, the first question is how and which CNT structure to disperse in the matrix.

For cost-effective and large-scale applications, melt blending is one of the most widely used methods to achieve CNT-containing composites [84], since it offers easy and continuous operation. Manufacturers have used this technique to make composite rubbers containing CNTs. Figure 10 shows a high-performance tire tread produced using only 0.7% weight fraction of MWNTs; TEM results confirmed that the CNTs were uniformly dispersed in the rubber matrix. The prepared tires showed optimal comprehensive performance with practical applications [85]. As-prepared CNT–polymer composites can be engineered for various applications, such as spinning of conductive fibers [86]. In addition, ongoing interest in three-dimensional (3D) printing also offers opportunities for use of CNT-based composite resins. Adding CNTs to the raw polymers results in feedstocks with improved properties for this technique. This method can produce polymer composites with CNTs randomly distributed in the matrix. The CNT loading is mostly below 10 wt%, as higher contents of CNTs are difficult to process due to the high viscosity resulting from the CNTs. Zheng et al. demonstrated preparation of MWNT–rubber composites with high CNT concentration of ca. 37 wt%. The results showed that the persistence length and reorientation of MWNTs during stretching have a significant impact on the mechanical properties [87]. Addition of CNTs into polymers can indeed enhance the tensile strength and toughness. However, note that current dispersion processes still face undesirable problems, as well as damage to CNTs, which may compromise the mechanical properties of the final composites. To circumvent this problem, various other techniques such as in situ polymerization with CNTs have also been developed [88].

Fig. 10 Application of rubber–CNT nanocomposites in high-performance tires: **a** use of CNTs in highly filled rubber/nanosilica tread composite to solve the problem of electrical charge release from energy-saving passenger tires; **b** application of rubber–CNT nanocomposite in high-performance engineering tires for reduced heat accumulation Reprinted from Ref. [85]. Copyright 2016, Elsevier

Instead of directly mixing CNTs with a resin matrix, another strategy to make CNT–polymer composites based on a special resin infiltration process has been described. Various CNT structures, including films, foams, fibers, and arrays, can be incorporated

into polymers based on this method; For example, well-dispersed SWNT papers can be prepared by filtration for subsequent impregnation with precursors and polymers [89]. Although these SWNTs are well dispersed, their random entanglement still limits the strength. More importantly, CNTs can be grown or deposited on traditional fibers (e.g., carbon fiber [90], glass fiber [91], and quartz fiber [92], etc.) to improve the mechanical properties of the composite due to improved load transfer between interfaces.

For mechanical applications, current CNTs are usually considered to be short fibers. Polymer composites with CNT fillers are always analogs of random, short-fiber composites. By comparison, traditional carbon fibers have long-fiber features. Organizing CNTs into aligned continuous fibers is very effective to increase the content of CNTs and obtain high-strength fibers. In most cases, the enhancements achieved in polymer composites including randomly distributed CNTs are limited. The actual strength of CNTs is therefore not fully utilized in such composites containing random short CNTs. However, reorganizing the dispersed CNTs into an aligned architecture is challenging. Cheng et al. reported that CNT carpets with high aspect ratio can be aligned based on well-controlled strategies. The aligned CNTs are treated with epoxidation functionalization, and further incorporated into bismaleimide (BMI) resin to form a high-strength bulk composite with 60 vol% CNT concentration [93, 94] (Fig. 11a). The tensile strength and Young's modulus of these composites reached 3081 MPa and 350 GPa, respectively, exceeding those of state-of-the-art unidirectional carbon-fiber-reinforced composites (Fig. 11b). Another method to achieve aligned CNTs is growth of vertically aligned CNTs on substrates, as discussed above. Continuous yarns or sheets can be produced from such aligned CNTs; however, their mechanical properties still require further

CNTs are highly conductive. As a result, conductive polymer composites, and increasing their value, have been applied for certain commercial applications. A certain type of CNT-based conductive composite is already used for dissipating electrostatic discharge, in conductive plastics, and other applications. Benefiting from the high conductivity, together with high aspect ratio (i.e., length-to-diameter ratio of 10^2 to 10^7), nonconductive polymers become conductive on addition of as little as 0.1 wt%, without compromising other properties [88, 95, 96]. On the other hand, use of CNTs also enhances the mechanical properties of conductive composites, whereas use of much higher content of carbon black or metal nanoparticles in conductive polymers may decrease the tensile strength of the composites. Low CNT content is desirable for conductive polymers, considering manufacturing and cost issues. The conductivity largely depends on the processing method, type of CNT, and polymer matrix applied [97]. Adding CNTs to polymers also results in other, multifunctional properties, e.g., thermal conductivity [98], electromagnetic interference shielding [99], etc.

Besides polymer composites, other composites have also received much attention, such as metal [100, 101], ceramic [102], and other composite materials [103]. Although these composites are designed for various aims, they face similar problems regarding production of CNT-based polymer composites. Indeed, if the challenges discussed above are solved, many techniques will benefit, enabling many high-volume CNT applications.

4.3 Energy Storage

4.3.1 Lithium-Ion Batteries

Lithium-ion batteries are widely used in electronics and laptops, and their applications are now extending to include electric vehicles and large-scale energy storage applications. Currently, battery charging takes more than 10 h due to the low conductivity of the electrode materials. Based on their reduced cost, CNTs are now being used in lithium-ion batteries. MWNT powders are ground into slurry to improve the conductivity of the electrode. A small amount of MWNTs can be added simply into the electrode by mechanical blending. Benefiting from this improvement, LIBs in electric vehicles can be charged in less than 1 h. Compared with traditional carbon black, CNTs offer long-range conductivity, resilient network structures for electrodes, better interfacial contacts, and thermally conductive networks, representing prominent advantages over traditional carbon black materials for improved Li-ion batteries [104–106].

Most cathode materials (e.g., LiFePO_4) face problems of low conductivity and limited ion transport in several current classes of cathode material. Obviously, CNTs are becoming important additives for cathodes of Li-ion batteries. By partially replacing carbon black (CB), it was reported that addition of CNTs to electrodes could result in formation of three-dimensional conductive scaffolds with effective charge transport (Fig. 12a, b) [107]. As a result, introduction of CNTs greatly improves the charging rate and stability of such battery electrodes (Fig. 12c). This strategy is now starting to be used to improve the power

Fig. 12 **a** SEM image of CNT/CB-modified LiFePO_4/C cathodes, as well as **b** structural illustration. **c** Cycling stability of LiFePO_4/C cathode with CNT/CB as conductive scaffold, compared with that made from CBs or CNTs. Reprinted from Ref. [107], American Chemical Society, copyright 2014. **d** Schematic diagram showing the Si/CNT hybrid nanostructures; **e** SEM image of the CNT array covered with Si nanoclusters Reproduced from Ref. [117], Copyright 2010, American Chemical Society

performance of batteries. For industrial applications, a uniform dispersion of CNTs in the cathode material is vitally important. Cnano technology limited has developed a method to disperse MWNTs by sand milling to form CNT slurry, with production of more than 10,000 t/a. CNT slurries are being used as conductive additives for Li-ion battery cathodes for EVs and smartphones, representing the largest application of CNTs in China.

For higher energy density, Li–S cathodes are being explored for use in next-generation Li-ion batteries. CNTs are used as effective scaffolds to improve the electrode performance of S [108–110]. By direct thermal treatment of SWNTs with S powder, S/SWNT composites can be prepared with tight adhesion of S on CNT

surfaces [111]. However, the capacity decay is still critical for actual applications of Li–S batteries. Interfacial modifications and porous structure engineering of CNTs, as well as rational combination of CNTs with other kinds of nanocarbon, are underway to achieve further improvements of Li–S batteries [112, 113].

CNTs can also be used for anode materials because they are composed of curved graphitic layers [114]. However, they usually display highly irreversible capacity during the initial cycles, which may be due to their high interfacial activity. Some posttreatments of CNTs are therefore necessary for use in battery anodes.

Instead of direct use as anode materials, it seems that making composite materials of CNTs and other active materials is an effective strategy for use of CNTs in batteries. Silicon (Si) is a promising anode material with theoretical capacity of 4200 mAh g^{-1} and low voltage plateau [115]. However, Si anodes suffer from large changes in volume during charge/discharge cycles and low electron conductivity, resulting in poor cycling stability and rate capacity. CNT/Si hybrids with entangled structure can be prepared by simple mechanical mixing [116], displaying improved rate capacity and cycling stability. Ordered nanostructured composites as battery electrodes are expected to minimize ion electron transport resistances, thereby offering much better performance. Aligned CNTs have therefore been used to form ordered nanostructured composites. Wang et al. reported deposition of Si on aligned CNTs by a CVD technique [117] (Fig. 12d, e), achieving reversible stable capacity and good rate capability. Gleb Yushin's group also reported that aligned CNTs coated with Si can be used to form thick ($\sim 1 \text{ mm}$) electrodes [118]. Such ordered nanostructured composite materials have great potential if they become readily available. Some other anode composites containing CNTs have also been prepared (electrode

Fig. 13 **a** Schematic process of aerosol-assisted heteroassembly of oxide nanocrystals and CNTs into hierarchically structured mesoporous composite particles. Modified from Ref. [119], Copyright 2015, Wiley–VCH, Weinheim, Germany. **b** SEM image of CNT/Fe₃O₄ composites, showing interwoven networks. **c** Compressive stress–strain curves of CNT/Fe₃O₄ composites, suggesting high structural durability Reprinted from Ref. [120]. American Chemical Society, copyright 2014

CNTs and active materials can be prepared and work well. CNTs are being considered for use as both a current-collector support for active materials and as free-standing electrodes without any binder. Jia et al. reported fabrication of binder-free electrodes based on a simple vacuum filtration method (Fig. 14a, b) [123]. In such structures, the particles of active material are tightly trapped in CNT networks (Fig. 14c), forming effective conductive pathways. Based on their tight entanglement, as-formed entangled electrodes show tensile strength approaching 1.2 MPa (Fig. 14d). By comparison, traditional carbon black–polyvinylidene fluoride bound electrodes show limited flexibility. For high-capacity electrode materials (e.g., V₂O₅, Fig. 14e, f) [124], binder-free electrodes represent a highly flexible architecture that can accommodate the volume change while retaining the conductive network. Although no binders were added, these electrodes worked well and showed high rate capacity and improved stability. Moreover, Peng's group incorporated lithium-based nanoparticles into CNT fibers to make a lithium-ion battery, which also performed stably after being stretched [125]. Such devices could be used in smart clothing and other applications.

Besides flexible electrodes, CNT paper may be produced from dispersions for use in the papermaking industry. This may enable lightweight and highly conductive current collectors for use in batteries with higher energy and power density. Interestingly, ground CNT paste, as well as other conductive pastes, can be incorporated onto metal substrates to form more effective collectors to load active materials. Construction of such mechanically flexible and deformable substrates to load active materials for battery electrodes enables facile fabrication of lightweight flexible energy-storage devices [126].

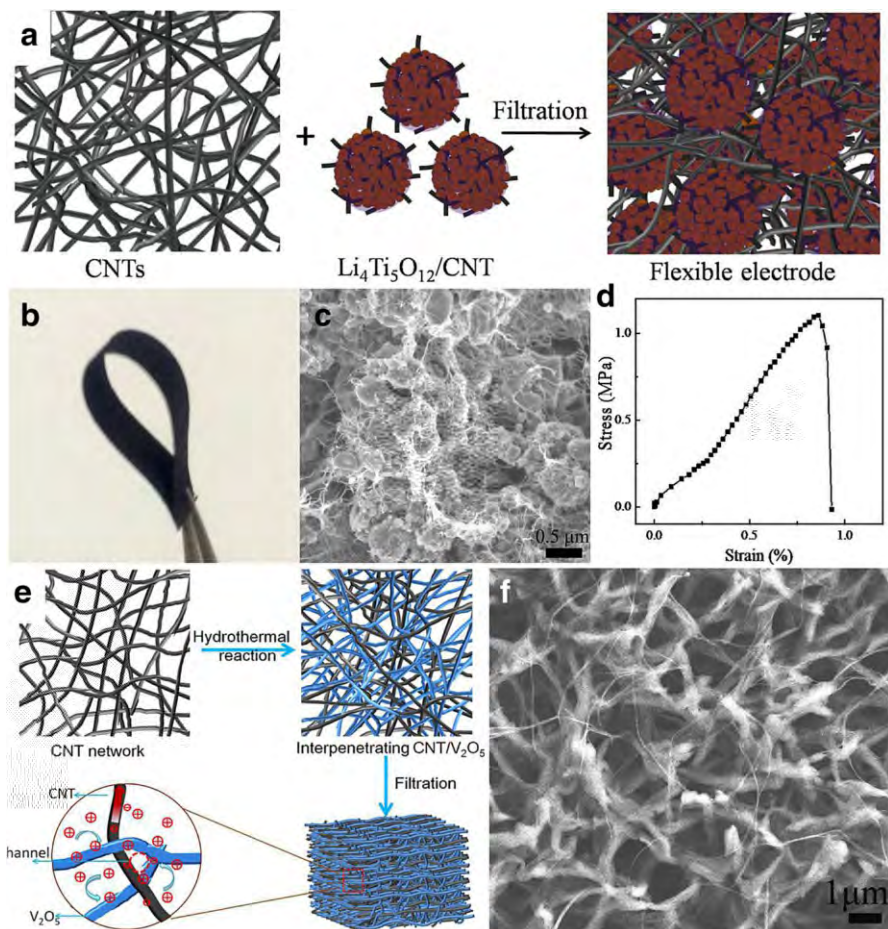


Fig. 14 **a** Fabrication of binder-free flexible $\text{Li}_4\text{Ti}_5\text{O}_{12}/\text{CNT}$ electrode based on simple vacuum filtration process. **b** Flexible electrode and **c** its cross-sectional morphology, showing intimate entanglement. **d** Stress–strain curve of flexible electrodes. Reprinted from Ref. [123]. Copyright 2013, Elsevier. **e** Schematic of synthesis of composites of ultralong CNTs and V_2O_5 nanowires with interpenetrating network structure. **f** SEM image of V_2O_5 nanowire networks and CNTs penetrating through the networks. Reproduced from Ref. [124]. Copyright 2012, Royal Society of Chemistry

4.3.2 Supercapacitors

Another promising energy storage device is the supercapacitor, which is known for its high power density, fast charging time, and long lifetime. The storage mechanism of this kind of device is based on storage of opposite charges between two closely spaced surfaces [127]. Based on this storage mechanism, it is expected that large specific surface area (typically over $1500 \text{ m}^2 \text{ g}^{-1}$) will be key to achieve supercapacitors with high specific capacitance by providing effective charge storage sites in the double layer. Activated carbons (AC) are currently the most common electrode materials for supercapacitors, due to their low cost. However, the

defective microstructure and disordered small pore structure of ACs limit performance.

Due to their high electrical conductivity and high specific surface area, CNTs (including both SWNTs and MWNTs) are being extensively studied for use in electrode materials for supercapacitors with both aqueous and nonaqueous electrolytes. In aqueous devices, KOH or H₂SO₄ are the most widely used electrolytes. The size of the ions is very small, around 0.5 nm, so nearly no diffusion limitation exists within the electrode. In this case, the capacitance of the electrode is mainly determined by its specific surface area. For MWNTs with specific surface area of 400 m² g⁻¹, the capacitance ranges from 5 to 200 F/g. It seems that there are no obvious advantages of MWNTs over AC. SWNTs could offer comparable surface area to AC in aqueous electrolyte. However, the high current cost of production and purification of SWNTs hampers their high-volume use.

One way to increase the capacitance of CNT electrodes is to modify the surface of the CNTs by acid or base treatment. Functional groups including OH, COOH, or C=O exhibit pseudofaradaic capacitance in the range of 4–135 F g⁻¹. Therefore, MWNTs with moderate surface area of 400 m² g⁻¹ exhibit capacitance comparable to commercial AC after such modifications [128]. This surface modification makes the CNTs hydrophilic, allowing quick access of ions from the aqueous electrolyte. In addition, it must be pointed out that heteroatom doping of CNTs represents an important strategy to enhance the pseudofaradaic capacitance [129].

Making CNT-based hybrid/composite materials for supercapacitors is another method to increase the pseudofaradaic capacitance. Many publications have reported CNT/metal oxides and CNT/conductive polymers for use in supercapacitors [130]. Faradaic reaction (or pseudocapacitance) is obtained in these nanostructures by tuning their structure and interfaces. The designed three-dimensional architectures can offer facile kinetics, thereby enabling production of energy storage devices with high energy and power and long lifetime. However, CNT/oxide materials suffer from low specific surface area (mostly <50 m² g⁻¹

Fig. 15 **a** Electrode fabrication from SWNT arrays. **b** Typical cell assembly based on SWNT electrode in 1 M Et₄NBF₄/propylene carbonate electrolyte. **c** Ragone plot of SWNT device at the cusp of bridging the energy gap between commercial supercapacitors and batteries. (*S1* Panasonic 2000F, *S2* Superfarad 250F, *S3* Saft Gen2, *S4* Saft Gen3, *S5* Maxwell 2700F, *S6* Panasonic 800F; *B1* Li-ion, *B2* NiHD, *B3* Pb-acid) Reprinted from Ref. [132]. Copyright 2010, Wiley–VCH, Weinheim, Germany

CNTs with high surface area, large bulk density, and ultrahigh purity offer a good platform to demonstrate the application of CNTs in high-voltage supercapacitors. Thus, several SWNT companies such as Gnnano in China, Zeon in Japan, and OCSiAl in Russia have tonnage capacity of SWNT production to focus on this market.

Although SWNTs are attractive for use in supercapacitors, they normally form nanotube bundles, so that the available surface area of the nanotubes is usually reduced. In addition, the current cost of SWNTs is still a major obstacle to their wide application. For MWNTs, the rise of graphene may remedy the disadvantages of each material. Composites combining CNTs and graphene have been proposed to prepare high-powder high-energy supercapacitors (Fig. 16a, b) [133, 134]. Recently, three-dimensional porous graphene fibers were reported for use in supercapacitor applications (Fig. 16c) [135]. The capacitance can be even better than with SWNTs, particularly at increasing current densities (Fig. 16d). In addition, similar to lithium-ion batteries, a great advantage is that CNTs enable fabrication of electrodes without binders or current collectors, which are attractive for use in flexible, stretchable, compressible, and fiber supercapacitors [136, 137].

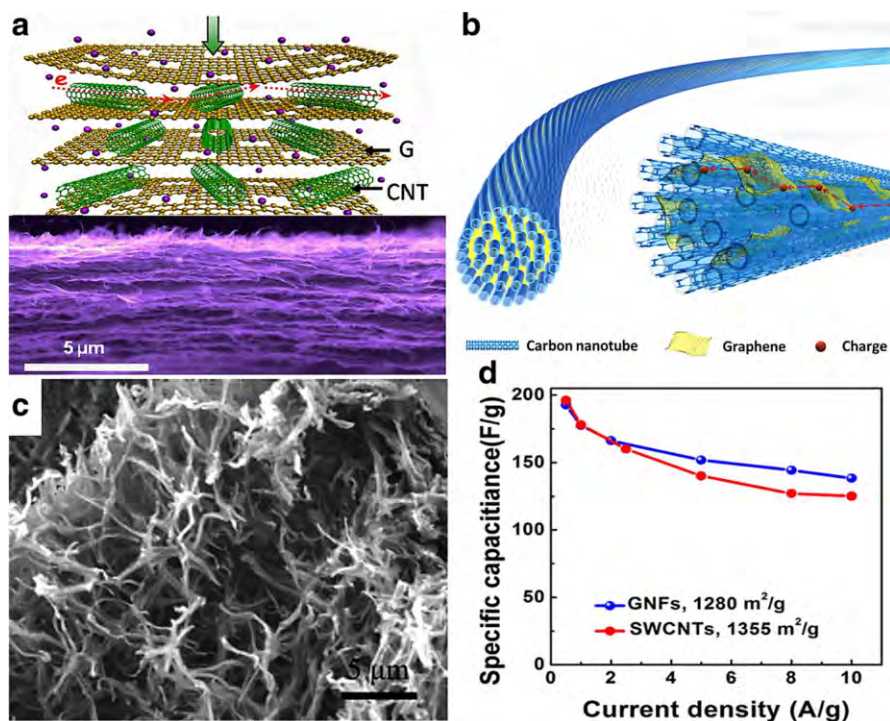


Fig. 16 **a** Schematic illustration of ion diffusion behavior for porous CNT-graphene film. Reprinted from Ref. [133]. Elsevier, copyright 2010. **b** Schematic illustration of structure of graphene-CNT composite fiber. Reproduced from Ref. [134]. Copyright John Wiley and Sons 2014. **c** Morphology of mesoporous graphene nanofibers (GNFs). **d** Comparison of specific capacitance of GNFs and SWNTs. Reproduced from Ref. [135]. Copyright 2014, American Chemical Society

4.4 Catalysis Applications

CNTs themselves as well as their composites can be engineered into efficient catalysts for use in sustainable energy applications. Different from traditional inorganic catalysts, CNTs can easily form a unique network structure that enables facile mass transport. They have inert properties, making them stable in strong acid and alkali solutions. Moreover, CNTs can also be used as catalyst supports for development of other candidate catalysts. These features make CNTs promising for application in catalysis. CNTs are therefore playing an increasingly important role in this research field [8].

As is well known, oxygen reduction reaction (ORR) catalysts are mostly based on platinum (Pt) and its alloys. However, Pt metal suffers from high cost and instability in actual applications. It is therefore very important to identify alternatives. At present, nanocarbon materials such as CNTs and graphene [138] have been developed as effective electrocatalysts or electrocatalyst supports. However, pristine CNTs usually show very limited performance for ORR due to their inactive surface.

To obtain the desired catalyst performance, introduction of heteroatoms into the CNT framework has been found to endow them with excellent activity. A breakthrough in this regard was the synthesis and use of vertically aligned N-doped CNTs as a metal-free electrode for ORR [61]. The performance of this electrocatalyst for oxygen reduction in alkaline cells revealed much better electrocatalytic activity, long-term operation stability, and tolerance to crossover effect compared with Pt. The reason for the ORR activity may be mostly ascribed to the carbon atoms with Lewis basicity next to pyridinic N, as confirmed in N-doped graphene [139]. To date, use of N-doped CNTs for ORR in alkaline electrolytes has been confirmed by many groups, and this work is being extended to other nanocarbon materials. However, the catalyst performance of N-doped CNTs is highly compromised in acidic media. CNTs offering excellent performance in both alkaline and acidic media are therefore desirable.

On the other hand, based on composite engineering, the surface of CNTs can be loaded with various catalysts with good dispersion, offering excellent electrocatalyst supports. One effective Pt-free ORR catalyst is the complex of MN_x , where M is one metal of Fe, Co, and Ni, coordinated by N-containing ligands such as phthalocyanine [140]. However, phthalocyanines have low conductivity and must be mixed with conductive carbon black to form electrodes. CNTs seem to be a better alternative. If well engineered, use of CNTs could significantly improve the activity of the catalyst for ORR. In this case, carbon ring nitrogen coordination of transition-metal catalysts can be achieved. Dai's group has reported the design and synthesis of many efficient CNT-based electrocatalysts. As a typical example, by unzipping CNTs by oxidation and ammonia treatment, a highly efficient NT-G-Fe electrocatalyst was prepared (Fig. 17a, b) [141]. The NT-G catalysts showed ORR activity comparable to that of state-of-the-art Pt/C in 0.1 M KOH (Fig. 17c), also offering promising performance in acid 0.1 M $HClO_4$ medium cells (Fig. 17d).

The development of high-performance catalysts for the hydrogen evolution reaction (HER) and oxygen evolution reaction (OER) also holds great promise for clean energy technologies. One of the typical reactions is water splitting. Making cost-effective electrocatalysts to replace precious iridium (Ir)- or Pt-based catalysts is an important theme. MWNTs modified by surface oxidation treatment, hydrothermal annealing, and electrochemical activation displayed unprecedented OER activity in alkaline media (Fig. 18a) [142]. Oxygen-containing functional groups such as ketonic $C=O$ on the outer wall of MWNTs are found to play crucial roles in catalyzing OER by altering the electronic structures of the adjacent carbon atoms and facilitating adsorption of OER intermediates. On the other hand, to further improve the activity, an effective approach is to make composite electrocatalysts by introducing CNTs. As shown in Fig. 18b, application of a multilayer covalent cobalt porphyrin framework on MWNTs resulted in a highly active electrocatalyst for water oxidation [143]. Nickel-iron layered double hydroxide (NiFe-LDH) nanoplates can also be loaded on MWNTs to form a composite OER electrocatalyst (Fig. 18c–e). The resulting NiFe-LDH/CNT complex exhibits higher electrocatalytic activity and stability for oxygen evolution compared with commercial precious-metal (Ir) catalysts [144]. In addition, such

Fig. 17 **a, b** TEM images of NT-G catalysts showing exfoliated graphene pieces attached to CNTs. Rotating-ring disk electrode polarization curves and peroxide yield of NT-G in **c** 0.1 M KOH and **d** 0.1 M HClO₄ Adapted from Ref. [141]. Copyright 2012, Macmillan

composite electrocatalysts may also find applications in photocatalytic and photoelectrochemical water splitting cells [8].

In the field of heterogeneous catalysis, porous carbon materials (e.g., mesoporous carbons) have been used to disperse and stabilize metal particles. As a catalyst support, the external surface area and interconnected pores of CNTs greatly improve diffusion of reactants and products, thereby increasing the catalytic activity and selectivity. A variety of inorganic metal catalysts, including molecular catalysts, metal nanoparticles, metal oxides or even more complex hierarchical hybrids, have been loaded onto CNTs for improved reaction performance [145]. Apart from the aforementioned applications, CNTs have also been utilized for desulfurization of

Fig. 18 **a** As-prepared surface-oxidized and electrochemically activated MWNTs for use as OER electrocatalyst. Reproduced from Ref. [142]. Copyright 2015, American Chemical Society. **b** Cobalt porphyrin loaded on MWNTs for efficient OER catalysis. Reproduced from Ref. [143]. Copyright 2015, American Chemical Society. **c** Schematic showing hybrid architecture and LDH crystal structure. **d** Morphology of NiFe-LDH/CNT hybrid. **e** iR-corrected polarization curves of NiFe-LDH/CNT hybrid and Ir/C catalysts on carbon fiber paper, measured in 0.1 and 1 M KOH Reproduced from Ref. [144]. Copyright 2013, American Chemical Society

diesel fuel, oil hydrocarbon aerobic oxidation, hydrodesulfurization processes, etc. [146]. Overall, direct use of CNTs as catalysts has been shown to be viable for several processes. The scope of such reactions has expanded considerably over the past year. Moreover, inspired by research on CNTs, interest in preparation of CNT-like materials for catalyst applications has been increasing [138].

4.5 Environmental Applications

4.5.1 Gas Filtration

In most cases, traditional fiber mats can achieve efficient filtration of megascopic particles, meeting application requirements. However, it is difficult to remove particles smaller than 1 μm from a gas flow. High filtration efficiency for such particles is important in many critical applications, such as release of nuclear-active materials, semiconductor manufacture, aerospace environments, pharmaceutical processing, and bioengineering.

It has been widely reported that introduction of nanofibers into macrofiber mats can significantly increase their filtration efficiency and improve the pressure drop of pristine macrofiber filters. CNTs with diameter around the nanoscale may enable highly efficient filtration [147]. CNTs themselves can be interwoven into a mat for filtration. However, this will lead to a large pressure drop, which leads to low efficiency. Alternatively, the combination of CNTs with traditional fiber mats to fabricate CNT-based filters may result in highly efficient air filtration. The challenge lies in control of the structure between the CNTs and filter fibers to avoid a large pressure drop.

As shown in Fig. 19a–f, Li et al. proposed a “gradient nanostructure filtration” concept to eliminate clogging of nanofiber filters [148]. When grown with only a small amount of 1.17wt% CNTs, the efficiency was greatly improved. The filters displayed the combination of high efficiency, low pressure drop, and long service lifetime at the same time. They fabricated hierarchical CNT/QF filters with gradient nanostructures where the content of the CNTs decreased exponentially along the axial direction of the filter, resulting in higher filtration efficiency and lower pressure drop [149]. Moreover, a high-efficiency particulate air filter based on an agglomerated CNT fluidized bed has been developed [150]. Indeed, based on its high efficiency, aerosols and peculiar smells in the air could also be removed using this filter. Recently, Yang et al. found that the CNT/QF filter also has very strong ability to remove O_3 from air in comparison with activated carbon. Such environmental applications represent a new field for CNTs [151].

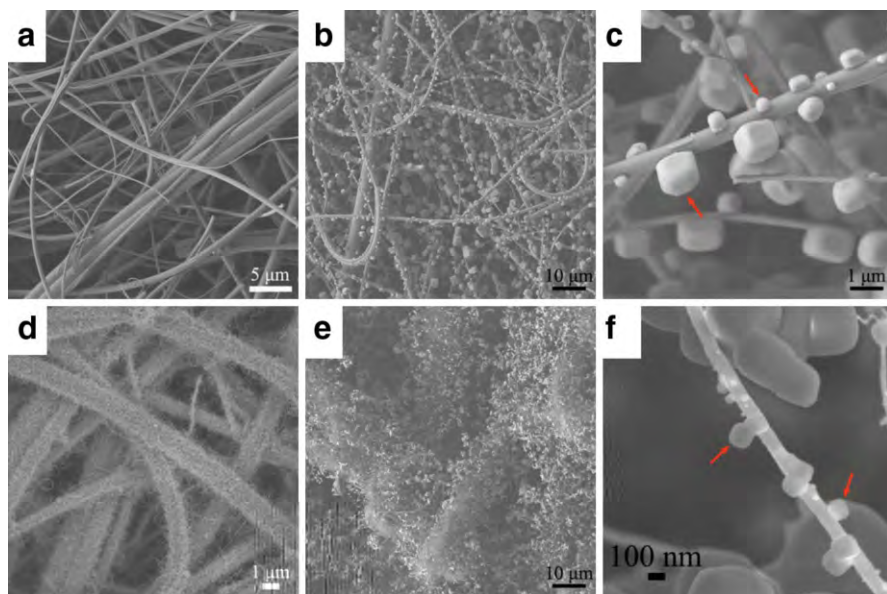


Fig. 19 SEM images of filters before and after filtration process. **a** Pristine quartz fiber (QF) filter; **b** NaCl aerosol particles deposited on QF filter; **c** NaCl aerosol particles deposited on single quartz fiber; **d** CNT/QF filter; **e** NaCl aerosol particles deposited on CNT/QF filter; **f** NaCl aerosol particles deposited on single CNT Reproduced from Ref. [148]. Copyright 2013, Royal Society of Chemistry

4.5.2 Water Absorption and Filtration

Another upcoming application domain for CNTs is water purification. Serious water pollution results in a great deal of damage to the environment, also affecting human health and animal and plant survival. Water pollution includes heavy metals, inorganic nonmetals, organic matter, etc., from both domestic and industrial wastewater. CNTs represent a special fiber material with many advantages. They are entangled into robust networks and offer mechanical strength and stability. CNTs have good performance for adsorption of contaminants from water due to their high affinity and selective adsorption capacity for contaminants, particularly organic pollutants, bacteria, and heavy metals. Production of portable filters containing CNT meshes has been reported for purification of contaminated drinking water [2]. In addition, by adding a suitable amount of MWNTs to polyamide (e.g., 15.5 wt%), a high-performance reverse osmosis composite thin membrane can be obtained, which not only improves the membrane performance in terms of flow and antifouling, but also inhibits chlorine degradation of the membrane [152].

More importantly, an interesting issue discussed by researches is water transport in the internal tubes of small-diameter CNTs. It has been found that transport of fluids using CNTs is orders of magnitude faster than for other nanoporous materials due to the unprecedented smoothness and regularity of CNT pores [153, 154]. In this case, aligned CNT membranes are being evaluated for use in desalination technology (Fig. 20) [155]. They can be embedded into a resin or ceramic matrix and then engineered with open ends for water purification. The results show that this kind of CNT filter has a water flux approximately three times higher than

Fig. 20 Carbon nanotube (CNT) membranes for water purification. The membrane facilitates water influx, rejects salts, and removes most pollutants Reprinted from Ref. [155]. Elsevier, copyright 2013

commercial ultrafiltration membranes and water transport approximately 70,000 times faster than conventional no-slip flow [156]. Moreover, by engineering the ends of CNTs using different functionalization strategies, such filters also display enhanced ability to gate molecular transport through the CNT cores [157]. These studies indicate that CNTs have potential to overcome the inherent limitations resulting from the trade-off between flux and selectivity of any membrane process. In this regard, CNT membranes are considered to have a bright future for use in next-generation water desalination. If this technique is scaled up, water desalination and purification may rapidly become promising [158].

Studies have shown that CNTs have good performance for adsorption of contaminants from water. Compared with traditional adsorbents, CNTs offer advantages of large adsorptive capacity and short adsorption equilibrium time. However, there are still some problems including high production cost, poor cycle stability, etc. Another major concern regarding CNTs for air and water filtration is environmental and human exposure to CNTs, since there are some reports that CNTs may damage human health [159]. Mechanical stability is very important for the safety of CNT-based filters. The structure of CNT-based filters should be designed to prevent CNT detachment from the filter under the force of fluid flow or other external forces. Such health and environmental concerns are also important for CNT production and their subsequent processing, application, recycling, etc. [160].

5 Summary and Outlook

CNTs display many extreme properties, such as superior mechanical strength, semiconducting properties, etc. However, these properties are only achieved when they have perfect structure. It is very important to control or even completely avoid defects at the atomic to macro level during CNT synthesis, as well as to achieve production scale-up. This is an engineering problem and currently represent the most challenging issue in the field of CNTs. Although this challenge seems difficult, such ultrahigh-strength materials and ultra-high-performance semiconductor materials are in great demand for future society.

Large-scale production of MWNTs has become available, now offering production capacity of more than thousands of tons per year. The processing techniques used are critical for their application. It is important to develop cost-effective and reliable processes for CNT processing depending on the application. Now, MWNT powders are milled into pastes, which are widely used in lithium-ion batteries. However, dispersion techniques and extended applications of this kind of material need to be further explored, especially to solve the dispersion problems of high-aspect-ratio and high-purity CNTs, and to identify applications.

Synthesis and scaled-up production of SWNTs with high aspect ratio and purity remain key issues for future development and applications of CNTs. Addressing these problems will benefit many critical applications.

Meanwhile, the development of CNTs has promoted research into other nanocarbons, currently including graphene. The combination of CNTs with other nanocarbons will open up new horizons for development of CNTs. Such rational

combinations will further enhance the potential applications of CNTs and other materials.

Looking ahead, CNTs have made great breakthroughs in energy storage applications. Considering the rapid development of EVs and other practical devices, it is very possible that CNTs will be used in industrial applications at levels up to several million tons per year in the next decade. In the field of CNT catalysis, the superior performance of doped Dirac carbon materials compared with Pt/C in ORR, OER, HER, etc., may enable rapid development in the chloralkali industry and fuel cells. Also, due to the significant advantages of SWNTs in load-bearing materials and conductive materials, it is believed that they will become key materials for use in high-end applications, e.g., in the aviation, aerospace, and military fields.

Acknowledgements We greatly appreciate the reviewers' constructive comments. This work was supported by the National Natural Science Foundation of China (Nos. 21306102 and 21422604, Prof. F. Wei), and partially by the National Natural Science Foundation of China (Nos. 51502347 Dr. X. Jia).

References

- Iijima S (1991) *Nature* 354:56
- De Volder MFL, Tawfick SH, Baughman RH, Hart AJ (2013) *Science* 339:535
- Zhang Q, Huang J-Q, Qian W-Z, Zhang Y-Y, Wei F (2013) *Small* 9:1237
- Endo M, Strano MS, Ajayan PM (2007) *Potential applications of carbon nanotubes*, Springer, Berlin Heidelberg, p 13
- Liu C, Cheng H-M (2013) *Mater Today* 16:19
- Baughman RH, Zakhidov AA, de Heer WA (2002) *Science* 297:787
- Endo M (1988) *ChemTech* 18:568
- Yan Y, Miao J, Yang Z, Xiao F-X, Yang HB, Liu B, Yang Y (2015) *Chem Soc Rev* 44:3295
- Sinnott SB, Andrews R, Qian D, Rao AM, Mao Z, Dickey EC, Derbyshire F (1999) *Chem Phys Lett* 315:25
- Liu C, Cheng H-M (2016) *J Am Chem Soc* 138:6690
- Chen Y, Zhang Y, Hu Y, Kang L, Zhang S, Xie H, Liu D, Zhao Q, Li Q, Zhang J (2014) *Adv Mater* 26:5898
- Yang F, Wang X, Zhang D, Yang J, Luo D, Xu Z, Wei J, Wang J-Q, Xu Z, Peng F, Li X, Li R, Li Y, Li M, Bai X, Ding F, Li Y (2014) *Nature* 510:522
- Murakami Y, Chiashi S, Miyauchi Y, Hu M, Ogura M, Okubo T, Maruyama S (2004) *Chem Phys Lett* 385:298
- Hata K, Futaba DN, Mizuno K, Namai T, Yumura M, Iijima S (2004) *Science* 306:1362
- Amama PB, Pint CL, McJilton L, Kim SM, Stach EA, Murray PT, Hauge RH, Maruyama B (2009) *Nano Lett* 9:44
- Chen Z, Kim DY, Hasegawa K, Noda S (2013) *ACS Nano* 7:619
- Nikolaev P, Bronikowski MJ, Bradley RK, Rohmund F, Colbert DT, Smith KA, Smalley RE (1999) *Chem Phys Lett* 313:91
- Resasco DE, Alvarez WE, Pompeo F, Balzano L, Herrera JE, Kitiyanan B, Borgna A (2002) *J Nanopart Res* 4:131
- Zhang R, Wen Q, Qian W, Su DS, Zhang Q, Wei F (2011) *Adv Mater* 23:3387
- Zhang R, Zhang Y, Zhang Q, Xie H, Qian W, Wei F (2013) *ACS Nano* 7:6156
- Zhang R, Ning Z, Zhang Y, Zheng Q, Chen Q, Xie H, Zhang Q, Qian W, Wei F (2013) *Nat Nanotech* 8:912
- Jiang K, Li Q, Fan S (2002) *Nature* 419:801
- Jiang K, Wang J, Li Q, Liu L, Liu C, Fan S (2011) *Adv Mater* 23:1154
- Xiang R, Luo GH, Qian WZ, Wang Y, Wei F, Li Q (2007) *Chem Vapor Depos* 13:533
- Kim DY, Sugime H, Hasegawa K, Osawa T, Noda S (2011) *Carbon* 49:1972

26. Dichiaro A, Bai J (2012) *Diam Rel Mater* 29:52
- 27 Zhang Q, Zhao M, Liu Y, Cao A, Qian W, Lu Y, Wei F (2009) *Adv Mater* 21:2876
28. Zhao M-Q, Zhang Q, Huang J-Q, Wei F (2012) *Adv Funct Mater* 22:676
29. Zhao M-Q, Zhang Q, Zhang W, Huang J-Q, Zhang Y, Su DS, Wei F (2010) *J Am Chem Soc* 132:14789
30. Zhao M-Q, Zhang Q, Jia X-L, Huang J-Q, Zhang Y-H, Wei F (2010) *Adv Funct Mater* 20:677
31. Zhang Q, Huang J-Q, Zhao M-Q, Qian W-Z, Wei F (2011) *ChemSusChem* 4:864
32. Wei F, Zhang Q, Qian W-Z, Yu H, Wang Y, Luo G-H, Xu G-H, Wang D-Z (2008) *Powder Technol* 183:10
33. Zhang Q, Zhao M-Q, Huang J-Q, Liu Y, Wang Y, Qian W-Z, Wei F (2009) *Carbon* 47:2600
34. Zhao M-Q, Zhang Q, Huang J-Q, Nie J-Q, Wei F (2010) *Carbon* 48:3260
35. Chen T-C, Zhao M-Q, Zhang Q, Tian G-L, Huang J-Q, Wei F (2013) *Adv Funct Mater* 23:5066
36. Zhang J, Terrones M, Park CR, Mukherjee R, Monthieux M, Koratkar N, Kim YS, Hurt R, Frackowiak E, Enoki T, Chen Y, Chen Y, Bianco A (2016) *Carbon* 98:78
- 37 Zhao M-Q, Liu X-F, Zhang Q, Tian G-L, Huang J-Q, Zhu W, Wei F (2012) *ACS Nano* 6:10759
38. Tian G-L, Zhao M-Q, Yu D, Kong X-Y, Huang J-Q, Zhang Q, Wei F (2014) *Small* 10:2251
39. Tang C, Zhang Q, Zhao MQ, Huang JQ, Cheng XB, Tian GL, Peng HJ, Wei F (2014) *Adv Mater* 26:6100
40. Zhu Y, Li L, Zhang C, Casillas G, Sun Z, Yan Z, Ruan G, Peng Z, Raji A-RO, Kittrell C, Hauge RH, Tour JM (2012) *Nat Commun* 3:1225
41. Lv R, Cui T, Jun M-S, Zhang Q, Cao A, Su DS, Zhang Z, Yoon S-H, Miyawaki J, Mochida I, Kang F (2011) *Adv Funct Mater* 21:999
42. Fan Z, Yan J, Zhi L, Zhang Q, Wei T, Feng J, Zhang M, Qian W, Wei F (2010) *Adv Mater* 22:3723
43. Zhao M-Q, Zhang Q, Huang J-Q, Tian G-L, Chen T-C, Qian W-Z, Wei F (2013) *Carbon* 54:403
44. Zhang WD, Phang IY, Liu TX (2006) *Adv Mater* 18:76
45. Wang Y, Wu J, Wei F (2003) *Carbon* 41:2939
46. Karousis N, Tagmatarchis N, Tasis D (2010) *Chem Rev* 110:5366
- 47 Premkumar T, Mezzenga R, Geckeler KE (2012) *Small* 8:1299
48. Ajayan PM, Tour JM (2007) *Nature* 447:1066
49. Nish A, Hwang J-Y, Doig J, Nicholas RJ (2007) *Nat Nano* 2:640
50. Gu J, Han J, Liu D, Yu X, Kang L, Qiu S, Jin H, Li H, Li Q, Zhang J (2016) *Small* 12:4993
51. Hersam MC (2008) *Nat Nano* 3:387
52. Preston C, Song D, Dai J, Tsinas Z, Bavier J, Cumings J, Ballarotto V, Hu L (2015) *Nano Res* 8:2242
53. Georgakilas V, Bourlinos A, Gournis D, Tsoufis T, Trapalis C, Mateo-Alonso A, Prato M (2008) *J Am Chem Soc* 130:873
54. Zhao Y, Yang L, Chen S, Wang X, Ma Y, Wu Q, Jiang Y, Qian W, Hu Z (2013) *J Am Chem Soc* 135:1201
55. Yu D, Xue Y, Dai L (2012) *J Phys Chem Lett* 3:2863
56. Ma X, Baldwin JKS, Hartmann NF, Doorn SK, Htoon H (2015) *Adv Funct Mater* 25:6157
- 57 Yang L, Jiang S, Zhao Y, Zhu L, Chen S, Wang X, Wu Q, Ma J, Ma Y, Hu Z (2011) *Angew Chem Int Ed* 123:7270
58. Thurakitseree T, Kramberger C, Zhao P, Aikawa S, Harish S, Chiashi S, Einarsson E, Maruyama S (2012) *Carbon* 50:2635
59. Wang X, Sun G, Routh P, Kim D-H, Huang W, Chen P (2014) *Chem Soc Rev* 43:7067
60. Shui J, Wang M, Du F, Dai L (2015) *Sci Adv* 1:e1400129
61. Gong K, Du F, Xia Z, Durstock M, Dai L (2009) *Science* 323:760
62. Qi C, Ma X, Ning G, Song X, Chen B, Lan X, Li Y, Zhang X, Gao J (2015) *Carbon* 92:245
63. Liu L, Ma W, Zhang Z (2011) *Small* 7:1504
64. Li Z, Liu Z, Sun H, Gao C (2015) *Chem Rev* 115:7046
65. Feng C, Liu K, Wu J-S, Liu L, Cheng J-S, Zhang Y, Sun Y, Li Q, Fan S, Jiang K (2010) *Adv Funct Mater* 20:885
66. Ma W, Song L, Yang R, Zhang T, Zhao Y, Sun L, Ren Y, Liu D, Liu L, Shen J, Zhang Z, Xiang Y, Zhou W, Xie S (2007) *Nano Lett* 7:2307
- 67 Ma W, Liu L, Zhang Z, Yang R, Liu G, Zhang T, An X, Yi X, Ren Y, Niu Z, Li J, Dong H, Zhou W, Ajayan PM, Xie S (2009) *Nano Lett* 9:2855
68. Niu Z, Zhou W, Chen J, Feng G, Li H, Ma W, Li J, Dong H, Ren Y, Zhao D, Xie S (2011) *Energy Environ Sci* 4:1440

69. Nasibulin AG, Kaskela A, Mustonen K, Anisimov AS, Ruiz V, Kivisto S, Rackauskas S, Tim-

111. Zhang SM, Zhang Q, Huang JQ, Liu XF, Zhu W, Zhao MQ, Qian WZ, Wei F (2013) Part Part Syst Charact 30:158
112. Song J, Gordin ML, Xu T, Chen S, Yu Z, Sohn H, Lu J, Ren Y, Duan Y, Wang D (2015) Angew Chem Int Ed 54:4325
113. Zhou G, Wang D-W, Li F, Hou P-X, Yin L, Liu C, Lu GQ, Gentle IR, Cheng H-M (2012) Energy Environ Sci 5:8901
114. Li X, Liu J, Zhang Y, Li Y, Liu H, Meng X, Yang J, Geng D, Wang D, Li R, Sun X (2012) J Power Sources 197:238
115. Magasinski A, Dixon P, Hertzberg B, Kvit A, Ayala J, Yushin G (2010) Nat Mater 9:353
116. Xue L, Xu G, Li Y, Li S, Fu K, Shi Q, Zhang X (2013) ACS Appl Mater Interfaces 5:21
117. Wang W, Kumta PN (2010) ACS Nano 4:2233
118. Evanoff K, Khan J, Balandin AA, Magasinski A, Ready WJ, Fuller TF, Yushin G (2012) Adv Mater 24:533
119. Jia X, Zhu X, Cheng Y, Chen Z, Ning G, Lu Y, Wei F (2015) Small 11:3135
120. Jia X, Cheng Y, Lu Y, Wei F (2014) ACS Nano 8:9265
121. Jia X, Zhang L, Zhang R, Lu Y, Wei F (2014) RSC Adv 4:21018
122. Choi SH, Lee J-H, Kang YC (2015) ACS Nano 9:10176
123. Jia X, Kan Y, Zhu X, Ning G, Lu Y, Wei F (2014) Nano Energy 10:344
124. Jia X, Chen Z, Suwarnasarn A, Rice L, Wang X, Sohn H, Zhang Q, Wu BM, Wei F, Lu Y (2012) Energy Environ Sci 5:6845
125. Zhang Y, Bai W, Cheng X, Ren J, Weng W, Chen P, Fang X, Zhang Z, Peng H (2014) Angew Chem Int Ed 53:14564
126. Zhou G, Li F, Cheng H-M (2014) Energy Environ Sci 7:1307
127. Pandolfo AG, Hollenkamp AF (2006) J Power Sources 157:11
128. Niu C, Sichel EK, Hoch R, Moy D, Tennent H (1997) Appl Phys Lett 70:1480
129. Hao L, Li X, Zhi L (2013) Adv Mater 25:3899
130. Wang G, Zhang L, Zhang J (2012) Chem Soc Rev 41:77
131. Lazzari M, Mastragostino M, Pandolfo A, Ruiz V, Soavi F (2011) J Electrochem Soc 158:A22
132. Izadi-Najafabadi A, Yasuda S, Kobashi K, Yamada T, Futaba DN, Hatori H, Yumura M, Iijima S, Hata K (2010) Adv Mater 22:E235
133. Jiang L, Sheng L, Long C, Fan Z (2015) Nano Energy 11: 47
134. Sun H, You X, Deng J, Chen X, Yang Z, Ren J, Peng H (2014) Adv Mater 26:2868
135. Cui C, Qian W, Yu Y, Kong C, Yu B, Xiang L, Wei F (2014) J Am Chem Soc 136:2256
136. Liu L, Niu Z, Chen J (2016) Chem Soc Rev 45:4340
137. Dong L, Xu C, Li Y, Huang Z-H, Kang F, Yang Q-H, Zhao X (2016) J Mater Chem A 4:4659
138. Xu Y, Kraft M, Xu R (2016) Chem Soc Rev 45:3039
139. Guo D, Shibuya R, Akiba C, Saji S, Kondo T, Nakamura J (2016) Science 351:361
140. Wu G, More KL, Johnston CM, Zelenay P (2011) Science 332:443
141. Li Y, Zhou W, Wang H, Xie L, Liang Y, Wei F, Idrobo J-C, Pennycook SJ, Dai H (2012) Nat Nano 7:394
142. Lu X, Yim W-L, Suryanto BHR, Zhao C (2015) J Am Chem Soc 137:2901
143. Jia H, Sun Z, Jiang D, Du P (2015) Chem Mater 27:4586
144. Gong M, Li Y, Wang H, Liang Y, Wu JZ, Zhou J, Wang J, Regier T, Wei F, Dai H (2013) J Am Chem Soc 135:8452
145. Melchionna M, Marchesan S, Prato M, Fornasiero P (2015) Catal Sci Technol 5:3859
146. Zhang W, Zhang H, Xiao J, Zhao Z, Yu M, Li Z (2014) Green Chem 16:211
147. Li P, Wang C, Zhang Y, Wei F (2014) Small 10:4543
148. Li P, Zong Y, Zhang Y, Yang M, Zhang R, Li S, Wei F (2013) Nanoscale 5:3367
149. Li P, Wang C, Li Z, Zong Y, Zhang Y, Yang X, Li S, Wei F (2014) RSC Adv 4:54115
150. Wang C, Li P, Zong Y, Zhang Y, Li S, Wei F (2014) Carbon 70:424
151. Yang S, Nie J, Wei F, Yang X (2016) Environ Sci Technol 50:9592
152. Inukai S, Cruz-Silva R, Ortiz-Medina J, Morelos-Gomez A, Takeuchi K, Hayashi T, Tanioka A, Araki T, Tejima S, Noguchi T, Terrones M, Endo M (2015) Sci Rep 5:13562
153. Holt JK, Park HG, Wang Y, Stadermann M, Artyukhin AB, Grigoropoulos CP, Noy A, Bakajin O (2006) Science 312:1034
154. Majumder M, Chopra N, Andrews R, Hinds BJ (2005) Nature 438:44
155. Das R, Ali ME, Hamid SBA, Ramakrishna S, Chowdhury ZZ (2014) Desalination 336:97

156. Baek Y, Kim C, Seo DK, Kim T, Lee JS, Kim YH, Ahn KH, Bae SS, Lee SC, Lim J, Lee K, Yoon J (2014) *J Membr Sci* 460:171
157. Hinds BJ, Chopra N, Rantell T, Andrews R, Gavalas V, Bachas LG (2004) *Science* 303:62
158. Kar S, Bindal RC, Tewari PK (2012) *Nano Today* 7:385
159. Nakanishi J, Morimoto Y, Ogura I, Kobayashi N, Naya, Ema, Endoh S, Shimada, Ogami A, Myojyo T, Oyabu T, Gamo, Kishimoto A, Igarashi T, Hanai S (2015) *Risk Anal* 35:1940
160. Nowack B, David R(,)-411.2(Fissan)-409.1oH, Morris H, Shatkin Stintz (,)-415.7(Zepp)-4073(R,)-414.2(Brouw Environ Int 59:1